Characterizing permafrost along the Alaska Highway, Southwestern Yukon,

Canada by

Joel D. Pumple

A thesis submitted in partial fulfillment of the requirements for the degree of

Master of Science

Department of Earth and Atmospheric Sciences

University of Alberta

Abstract

The Alaska Highway through Southwestern Yukon is located in the discontinuous permafrost zone with many areas of the highway corridor associated with degrading permafrost. Given the strategic value of the corridor, it is critical to have a clear understanding of permafrost characteristics and distribution, particularly in the context of a changing climate. In the Beaver Creek area, the Alaska Highway traverses both glaciated and non-glaciated terrain dating from the last glacial maximum. Permafrost characteristics are strongly influenced by regional glacial history, including the distribution of relict Pleistocene syngenetic permafrost. This thesis characterizes permafrost along the Alaska Highway between Beaver Creek and the Alaska border using a multidisciplinary approach. Our surveys include electrical resistivity tomography (ERT), airborne electromagnetics (AEM), geomorphological mapping, permafrost drilling, cryostratigraphic interpretations, geochemical analyses, and environmental monitoring to define the distribution and extent of permafrost within the study area. Using a combination of AEM and ERT data, we are able to define boundaries between non-glaciated terrain and glaciated terrain, highlight regional bedrock geology, outline valley fill geometry, image the thermal impact of small and large scale surface water features, and estimate the depth of permafrost. Radiocarbon dating and stable isotope analyses of $\delta^{18}O$ and $\delta^{2}H$ combined with detailed cryostratigraphy highlight the ice-rich nature of shallow Holocene permafrost and confirmed the presence of relict late Pleistocene ground ice at depth. The outcomes from this study will assist in the development of future mitigation strategies and maintenance plans for the highway.

Preface

This thesis is organized into 6 chapters, including introduction, methods, site descriptions, two manuscripts and conclusions. Chapters 4 and 5 represent the two manuscripts. Chapter 4 was published in October of 2015 as a short conference paper in the proceedings of the GeoQuebec 2015 conference and chapter 5 has not yet been published. I (Joel Pumple) co-authored chapter 4 with Duane Froese (University of Alberta) and Fabrice Calmels (Yukon Research Centre). Duane Froese assisted in designing the outline of the paper and Fabrice Calmels was involved with collecting the field data used in the paper. I (Joel Pumple) wrote the majority of the paper and created all the figures. Duane Froese and Fabrice Calmels edited the paper and provided constructive feedback through the editing process. Chapter 5 is a manuscript intended for publication in a journal in the near future. I (Joel Pumple) co-authored this manuscript with Duane Froese (University of Alberta), Fabrice Calmels (Yukon Research Centre), and Burke Minsley (USGS). Duane Froese assisted in designing the outline of the paper and Fabrice Calmels helped with collecting the field data used in the paper. I (Joel Pumple) wrote the majority of the paper and created most of the figures with the exception of the AEM figure which Burke Minsley provided and I (Joel Pumple) edited. Duane Froese and Fabrice Calmels edited the paper and provided constructive feedback through the editing process. Burke Minsley provided the AEM data and insight towards possible correlations with the ERT and borehole data.

Acknowledgements

Contents

List of Figures

List of Tables

Chapter 1: Introduction

Approximately 23% of Earth's land surface, and nearly 50% of Canada, is underlain by

permafrost (French and Shur 2010). The majority of permafrost occurs most frequently and

extensively in the Northern Hemisphere at latitudes greater than 50 degrees (Anisimov and

Nelson 1996). This area is split into three zones based on extent: continuous, discontinuous, and

isolated patches (Brown et *al*. 1997; Figure 1.1).
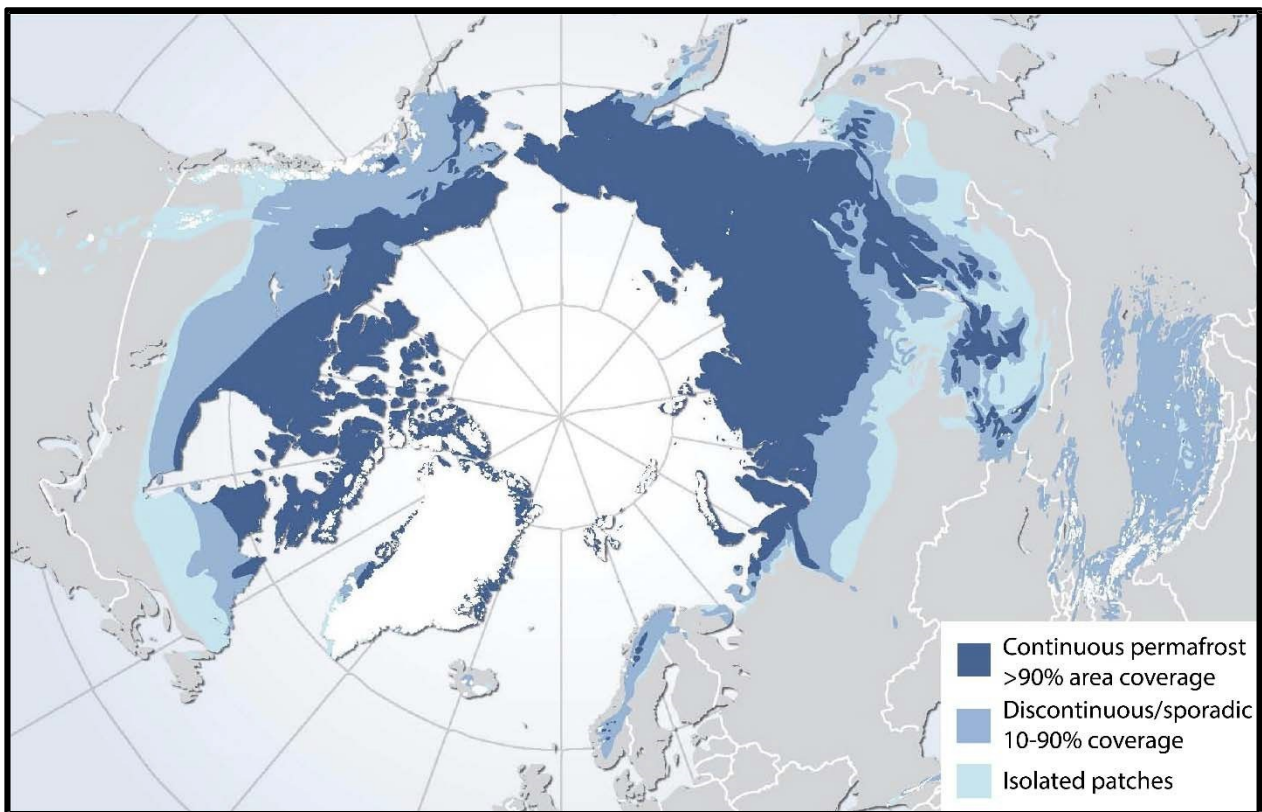
Figure 1.1: Map showing distribution of permafrost zones within the Northern Hemisphere
(prepared by Hugo Ahlenius (UNEP/GRID-Arendal) and based upon Brown et *al*. 1997).

Beyond this spatial distribution, permafrost can also be divided into three genetic histories;

epigenetic, syngenetic, and polygenetic (French and Shur 2010). Epigenetic permafrost forms

following deposition of host sediments and syngenetic permafrost forms concurrently with

deposition (French and Shur 2010; Figure 1.2).
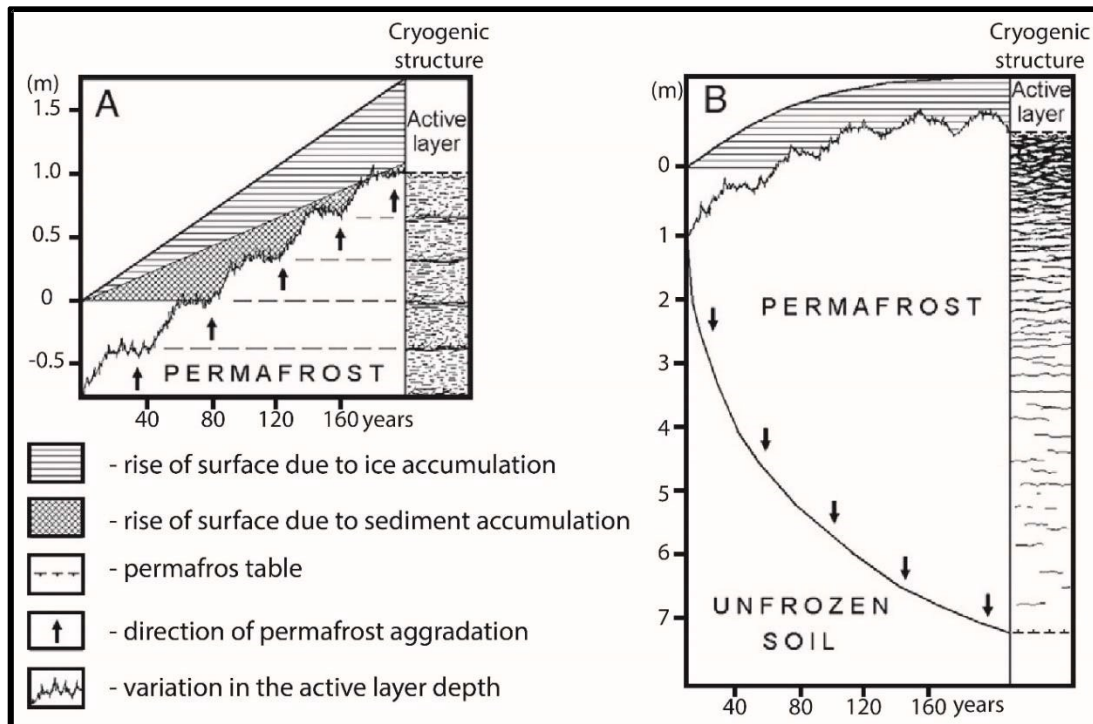
Figure 1.2: Formational process of (A) syngenetic and (B) epigenetic permafrost. Image modified from French and Shur (2010).

Polygenetic permafrost occurs when a single stratigraphic unit contains both epigenetic and syngenetic permafrost (Murton and French 1994; French and Shur 2010). Most commonly, syngenetic permafrost occurs within the continuous permafrost zone, whereas the discontinuous permafrost zone is largely epigenetic permafrost (Murton and French 1994; French and Shur 2010). The ice volume content in permafrost varies greatly depending on its genetic history. Syngenetic permafrost is often characterized by ice rich material including loess or loess-like silty sediments and/or peat and exhibits a rhythmically ordered habit (i.e. layered or lenticular cryostructure) (Murton and French 1994; French and Shur 2010). Epigenetic permafrost tends to have a lower ice volume content relative to syngenetic and is often associated with a reticular or structureless cryostructure (Murton and French 1994; French and Shur 2010). The distribution and thickness of syngenetic and epigenetic permafrost is jointly controlled by regional climate, aspect, elevation, local vegetation cover

and surfaces disturbances including fires, mass movements and anthropogenic activates (Williams and Burn 1996; Burn 1998; Huscroft et *al*. 2003; Shur and Jorgenson 2007; Reyes et *al*. 2010; French 2011; Calmels et *al*. 2012; Kanevskiy et *al*. 2014). Within the discontinuous permafrost zone in Southern Yukon, thick syngenetic ice-rich permafrost preserved from the Late Pleistocene and relatively thinner epigenetic ice-rich permafrost are divided by the McConnell glacial boundary (Duk-Rodkin 1999; Ward et *al*. 2007).

The Late Pleistocene McConnell Glaciation in Southwestern Yukon

During the Late Pleistocene southern Yukon was affected by the advance of the Cordilleran ice-sheet which reached its maximum extent ca. 20 ka (Matthews et *al*. 1990; Jackson et *al*. 1991; Jackson and Harington 1991; Duk-Rodkin 1999; Figure 1.3).
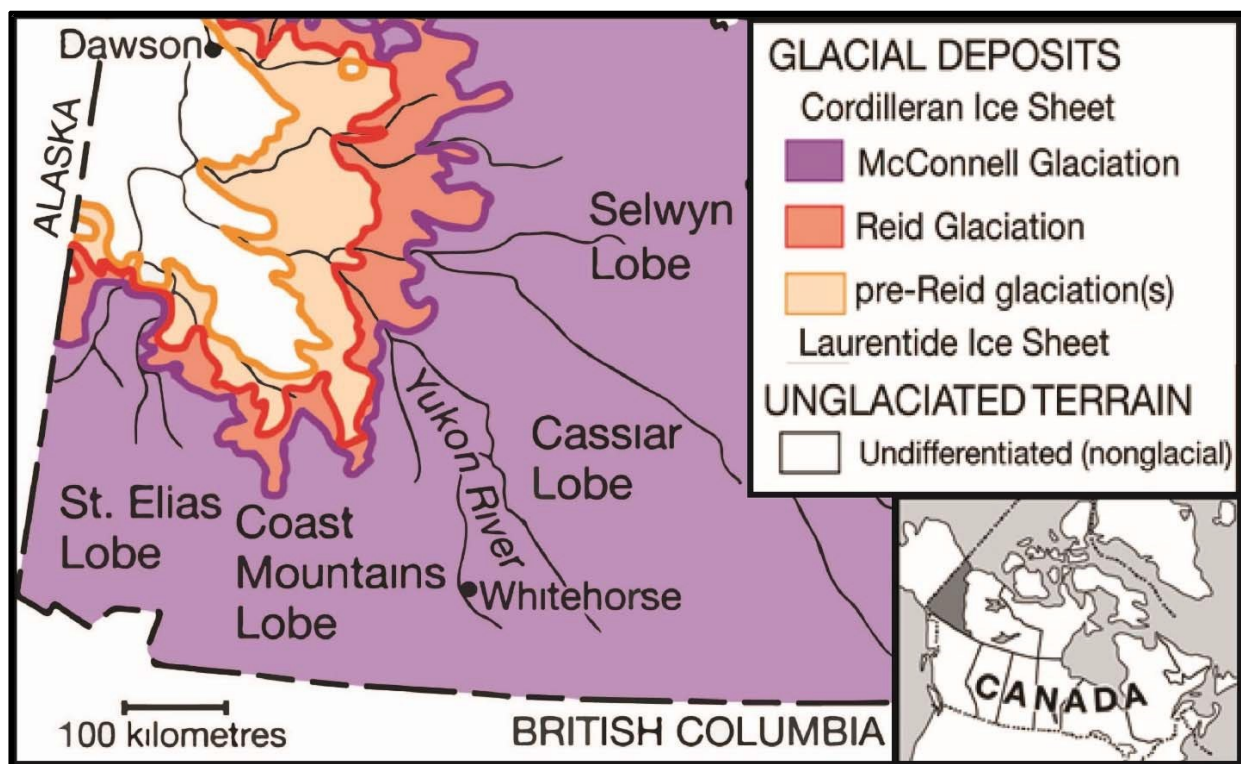
Figure 1.3: Map of Southwestern Yukon, Canada, showing the maximum extent of past glaciations that affected Yukon (based on Ward et *al*. (2007) modified from Duk-Rodkin (1999)).

The Cordilleran Ice Sheet is better termed an ice-complex defined by a combination of topographically controlled coalescing valley glaciers and piedmont lobes (Jackson et *al*. 1991). The glaciers that advanced northward into southern Yukon were also not nearly as thick as their continental counterpart, holding an average thickness equal to the local topographic highs (Jackson et *al*. 1991). The Late Pleistocene Cordilleran advance was the least extensive recorded within Yukon (Jackson et *al*. 1991). It is hypothesized that this restricted extent is due to the climate of Interior Yukon and Alaska and the pronounced rain shadow effect of the St. Elias Mountains (Figure 1.4).
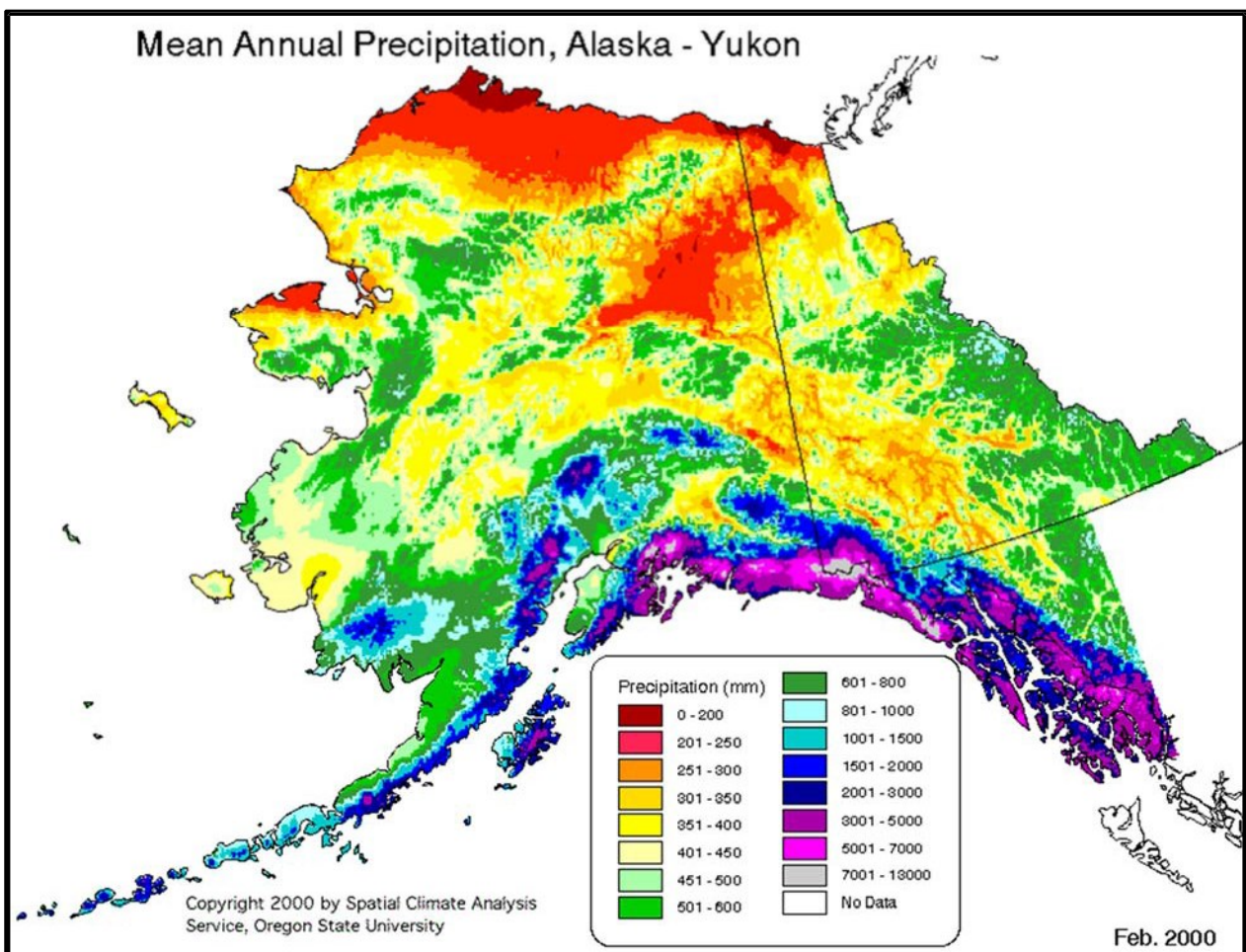
Figure 1.4: Map showing Mean Annual Precipitation for Alaska and Yukon (PRISM Climate Group 2000).

The extent of the Late Pleistocene (McConnell) glaciation in Southwestern Yukon was

4

mapped by Rampton in 1978. Based on Rampton's (1978) surficial maps the St. Elias Lobe

pushed northward to the Beaver Creek area, stopping just south of the present day town site.

Thus terrain north of Beaver Creek was not glaciated during the Late Pleistocene. The

proximity to the maximum extent of the St. Elias Lobe provides an opportunity to investigate

the paleo-periglacial environment and related permafrost characteristics. One of the central

questions in this thesis is whether or not relict Pleistocene permafrost is present within the

study area given the proximity of the Late Pleistocene glacial boundary.

Cryostratigraphy and water isotopes

Cryostratigraphy is a branch of geocryology and is defined by French and Shur (2010) as the

study of frozen layers in Earth's crust. If combined with radiocarbon dating, cryostratigraphy

can provide a robust approach to correlation between permafrost boreholes. Additionally,

sediment pore water isotopes can help provide a simple differentiation between glacial and

interglacial paleoclimates with $\delta^{18}O$ values of ca. $< -24‰$ and $> -24‰$ respectively (Kotler

and Burn 2000; Lacelle 2011). Elsewhere in Yukon, relict permafrost has been discovered

preserved beneath the surface (Froese et *al.* 2008; Lacelle et *al*. 2009). If Pleistocene

permafrost is present it provides two important truths about the region: (1) relict Pleistocene

permafrost has remained stable through at least the present interglacial period and (2) the

landscape contains ice-rich permafrost at depth, important information for current and future

infrastructure in the region.

The Alaska Highway

The Alaska Highway, originally constructed by the U.S. Army Corps of Engineers during the

1940s, provides vital road access between Northern British Columbia and Alaska (Lundberg 2013, Figure 1.5). The section of the highway between Whitehorse and Delta Junction lies mainly in the discontinuous permafrost zone.

Figure 1.5: Historical map of the Alaska Highway sourced from the Yukon Archives. United States. Federal Works Agency. Public Roads Administration, 1943. Map H-1179 (annotated copy).

The initial and continued disturbance caused by the highway construction and maintenance has resulted in a change in the natural ground cover resulting in a change in the ground temperature. This change in ground temperature or warming of the permafrost below the highway results in ground subsidence proportional to the excess ground ice present below the highway. Excess ground ice is defined in this thesis as the volume of ground ice which exceeds the total pore volume of the sediment under natural unfrozen conditions. Continued road maintenance is a shared interest of Canadian and U.S. governments as it promotes

tourism and trade through Western Canada and Alaska. The costs of maintaining the Alaska Highway are much more substantial than other highways due to the nature of the ground on which it was constructed. The need for a clear understanding of the subsurface beneath the Alaska Highway increases with continued ground destabilization in permafrost areas containing infrastructure (Throop et *al*. 2012).

Thesis objectives and organization

This thesis focuses on characterizing permafrost within the study area in terms of its cryostructures, ground ice content, grain size, ground ice stable isotopes (δ^{18}O, δD), organic content, and extent. Using the data from these proxies, three areas with different geological histories have been defined based on their spatial and/or temporal relation with the Late Pleistocene (last glacial maximum) glacial limit that crosscuts the study area. Electrical resistivity tomography (ERT) and airborne electromagnetic (AEM) surveys allowed for the extrapolation of borehole results and both local and regional mapping of permafrost.

The objectives of this thesis are:

1) Characterize permafrost across the study area based on cryostratigraphic and isotopic borehole results;
2) Define local relations between individual site locations and the Late Pleistocene glacial limit;
3) Extend borehole results with ERT and AEM surveys to map local and regional permafrost dynamics; and
4) Assess permafrost resilience at southern locations through the presence of relict permafrost.

Organization of thesis

Chapter 2 covers the field and laboratory methods used in this study and provides foundational information on some of the core techniques utilized including cryostratigraphy, stable isotopes (^{18}O, ^{2}H, ^{13}C and ^{15}N), radiocarbon dating, and geophysics (ERT and AEM). Chapter 3 details the descriptions and interpretations for each borehole site within the study area and concludes with a general discussion and conclusion. Chapter 4 presents a short manuscript published in the 2015 GEOQuebec proceedings titled "Characterizing permafrost valley fills along the Alaska Highway, Southwest Yukon". Chapter 5 presents a manuscript titled "Ground based and airborne methods along the Alaska Highway in the discontinuous permafrost zone, Southwestern Yukon". Chapter 6 presents the thesis conclusions and recommendations for future work.

References

Anisimov, O.A., and Nelson, F.E. 1996. Permafrost and global warming; strategies of adaptation. In Edited by Springer: New York, NY, United States, United States, pp. 440-449.

Brown, J., Ferrians, O.J.J., Heginbottom, J.A. and Melnikov, E.S. (1997). International Permafrost Association Circum-Arctic Map of Permafrost and Ground Ice Conditions, Scale 1:10,000,000. U.S. Geological Survey.

Burn, C.R. 1998. The response (1958-1997) of permafrost and near-surface ground temperatures to forest fire, Takhini River valley, southern Yukon Territory. Canadian Journal of Earth Sciences, 35: 184-199.

Calmels, F., Froese, D.G., and Clavano, W.R. 2012. Cryostratigraphic record of permafrost degradation and recovery following historic (1898-1992) surface disturbances in the klondike

region, central yukon territory 1,2. Canadian Journal of Earth Sciences, 49: 938-952.

Duk-Rodkin, A. 1999. Glacial limits map of Yukon Territory. Geological Survey of Canada, Open File 3694, Indigenous and Northern Affairs Canada Geoscience Map 1999-2, scale 1:1 000 000.

French, H., and Shur, Y. 2010. The principles of cryostratigraphy. Earth-Science Reviews, **101**: 190-206.

French, H., 2011. Frozen sediments and previously-frozen sediments. Geological Society, London, Special Publications, 354 (1), 153-166.

Froese, D.G., Westgate, J.A., Reyes, A.V., Enkin, R.J., and Preece, S.J. 2008. Ancient permafrost and a future, warmer Arctic. Science, **321**: 1648-1648.

Huscroft, C.A., and Lipovsky, P.S. 2003. Climate change and periglacial landslide activity in south-western Yukon Territory. EOS, Transactions, American Geophysical Union, **84**: @AbstractC21B-0811.

Jackson, L.E., and Harington, C.R. 1991. Middle Wisconsinan mammals, stratigraphy, and sedimentology at the Ketza River site, Yukon Territories. Géographie Physique et Quaternaire, **45**: 69-77.

Jackson, L.E., Jr., Ward, B.C., Duk-Rodkin, A., and Hughes, O.L. 1991. The last Cordilleran ice sheet in southern Yukon Territory. Géographie Physique et Quaternaire, **45**: 341-354.

Kotler, E., Burn, C.R., 2000. Cryostratigraphy of the Klondike "muck" deposits, west-central Yukon Territory. Canadian Journal of Earth Sciences, 37, 849–861.

Lundberg, M. 2013. The Alaska Highway: The road to North America's last frontier. PR

Distributing, 4.

Lacelle, D., St-Jean, M., Lauriol, B., Clark, I.D., Lewkowicz, A., Froese, D.G., Kuehn, S.C., and Zazula, G. 2009. Burial and preservation of a 30,000 year old perennial snowbank in Red Creek valley, Ogilvie Mountains, central Yukon, Canada. Quaternary Science Reviews, **28**: 3401-3413.

Lacelle, D. 2011. On the delta ^{18}O, delta D and D-excess relations in meteoric precipitation and during equilibrium freezing; theoretical approach and field examples. Permafrost and Periglacial Processes, **22**: 13- 25.

Mackay, J. R., 1972. The world of underground ice. Annals of the Association of American Geographers, 62 (1), 1-22.

Matthews, J.V., Jr., Schweger, C.E., and Hughes, O.L. 1990. Plant and insect fossils from the Mayo Indian Village section (central Yukon); new data on middle Wisconsinan environments and glaciation. Géographie Physique et Quaternaire, **44**: 15-26.

Meyer, H., Schönicke, L., Wand, U., Hubberten, H.W., Friedrichsen, H., 2000. Isotope studies of hydrogen and oxygen in ground ice – experiences with the equilibration technique. Isotopes in Environmental and Health Studies, 36 (2), 133-149.

Popov, A.I., Rozenbaum, G.E., and Tumel', N.V. 1985. Kriolitologiya. Izd. Mosk. Univ. : Moscow, USSR, USSR. PRISM Climate Group, Oregon State University, http://prism.oregonstate.edu, created February 2000.

Rampton, V.N. 1978. Surficial geology and geomorphology; Mirror Creek, Yukon Territory. Geological Survey of Canada: Ottawa, ON, Canada, Canada.

Reyes, A.V., Froese, D.G., and Jensen, B.J.L. 2010. Permafrost response to last interglacial

warming; field evidence from non-glaciated Yukon and Alaska. Quaternary Science Reviews, **29**: 3256-3274.

Throop, J., Lewkowicz, A.G., and Smith, S.L. 2012. Climate and ground temperature relations at sites across the continuous and discontinuous permafrost zones, northern Canada. Canadian Journal of Earth Sciences, **49**: 865-876.

Ward, B.C., Bond, J.D., and Gosse, J.C. 2007. Evidence for a 55-50 ka (early Wisconsin) glaciation of the Cordilleran ice sheet, Yukon Territory, Canada. Quaternary Research, **68**: 141-150.

Chapter 2: Methods

Distribution of ice-rich Pleistocene age permafrost near the McConnell glacial boundary in

Southern Yukon is poorly understood (Ward et *al*. 2007; Duk-Rodkin 1999). Current and

future infrastructure in this area would benefit greatly from additional permafrost research.

This thesis aims to characterize the distribution and history of permafrost within the study area

using a multidisciplinary approach including geophysics, permafrost drilling, cryostratigraphy,

and geochemical analyses.

This chapter covers methods applied during the study starting with the field methods followed

by a brief background and methodology for cryostratigraphy, stable isotopes, radiocarbon

dating and geophysics in the capacity they were utilized.

Field methods

All drilling and ERT site locations were recorded using a Garmin global positioning system

(GPS) device with a precision of +/- 12 meters. Vegetation at each site was recorded with a

digital camera and the dominant plant assemblage was noted. Each site location was selected

based on topography, aspect, surficial geology following Rampton (1978), and vegetation

cover. The core samples provide direct information on the local permafrost whereas

geophysical surveys provide a better understanding of the extent and thickness of permafrost in

the local area (ERT) or across the study region (AEM). In total fourteen boreholes were

drilled within the study area using a portable earth drill (Figure 2.1; Calmels et *al*. 2005) with

an average depth of four meters. All cores recovered from the boreholes were bagged and

labeled with a unique site name and core number. The collected cores were then stored in a

Figure 2.1: Two person operated earth-drill (left) (Calmels et *al*. 2005) and a 4 inch diameter diamond tooth core barrel used for drilling permafrost cores (right).

portable cooler on site and at the end of the day transferred to a deep freeze (-20 °C). Upon

completion of each field season (2013 and 2014), the cores were transported to the University

of Alberta via a deep freeze on a truck bed (2013) and coolers on an Airnorth cargo flight

(2014). Once at the University of Alberta the cores were cut lengthwise in half using a rock

saw in the department of Earth and Atmospheric Sciences (EAS). This facilitated easy

subsampling for laboratory analyses. The halved cores flat surface was easily scraped clean

with a razor blade to show cryostructures in detail. Each core was then photographed with a

measuring tape, set to each core's depth of retrieval, as scale and a label displaying each core's

unique site name and core number. Once the half-cores were photographed they were cut into

shorter lengths for additional analyses.

Cryostratigraphy

Cryostratigraphy is a branch of geocryology defined by French and Shur (2010) as the study of

frozen layers in Earth's crust. Geocryology is the study of frozen ground including thermal

dynamics and mechanical properties of frozen sediments (Williams and Smith 1989). Modern

sedimentology (Boggs 1987) and Russian geocryology (Yershov 1998) provide a strong

foundation for most of the concepts and terms used in contemporary cryostratigraphy (Murton

and French 1994). Cryostratigraphy is not unlike sedimentology in that the focus is on

description, classification and origin of the sedimentary material under investigation. However,

cryostratigraphy differs from sedimentology by including the abundance and distribution of

ground ice relative to the surrounding sediment and vice versa. It is by describing and

classifying the relation of sediment to ice in ice-dominant stratigraphy that cryostratigraphy

differs from Russian geocryology (Murton and French 1994). Cryostratigraphy has, and

continues to provide, a more detailed understanding of the shallow subsurface in permafrost

environments.

Cryostructures

A cryostructure is defined by the geometry and distribution of ice and sediment found within a

sample of permafrost (Murton and French 1994; Figure 2.2). It has been noted that certain

cryostructures are related to the genetic history of the host permafrost. Syngenetic permafrost

typically contains an ice-rich sediment displaying a rhythmically ordered habit (ie. layered or

lenticular cryostructure) (French and Shur 2010). Epigenetic permafrost tends to have a lower

ice volume content compared to syngenetic and is often associated with reticular or structureless cryostructures (French and Shur 2010).

This study has adopted the cryostructure classification scheme as used by Murton and French (1994). They presented seven cryostructures: structureless (Si), lenticular (Le), layered (La), regular reticular (Rr), irregular reticular (Ri), crustal (Cr), and suspended (Su). Each cryostructure is defined below and examples are given in Figures 2.3 and 2.4 from core samples along the Alaska Highway.

Structureless (Si); Although this cryostructure is identified by Murton and French (1994) as lacking a cryostructure, it is still an important term to help differentiate between cryostratigraphic layers. Structureless is simply when ice is not visible in frozen sediments and is most common in sands and gravels with low silt and clay content (Murton and French 1994; Figure 2.3).

Lenticular (Le); The cryostructure known as lenticular can represent either ice lenses in sediment or sediment lenses in ice (Murton and French 1994; Figure 2.3). The lenses can have any orientation, which is included in their description along with the length, thickness, and spatial relationship to other lenses: parallel or non-parallel combined with curved, wavy, or planar (Murton and French 1994). This cryostructure most commonly occurs in fine-grained sediments such as clay, silt, or fine-grained sands (Murton and French 1994). The orientation of the freezing front and any structural sedimentary influences are reflected in the orientation of the lenses (Murton and French 1994). This cryostructure is most often associated with syngenetic permafrost.

Layered (La); Layered Cryostructure contains layers of sediment and/or ice that are continuous. This cryostructure is described similar to lenses in terms of orientation (Murton and French 1994; Figure 2.3). This cryostructure occurs in ice-wedges, glacial ice, segregated ice, intrusive ice, and ice-rich sediments (Murton and French 1994). Layered cryostructure appears at variable depths with most occurring above three meters depth. This cryostructure is often found in conjunction with lenticular, and crustal cryostructures.

Reticulate (R); Reticulate cryostructure is a three-dimensional grid-like structure made up of ice veins and mud-rich sediment blocks (Murton and French 1994; Figure 2.4). This cryostructure is divided into two types: regular reticulate (Rr) where the ice grid is orientated with rectangular prism mud blocks; and irregular reticulate (Ri) where a non-orientated ice grid surrounds non-uniform mud blocks (Murton and French 1994). Reticulate cryostructures are most commonly associated with epigenetic permafrost and form through infilling of shrinkage cracks (Murton and French 1994).

Crustal (Cr); Murton and French (1994) define crustal as an ice rim or crust surrounding a clast and speculate that it is the best-known and least common cryostructure (Figure 2.4). This feature is often found just beneath the active layer where there is an ample supply of water and thick ice crusts form around frost susceptible clasts in an often silt-rich sediment (Murton and French 1994).

Suspended (Su); A suspended cryostructure consists of sediment surrounded by ice and appear to be suspended in the ice body (Murton and French 1994; Figure 2.4). The suspended grains

can range in size from silt to boulder, and in composition from sediment to wood (Murton and

French 1994). This cryostructure is most often found in massive ice bodies or just beneath the

active layer (Murton and French 1994).

A

CRYOSTRUCTURE AND CODE	SEDIMENT		ICE		OCCURRENCE AS OR WITHIN	
structureless (Sl)	sand gravel		pore		ice in sand + gravel	
lenticular (Le)	muddy peat mud (fine sand)	sand	segregated	crack infill	ice/sediment lenses massive ice icy sediments	(ice wedges) (composite sand-ice wedges) (dilation-crack ice)
layered (La)	muddy peat mud (fine sand)	sand	segregated intrusive	crack infill	ice/sediment layers massive ice icy sediments	ice wedges composite sand-ice wedges dilation-crack ice
regular reticulate (Rr)	mud		segregated		ice in mud	
irregular reticulate (Ri)	mud		segregated		ice in mud	
crustal (Cr)	mud frost-susceptible clasts		segregated			
suspended (Su)	mud sand gravel	mud sand gravel	segregated intrusive		icy layer at top of permafrost ice dykes in mud	ice lenses massive ice icy sediments ice dykes

B

	LAYERED		LENTICULAR	
	parallel	non-parallel	parallel	non-parallel
planar				
wavy				
curved				

Figure 2.2: Classification of cryostructures proposed by Murton and French (1994), ice is
shown in white and sediment in black. (A): cryostructures and codes. (B): additional terms
and illustrations to further describe layered and lenticular cryostructures.

Structureless	
Ice-poor peat with no visible excess ice.	Ice-poor inorganic silt with no visible excess ice.
Lenticular	
Ice-rich silts with visible excess ice in the form of wavy non-parallel lenticular and layered cryostructures.	Ice-poor silts with visible excess ice in the form of wavy non-parallel micro-lenticular and vertical and horizontal layered cryostructures.
Layered	
Ice-poor silts layered with visible excess ice in the form of non-parallel layered cryostructure.	Ice-rich silts with visible excess ice in the form of wavy parallel lenticular and parallel layered cryostructures.

Figure 2.3: The cryostructures in this study shown in photographed cores from the Alaska Highway study area and short descriptions, including structureless, lenticular, and layered.

Reticulate

Ice-poor inorganic silts surrounded by visible excess ice in the form of regular reticulate cryostructures.

Ice-poor inorganic silts encompassed by visible excess ice in the form of irregular reticulate cryostructure.

Crustal

Ice-rich peat with visible wood graments and excess ice in the form of crustal cryostructures concentrated around the wood fragments.

Ice-rich organic silts with visible wood frgaments and excess ice in the form of non-parallel wavy micro lenticular (silts) and crustal (wood fragments)cryostructures.

Suspended

Ice-poor inorganic and organic silts suurounded by visible excess ice creating a suspended cryostructures.

Ice-poor inorganic silts surounded by visible excess ice creating a suspended cryostructure.

Figure 2.4: The cryostructures in this study shown in photographed cores from the Alaska Highway study area and short descriptions, including reticulate, crustal, and suspended.

Cryofacies

As defined by Murton and French (1994), a cryofacies is based on the volumetric ice content

and ice crystal size within a given cryostratigraphic layer. Murton and French (1994) define

five types of cryofacies from pure ice to ice-poor sediment. These types are then sub-divided

based on the main sediment types present and given an abbreviated name based on their

mnemonic code. An example of the mnemonic code used would be IRS (ice-rich sand) or MtI

(mud-poor ice). A few additions have been made to this mnemonic code to ensure inclusivity

of all sedimentological components present. Additions to this mnemonic code can be found in

Table 2.1 along with their definitions.

Table 2.1: Modified from Murton and French (1994), this table represents a mnemonic code
used when describing cryofacies. * O acts as a modifier to any of the letters in the code by
indicting the constituent has a visible organic component. ** A subscript letter is to be used with
the first, third, and fourth letters to indicate the constituents' relative abundance. *** The third
and fourth letters are optional depending on the amount of constituents present. The first and
second letter represent the primary and secondary constituents respectively. The third and fourth
letters represent the tertiary and quaternary constituents if needed.

First – Fourth*** Letter			
Letter	Definition	Subscript Letter**	
G	gravel	Letter	Definition
S	sand	t	trace (1-10%)
M	silt/clay	l	little (10-20%)
P	peat	s	some (20-35%)
I	ice	a	and (35-50%)
W	wood		
O*	organic		

A total of seven cryofacies were defined in the Alaska Highway study. Photographs and a

short description of each cryofacies can be found in Figure 2.5. Detailed descriptions of each

cryofacies follow.

Cryofacies 1 (IaPOMWl); Ice-rich peat with little organic silt present and wood fragments.

The ice-rich structureless peat with visible wood fragments showing crustal cryostructure.

This cryofacies represent a continuation of the modern peat visible at the present day surface.

Cryofacies 2 (IaMOPl); Ice-rich cryoturbated to flat lying peat or organic-rich sandy silts; may contain wood fragments, and gravel. The sandy silts contain parallel layered (0.2-2.5 cm thick) or non-parallel wavy lenticular ice (0.1-0.8 cm thick). The peat displays non-parallel wavy lenticular (0.3-1.2 cm thick; Murton and French 1994) and the ash (if present) and sand or gravel rich layers are structureless. Crustal cryostructure commonly surrounds wood fragments where present.

Cryofacies 3 (IlOMWt); Flat lying to cryoturbated sandy silt with variable organic content, gravel, peat, ash (if present) and wood fragments with moderate to low ice content. Vertical and horizontal ice layers (0.1- 1.1cm thick) are visible throughout. Silt layers contain non-parallel wavy lenticular (0.3-6.0 mm thick; Murton and French 1994). The sections of peat are structureless to parallel wavy lenticular (0.1-1.0 cm thick) and the wood fragments have a crustal cryostructure. Ash and coarse sandy silt sections are structureless.

Cryofacies 4 (ItM); Ice-poor inorganic sandy silt with gravel; structureless cryostructure. Few vertical ice veins are observed (0.5 – 15 mm thick and up to 40 cm in observable length).

Cryofacies 5 (ItMWt); Cryoturbated ice-poor structureless grey sandy inorganic silt with wood fragments throughout.

Cryofacies 6 (MaI); Sediment-rich ice with suspended brown silt likely pool ice.

Cryofacies 7 (MtI); Ice with a trace of silt. This cryofacies displays visible vertical foliations

with traces of suspended fine-grained sediment in a ground ice body indicative of ice wedge

ice.

Cryofacies				
		#	Description	
1	2	1	Ice-rich structureless peat with visible wood fragments suspended in peat and crustal cryostructure.	
3	4	2	Ice-rich cryoturbated to flat lying peat or organic-rich sandy silts; may contain ash, wood fragments, and gravel. Sandy silts have parallel layered (0.2-2.5 cm thick) or non-parallel wavy lenticular ice (0.1-0.8 cm thick). Peat displays non-parallel wavy lenticular (0.3-1.2 cm thick). Ash (if present) and sand or gravel rich layers are structureless. Crustal cryostructure commonly surrounds wood fragments.	
5	6	3	Flat lying to cryoturbated sandy silt with variable organic content, gravel, peat, ash (if present) and wood fragments with moderate to low ice content. Vertical and horizontal ice layers (0.1-1.1cm thick) visible throughout. Silt contains non-parallel wavy lenticular (0.3-6.0 mm thick). Sections of peat are structureless to parallel wavy lenticular (0.1-1.0 cm thick) and wood fragments have a crustal cryostructure. Ash and coarse sandy silt are structureless.	
7		4	Ice-poor sandy silt with gravel; structureless cryostructure.	
		5	Cryoturbated ice-poor structureless grey sandy silt, organic silt, and wood fragments throughout.	
		6	Sediment-rich ice with suspended brown silt; pool ice or karst ice.	
		7	Foliated sediment-poor ice with subvertical gas bubble foliations; ice wedge ice.	

Figure 2.5: Images and descriptions of each cryofacies found in the study area. The classification scheme followed Murton and French (1994).

Cryofacies assemblage

A cryofacies assemblage is a group of associated cryofacies that represent a distinctive

cryostratigraphic unit (Murton and French 1994). Cryofacies assemblages allow for borehole

correlations based on significant cryostratigraphic transitions. Two cryofacies assemblages

have been identified from the above cryofacies section. Cryofacies assemblage 1 (upper unit)

includes cryofacies 1, 2, and 3. A sharp drop in the organic and ice content of the sediments marks the transition to cryofacies assemblage 2 (lower unit) containing cryofacies 4, 5, 6, and 7.

Ice volume measurements

Ice volume measurements were taken approximately every 20cm in each borehole using a water displacement method. The frozen sample was weighed using a XP-1500 Denver Instrument scale with a stated accuracy of +/-0.05g and lowered into a four inch diameter PVC tube pre-filled with 1.5 litres of water. Water was then extracted from the tube until the initial water level (1.5L) was achieved (Figure 2.6). The amount of water displaced was measured using a 250ml graduated cylinder with a stated accuracy of +/- 2ml. The sample was then removed from the tube, transferred to a clean tin tray, and placed in a drying oven at 60°C overnight to dry. The dry sample was then weighed using the same scale, crushed using a mortar and pestle, vacuum sealed in a clear plastic bag using a Food Saver vacuum sealer (V2244), and labeled according to the borehole and range of depth covered by the sample. Assuming the density of ice to be $0.9167g/cm^3$, the following equation was then used to calculate a volumetric ice content (VIC):

$$VIC\ (\%) = \frac{(M_t - M_d) \times 0.9167}{V_t} \times 100$$

M_t in the above equation represents the total frozen mass of the sample, M_d the total dry mass and V_t the total frozen volume. The precision of this ice volume measurement method was found to be +/- 2% based on repeat measurements. See appendix A for results tables.

Figure 2.6: PVC tube set for measuring IVC with clear rubber hose attached to the bottom control valve for precise drainage into graduated cylinder.

Grain size measurements

The dried and vacuum sealed samples remaining from the ice volume measurements were weighed using an XP-1500 Denver Instrument scale with a stated accuracy of +/-0.05g and placed in the top sieve of the sieve shaker for grain size analyses. Five sieves were used in the grain size separation: >2mm, >425um, >150um, >75um, and >45um. Each size fraction was weighed separately including material smaller than 45um. All separate size fraction weights were divided by the initial weight and multiplied by 100 to give a relative percent value. See appendix B for results tables.

Tephra preparation

All visible tephra layers were sampled and four were selected to represent the layers observed. The tephra samples were removed from the frozen core samples, transferred into a labelled aluminum tray, and placed in the drying oven at 60 °C overnight. The dried samples were wet sieved using the following four sieves from the Canadian Standard Sieve Series: 250um, 150um, 75um, and 45um. The sieves were cleaned between samples using an Elma Transsonic Digital S ultrasonic bath. Anything less than 45um was washed out and the remaining size fractions were transferred to 3 inch ceramic bowls, vacuum dried on P8 filter paper and placed in the drying oven until completely dry. The dry size fractions were then transferred to separate labelled snap cap plastic vials. Five to six grams of the size fraction >150um and <75um was transferred into a 15ml centrifuge tube. A premixed solution of lithium heteropolytungstates (LST) in water with a density of 2.42 g/ml was added to the centrifuge tube to fill it to the 12ml level. The tube was then capped and shaken by hand to thoroughly mix the tephra with the LST solution. Once mixed the centrifuge tubes were balanced and loaded into the centrifuge for a 10 minute cycle at 2500rpm. Centrifuged samples were decanted into new 15ml centrifuge tubes and diluted with de-ionized water. The decanted material contained mostly tephra and, once completely rinsed of LST, was dried in the oven at 60 °C on P8 filter paper. The dry tephra samples were then transferred to one of the six small holes (diameter of 4mm) in a plastic puck (5 mm thick with a diameter of 25 mm) and sealed in with epoxy. Once the epoxy had cured the puck was polished, labelled, carbon coated, and analyzed for glass major element composition on the Microprobe in the EAS department at the University of Alberta (Jensen et *al.* 2008).

Stable isotopes

Oxygen and hydrogen

Stable isotopes from oxygen and hydrogen can be used as proxies for past climate (Mariotti et al. 1980; Amundson et al. 2003; Opel et al. 2011). Ratios of isotopes from these elements are reported in δ-notation in parts per thousand (‰) using the following equation, in which R_{sample} is the molar ratio (e.g. $^{18}O/^{16}O$) of a specific sample and $R_{standard}$ is the molar ratio of Vienna Standard Mean Ocean Water (VSMOW):

$$\delta = \left(\frac{R_{sample}}{R_{standard}} - 1\right) \times 1000 \text{ ‰}$$

The ratio of $^{18}O/^{16}O$ in oxygen gives a $\delta^{18}O$ value and the ratio of H^2/H in hydrogen give a δD value. Displaying these two ratios in a co-isotope plot allows for predictions about the paleoclimate at the time of deposition. It has been noted that global isotope values of precipitation plot along a regression slope of 8 which has been named the global meteoric water line GMWL ($\delta D = 8*\delta^{18}O +10$; Epstein and Mayeda 1953; Craig 1961). The intercept value of 10 is representative of the deuterium excess d (d=δD-8*$\delta^{18}O$; Dansgaard 1964). Deuterium excess (d) is another climate proxy for the temperature and relative humidity of the air in the source region (Lacelle 2011). Recently more detailed local isotope analyses have been carried out on precipitation in the Northern Hemisphere during a project called Global Network of Isotopes in Precipitation (GNIP). GNIP found that local d-excess varied significantly across the Arctic (Lacelle 2011). High d values represent coastal influenced systems and low values represent continental influenced systems (Lacelle 2011). The majority of the water isotope results used in this thesis were analyzed on the Picarro water isotope

analyzer in the EAS department at the University of Alberta. The Picarro can run up to 40

samples (Figure 2.7).

Figure 2.7: Picarro water isotope analyzer in the EAS department at the University of Alberta.

Standards and unknowns are loaded in the same tray (see Figure 2.8 for tray layout) and the

septum is changed every three full runs or every 1200 injections. The syringe (SGE 5 μL

removable needle, part number 001984) was cleaned before and after every run and lasted an

average of two runs before needing to be replaced. The Picarro achieves a precision of $\pm$ 0.1‰

on $\delta^{18}O$ and $\pm$ 0.5 ‰ on δD (Gupta et *al*. 2009). The standards used are outlined below in

Table 2.2.
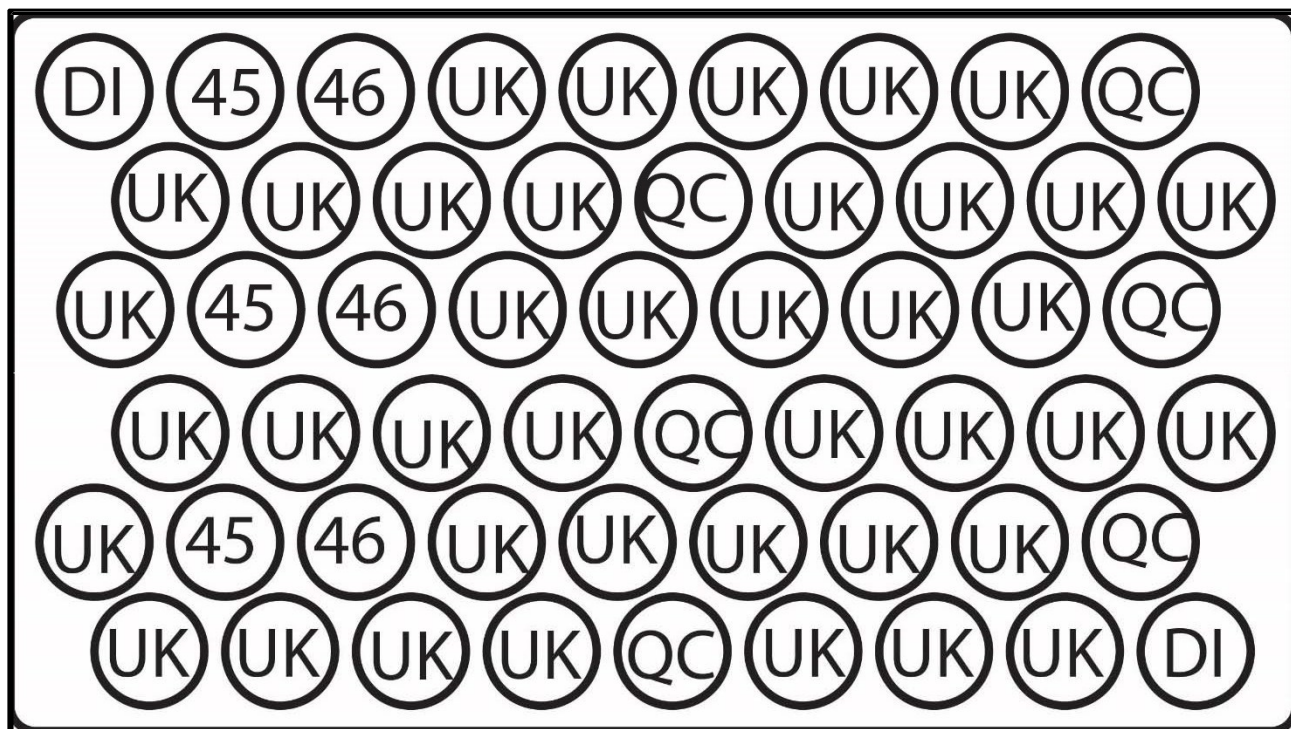
Figure 2.8: Tray layout used during water isotope analyses; UK= unknown, DI= deionized water (rinse), QC= secondary standard, 45 and 46= USGS standards USGS45 and USGS46.

Table 2.2: Water standards used on the Picarro for this study.

Standards	δ^2H VSMOW	δ^{18}O VSMOW	Reference
USGS45	-10.3	-2.24	U.S. Geological Survey, 2012a
Evian (QC)	-73.7	-10.29	Chesson et *al.* 2010
QCDI (QC)	-148.9	-19.08	based on repeat analysis
USGS46	-235.8	-29.8	U.S. Geological Survey, 2012b
LW2	-271.8	-33.94	A. Kwan 2013, pers. comm.

Ten to fifteen centimeter frozen core sections were sampled at a 10-20cm interval, vacuum sealed in a clear plastic bag using a Food Saver vacuum sealer (V2244), labeled according to the borehole and depth range covered by the sample and left to thaw at a controlled temperature (4˚C) in the laboratory fridge. The water was then extracted from the sample bag using a sterile plastic 3ml syringe and transferred to a glass 2ml vial through a 0.2μm syringe tip filter to ensure no fine particulates were transferred. The glass vial was labelled, filled to the top to

ensure there was no head space and capped with a small plastic screw cap. A small portion of

the first water samples collected from the study area were run on the Los Gatos Research

(LGR) model DLT-100 water isotope analyzer (Figure 2.9).

Figure 2.9: Los Gatos Research (LGR) model DLT-100 water isotope analyzer in the EAS department at the University of Alberta.

The LGR can run 20-30 unknown samples at a time. The ratio of standards to unknowns is

slightly different from the Picarro. Similar to the Picarro, two standards are used: one enriched

and one depleted as well as a laboratory secondary standard. The LGR achieves a precision of

± 0.15‰ on $\delta^{18}O$ and ± 2 ‰ on δD (Kurita et *al*. 2012). For more information on the

standards used, please see Table 2.3.

Table 2.3: Water isotope standards used on the LGR in this study.

Standards	δ^2H (‰)	δ^{18}O (‰)	Reference
LW2	-271.8	-33.94	A. Kwan 2013, pers. comm.
USGS45	-10.3	-2.24	U.S. Geological Survey, 2012a
Evian	-73.7	-10.29	Chesson et al. 2010

Nitrogen and carbon

The stable isotopes of nitrogen ^{15}N and ^{14}N from plant or animal remains samples can also be used as proxies for past climate when expressed as a δ^{15}N value. Amundson et al. (2003) discovered a negative trend in δ^{15}N with decreasing mean annual temperature (MAT) and increasing mean annual precipitation (MAP), although it was noted that MAP had less of an impact on this trend when compared to MAT (Amundson et al. 2003). Amundson et al. (2003) also found a latitudinal gradient in the global δ^{15}N results showing a depleting trend with increasing latitude. However, this relationship has not been observed within some North American animal species (Cormie and Schwarcz 1996).

Carbon stable isotopes ^{13}C and ^{12}C or more specifically δ^{13}C can be used as a supportive paleoclimate proxy for northern studies (Szpak et al. 2010). Pedogenetic effects along with the input signal from vegetation control the δ^{13}C values in bulk soil organic matter (SOM) (Zech et al. 2007). The difference in δ^{13}C between C3 (~-27‰) and C4 (~-14‰) plants has been found to cause variations within northern sediment records (Zech et al. 2007).

A total of 39 carbon and nitrogen isotopes samples were taken directly from the frozen cores and transferred to sterile 15 ml centrifuge tubes. Any moisture was removed from the sample using a freeze dryer and the sample was mixed well in the centrifuge tube. Each sample was then transferred to a pre- weighed 9X5 mm tin capsule and the total sample weight was measured using the EW-11336-02 Mettler Toledo Excellence XS Dual Range micro balance

in the EAS department. The capsules were then folded shut, pinched into a small sphere and placed in a 96-well tray with a record of the samples position. These samples were then shipped to University of California, Berkley Center for Stable Isotope Biogeochemistry for analysis.

Radiocarbon dating

Carbon has a radioactive isotope ^{14}C created in the upper atmosphere and incorporated into organisms through the uptake of CO_2. Radiocarbon dating uses the steady decay of ^{14}C ($t_{1/2}$=5568 years) to date material up to an age of ca. 50,000 ^{14}C years. BP (Stuiver and Polach 1977). This is done through the comparison of $^{14}C/^{12}C$ ratio within an organism once it has ceased active exchange of ^{14}C with the atmosphere (Stuiver and Polach 1977).

Nineteen samples (17 unknowns and 2 standards) were ^{14}C-dated for this study. The material selected for dating was mostly large mass (>3 mg) woody marco-fossils with the exception of one small mass (0.013 mgC) grass sample (BH12B-485). The analyses included a small mass (0.13mgC) sample of each standard and both were within error of their known values. Radiocarbon samples were prepared using an Acid-Base-Acid pre-treatment at the University of Alberta, in which samples were placed in sterilized glass culture tubes heated to 70°C and soaked for 30 minutes in 1M HCl, followed by 30 min washes of 1M NaOH until the solution was clear, and then a 30 minute 1M HCl wash. Samples were then neutralized through rinsing with ultrapure water, placed in a freezer until frozen and then freeze-dried. Prepared samples were analyzed at the Keck Accelerator Mass Spectrometry Lab at the University of California, Irvine.

Table 2.4: Radiocarbon standards used in this study.

Standards	Age (^{14}C BP)	Material	Reference
FIRI-F	4,510	wood shavings	Boaretto et al. 2002
AVR07-PAL	non-finite, last interglacial (MIS 5e)	wood shavings	Reyes et al. 2010

Due to the levels of ^{14}C produced in the atmosphere fluctuating over the last 60,000 years, radiocarbon results must be calibrated using the 'IntCal13' calibration curve (Reimer et al. 2013). All ages were calibrated using Calib radiocarbon calibration version 7.1html and reported as calendar years before present (Cal yrs. BP) with BP defined as 1950 AD (Stuiver and Polach 1977; Stuiver and Reimer, 2015).

Geophysics

Electrical Resistivity Tomography (ERT) is a geophysical method that measures the resistivity (R) of material in the sub-terrain to multiple frequencies of electrical currents sent between evenly spaced electrodes. Together the measuring array, number of electrodes, and spacing of electrodes control the extent of the ERT results. The spacing of electrodes also controls resolution and depth of results with resolution decreasing and depth increasing as spacing increases. ERT results alone can be very difficult to accurately interpret without additional site specific data (Loke and Barker 1996; Lewkowicz et al. 2011).

The ERT system used during this project was an Iris Syscal Junior switch 48, which uses an internal switching board for 48 electrodes to deliver multi-frequency pulses of electrical current to electrodes from its onboard 200 W power source achieving a resistivity accuracy of 0.5% (Figure 2.10). Five of the seven surveys used 48 electrodes with a 5 m spacing and a Wenner array for a total survey length of 235 m and reached a depth of 42 m. The remaining

two used 48 electrodes with a 2.5 m spacing and a Wenner array for a total survey length of
117 m and reached a depth of 20 m The surveys were inverted using RES2DINV (Loke and
Barker 1996).

Figure 2.10: Iris Syscal Junior switch 48, the ERT system that was used during this study
(http://www.uclm.es/dep/geologica/imagenesprospeccion/image00.jpg).

Airborne electromagnetics (AEM) is a regional scale geophysical method which provides
large three dimensional datasets that in the past have been used as a way to study permafrost
in and around large scale surface features such as rivers or lakes (Minsley et *al*. 2012). Similar
to the AEM survey discussed in Minsley et *al*. (2012), an AEM survey was carried out in
2005, again by the United States Geological Survey (USGS) as a part of a study along the
Alaska Highway within Alaska. The southern reaches of this survey crossed the border and
covered the northern section of this projects study site, providing the opportunity to expand the
geophysical results. The methods used during this survey can be found in Ball et *al*. (2011).
Chapter 5 includes the AEM results and interpretations.

References

Amundson, R., Austin, A.T., Schuur, E.A.G., Yoo, K., Matzek, V., Kendall, C., Uebersax, A., Brenner, D., and Baisden, W.T. 2003. Global patterns of the isotopic composition of soil and plant nitrogen. Global Biogeochemical Cycles, **17**: 31.01-31.01.

Astley, B.N., and Delaney, A.J. 2008. Permafrost delineation near Fairbanks, Alaska, using geophysical techniques. Extended Abstracts - International Conference on Permafrost, **9**: 9-10.

Boaretto, E., Bryant, C., Carmi, I., Cook, G., Gulliksen, S., Harkness, D., Heinemeier, J., McClure, J., McGee, E., Naysmith, P., Possnert, G., Scott, M., van, d.P., and van Strydonck, M. 2002. Summary findings of the Fourth International Radiocarbon Intercomparison (FIRI) (1998-2001). Journal of Quaternary Science, **17**: 633-637.

Boggs, S., Jr. 1987. Principles of sedimentology and stratigraphy. Merrill Publ. Co.: Columbus, OH, United States, United States.

Calmels, F., Gagnon, O., and Allard, M. 2005. A portable earth-drill system for permafrost studies. Permafrost and Periglacial Processes, **16**: 311-315.

Chesson, L.A., Bowen, G.J., Ehleringer, J.R., 2010. Analysis of the hydrogen and oxygen stable isotope ratios of beverage waters without prior water extraction using isotope ratio infrared spectroscopy. Rapid Communications in Mass Spectrometry, 24, 3205-3213.

Cormie, A.B., and Schwarcz, H.P. 1996. Effects of climate on deer bone delta ^{15}N and delta ^{13}C; lack of precipitation effects on delta ^{15}N for animals consuming low amounts of C (sub 4) plants. Geochimica et Cosmochimica Acta, **60**: 4161-4166.

Craig, H. 1961. Standard for reporting concentrations of deuterium and oxygen-18 in natural waters. Science, **133**: 1833-1834.

Dansgaard, W. 1964. Stable isotopes in precipitation. Tellus XVI, **4**: 436-468.

Duk-Rodkin, A. 1999. Glacial limits map of Yukon Territory. Geological Survey of Canada, Open File 3694, Indigenous and Northern Affairs Canada Geoscience Map 1999-2, scale 1:1 000 000.

Epstein, S. and Mayeda, T. 1953. Variation of ^{18}O content of waters from natural sources. Geochimica et Cosmochimica Acta, **4**: 213-224.

French, H., and Shur, Y. 2010. The principles of cryostratigraphy. Earth-Science Reviews, **101**: 190-206.

Gupta, P., Noone, D., Galewsky, J., Sweeney, C., and Vaughn, B.H. 2009. A new laser-based, field-deployable analyzer for laboratory-class stable isotope measurements in water. Geochimica et Cosmochimica Acta, **73**: A480-A480.

IAEA/WMO (2015). Global Network of Isotopes in Precipitation. The GNIP Database. Accessible at: http://www.iaea.org/water.

Jouzel, J., Merlivat, L., and Lorius, C. 1982. Deuterium excess in an East Antarctic ice core suggests higher relative humidity at the oceanic surface during the last glacial maximum. Nature, **299**: 688-691.

Kurita, N., Newman, B.D., Araguas-Araguas, L., and Aggarwal, P. 2012. Evaluation of continuous water vapor dD and d18O measurements by off-axis integrated cavity output spectroscopy. Atmospheric Measurement Techniques, 5: 2069-2080.

Lacelle, D. 2011. On the delta ^{18}O, delta D and D-excess relations in meteoric precipitation and during equilibrium freezing; theoretical approach and field examples. Permafrost and Periglacial Processes, **22**: 13- 25.

Lewkowicz, A.G., Etzelmuller, B., and Smith, S.L. 2011. Characteristics of discontinuous permafrost based on ground temperature measurements and electrical resistivity tomography, southern Yukon, Canada. Permafrost and Periglacial Processes, **22**: 320-342.

Loke, M.H., and Barker, R.D. 1996. Practical techniques for 3D resistivity surveys and data inversion. Geophysical Prospecting, **44**: 499-523.

Minsley B.J., Abraham J.D., Smith B.D., Cannia J.C., Voss C.I., Jorgenson M.T., Walvoord M.A., Wylie B.K., Anderson L., Ball L.B., Deszcz-Pan M., Wellman T.P., Ager T.A., 2012. Airborne electromagnetic imaging of discontinuous permafrost. Geophysical Research Letters 39: L02503. DOI: 10. 1029/2011GL050079.

Murton, J.B., and French, H.M. 1994. Cryostructures in permafrost, Tuktoyaktuk coastlands, western Arctic Canada. Canadian Journal of Earth Sciences, **31**: 737-747.

Opel, T., Dereviagin, A.Y., Meyer, H., Schirrmeister, L., and Wetterich, S. 2011. Palaeoclimatic information from stable water isotopes of Holocene ice wedges on the Dmitrii Laptev Strait, northeast Siberia, Russia. Permafrost and Periglacial Processes, **22**: 84-100.

Pastick, N.J., Jorgenson, M.T., Wylie, B.K., Minsley, B.J., Ji, L., Walvoord, M.A., Smith, B.D., Abraham, J.D., and Rose, J.R. 2013. Extending airborne electromagnetic surveys for regional active layer and permafrost mapping with remote sensing and ancillary data, Yukon Flats ecoregion, central Alaska. Permafrost and Periglacial Processes, **24**: 184-199.

Reimer, P.J., Bard, E., Bayliss, A., Beck, J.W., Blackwell, P.G., Ramsey, C.B., Buck, C.E., Cheng, H., Edwards, R.L., Friedrich, M., Grootes, P.M., Guilderson, T.P., Haflidason, H., Hajdas, I., Hatte, C., Heaton, T.J., Hoffmann, D.L., Hogg, A.G., Hughen, K.A., Kaiser, K.F., Kromer, B., Manning, S.W., Niu, M., Reimer, R.W., Richards, D.A., Scott, E.M., Southon, J.R., Staff, R.A., Turney, C.S.M., and van, D.P. 2013. IntCal13 and Marine13 radiocarbon age calibration curves 0-50,000 years cal BP. Radiocarbon, **55**: 1869-1887.

Reyes, A.V., Froese, D.G., and Jensen, B.J.L. 2010. Permafrost response to last interglacial warming; field evidence from non-glaciated Yukon and Alaska. Quaternary Science Reviews, **29**: 3256-3274.

Stevenson, B.A., Kelly, E.F., McDonald, E.V., and Busacca, A.J. 2005. The stable carbon isotope composition of soil organic carbon and pedogenic carbonates along a bioclimatic gradient in the Palouse region, Washington State, USA. Geoderma, **124**: 37-47.

Stuiver, M., and Polach, H.A. 1977. Discussion; reporting of C-14 data. Radiocarbon, **19**: 355-363.

Szpak, P., Groecke, D.R., Debruyne, R., MacPhee, R.D.E., Guthrie, R.D., Froese, D.G., Zazula, G.D., Patterson, W.P., and Poinar, H.N. 2010. Regional differences in bone collagen delta ^{13}C and delta ^{15}N of Pleistocene mammoths; implications for paleoecology of the Mammoth Steppe. Palaeogeography, Palaeoclimatology, Palaeoecology, **286**: 88-96.

U.S. Geological Survey, 2012a. Report of Stable Isotopic Composition, Reference Material USGS45, Reston, VA.   http://isotopes.usgs.gov/lab/referencematerials/USGS45.pdf.

U.S. Geological Survey, 2012b. Report of Stable Isotopic Composition, Reference Material USGS46, Reston, VA.   http://isotopes.usgs.gov/lab/referencematerials/USGS46.pdf.

Yershov, E.D. 1998. Studies in Polar Research: General Geocryology. Cambridge University Press, United Kingdom.

Zech, M., Zech, R., and Glaser, B. 2007. A 240,000 year stable carbon and nitrogen isotope record from a loess-like palaeosol sequence in the Tumara Valley, northeast Siberia. Chemical Geology, **242**: 307-318.

Chapter 3: Cryostratigraphy, Geophysical Results, Site Descriptions and Interpretations.

This chapter introduces the general study area. It also contains site specific descriptions and interpretations ending with general discussions and conclusions.

General site description

The study area is located in Southwestern Yukon, Canada centralized around Beaver Creek, Yukon along the Alaska Highway. Climate in the Beaver Creek area is sub-continental and characterized by a mean annual temperature of -4.9 °C as recorded by the Beaver Creek airport weather station. A 40 km section of the Alaska Highway, ten kilometers north of Beaver Creek and thirty kilometers to the south encapsulates the data collection sites used in this study. This region of Southwestern Yukon is in the discontinuous permafrost zone (DPZ), an area of meta-stable warm permafrost, making it a suitable area to study the characteristics of permafrost as it approaches thaw temperatures (Figure 3.1; Throop et *al.* 2012). The dominant vegetation in the study area is a combination of moss-sphagnum and sedge-tussock communities coupled with low-density black spruce and dwarf birch in the lowlands and high density white spruce or poplar in the uplands. Similar to the findings of Jorgensen et *al.* (2010), the north and south slope aspects exhibit differing vegetation assemblages and densities.

The McConnell (ca. 20 ka BP) glacial limit, as mapped by Duk-Rodkin (1999) cross cuts this study area giving us an opportunity to investigate both glacial and non-glacial deposits (Figure 3.2). Based on Rampton's (1978) surficial map (Figure 3.3), the McConnell glacial limit is just south of Beaver Creek and it is assumed that terrain south of the limit is glacial and material north is largely non-glacial with the exception of the Reid Glaciation as seen in both Figure 3.2 and Figure 3.4.
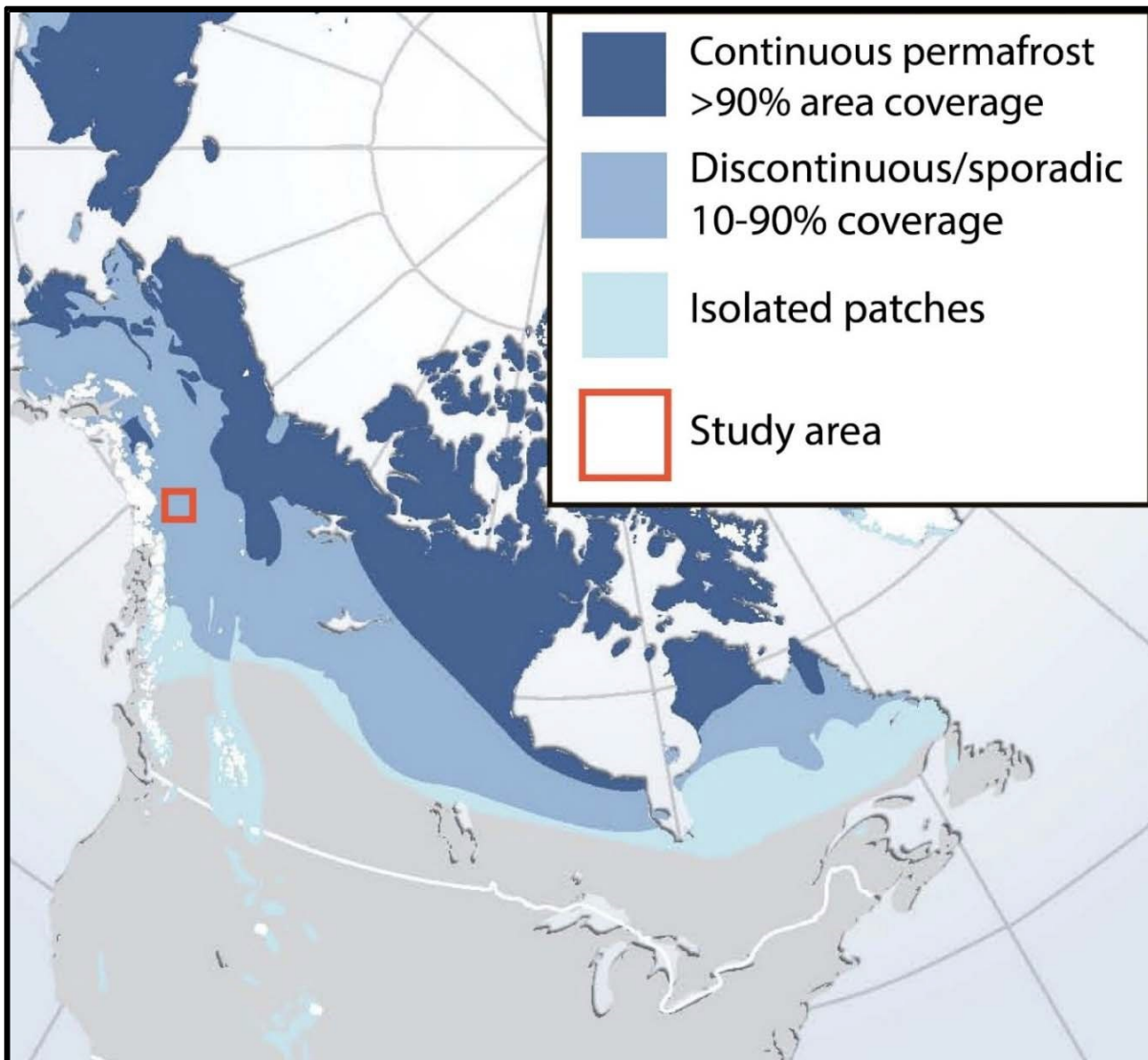
Figure 3.1: Map showing distribution of permafrost zones within North America. The study sites discussed in this chapter all fall within the red square in the map above (based on Heginbottom et *al.* 1995).

A second boundary has been added to Figure 3.4 based on Rampton's (1978) surficial map and represents the assumed extent of terrain directly influenced by the discharge of McConnell melt water through the study area. The inferred outwash channels indicated in Figure 3.4 are based on the distribution of fluvial and glaciofluvial material as mapped by Rampton (1978).
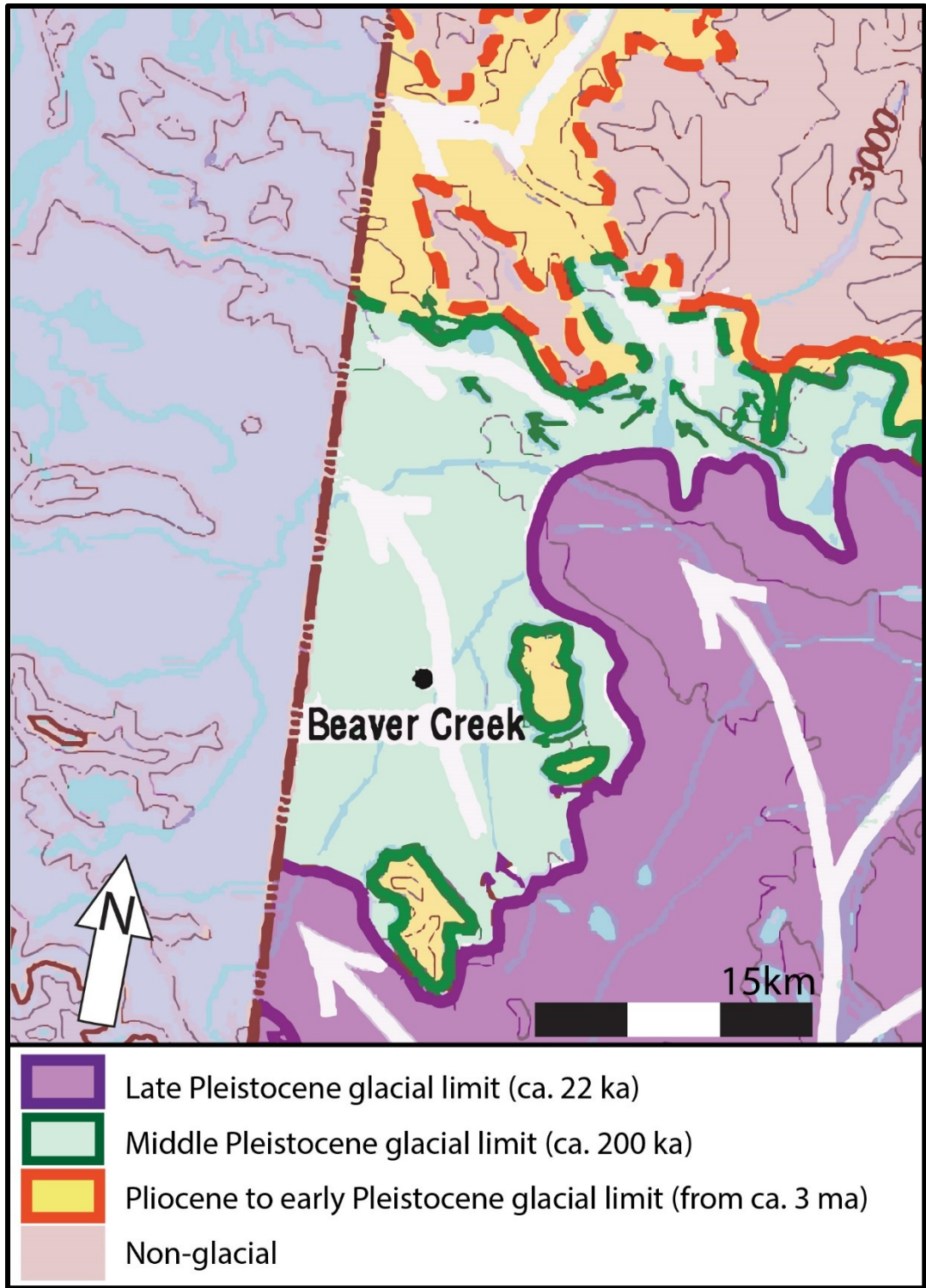
Figure 3.2: Map showing past glacial extents within Yukon created by the Geological survey of Canada in 1999 using cumulated published and unpublished material (Duk-Rodkin 1999). Dashed and solid glacial limits are interpolated and established respectively. Large white arrows indicate paleoflow direction of glacial ice and smaller coloured arrows indicate meltwater channels associated with respective glacial limits.
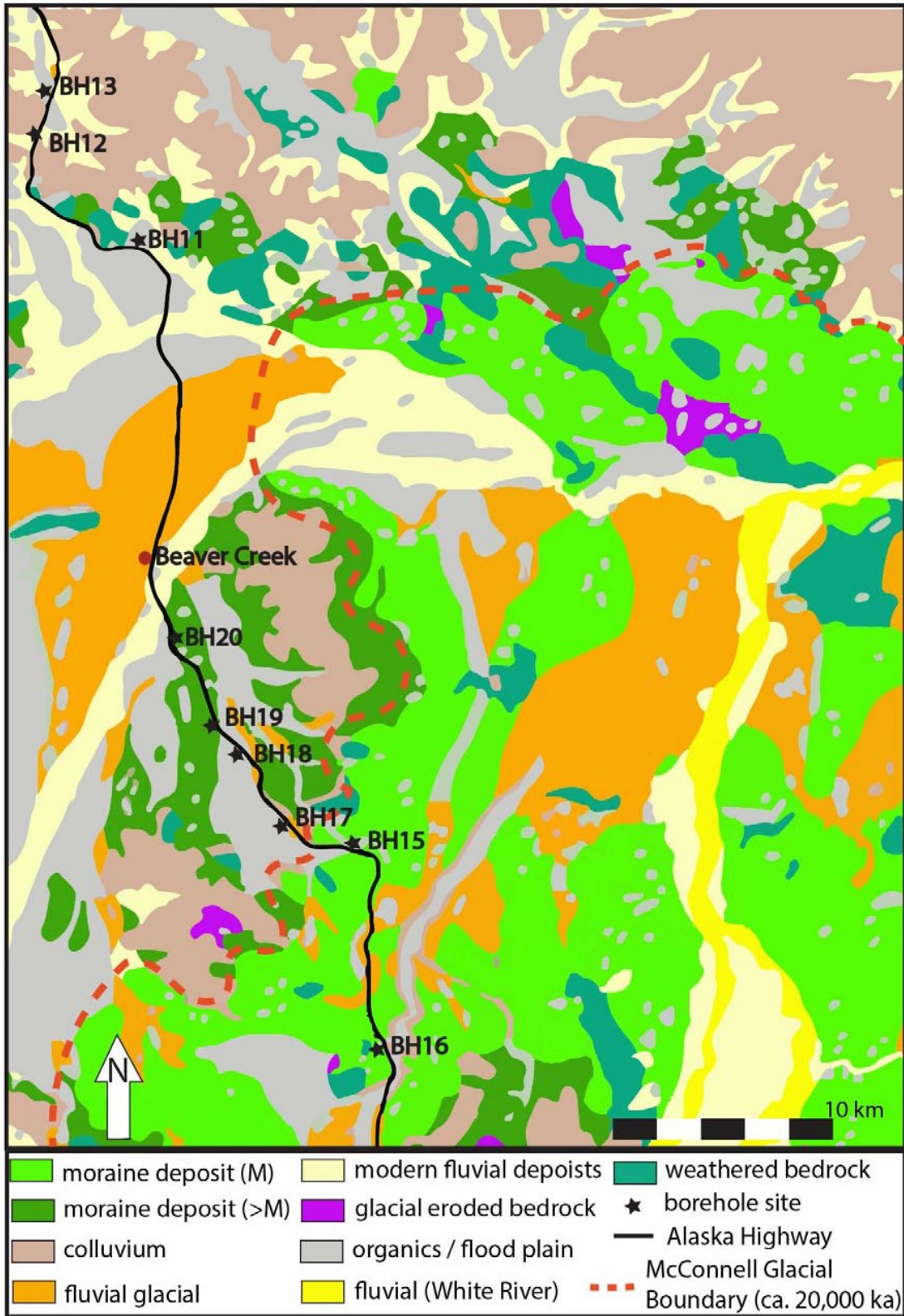
Figure 3.3: Rampton's (1978) surficial map with borehole sites and McConnell glacial extent (red dashed line) included. M = McConnell age (20 ka) and >M = Pre McConnell age (>20 ka).

Figure 3.4: Satellite imagery of study area with all borehole locations marked and the Alaska Highway marked by the solid black line. The red dashed line represents the McConnell glacial extent based on a surficial map of the area (Rampton, 1978), light blue represents extent of

terrain directly impacted by discharge of McConnell melt water with blue arrows indicating assumed water flow directions (images captured from Google Earth, Data SIO, NOAA, U.S. Navy, NGA, GEBCO, Image © 2015 DigitalGlobe, © 2015 Google, Image Landsat, Image IBCAO).

The sites investigated in this study are describe below moving south to north through the study area. Each site description gives a general overview, description of the cryostratigraphy, and geochemical results including radiocarbon dates followed by site specific interpretations. Based on Figures 3.3 and 3.4, each site's location is defined relative to the most recent glacial boundary as follows; glacial, non-glacial outwash, or non-glacial. Site locations are listed in Table 3.1 and shown in Figure 3.3.

Table 3.1: Site locations table including coordinates and highway kilometer markers for each site.

Locality	Elevation (m)	Latitude (WGS84) (Dec. Deg.)	Longitude (WGS84) (Dec. Deg.)	Kilometre
BH16	778	62.11522	-140.40841	1844.25
BH15	757	62.16118	-140.42489	1853.75
BH17	751	62.16828	-140.45744	1875.25
BH18	727	62.18278	-140.4756	1860.5
BH19	721	62.18947	-140.49085	1862.5
BH20	696	62.20693	-140.50879	1866
BH11	628	62.5101	-140.88862	1886.25
BH12E	606	62.55138	-140.97692	1894.25
BH12F	597	62.55591	-140.97339	1894.75
BH12	596	62.554367	-140.974483	1894.5
BH12B	600	62.55709	-140.97242	1895
BH13	583	62.34209	-140.57761	1896.5

Site specific descriptions and interpretations

BH16 descriptions

BH16 is located at N 62.11522 and W 140.40841 (kilometre 1844.25) at an elevation of 778 m and is the most southern site in the study area. This site is south of a small thaw lake in a flat wet area which is poorly drained (Figure 3.5). Surface cover at the site consists of low density black

Figure 3.5: Satellite image of BH16 site location and surrounding area (images captured from Google Earth, Data SIO, NOAA, U.S. Navy, NGA, GEBCO, Image © 2015 DigitalGlobe, © 2015 Google, Image Landsat, Image IBCAO).

spruce, dwarf birch, low lying willows shrubs, medium density tussocks coupled with a well-established sphagnum. Rampton (1978) mapped this area as eOp (organics over fluvial sediments) with szdMb (blanket of moraine sand, silt, mixture) encompassing the eOp (Figure 3.3). Only one borehole was drilled at this site with core samples collected to a depth of 2.06 m (Figure 3.6). The frozen front was encountered at 47 cm depth in late July 2013 with the unfrozen surface cover consisting of 47 cm of peat mixed with organic rich silts. The base of the active layer was observed in the core results at a depth of 59 cm in the form of several lenses of ice with an average thickness of 0.7 cm. Two of the seven cryofacies are found in the core. Throughout the core, cryofacies 2 (ice-rich sediment) is observed with cryofacies 3 (ice-poor sediment) being present only in the bottom 18 cm.

Two $\delta^{18}O$ and δD samples were collected from 78 cm and 158 cm depth along with seven

IVC and six grain size measurements throughout the core (Figure 3.6). The $\delta^{18}O$ and δD

results are -21.3‰ and - 168.3‰ at 78 cm depth and -22.1‰ and -182.7‰ at 158 cm depth.

Figure 3.7 is a plot of the co-isotope relations between $\delta^{18}O$ and δD for all of the isotopic

data discussed in this study. The average IVC is 73% with the bottom of the core recording

the lowest ice volume. Grain size is a mixture of sand, silt/clay and gravel in decreasing

abundance with the exception of the bottom core where gravel makes up 35% of material.

White River Ash was not observed within the core. No radiocarbon dates were obtained from

the core.

Figure 3.6: Core results for BH16, including water isotopes, grain size, ice volume content and cryostratigraphic interpretations.

Figure 3.7: Co-isotope relations between δ18O and δD for all water samples analyzed in this study. Both a global meteoric water line (GMWL) (Craig 1961) and a local meteoric water line (LMWL) were included for reference. The LMWL is based on data from both Whitehorse and Mayo out of the GNIP database. BH11 samples are discussed in the BH11 site interpretations of this chapter. The light blue line represents the trend line of the isotope data from this study.

BH16 interpretations

Based on the water isotope results and the cryostratigraphy this core represents Holocene aged

material (> -24 ‰ δ^{18}O; Kotler and Burn 2000). The proximity of a bedrock high (~100 m

difference) just 150 m to the west of this site along with the presence of angular gravels

throughout the core suggests colluvium deposition. Rampton (1978) mapped this area as

moraine deposition from the McConnell Glaciation (ca. 20,000 Ka) and thus the site location

falls within the glacial boundary as mapped in Figure 3.4. The isotope data do not provide any

insight into the site's glacial history. No definitive evidence was collected to determine

whether this site is within the glacial or non-glacial terrain. However it is assumed to be glacial

as Rampton (1978) found (Figure 3.3).

BH15 descriptions

BH15 is located at 62.268867 N and 140.707567 W (kilometre 1853.85) at an elevation of

752 m. This site is on a gentle south facing slope of a large bedrock high. The area around this

site contains thaw lakes in the lowland areas and exposed bedrock in the steep faced upland

areas with the vegetation density increasing towards the upland areas (Figure 3.8). Surface

cover at the site consists of medium density black spruce, dwarf birch, low density tussocks

coupled with a well-established sphagnum. Rampton (1978) mapped this area as mostly eOp

(thick, level peat bog over glaciofluvial sediments) encompassed by szdMb (blanket of

moraine sand, silt, mixture) (Figure 3.3).

Figure 3.8: Satellite image of BH15 site location and surrounding area (images captured from Google Earth, Data SIO, NOAA, U.S. Navy, NGA, GEBCO, Image © 2015 DigitalGlobe, © 2015 Google, Image Landsat, Image IBCAO).

A single borehole was drilled and core collected to a depth of 3 m (Figure 3.9). The frozen front was encountered at a depth of 32 cm in late July 2013 with the unfrozen surface cover consisting of 32 cm of peat. The base of the active layer was observed in the core at a depth of 42 cm in the form of a 2 cm thick ice layer. Three cryofacies are observed in the core. Cryofacies 1, 2, and 3 are interbedded with cryofacies 1 marking the ice-rich peat layers, cryofacies 2 (ice-rich sediment), and cryofacies 3 (ice-poor sediment).

Five $\delta^{18}O$ and δD values were obtained, ranging from -21.1‰ to -21.4‰ and -163.7‰ to -167.8‰ respectively. The average IVC is 76% with the bottom of the core recording the lowest ice volume content. The grain size is a mixture of mostly silt and clay with increasing sand content at depth.

The White River Ash (WRA) (A.D. 833–850; Jensen et *al.* 2014) appears in a cryoturbated

section between 70 cm and 108 cm depth. No radiocarbon date was collected from the core.
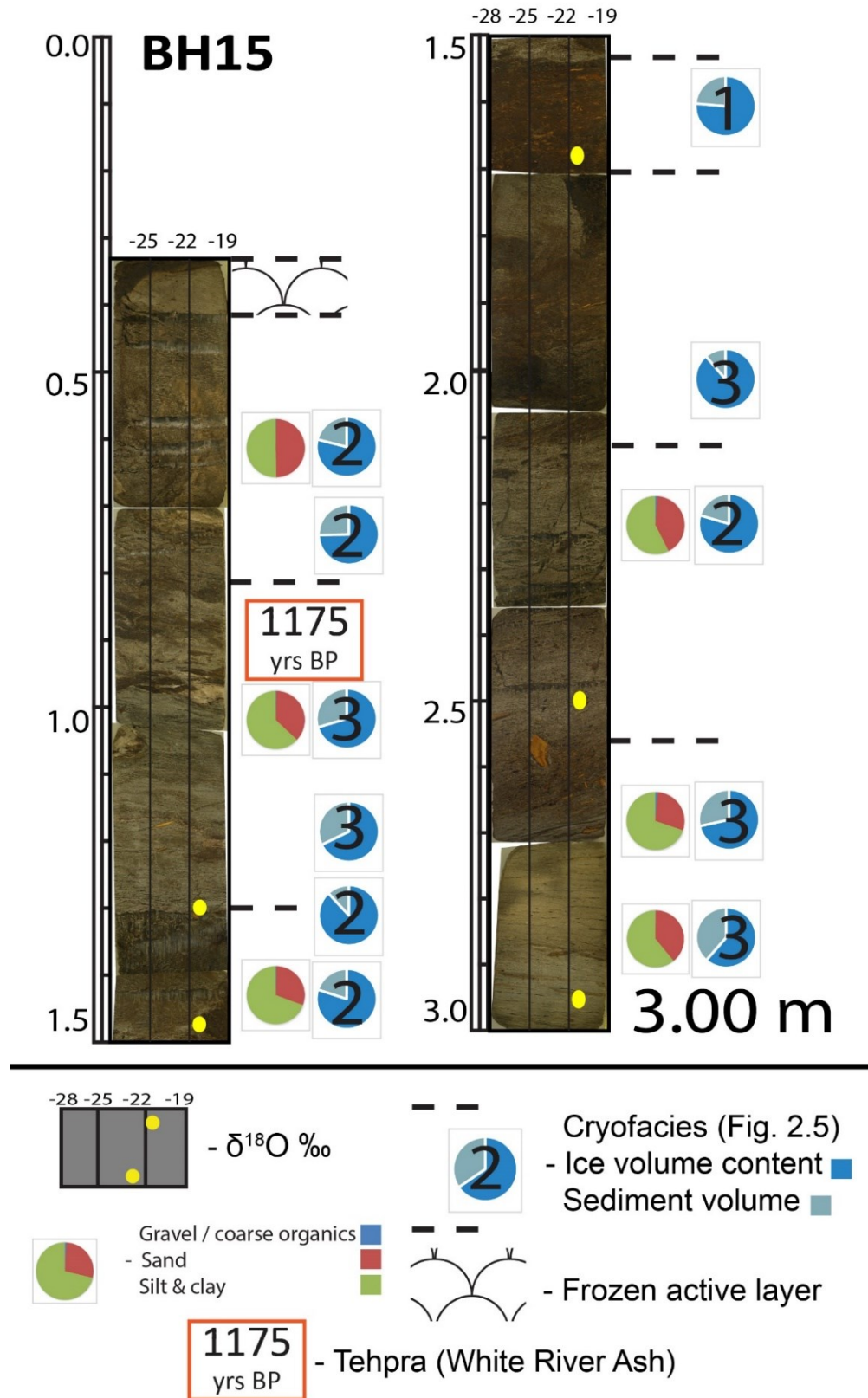
Figure 3.9: Core results for BH15, including water isotopes, grain size, tephra, ice volume content and cryostratigraphic interpretations.

BH15 interpretations

No radiocarbon dates were obtained from this core but based on the water isotope results and the cryostratigraphy, this core represents Holocene aged material (> -24 ‰ δ^{18}O; Kotler and Burn 2000). Cryofacies 1 (ice-rich peat) appears once at a depth of 1.54 m and is 15 cm thick. This indicates that the site experienced a hiatus in sediment input into the area during or following the formation of cryofacies 1 (ice- rich peat). Outside of this hiatus the sediment source was most likely alluvial in nature, depositing the sediment observed within cryofacies 2 (ice-rich sandy silts) and 3 (ice-poor sandy silts) sourced from the surrounding uplands to the north, which drain south across the site into the large ponds visible on the south side of the highway (Figure 3.8). The isotope data do not provide any insight into the sites glacial history. No definitive evidence was collected to determine whether this site is within the glacial or non-glacial terrain. However it is assumed to be glacial as according to Rampton (1978) this site is within the McConnell Glacial boundary (Figure 3.3).

BH17 descriptions

BH17 is located at N 62.16828 and W 140.45744 (kilometre 1857.2) at an elevation of 751 m. This site is located on the west side of the highway opposite a low relief bedrock feature which drains across the highway into a small tributary of Beaver Creek (Figure 3.10). The vegetation density increases towards the upland areas. Surface cover at this site consist of low density black spruce, dwarf birch, medium density tussocks coupled with a well-established sphagnum. Rampton (1978) mapped this area as mostly eOp (organics over glaciofluvial sediments) with szdMb (blanket of moraine sand, silt, mixture) encompassing the eOp (Figure 3.3).

Figure 3.10: Satellite image of BH17 site location and surrounding area (images captured from Google Earth, Data SIO, NOAA, U.S. Navy, NGA, GEBCO, Image © 2015 DigitalGlobe, © 2015 Google, Image Landsat, Image IBCAO).

A single borehole was drilled at the site and core collected to a depth of 2.74 m (Figure 3.11).

The frozen front was encountered at 49 cm depth in late July 2013 with the unfrozen surface

cover consisting of 39 cm of peat with the last 10cm showing an increasing content

downwards of organic rich silts. The base of the active layer was observed in the core at a

depth of 53 cm in the form of several lenses of ice with average thickness of 0.3 cm. Three

cryofacies are observed in this core. Just below the base of the active layer cryofacies 1 is

present for 12 cm followed by a repeating sequence of cryofacies 2 (ice-rich sediment) and

cryofacies 3 (ice-poor sediment). The seven $\delta^{18}O$ and δD values collected range from -21.5‰

to -23.1‰ and -169.7‰ to -182.2‰ respectively. The average IVC is 69% with the bottom of

the core recording the lowest ice volume content. The grain size is a mixture of silt/clay and

sand in decreasing abundance.

No radiocarbon dates were obtained from the core. The WRA, ~1175 yrs BP (A.D. 833–850;

Jensen et *al*. 2014), is present in a cryoturbated section between 95cm and 110cm depth.
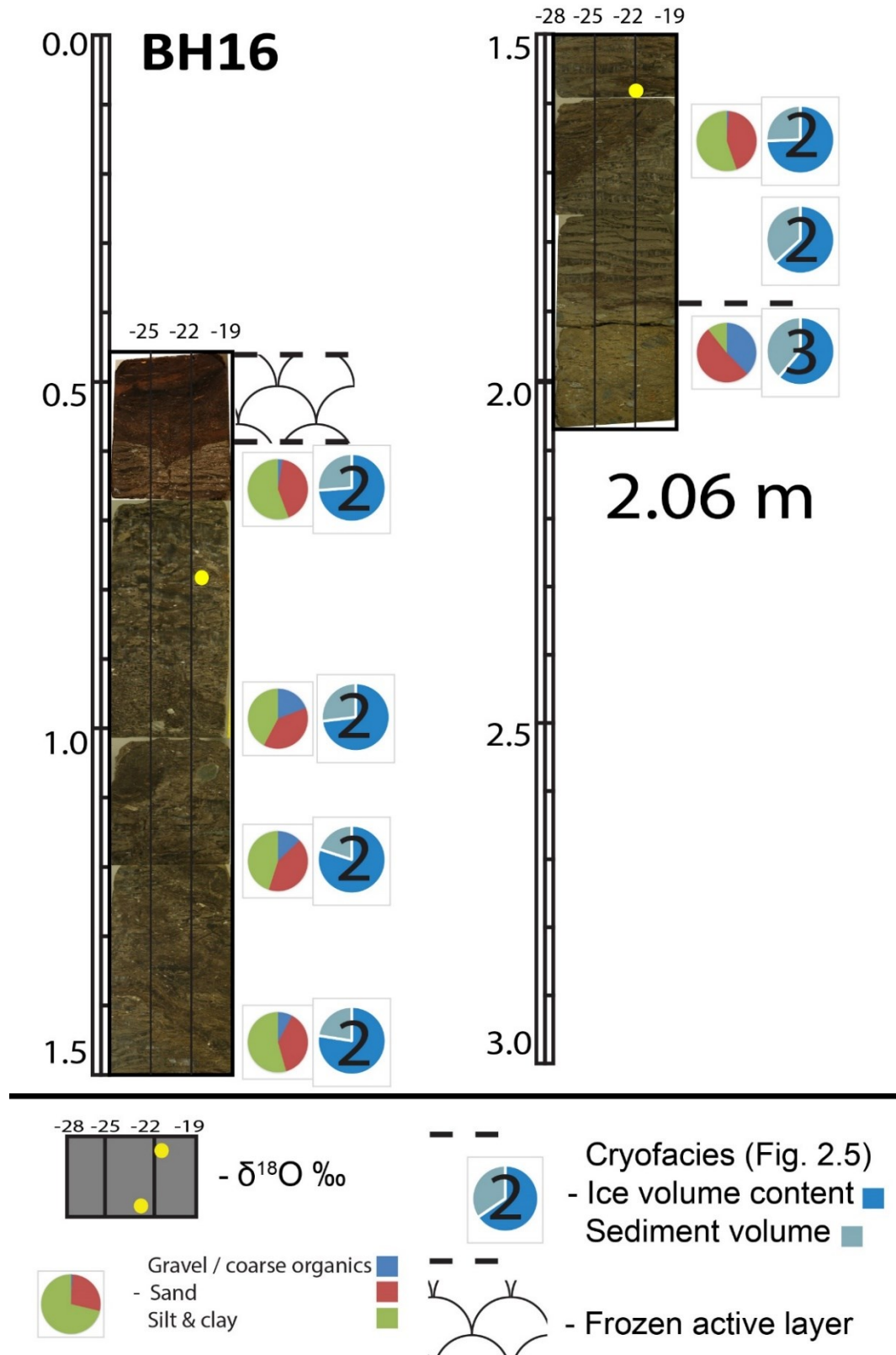
Figure 3.11: Results for BH17, including water isotopes, grain size, ice volume content and cryostratigraphic interpretations.

BH17 interpretations
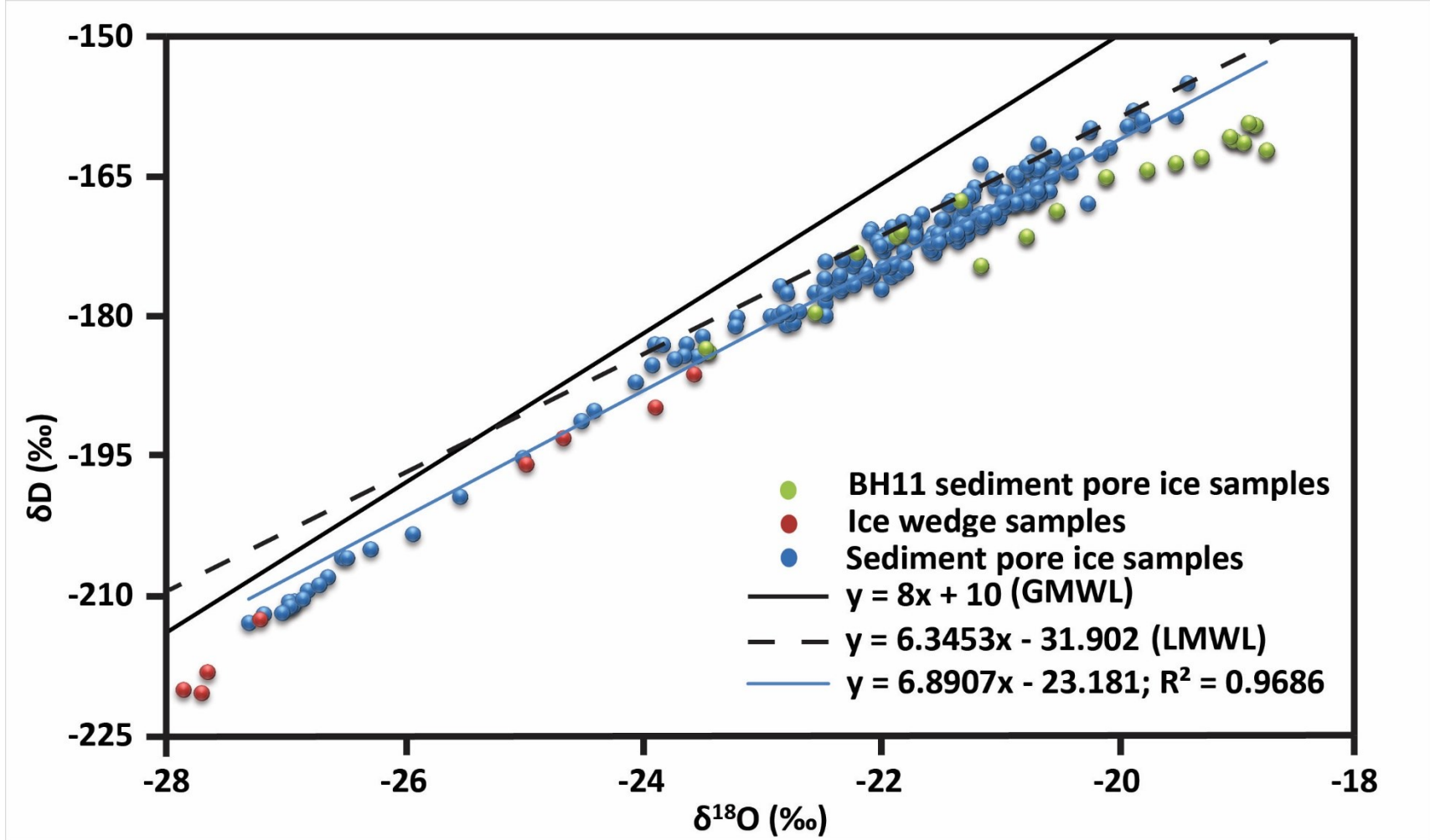
No radiocarbon dates were obtained from this core but based on the water isotope results and the cryostratigraphy this core represents Holocene aged material (> -24 ‰ $\delta^{18}O$; Kotler and Burn 2000). Cryofacies 1 is present at a depth of 55 cm and is 18 cm thick. This is a continuation of the modern peat surface. Below this peat accumulation, the sediment source was most likely alluvial in nature depositing the sandy silts eroded from the slope to the east draining into the large northward flowing stream on the west side of the highway. The isotope data do not provide any insight into the sites glacial history. No definitive evidence was collected to determine whether this site is within the glacial or non-glacial terrain. Depending on the interpretation of Rampton (1978) this site is incidental with the McConnell Glacial boundary and therefore the interpretation of the glacial history is inconclusive (Figure 3.3).

BH18 descriptions

BH18 is located at N 62.18278 and W 140.4756 (kilometre 1860.4) at an elevation of 727 m. BH18 is located west of the highway and 20 m north of a small tributary to Beaver Creek which drains northward (Figure 3.12). Surface cover at this site consist of low density black spruce, dwarf birch, medium density tussocks coupled with a well-established sphagnum. Rampton (1978) mapped this area as mostly eOp (organics over glaciofluvial sediments) with szdMb (blanket of moraine sand, silt, mixture) encompassing the eOp (Figure 3.3).

Figure 3.12: Satellite image of BH18 site location and surrounding area (images captured from Google Earth, Data SIO, NOAA, U.S. Navy, NGA, GEBCO, Image © 2015 DigitalGlobe, © 2015 Google, Image Landsat, Image IBCAO).

A single borehole was drilled with core obtained to a depth of 3.08 m (Figure 3.13). The frozen front was encountered at 49 cm depth in late July 2013 with the unfrozen surface cover consisting of 30 cm of peat overlain by 19 cm of dark brown organic rich silts. The base of the active layer was observed in the core at a depth of 56 cm in the form of a micro-lenticular cryostructure and repeating ice layers from 0.3 to 1 cm thick. Three cryofacies are observed in this core. A repeating sequence of cryofacies 2 (ice-rich sediment) and cryofacies 3 (ice-poor sediment) is present from the top of the permafrost table to 2.75 m depth where cryofacies 4 (ice-poor structureless sediment) is present in the sediment from 2.75 m depth to the base of the core.

Nine δ^{18}O and δD values obtained from the core range from -21.4‰ to -24.2‰ and -170.9‰

to -189.7‰ respectively. The average IVC is 75% with the bottom of the core recording the

lowest ice volume content.

Grain size is a mixture of silt/clay and sand in decreasing abundance with the sand component

becoming dominant towards the base of the core.

One wood macro sample was dated from the core at a depth of 286 cm and returned a median

calibrated age of 11260 Cal yrs. BP. See Table 3.2 for total listing of radiocarbon results. The

WRA is not observed in the cores from this site.

Table 3.2: Radiocarbon results. Note: the two small weight samples BH12B-485 and BH11-510-520 were run with equal weight standards which fell within the expected range.

Sample	Cal yrs. BP	14C yrs. BP	±	UCIAMS #	Material
BH12F-386	7795	6960	15	156126	wood
BH12-433	5175	4555	20	142056	wood
BH12B-191	4195	3810	15	156127	wood
BH12B-264	5465	4720	20	156134	wood
BH12B-385	8140	7335	15	156133	wood
BH12B-485 .013mgC	8860	7960	330	156130	grass
BH12E-191	7310	6385	20	156128	wood
BH12E-358	non-finite	>50800		156138	wood
BH12E-466	non-finite	>55500		156139	wood
BH12E-566	non-finite	>50800		156129	wood
BH12E-566	non-finite	>53400		156135	wood
BH13-480-485	7835	6995	25	142057	wood
BH18-286-Mid	11260	9875	25	167481	wood
BH20-233-210-227	13340	11490	25	167480	wood
BH20-293-260-266	10245	9105	35	167478	wood
BH20-456-Mid	non-finite	>48800		167477	wood
BH11-510-520 .16mgC	10935	9570	40	142058	wood

Figure 3.13: Results for BH18, including water isotopes, grain size, ice volume content, radiocarbon date and cryostratigraphic interpretations.

BH18 interpretations

The one radiocarbon date from the base of this core in addition to the water isotope and cryostratigraphy suggest the core sampled Holocene aged material (> -24 ‰ δ^{18}O; Kotler and Burn 2000). Ice rich organic sandy silts dominate the upper 2 m of the core with a sharp transition at 1.97 m depth to ice-poor inorganic sandy silts to the base of the core. Rampton (1978) maps the site as peat and organics overlying glacial fluvial sediments with the nearby stream and riparian zone mapped as glacial fluvial sediments (eOp). The sediment source for this site is most likely the nearby stream through flooding events. The upper ice-rich organic-rich portion of the core likely represents flooding events during the Holocene. The isotope data do not provide any insight into the sites glacial history. No definitive evidence was collected to determine whether this site is within the glacial or non-glacial terrain. Based on Rampton's initial interpretations, it is most likely this site is located outside the McConnell Glacial boundary but within the melt water discharge area and so is in the on-glacial outwash terrain.

BH19 descriptions

BH19 is located at N 62.18947 and W 140.49085 (kilometre 1862.3) at an elevation of 721 m. The site is on the west side of the Alaska Highway where the terrain slopes gently east towards a small tributary of Beaver Creek (Figure 3.14). Surface cover at this site consist of low density black spruce, dwarf birch, medium density tussocks coupled with a well-established sphagnum. Rampton (1978) mapped this area as mostly eOp (organics over glaciofluvial sediments) with szdMb (blanket of moraine sand, silt, mixture) encompassing the eOp (Figure 3.3).
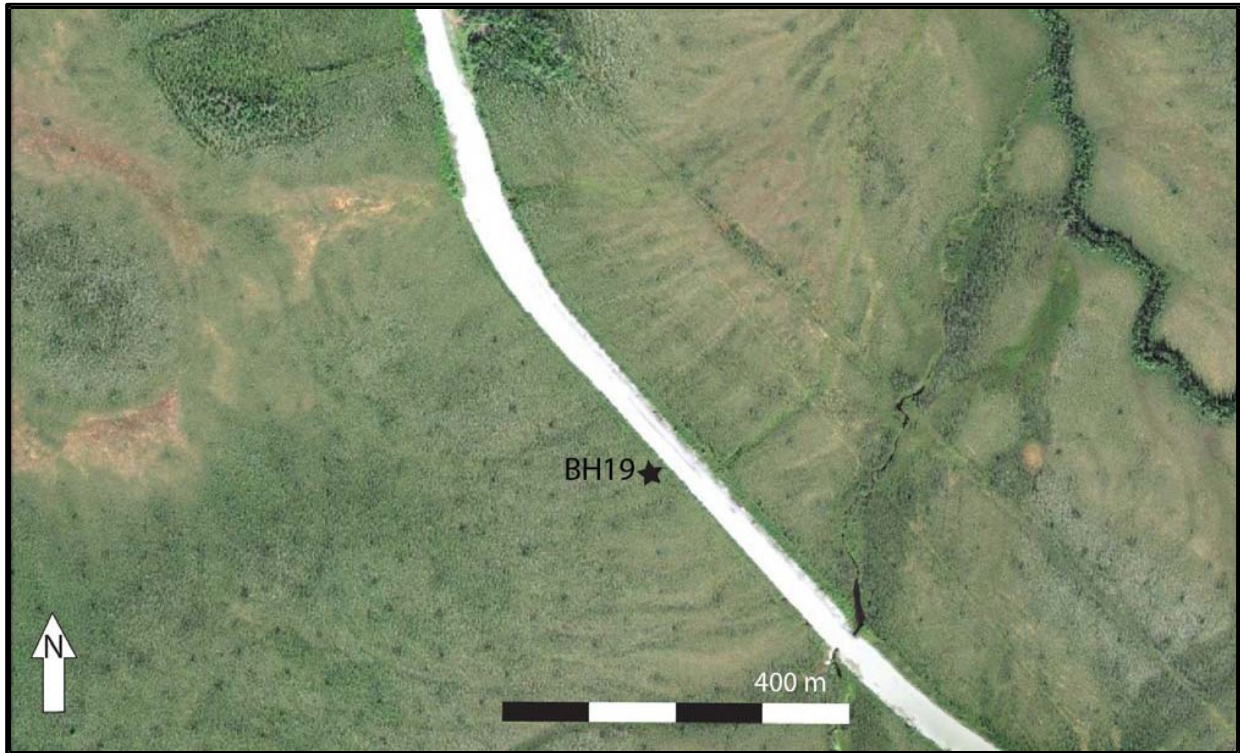
Figure 3.14: Satellite image of BH19 site location and surrounding area (images captured from Google Earth, Data SIO, NOAA, U.S. Navy, NGA, GEBCO, Image © 2015 DigitalGlobe, © 2015 Google, Image Landsat, Image IBCAO).

A single borehole was drilled with core obtained to a depth of 2.61 m (Figure 3.15). The frozen front was encountered at 39 cm depth in late July 2013 with the unfrozen surface cover consisting of 39 cm of peat which was mixed with coarse organics near the freezing front. The base of the active layer was estimated in the core at a depth of 42 cm in the form of several lenses of ice with an average thickness of 0.7 cm. Three cryofacies are observed in this core. Cryofacies 2 (ice-rich sediment) extends from the base of the active layer to 92 cm depth where cryofacies 7 (sediment-poor ice) continues to 2.3 m depth followed by 30 cm of cryofacies 4 (ice-poor structureless sediment).

Three $\delta^{18}O$ and δD values collected range from -21.3‰ to -23.6‰ and -168.9‰ to -186.3‰ respectively. The average IVC is 84% with the bottom of the core recording the lowest ice volume content. The extreme IVC values from the ice wedge samples were included in the

overall average IVC. Grain size is an even split of silt/clay and sand. No radiocarbon date was collected from the core. The WRA does not appear in the core.
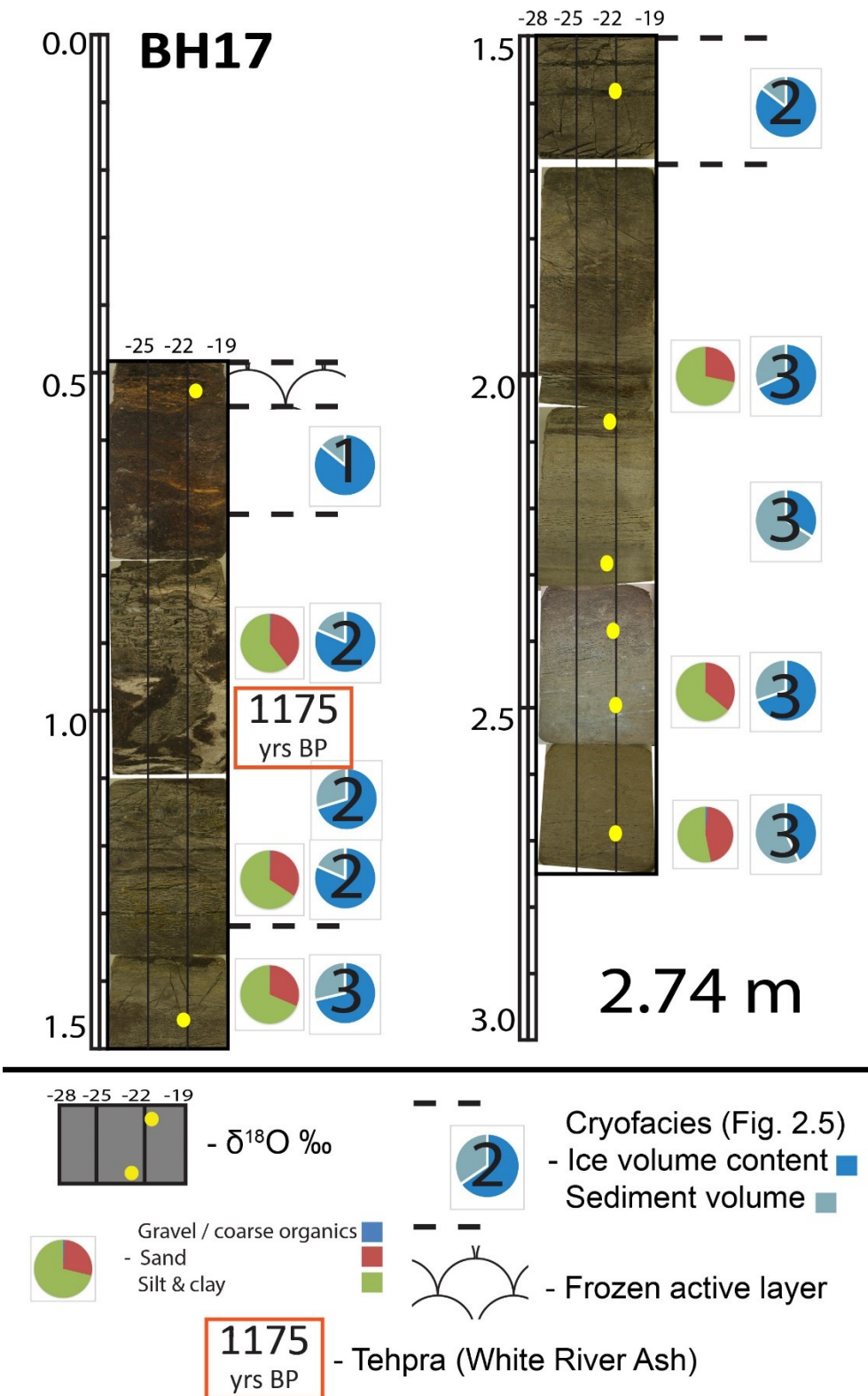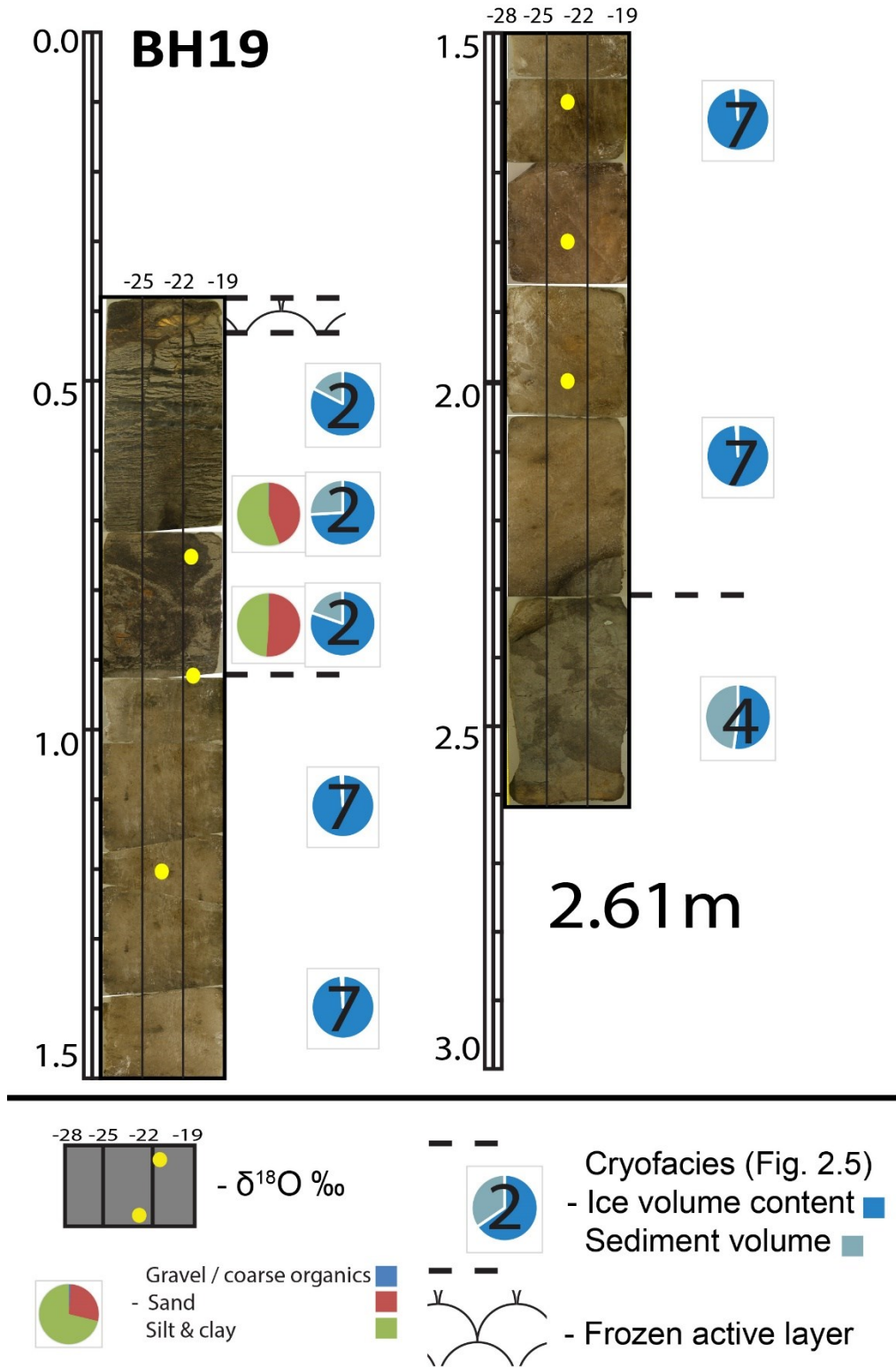
Figure 3.15: Results for BH19, including water isotopes, grain size, ice volume content and cryostratigraphic interpretations.

BH19 interpretations

The active layer at this site consisted almost entirely of peat with a thickness of ~38 cm. Below this depth was 50 cm of ice-rich organic sandy silt followed by a sharp transition to sediment-poor ice interpreted as ice wedge ice. The top of the ice wedge was sampled at 91 cm depth and the base at 2.35 m depth. The pore ice isotopes suggest an interglacial climate during deposition (> -24 ‰ δ^{18}O; Kotler and Burn 2000) with the exception of the ice wedge which has an average δ^{18}O value of -25.0‰. This depletion relative to the surrounding sediments can be explained by the ice wedge capturing more of the winter isotopic signal (snow pack and melt) versus the summer (rain and runoff). The sediments above and below the ice wedge were most likely deposited by alluvial input along the low gradient slope at the site. The location of this site as mapped by Rampton (1978) falls on the border between peat and organics overlying glacial fluvial sediments and moraine from the Reid glaciation. The isotope data do not provide any insight into the site's glacial history. No definitive evidence was collected to determine whether this site is within the glacial or non-glacial terrain. Rampton's (1978) initial interpretations locate this site outside the McConnell Glacial boundary but within the melt water discharge area.

BH20 and BH20B descriptions

BH20 and BH20B are located at N 62.20693 and W 140.50879 (kilometre 1866) and an elevation of 696 m. BH20/20B sites are located in the middle of a large flat poorly drained lowland area containing several thaw lakes (Figure 3.16). Surface cover at this site consists of low density black spruce, dwarf birch, medium density tussocks coupled with a well-established sphagnum. Rampton (1978) mapped this area as mostly eOp (organics over
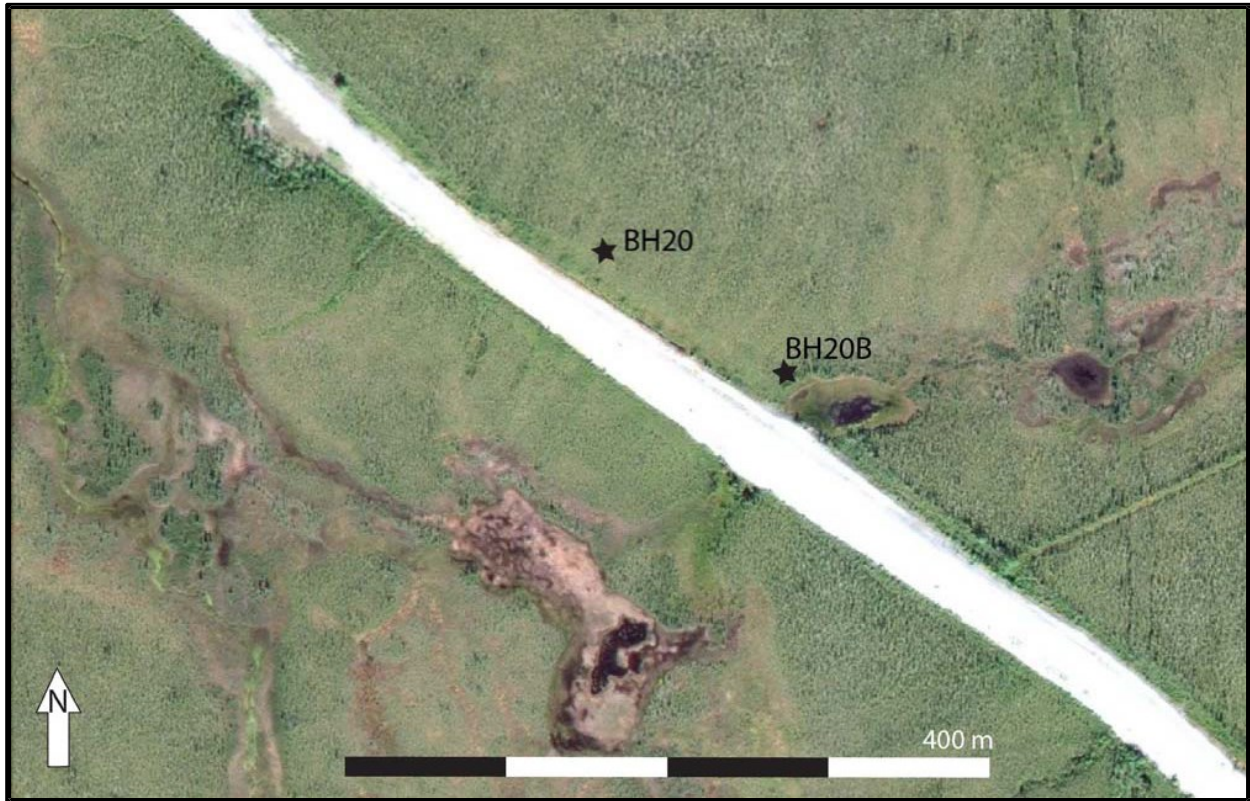
Figure 3.16: Satellite image of BH20/20B site location and surrounding area (images captured from Google Earth, Data SIO, NOAA, U.S. Navy, NGA, GEBCO, Image © 2015 DigitalGlobe, © 2015 Google, Image Landsat, Image IBCAO).

glaciofluvial sediments) with szdMb (blanket of moraine sand, silt, mixture) encompassing the

eOp (Figure 3.3).

The depths of BH20 and BH20B are 4.8 m (Figure 3.17) and 5.1 m (Figure 3.18) respectively.

Cores from both boreholes were collected, however only cores from BH20 were analyzed

beyond cryostratigraphic interpretations. The frozen front in BH20 was encountered at 67 cm

depth in late July 2013 with the unfrozen surface cover consisting of 32 cm of peat overlaying

35 cm of organic rich silts. The base of the active layer was estimated at a depth of 81 cm in

the form of micro-lenticular cryostructure. Four cryofacies are observed in these boreholes.

From top to bottom the cryofacies include cryofacies 2 (ice-rich sediment), cryofacies 3 (ice-

poor sediment), cryofacies 4 (ice-poor structureless sediment), and finally cryofacies five (ice-

poor grey inorganic silts with graminoid macrofossils). Less than 10 m away from BH20,

BH20B displays a similar cryostratigraphic record. BH20B is located 3 m from ponding water due to a collapsed culvert. The frozen front in BH20B was encountered at 33 cm depth in late July 2014 with the unfrozen surface cover consisting of 32 cm of peat overlying 1 cm of inorganic silt. The base of the active layer was estimated at a depth of 50 cm in the form of lenticular cryostructure. BH20B contains cryofacies 2, 3 and 4 appearing in a repeating order. The WRA appears in BH20B in a cryoturbated section between 50 cm and 60 cm depth.

Sixteen $\delta^{18}O$ and δD values analyzed range from -22.1‰ to -26.2‰ and -176.2‰ to -203.3‰ respectively. The average IVC is 72% with the bottom of the core recording the lowest ice volume content. Grain size is a mixture of silt/clay and sand in decreasing abundance with the sand constituent becoming dominant in some sections of the core.

Three radiocarbon dates were collected from BH20 at depths of 220 cm, 260 cm and 470 cm with median calibrated ages of 13337, 10246, and >48800 (non-finite) Cal yrs BP respectively (Table 3.2). WRA, ~1175 yrs BP (A.D. 833–850; Jensen et *al.* 2014), is observed in both BH20 and BH20B core at 75 cm and 60 cm depth respectively.

An ERT survey at this site used 48 electrodes with a 5 m spacing in a Wenner array for a total survey length of 235 m and depth of 42 m (Figure 3.19). This survey shows two heterogeneous units with the upper unit displaying high resistivity values (3500 – 12,000 Ωm) and an average thickness of 11 m. The lower unit shows low resistivity values (550 – 3500 Ωm) with the lowest values concentrated in the centre of the unit and an observable thickness of 32 m.
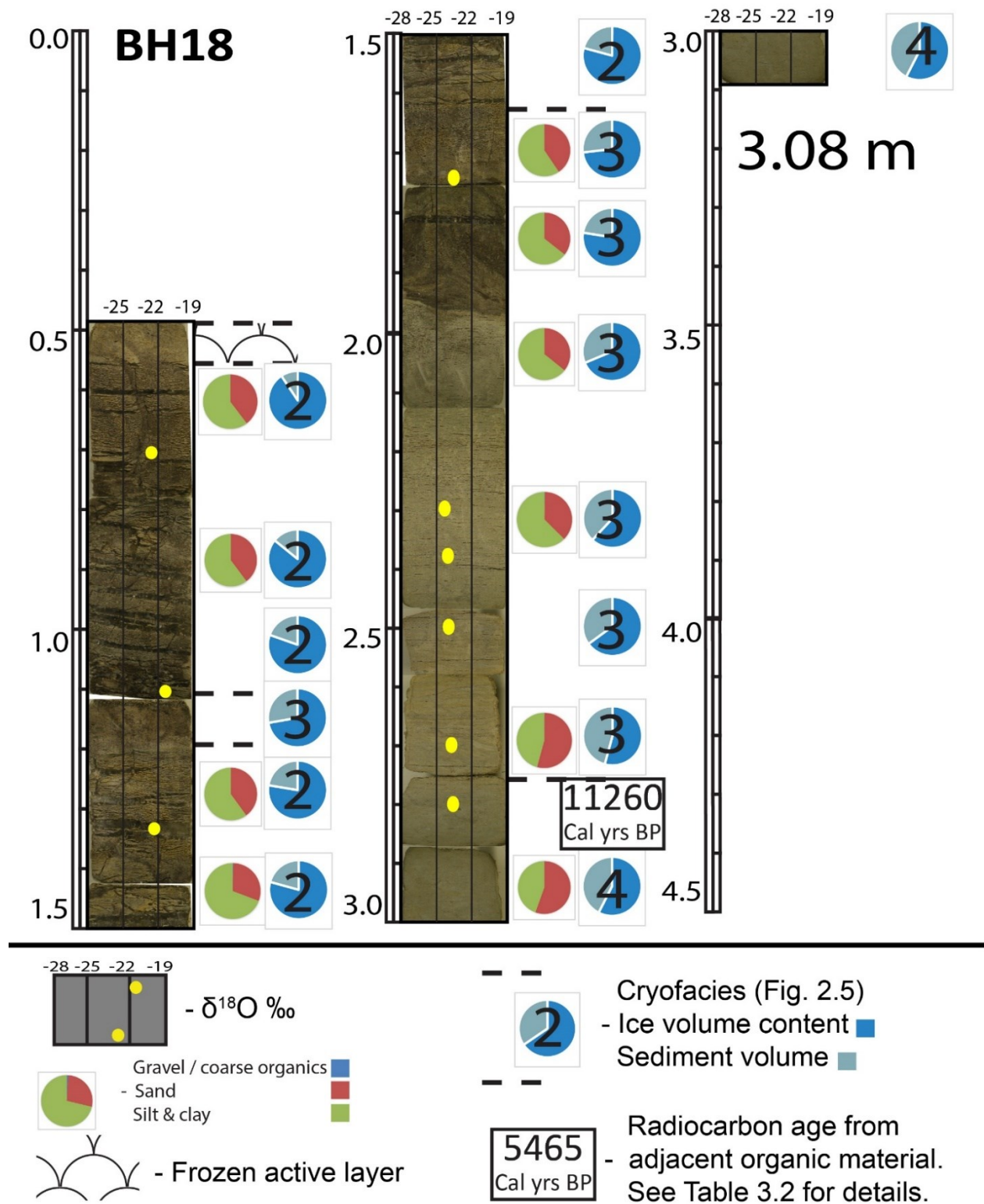
Figure 3.17: Results for BH20, including water isotopes, grain size, ice volume content, radiocarbon dates, and cryostratigraphic interpretations.
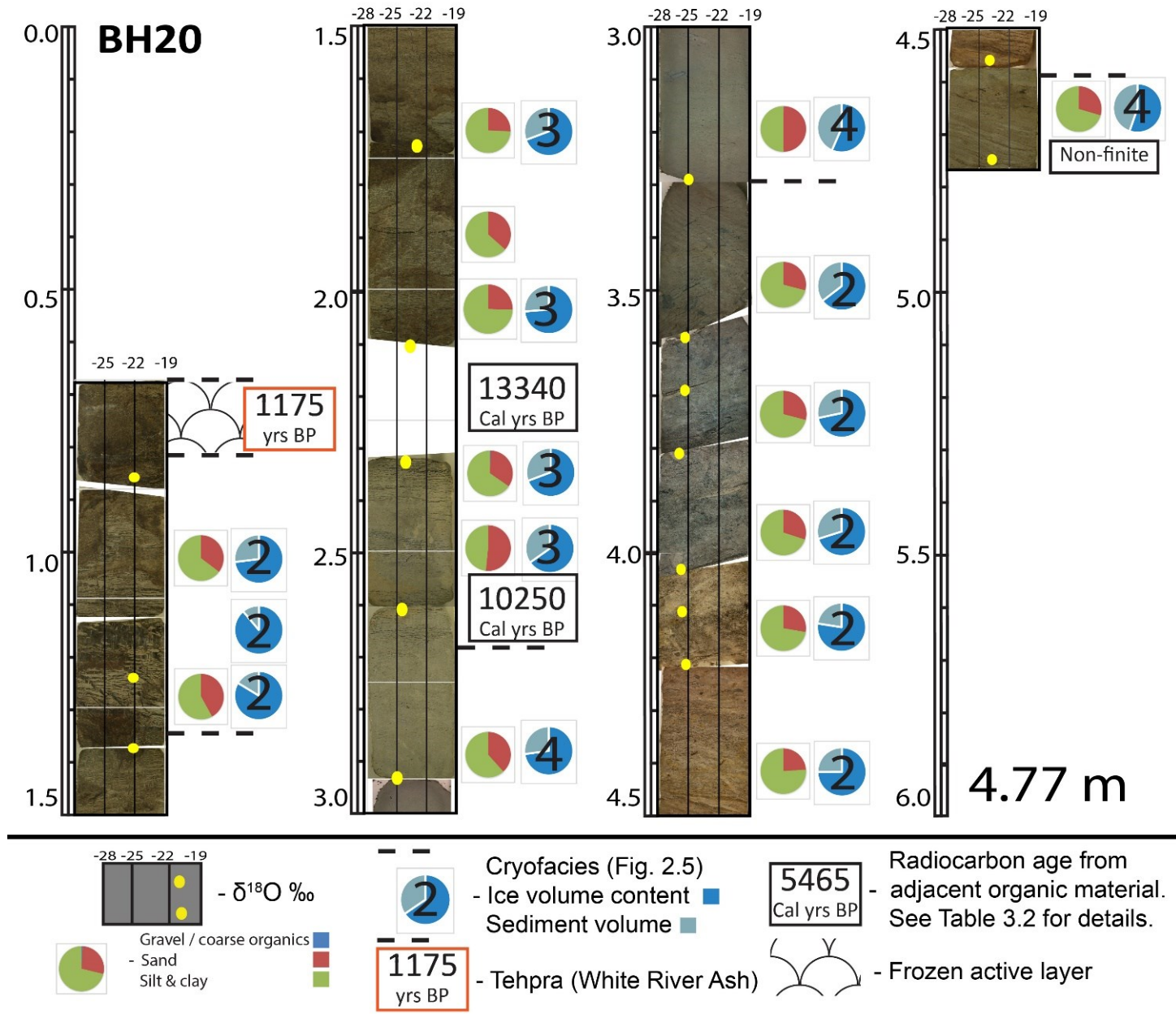
Figure 3.18:
Cryostratigraphic
interpretations
for BH20B.
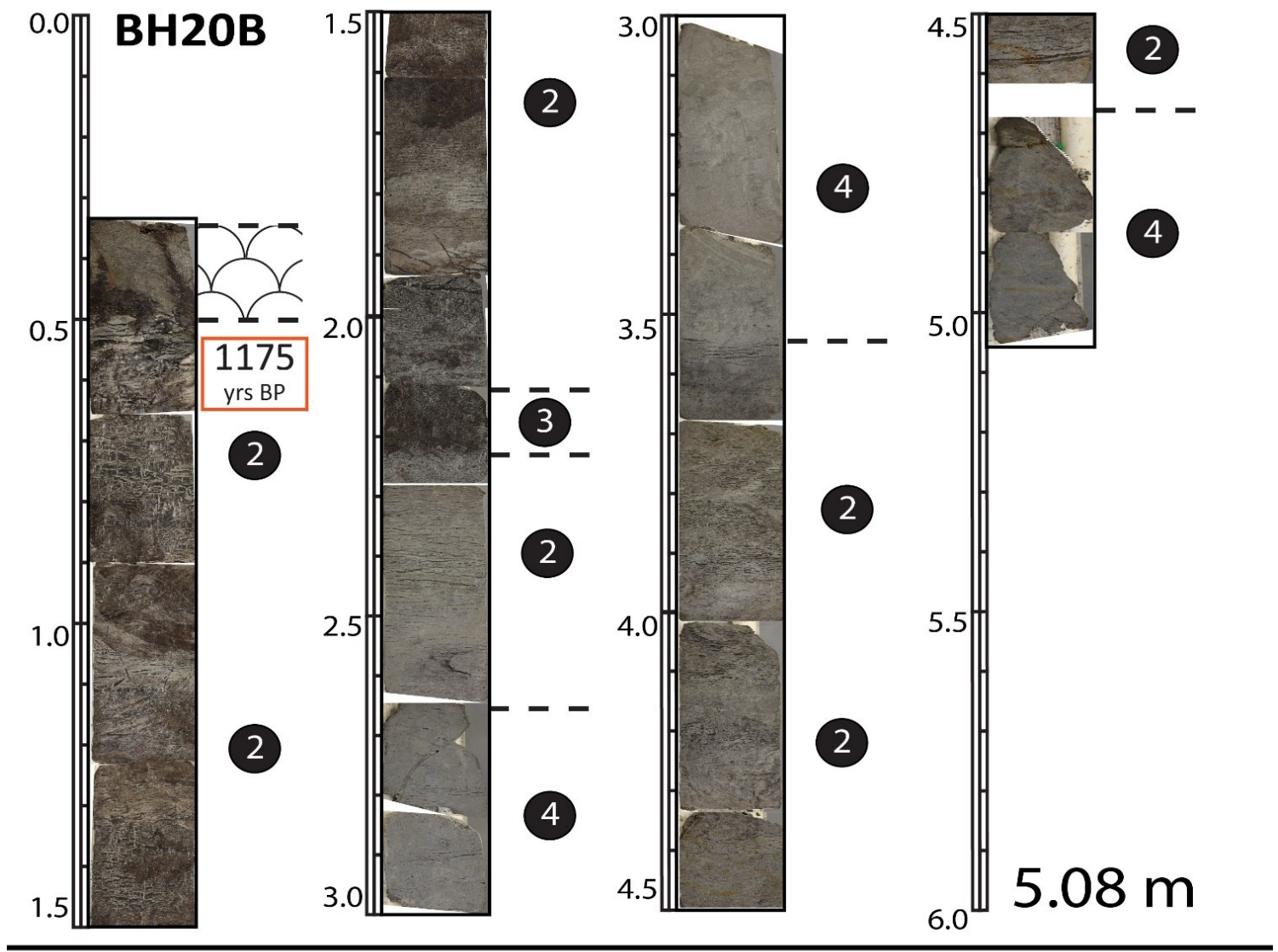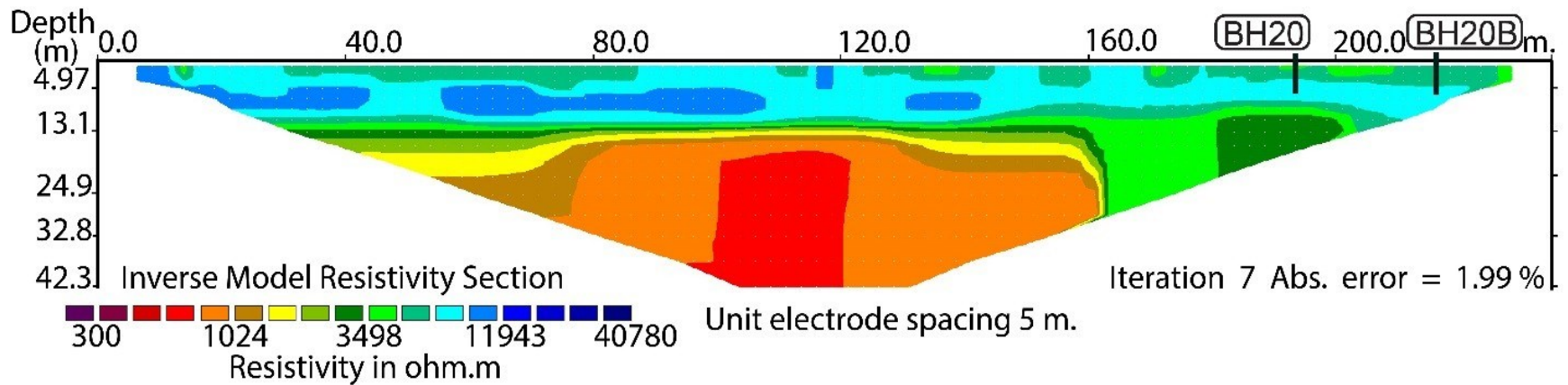
Figure 3.19: ERT results for BH20 with borehole location marked. Survey used 48 electrodes with a 5 m spacing and a Wenner array. Inversions were carried out using RES2DINV (Loke and Barker 1996).

BH20 and BH20B interpretations

The radiocarbon dates from BH20 indicate that the core includes sediments of Pleistocene age. However, the pore ice isotopes more closely reflect a warm interglacial climate (> -24 ‰ $\delta^{18}O$; Kotler and Burn 2000). This contradiction is likely due to past degradation of the local permafrost. Due to the cryoturbated state of the organic rich silts from the base of the active layer to ~270 cm depth it is difficult to deduce the depositional setting and thus connect them to the glacial fluvial activity associated with the McConnell melt water passing through the area. The radiocarbon date from 220 cm depth is assumed to be detrital material from older eroded material upstream whereas the date from 260 cm depth is assumed to be in-situ based on the cryostructures above and below. This presence of water on or near the surface of the site location would have caused underlying permafrost to thaw resulting in a mixing of surface and pore waters overprinting the isotopic signal of the Pleistocene material (Kanevskiy et *al.* 2014; Abraham et *al.* 2012).

The ERT survey from this site shows a low resistivity unit (3500-9000 Ωm) over a relatively high resistivity unit (9000-12000 Ωm). The low resistivity unit is continuous across the entire survey from the base of the active layer to 5 m depth. The vertical high resistivity features likely represent ice wedges however none were sampled or observed at the site. The high resistivity unit in this survey extends across the entire survey from ~5 m to 13 m depth. The higher resistivity values seen in the survey likely represent sediment–poor ice. Rampton's (1978) initial interpretations locate this site outside the McConnell Glacial boundary and in between two discharge channels as seen in Figures 3.3 and 3.4. Based on the sites location and core results it is likely that BH20 and BH20B represent the degraded Pleistocene age permafrost. The degradation was likely caused by either present and/or past close proximity of

a thaw pond or past close proximity of a glacial drainage channel. The taliks created by these bodies of water, if close enough, would have caused local permafrost thaw. Evidence of permafrost thaw can be seen in the form of cryofacies 4 within both core results at depth. Thus it is likely this site is a non-glacial site with evidence of past permafrost degradation at depth.

BH11 descriptions

The site is located at N 62.5101 and W 140.88862 (kilometre 1886.25) at an elevation of 628 m. The area has several thaw lakes surrounded by bedrock topographic highs (Figure 3.20). The dominant vegetation in the higher, dry areas is a mixture of white and black spruce, dwarf birch, and sphagnum. The lower wet areas are dominated by dense tussocks and peat with sparse black spruce and dwarf birch. This site is located at the edge of a large lowland area which Rampton (1978) mapped as zcsFp (silt, clay, sand, fluvial outwash plain) surrounding the active streams in the lowlands and overlain by eOp (organics over lying flood plain deposits) in the majority of the lowland area (Figure 3.3).

Figure 3.20: Satellite image of BH11 site location and surrounding area (images captured from Google Earth, Data SIO, NOAA, U.S. Navy, NGA, GEBCO, Image © 2015 DigitalGlobe, © 2015 Google, Image Landsat, Image IBCAO).

A single borehole was drilled and core obtained to a depth of 5.9 m. The frozen front was encountered at a depth of 64 cm in late July 2013 with the unfrozen material consisting of 15 cm of peat overlying 49 cm of organic silt. The base of the active layer was estimated in the core results at a depth of 90 cm in the form of a several repeating ice layers (Figure 3.21). Three cryofacies are observed in this core (Figure 2.4). Throughout the core, cryofacies 2 (ice-rich sediment) and 3 (ice-poor sediment) are interbedded. Cryofacies 1 (ice-rich peat) appears near the base of the core. The White River Ash (WRA) can be seen in the active layer between 65 and 70 cm depth. Water isotopes $\delta^{18}O$ and δD were sampled throughout the core along with IVC and grain size.

The $\delta^{18}O$ and δD range from -18.7‰ to -23.5‰ and -158.0‰ to -183.9‰ respectively. In the

72

first 180 cm of collected core the d-excess has an average value of 3.61‰ followed by the

remainder of the core having a negative signal of -7.6‰. The IVC is above 60% for most of

the core and the grain size is a mixture of sand and silt sized material with the exception of

the bottom meter where a large 80 cm thick peat layer is encountered followed by 20 cm of

coarse sandy pebble material.

A single radiocarbon date was collected from the core at a depth of 515 cm and returned a

median calibrated age of 10935 cal yrs BP (Table 3.2). The White River Ash (WRA) ~1175

yrs BP (Jensen et *al.* 2014) can be seen in the active layer between 65 and 70 cm depth.

An ERT survey was carried out at this site and ground temperature sensors were installed to a

depth of 12 m. The ERT survey used an electrode spacing of 2.5 m and a Wenner array

resulting in a total survey length and depth of 117.5 m and 21.5 m respectively. The ERT

survey crossed largely saturated organic soils consisting mostly of medium density tussocks

and sphagnum. There is a sharp transition at 3.5 m depth from an upper heterogeneous low

resistivity unit (300 – 6000 Ωm) to a homogeneous high resistivity unit (6000-30,000 Ωm)

extending from 3.5 m to between 17 m and 21.5 m depth (Figure 3.22).

Figure 3.21:
Borehole results
for BH11,
including water
isotopes, grain
size, ice volume
content,
cryostratigraphic
interpretations,
and radiocarbon
results.
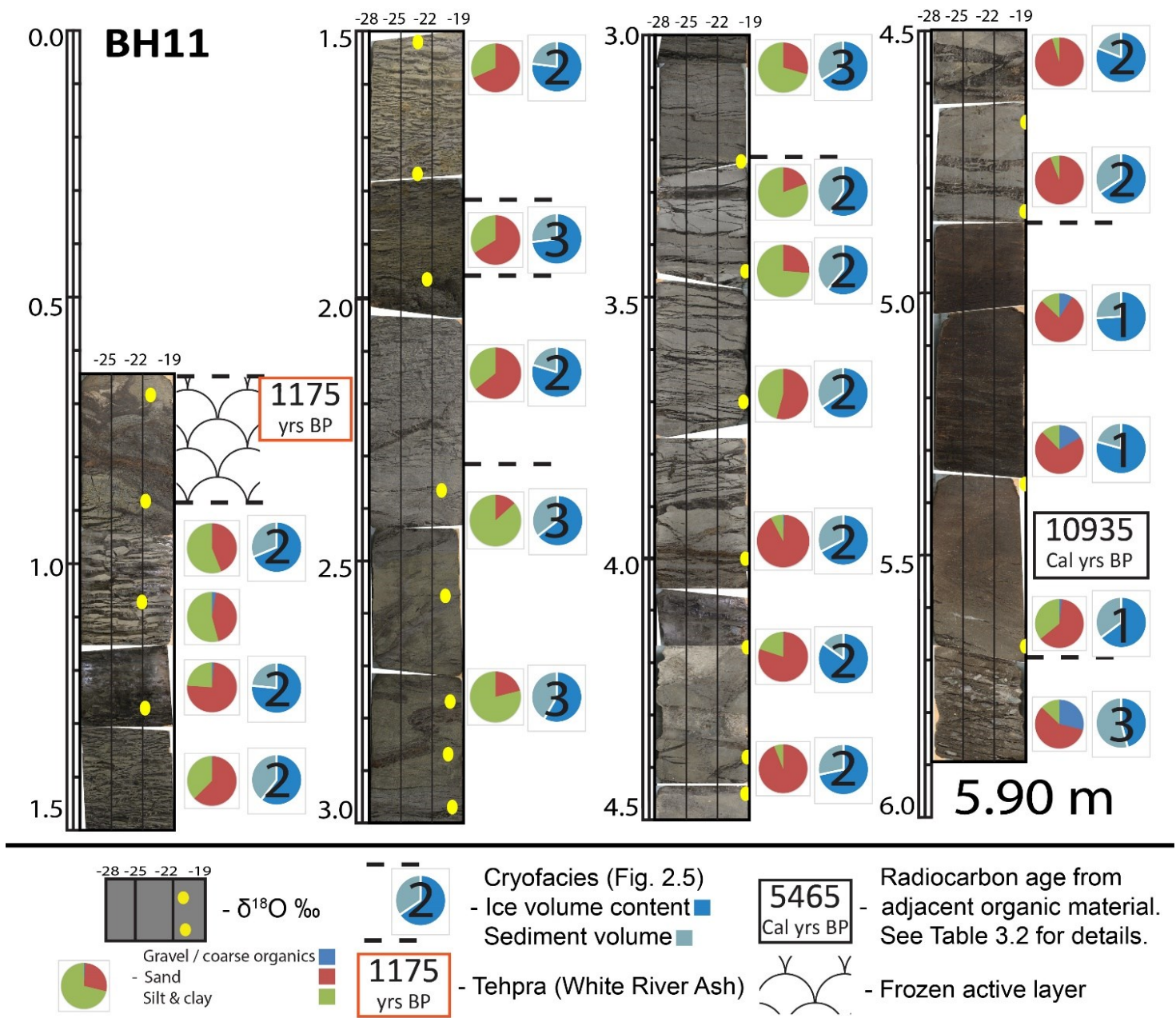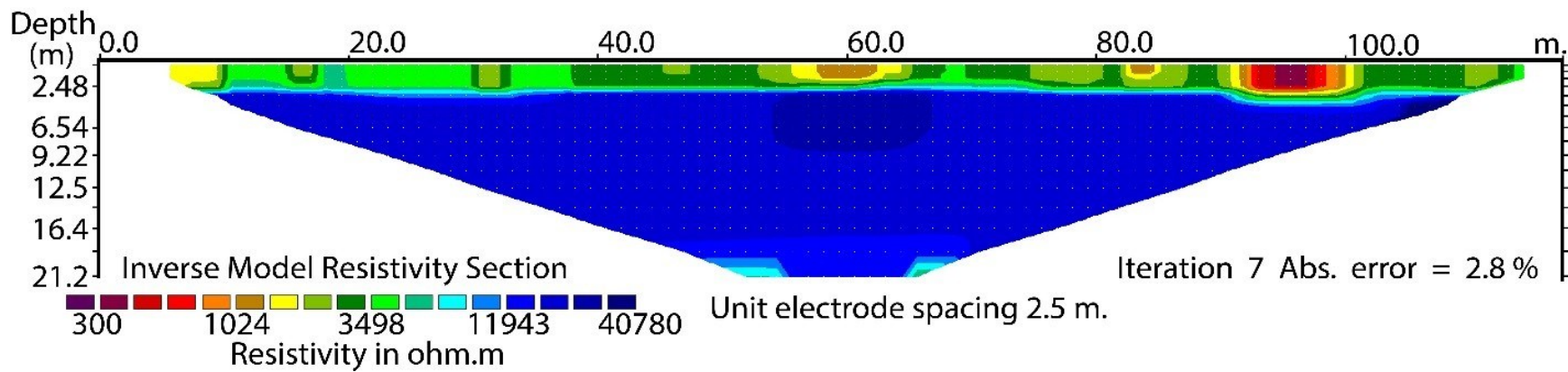
Figure 3.22: ERT results for BH11 without borehole location due to survey location not overlapping with borehole. This survey used 48 electrodes with a 2.5 m spacing and a Wenner array. Inversions were carried out using RES2DINV (Loke and Barker 1996).

BH11 interpretations

The radiocarbon date from the base of the core suggests this core samples the Holocene depositional record at the site. The pore ice isotopes confirm a warm interglacial climate during deposition (> -24 ‰ δ ^{18}O; Kotler and Burn 2000). The early Holocene thermal maximum is visible in the enriched water isotopes towards the base of the core, followed by a trend towards cooler temperatures in the Late Holocene (Figure 3.21). A large thaw lake can be seen to the east of this site at this location as seen in Figure 3.20. The proximity of the large thaw lake and the sharp transition in d-excess and sediment organic content at 200 cm depth suggest it is likely that thaw lakes once occupied this site (Turner et *al.* 2014). The negative signal would develop if the lake experienced extended periods of evaporative loss and minimal rain water input (Turner et *al*. 2014; Figure 3.23 and 3.7).
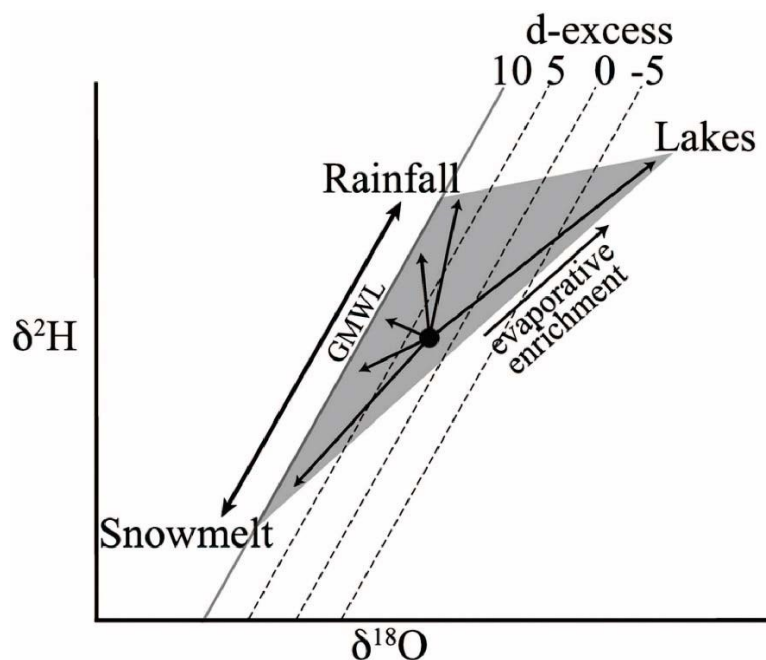
Figure 3.23: Schematic co-isotope plot taken from Turner et al. (2014) showing the expected isotope compositional range of river water (black circle) and probable trajectories depending on source water contributions.

The inorganic sediments likely represent a thaw lake deposit which would explain the signal being carried into the underlying sediments through the talik (Mackay and Burn 2002; Abraham et *al.* 2012). The ice volume content is high throughout the core due to the high density of ice-rich layered and lenticular cryostructures. The site was picked based on interpretation that it is a lithalsa and the observed cryostructures are indicative of their syngenetic aggradational ice-rich nature (Calmels et *al.* 2008). Based on the core results and Google Earth imagery it is likely BH11 started with colluvium input from the nearby bedrock slopes during the Late Pleistocene. This was followed by vegetation establishing in the early Holocene in the form of peat with the runoff from the nearby bedrock providing ample water. This peat continued to aggrade with permafrost until the area was flooded by the formation of a thaw lake which persisted throughout the middle Holocene and into late Holocene when it subsequently drained. The drained lake basin then experienced rapid aggradation of permafrost and establishment of the present day surface vegetation.

The ERT survey done at the site displays a sharp transition not observed within the core results. The transition occurs at 3.5 m depth and hints at a transition from a low resistivity unit (300 – 6000 Ωm) representing partially thawed ice rich silts/peat to a high resistivity unit (6000-30,000 Ωm) likely representing sediment-poor ice or pure ice. This type of transition is encountered at BH12 where the core results agree with the ERT and the high resistivity unit displaying similar values as seen at BH11 is sediment-poor ice interpreted as ice wedge ice, Pleistocene in age. The contradiction between the borehole and the ERT survey can be explained by the survey line position of the ERT not directly overlying the borehole location and instead being offset by ~1 m. Also the borehole is located on top of a local micro topographical high (palsa) creating an elevational offset of ~1 m between the top of the

borehole and the ERT survey. In regards to the heterogeneity of the upper unit there are a few small scale, almost stagnant, streams crosscutting the survey line which are highlighted by the steep sided low resistivity patches in the upper 3.5 m of the survey (Figure 3.22). Without directly sampling this high resistivity lower unit, only a speculation can be drawn about its similarity to the BH12 site. The isotope data do not provide any insight into the site's glacial history. However, Rampton's (1978) initial interpretations suggest the site is located outside the McConnell Glacial boundary. Additionally, it is likely outside of the melt water drainage area based on the high resistivity layer observed in the ERT survey suggesting the presence of ice-rich permafrost at depth.

BH12 valley borehole sites

The following four sites are located within an east-west trending modern day valley bottom, in an area which Rampton (1978) mapped as mostly zcsFp (silt, clay, sand, fluvial outwash plain) encompassed by dszCb (mixed fragments of sand and silt Colluvium blanket) (Figure 3.3). The area has two streams in the valley bottom and large bedrock highs along the north-south valley edges. The dominant vegetation in the upland areas is a mixture of white and black spruce, dwarf birch, and sphagnum and tussock floor cover. The lowland areas are dominated by dense tussocks and sphagnum with sparse black spruce and dwarf birch. The relative location of each borehole site within the valley bottom can be seen in Figure 3.24. All BH12 valley sites are located within the non-glacial terrain based on core results, ERT surveys and Rampton's (1978) surficial map.
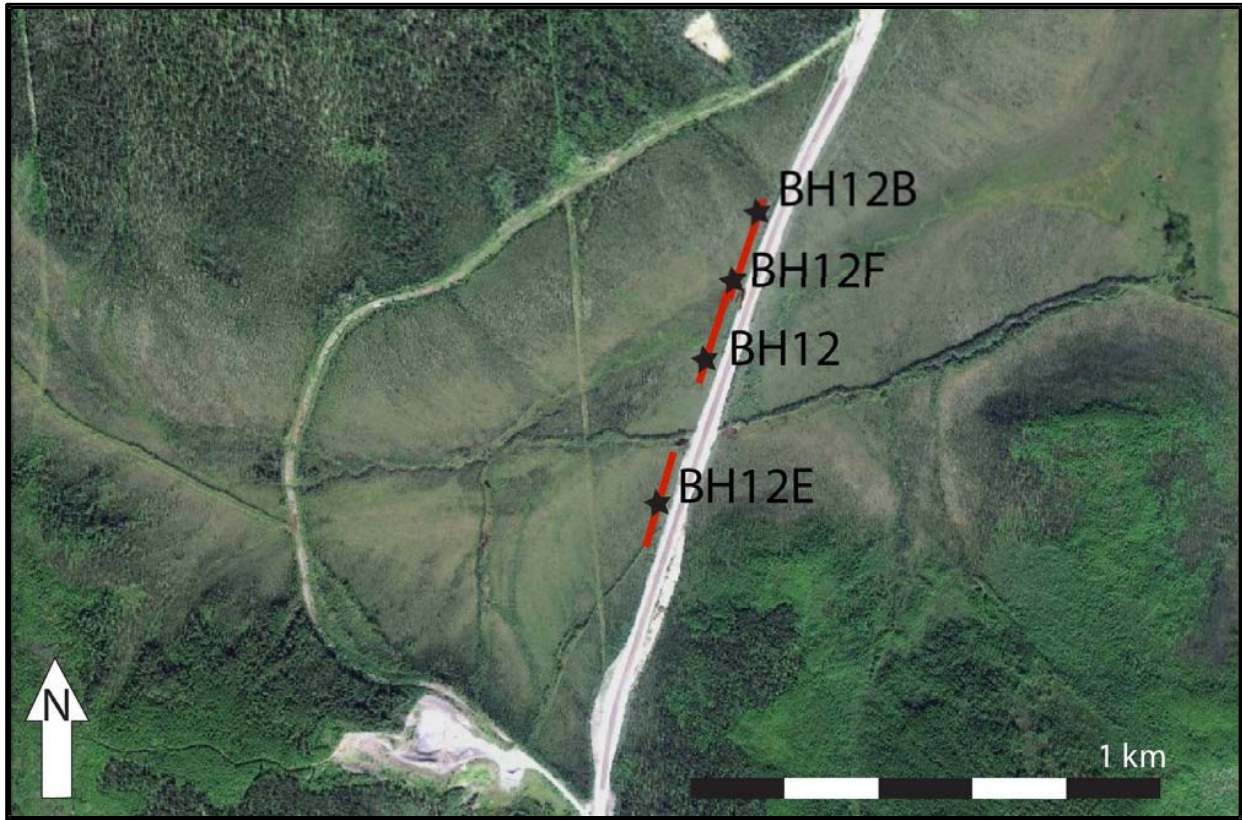
Figure 3.24: Satellite image showing the relative location of the four BH12 valley borehole sites including ERT survey lines marked by the solid red lines (images captured from Google Earth, Data SIO, NOAA, U.S. Navy, NGA, GEBCO, Image © 2015 DigitalGlobe, © 2015 Google, Image Landsat, Image IBCAO).

BH12 description

BH12 is located within an east-west trending valley bottom towards the southern slope at N 62.55437, W 140.97448 (kilometre 1894.5) at an elevation of 597 m. The depth of the borehole at this site is 4.32 m (Figure 3.25). The frozen front was encountered at a depth of 37 cm in late July 2013 with the unfrozen material consisting of 34 cm of peat and 3 cm of organic silt. The base of the active layer was estimated in the core results at a depth of 41 cm in the form of a 1 cm thick ice layer. Three cryofacies are observed in this core. Throughout the core, cryofacies 1, 2, and 3 are interbedded, with cryofacies 1 marking the ice-rich peat layers, cryofacies 2 the ice-rich sediment and cryofacies 3 the ice-poor sediment (Figure 3.25).

The $\delta^{18}O$ and δD range from -19.4‰ to -21.8‰ and -155.0‰ to -174.1‰ respectively. Six

sediment samples from this core were analyzed for carbon isotopes. The average $\delta^{13}C$ in the

BH12 core is -25.8‰. The average IVC is 76% for most of the core and the grain size is

dominated by silt to clay sized particles outside of the peat horizons.

A single date was sampled from the core at a depth of 420 cm and returned a median

calibrated age of 5176 Cal yrs BP (Table 3.2). The WRA (~1175 yrs BP; A.D. 833–850;

Jensen et *al*. 2014) is visible in a cryoturbated section of the core between 110 and 120 cm

depth.

Two ERT surveys were collected at this site and ground temperature sensors were installed to

a depth of 9.5 m along with a weather station collecting air temperature, wind speed and wind

direction measurements. The first survey used 48 electrodes at a 5 m spacing in a Wenner

array resulting in a total survey length of 235 m and survey depth of 42 m. The borehole

location (BH12) marked on Figure 3.25 collected the first 5 m of the subsurface; a

heterogeneous low resistivity unit (400 – 9000 Ωm). This is underlain by a homogeneous high

resistivity unit (9000 – 30,000 Ωm) extending on average from 5 m depth to 19 m depth. This

high resistivity unit is interrupted between the 120 m and 160 m electrodes. It is noted that the

lowest resistivity values in the survey are located above and below this point (130 m marker;

Figure 3.26). Below the high resistivity unit is a heterogeneous low resistivity unit (300 – 5000

Ωm) which displays a concentration of low resistivity values directly below an active stream

on the surface (130 m marker; Figure 3.26). The second survey used the same number of

electrodes and Wenner array but with a 2.5 m spacing resulting in a survey length of 117 m

and a survey depth of 21 m. This survey shows the southern 100 m of the longer survey at this

site with a higher resolution. The boundary between the overlying low resistivity and

underlying high resistivity units appears less flat lying and more undulating in nature compared to the 235 m survey. Overall the thickness of each unit remains the same in each survey.
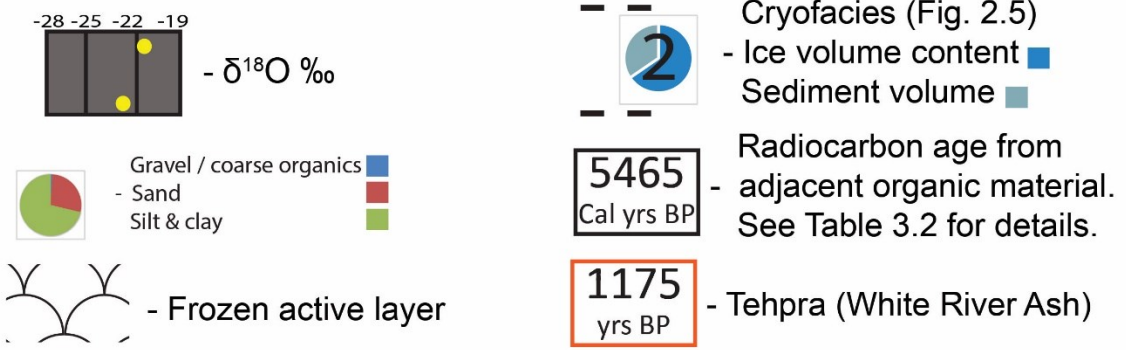
Figure 3.25: Results for BH12, including water isotopes, grain size, ice volume content, cryostratigraphic interpretations, and radiocarbon results.

Figure 3.26: ERT results for BH12 with borehole location marked. Surveys used 48 electrodes with both a 5 m and 2.5 m spacing and a Wenner array. Inversions were carried out using RES2DINV. The top survey is the 2.5 m spacing and represents a higher resolution image of first 100 m within the bottom survey (Loke and Barker 1996).

BH12 interpretations

BH12 is located in a valley bottom along with the present day stream which carries sediment through the valley bottom while thawing underlying permafrost. The radiocarbon date from the base of the core suggests this core samples deposition at this site from middle Holocene to present day. The pore ice isotopes confirm a warm interglacial climate during deposition (> -24 ‰ δ^{18}O; Kotler and Burn 2000). The cryostratigraphic results point to three periods of low sediment input, not including the present day, allowing for establishment of vegetation on the surface. Outside of these stable times there is evidence of sediment input with the mechanism of transport most likely water. This can be confirmed by the high concentration of wood detritus and variable fine grained sediment. The sediment source is most likely a combination of alluvial input from the nearby slopes and flooding of the valley bottom stream. The δ^{13}C values are consistent with what would be expected from C3 plants dominating the decayed organic material (Ma et *al*. 2012). The borehole at this site collected exclusively Holocene material which in the ERT survey is represented by the upper heterogeneous low resistivity unit (Figure 3.26). The vertical sections of high resistivity material seen in both surveys within the upper unit are interpreted as Holocene age ice wedges. This interpretation is based on the ERT results as well as direct sampling and observation of several ice wedges during the construction of a transecting ditch constructed by Yukon Highway and Public Works in June of 2014. The underlying homogeneous high resistivity material is interpreted as ice-rich silts to sediment-poor ice wedge ice deposited prior to or during the Late Pleistocene based on the results from BH12E. The position of BH12 within the survey and recorded depth of the core retrieval show that the transition to the lower unit is less than 1 m below the bottom of the core. The lowest unit within this survey cannot be interpreted due to a lack of data from this

depth.

The low resistivity values located at the 130 m mark in the 5 m spacing survey seen in Figure 3.26 are due to an active stream on the surface causing the surrounding permafrost to thaw, resulting in higher liquid water content in the sediments and therefore lower resistivity values (Hilbich et *al*. 2008). The impact of the stream can be seen in the underlying high resistivity unit which is absent below the stream again due to the thawing effect of the moving water on the surface. A second area of low resistivity values in the upper unit between the 160 m and 200 m marks is due to increased ponding of water on the surface caused by inefficient drainage along the base of the embankment of the highway.

BH12B description

BH12B is located on the northern slope of the valley at N 62.55709, W 140.97242 (kilometre 1895) at an elevation of 600 m. The core from this site reached a depth of 5.83 m (Figure 3.27). The frozen front was encountered at a depth of 29 cm in late July 2014 with the unfrozen material consisting of 27 cm of peat overlying 2 cm of organic silt. The base of the active layer is estimated by an abrupt drop in cryoturbation and colour change observed at 43 cm depth. Four cryofacies are observed at BH12B. The core displays a very similar record to BH12 and BH12F above 5 m depth with cryofacies 1 (ice-rich peat), 2 (ice-rich sediment), and 3 (ice-poor sediment) appearing throughout. Within BH12B cryofacies 4 contains a large vertical ice vein (40 cm long and 1cm thick).

Water isotopes $\delta^{18}O$ and δD in the upper 5 m of the core range from -20.8‰ to -22.5‰ and -164.0‰ to -176.0‰ respectively. Cryofacies 4 (ice-poor structureless sediment) is at 5.5 m depth with pore water isotopes $\delta^{18}O$ and δD ranging from -23.6‰ to -23.9‰ and d -184.3‰

to -185.3‰ respectively. Eleven sediment samples from this core were analyzed for carbon isotopes. The average δ ^{13}C for BH12B is -25.08‰ excluding four data points due to the likely influence of carbonate content on the δ ^{13}C signal. The average IVC is 58% for most of the core and the grain size is a mixture of silt/clay and sand.

Four organic samples were dated from the core with the oldest median calibrated age of 8858 Cal yrs BP at 4.7 m depth (Table 3.2). The WRA (~1175 yrs BP; A.D. 833–850; Jensen et *al*. 2014) is visible in a thick cryoturbated layer between 135 cm and 150 cm depth.

The ERT survey completed at this site used 48 electrodes with a 5 m spacing in a Wenner array giving a total survey length and depth of 235 m and 42 m respectively. The position of BH12B is marked on Figure 3.18 and Figure 3.23 along with BH12F which fell within the same survey. This survey shows similar results to the BH12 surveys in that the same low resistivity upper unit and high resistivity lower unit are observed. Within this survey the upper unit's resistivity ranges from 1000 – 5000 Ωm with an average thickness of 5 m (Figure 3.28). The underlying unit's resistivity ranges from 5000 – 22000 Ωm with and average thickness of 8 m. The underlying high resistivity unit thickens towards the south but is likely skewed by the increasing uncertainty in the ERT results towards the surveys edge.

Figure 3.27:
Results for
BH12B,
including water
isotopes, grain
size, ice volume
content,
cryostratigraphic
interpretations,
and radiocarbon
results.
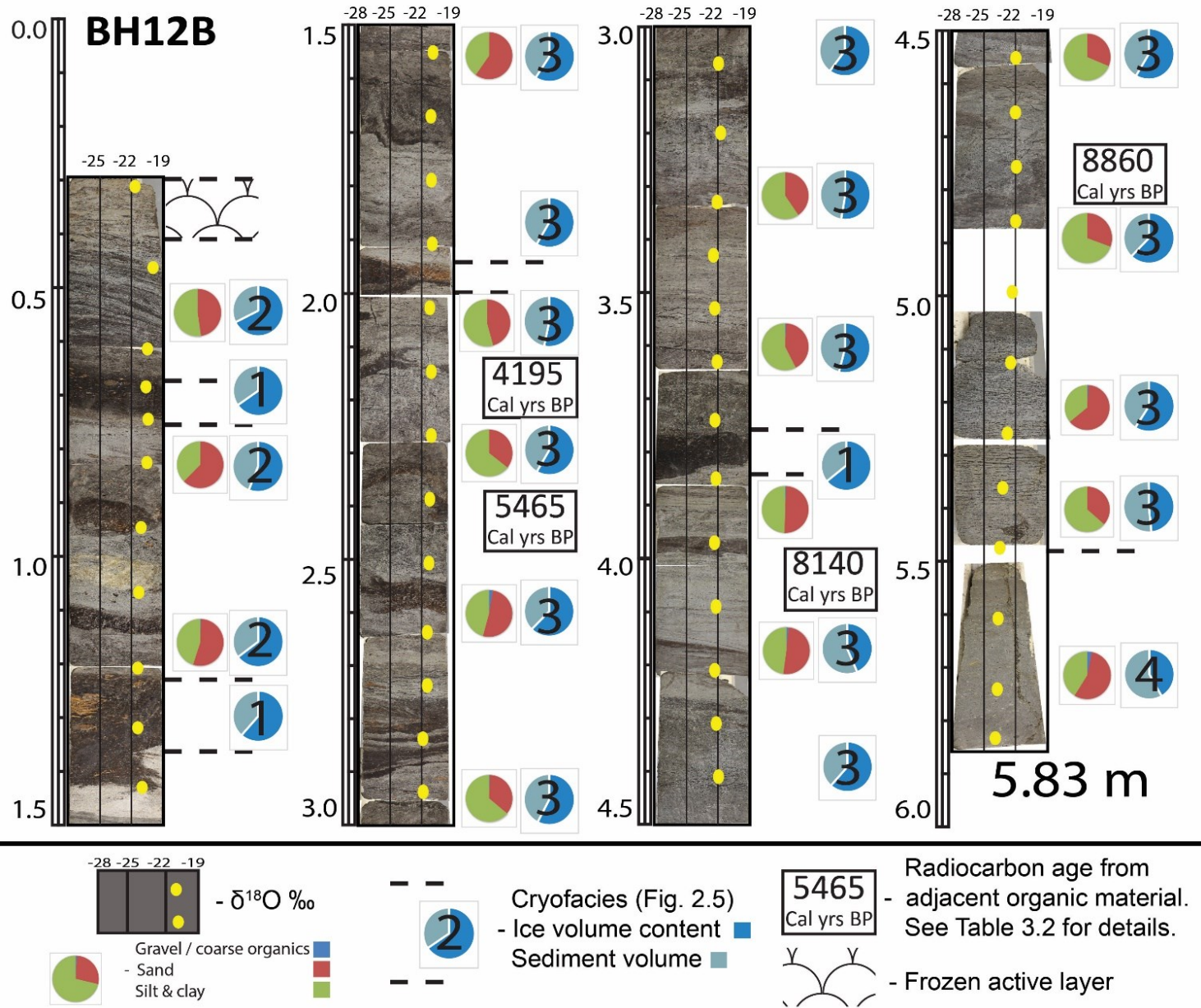
Figure 3.28: ERT results for BH12B with borehole location marked. Survey used 48 electrodes with a 5 m spacing and a Wenner array. Inversions were carried out using RES2DINV (Loke and Barker 1996).

BH12B interpretations

BH12 is located on the south facing slope in the BH12 valley study site. The four radiocarbon dates throughout this core suggest the depositional record sampled extends from the early Holocene to present day. The $\delta^{13}C$ values are consistent with what would be expected from C3 plants dominating the decayed organic material (Ma et *al*. 2012). The pore ice isotopes confirm a warm interglacial climate during deposition of most of the observed core. However, the bottom 35 cm returned the most depleted water isotope values as well as a clear trend towards continued depletion. These depleted isotope values, associated with cryofacies 4, mark the stratigraphic transition from polygenetic Holocene permafrost to syngenetic Late Pleistocene permafrost (< -24 ‰ $\delta^{18}O$, Kotler and Burn 2000; Figure 3.27). The vertical ice vein observed within the base of the core is most likely the result of thawing ice rich permafrost and subsequent refreezing in a semi-closed freezing system (Mackay 1973).

The cryostratigraphic results point to four periods of low sediment input, not including the present day, allowing for establishment of vegetation on the surface. Three of these horizons were formed after 5464 Cal yrs BP median calibrated age at 2.4 m depth, similar to the BH12 site. Outside of these stable times there is evidence of sediment input with the mechanism of transport most likely a combination of moving water and gravity. The WRA (~1175 yrs BP; A.D. 833–850; Jensen et *al*. 2014) is located at 1.4 m depth with two peat horizons above and two below. The sediment source is most likely a combination of alluvial input from valley slope and colluvium from valley slope.

The ERT from this site displays that BH12B reaches the transition between the upper and lower units but does not extend into the high resistivity values of the underlying unit. This is confirmed by the core results from the bottom of the borehole which shows the start of a

negative trend in the water isotopes. The overall lower resistivity values in the overlying unit and the decrease in thickness of the underlying unit, relative to the rest of the valley surveys, can be explained by the southern aspect of this site. However, it is likely this is compounded by the northward shrub and tree densification increasing captured windblown snow which amplifies the insulating factor during the winter (Burn 1998; Jorgenson et *al.* 2010). Similar to BH12, the underlying high resistivity unit is interpreted as being deposited prior to or during the Late Pleistocene. The lowest unit within this survey cannot be interpreted due to a lack of data.

BH12E description

BH12E is located on the southern slope (north aspect) of the valley at N 62.55138, W 140.97692 (kilometre 1894.25) at an elevation of 613 m. The core from this site reached a depth of 5.86 m (Figure 3.29). The frozen front was encountered at a depth of 28 cm in late July 2014 with the unfrozen material consisting of 21 cm of peat and 7 cm of organic silt. The base of the active layer, estimated by a 2 cm thick horizontal ice layer, is visible at 40 cm depth. Five cryofacies were encountered at BH12E. Cryofacies 2 (ice-rich sediment) runs from the top of the permafrost table uninterrupted to a depth of 2.87 m. The majority of sedimentary layers within this section were flat lying with minimal cryoturbation observed. Cryofacies 4 (ice-poor structureless sediment) extends from 2.87 m to 3.32 m depth. Between 3.33 m and 5.56 m depth cryofacies 5 is made up of cryoturbated ice-poor structureless organic grey sandy silt with wood fragments throughout. Underlying cryofacies 5 is cryofacies 6 (sediment–rich ice) approximately 20 cm thick. Cryofacies 7 (sediment-poor ice) underlying cryofacies 6 has visible sub-vertical bubble foliations throughout. The average

IVC is 64% for most of the core and the grain size is a mixture of silt/clay and sand.

Water isotopes $\delta^{18}O$ and δD in the top 2.87 m of core range from -20.5‰ to -22.8‰ and -163.2‰ to -180.0‰ respectively. Underlying this from 2.87 m to 3.32 m depth the $\delta^{18}O$ and δD range from -23.6‰ to -24.1‰ and -183.1‰ to -187.1‰ respectively. Cryofacies 6 (sediment-rich ice) and cryofacies 7 (sediment-poor ice) between 5.6 and 5.86m depth record $\delta^{18}O$ of -27.65‰ and -27.70‰ respectively. Twenty sediment samples from the core were analyzed for carbon and nitrogen isotopes. The average $\delta^{13}C$ for cryofacies 3, 4 and 5 are -25.1‰, -16.6‰ and -24.0‰ respectively. Cryofacies 4 results are not accurate, most likely due to influence of carbonate content on $\delta^{13}C$ signal. The average $\delta^{15}N$ for cryofacies 3, 4 and 5 are 2.2‰, 2.6‰ and -0.3‰ respectively.

Five organic samples from throughout the core were dated with the youngest median calibrated age 7308 Cal yrs BP at a depth of 1.95 m (Table 3.2). The remaining four samples from 3.4 m, 4.45 m, and a duplicate at 5.66 m depth were all non-finite indicating a minimum age for the unit of >57000 14C age BP (Table 3.2). The WRA was not observed in this core. The ERT survey collected at this site used 48 electrodes with a 5 m spacing resulting in a 235 m survey length and 42.9 m depth. This survey's results are consistent with the results found at BH12 and BH12B in that the same low resistivity upper unit overlies a high resistivity unit. Within this survey the upper unit's resistivity ranges from 1000 – 9000 Ωm with an average thickness of 5 m. The lower unit's resistivity ranges from 9000 – 40,000 Ωm with an average thickness of 11 m. The lower unit appears to thicken towards the south and has a discontinuity at metre marker 30 in Figure 3.30.
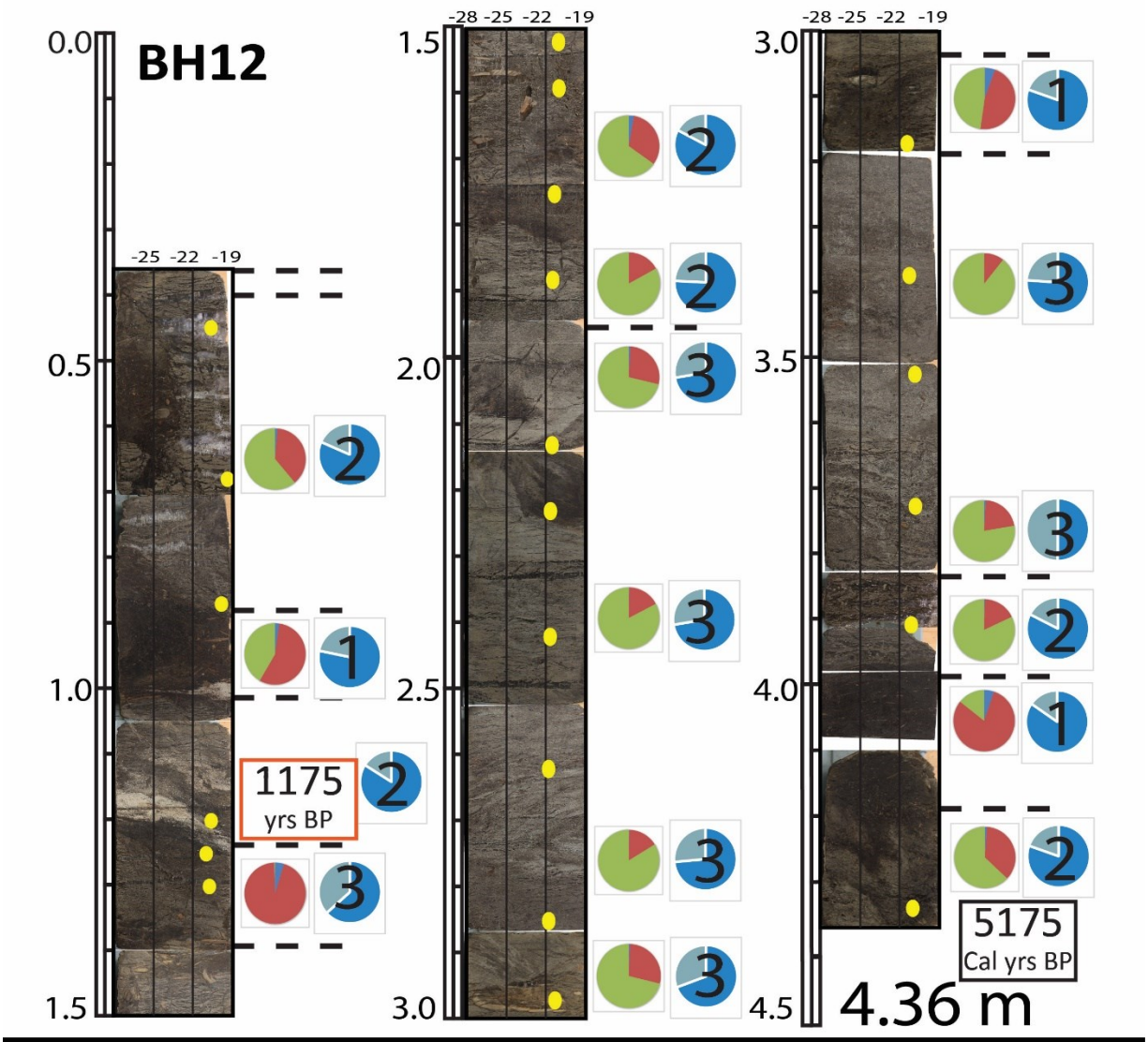
Figure 3.29: Results for BH12E, including water isotopes, grain size, ice volume content, cryostratigraphic interpretations, and radiocarbon results.
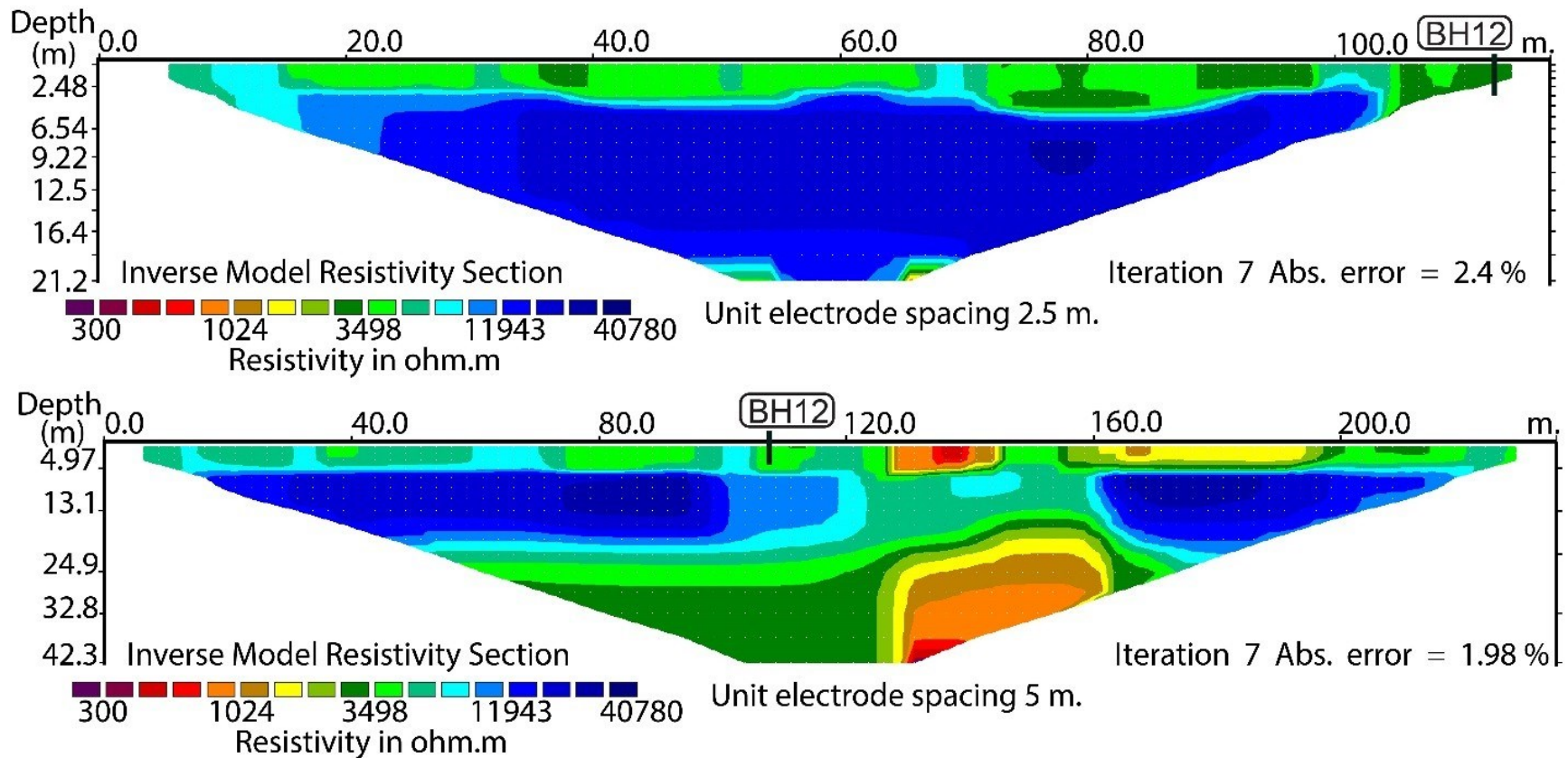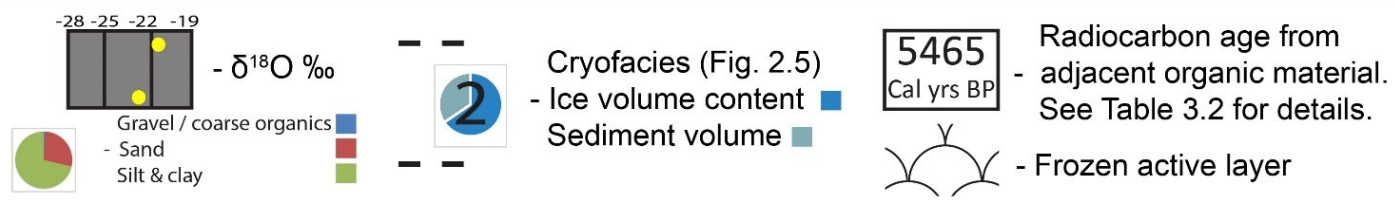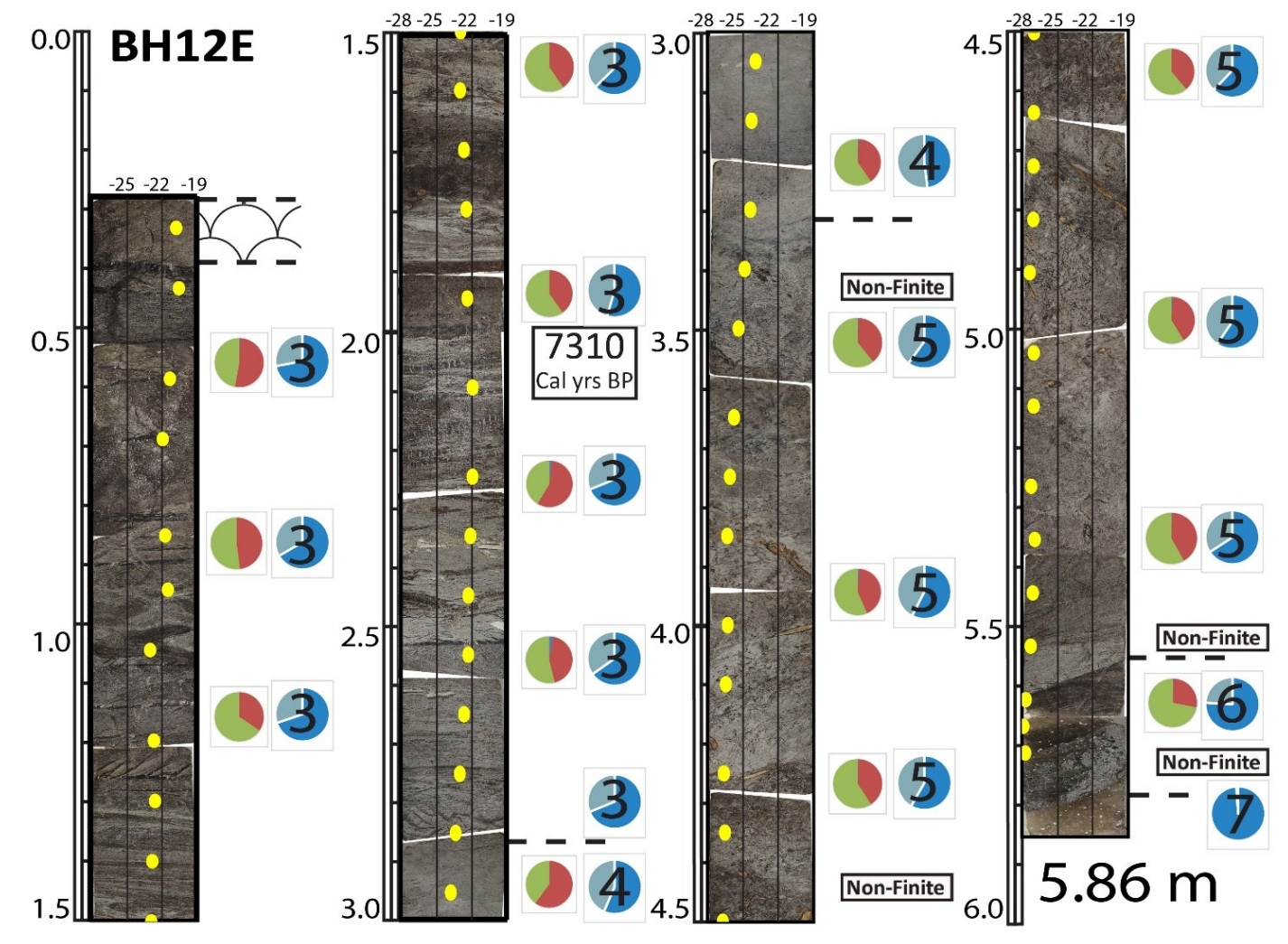
Figure 3.30: ERT results for BH12E with borehole location marked. Survey used 48 electrodes with a 5 m spacing and a Wenner array. Inversions were carried out using RES2DINV (Loke and Barker 1996).

BH12E interpretations

BH12E is located on the southern north facing slope in the BH12 valley study site. The cryostratigraphic results point to a steady input of sediment and minimal vegetation growth with the exception of grasses. The lack of peat horizons relative to the BH12B site is consistent with the aspect of each site and the resulting sun exposure. The mechanism of transport for sediment into this site was most likely dominated by wind transport with periodic input from moving water and mass movements from the bedrock high to the southeast.

Out of the five radiocarbon dates collected from this core, four returned non-finite results suggesting the sedimentary record is >57000 14C age BP. The one finite result from the core is 7308 Cal yrs BP median calibrated age collected at 1.9 m depth. From the base of the active layer to 2.5 m depth the water isotopes confirm a warm interglacial climate during deposition. However, from 2.85 m depth to the base of the core there is a trend towards depletion ranging from $\delta^{18}O$ -23.0‰ to -27.9‰. The isotopic values, cryostructures, and radiocarbon dates from cryofacies five, six and seven together indicate an origin typical of Pleistocene silts found across unglaciated Yukon and Alaska (Froese et *al*. 2009; Schirrmeister et *al*. 2013). Overlying these sediments is cryofacies 4 (ice-poor structureless sediment) which likely represents a paleo-thaw unconformity based on the structureless cryostructure throughout, change in water isotope values, and non-conformable radiocarbon dates above and below (Kotler and Burn 2000; French and Shur 2010). A sharp transition in pore water isotopes is not observed within the core to support this unconformable nature of the underlying and overlying material. This is likely due to the underlying depleted pore water isotopes mixing with the overlying relatively enriched pore water isotopes creating the observed smooth mixing line across the boundary. This thaw unconformity records thermal degradation and removal of the Late Pleistocene

material which would have been deposited prior to and during the McConnell Glaciation (Jackson et *al*. 1991; Kotler and Burn 2000; Jorgenson et *al*. 2010; Reyes et *al*. 2010). This degradation continued until the active layer stabilized in Holocene sediments.

The $\delta^{13}C$ values are consistent with what would be expected from C3 plants dominating the decayed organic material except in cryofacies 4 where the values are more representative of C4 plants. However, this is most likely due to the presence of carbonates within this unit causing an enrichment in the $\delta^{13}C$ (Ma et *al*. 2012). The $\delta^{15}N$ values suggest a warm continental environment with the exception of cryofacies 5 where the average value falls below zero (Amundson et *al*. 2003). This shift in $\delta^{15}N$ is incidental with the cryostratigraphic change from cryofacies 4 to 5. However this shift is the opposite of what would be excepted when moving from Holocene to Pleistocene sediments based on a previous study (Newsome et *al*. 2011). The ERT survey obtained at the site displays the same units observed at BH12 and BH12B with two differences: (1) the upper low resistivity unit has higher overall resistivity values and (2) the underlying high resistivity unit shows a greater average thickness of 11 m which can be contributed to the sites northern aspect. In addition, it is likely this is compounded by the low shrub and tree density causing a decrease in surface snow depths which decreases the insulating factor during the winter (Burn 1998; Jorgenson et *al*. 2010). BH12E is the only borehole which intersected the high resistivity values seen in the lower unit. As mentioned above the material responsible for these values has been interpreted as ice wedge ice (Figure 3.29 and 3.30). This material was most likely deposited in the area prior to or during the Late Pleistocene. The lowest unit observed in the ERT survey cannot be interpreted due to insufficient data.

BH12F description

BH12F is located between BH12 and BH12B within the valley bottom closer to the northern slope at N 62.55591, W 140.97339 (kilometre 1894.75) at an elevation of 597 m. The depth of the borehole at the site is 4.52 m (Figure 3.31). The frozen front was encountered at a depth of 38 cm in late July 2014 with the unfrozen material consisting of tussock and peat. The base of the active layer was estimated in the core results at a depth of 54 cm based on a 4 mm ice layer. Throughout the core, cryofacies 1 (ice-rich peat), 2 (ice-rich sediment), and 3 (ice-poor sediment) are interbedded.

The δ^{18}O and δD ranges from -19.8‰ to -21.7‰ and -159.6‰ to -171.5‰ respectively. Five sediment samples from the core were analyzed for carbon isotopes. The average δ^{13}C for cryofacies 3 is -25.3‰. The average IVC is 62% for most of the core and the grain size is a mixture of silt/clay and sand.

A median calibrated radiocarbon age of 7793 Cal yrs BP was collected at 3.7 m depth (Table 3.2). The WRA is visible in a cryoturbated layer between 180 cm and 200 cm depth.

For a description of the ERT survey at this site please see BH12B site descriptions and Figure 3.28.
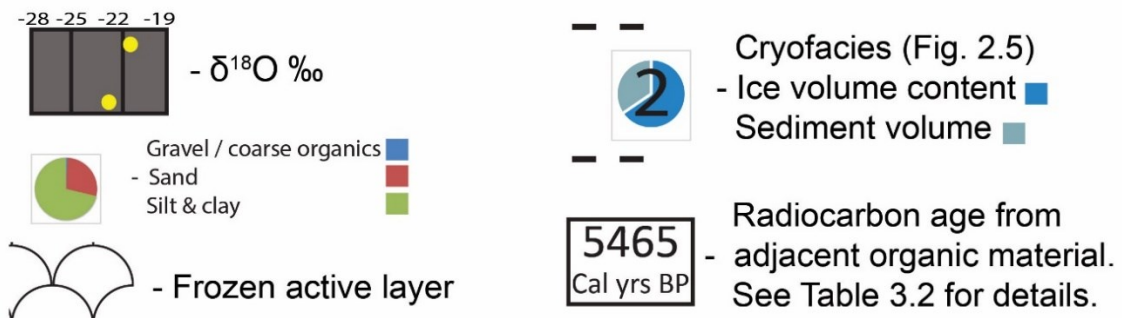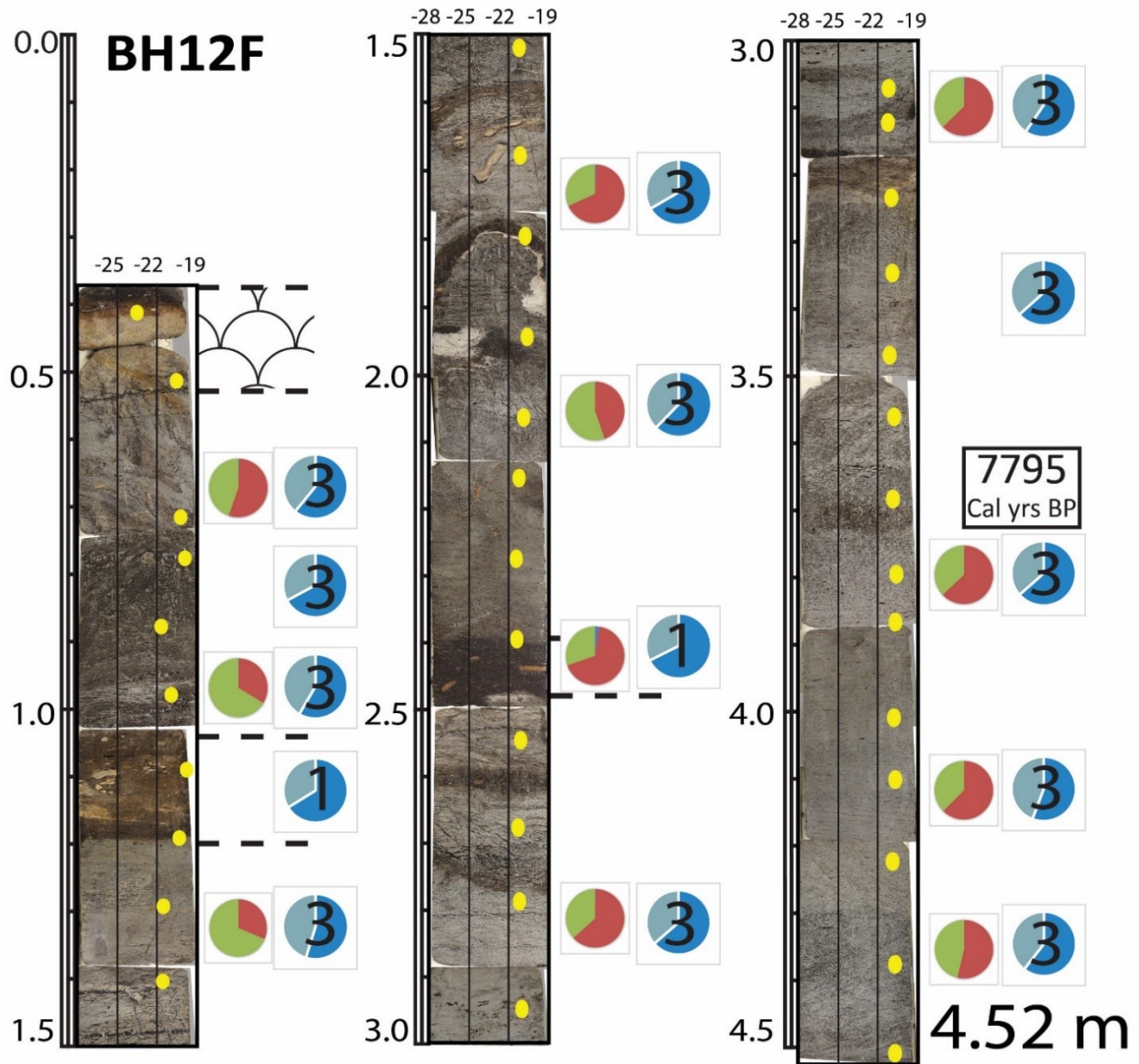
Figure 3.31: Results for BH12F, including water isotopes, grain size, ice volume content, cryostratigraphic interpretations, and radiocarbon results.
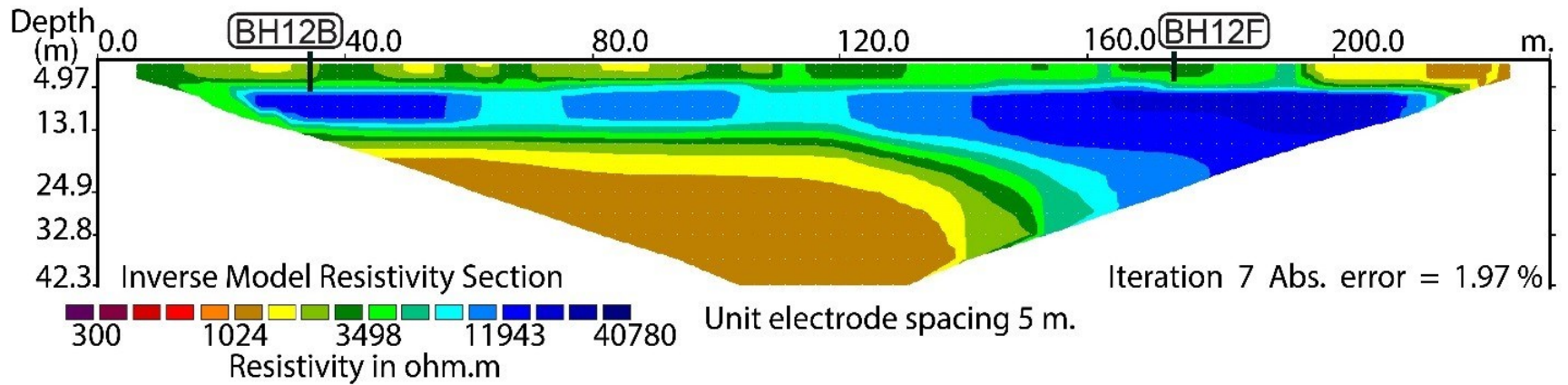
BH12F interpretations

BH12F is located within the same wide flat valley bottom as BH12, home to the present day stream which carries sediment through the valley bottom. The radiocarbon date from the base of the core suggests this core captures deposition at this site from the middle Holocene to present day. The pore ice isotopes confirm a warm interglacial climate during deposition. The cryostratigraphic results point to two periods, not including the present day, where peat was able to establish on the surface. Outside of two stable times there is evidence of sediment input with the mechanism of transport most likely water. This can be confirmed by the high concentration of wood detritus and variable fine grained sediment. The sediment source is most likely a combination of alluvial input from the nearby slopes and flooding of the valley bottom stream.

Due to the limited depth of core retrieval (4.52 m) at this site the lower high resistivity unit seen in the ERT survey (Figure 3.28) was not sampled. The radiocarbon date from this core at 3.7 m depth suggests the transition to the lower unit is very close to the base of the core. The pore water isotopes are within the Holocene expected range and show no signs of depletion at the base of the core. The $\delta^{13}C$ values are consistent with what would be expected form C3 plants dominating the decayed organic material (Ma et *al.* 2012).

BH13 and BH13B descriptions

BH13 and BH13B sites are located at N 62.34209 and W 140. 57761 (kilometre 1896.35) at an elevation of 583 m. Similar to the BH12 valley site, BH13 is within the bottom of an east-west trending valley just north of BH12 along the Alaska Highway. Rampton (1978) mapped this area as mostly eOp (organics overlying flood plain) encompassed by zcsFap (silt, clay, sand,

fluvial outwash plain) (Figure 3.3). The area has several large thaw lakes within the valley

bottom unit (eOp) and, similar to the BH12 valley site, this valley site has bedrock topographic

highs to the north and south of the valley (Figure 3.32).
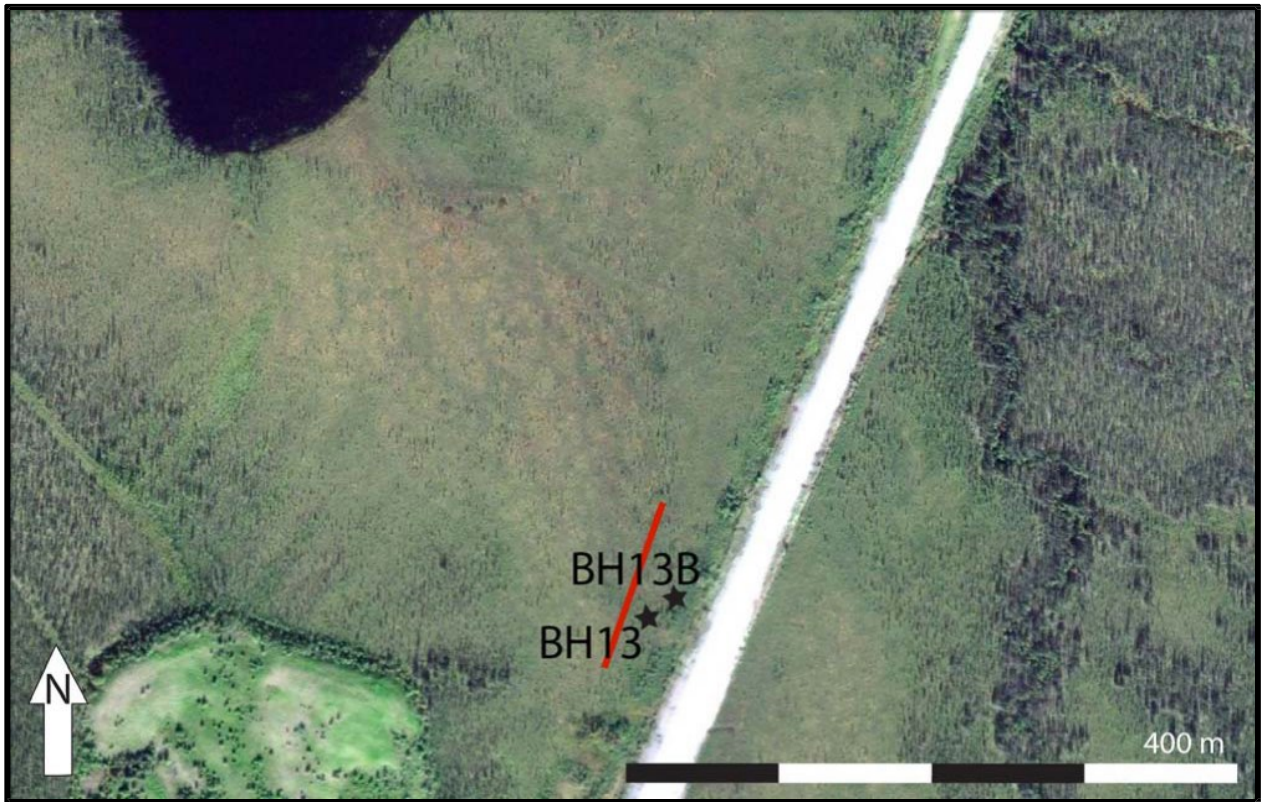
Figure 3.32: Satellite image showing the relative location of BH13 and BH13B borehole sites including ERT survey lines marked by the solid red line (images captured from Google Earth, Data SIO, NOAA, U.S. Navy, NGA, GEBCO, Image © 2015 DigitalGlobe, © 2015 Google, Image Landsat, Image IBCAO).

The dominant vegetation in the higher dry areas is a mixture of white and black spruce, dwarf

birch, and sphagnum. The lower wet areas are dominated by dense tussocks and sphagnum with

sparse black spruce and dwarf birch.

Two boreholes were drilled less than 25 m apart at this site. BH13 (Figure 3.33) cross cut an

ice wedge and BH13B (Figure 3.34) did not. BH13 and BH13B reached depths of 4.85 m and

2.82 m respectively. The frozen front was encountered at a depth of ~33 cm in each core in

late July 2013 with the unfrozen material consisting of peat. The base of the active layer was

estimated in the core results at a depth of ~45 cm in each core based on crustal icing on coarse organics. Four cryofacies are found in the core. Throughout the core, cryofacies 1 (ice-rich peat), 2 (ice-rich sediment), and 3 (ice-poor sediment) are interbedded.   Cryofacies 7 (sediment –poor ice) is present in BH13 from 3.2 m to 4.4 m depth.

$\delta^{18}O$ and δD were sampled throughout the core along with IVC and grain size. In BH13 $\delta^{18}O$ and δD ranges from -19.5‰ to -25.4‰ and -158.6‰ to -197.6‰ respectively whereas BH13B has an enriched range for $\delta^{18}O$ and δD from -20.1‰ to -20.7‰ and -162.6‰ to -166.4‰ respectively. A single organic sample was dated from BH13 at a depth of 480 cm and returned a median calibrated age of 7836 Cal yrs BP (Table 3.2). WRA is not visible in either core at this site.

An ERT survey was obtained at this site using 48 electrodes at a 2.5 m spacing in a Wenner array resulting in a 117.5 m survey with a depth of 21.5 m (Figure 3.35). The survey shows a heterogeneous low resistivity unit (375 – 3500 Ωm) at the top of the survey with an average thickness of 2.5 m. Underlying this is a homogeneous high resistivity unit (3500 – 30,000 Ωm) extending from 2.5 m depth to the base of the survey at 21.2 m depth. The contact between the two units appears sharp with the exception of a ~40 m space between the 80 m and 117.5 m markers where the underlying unit appears much lower in resistivity and therefore the contact is more difficult to observe.

Figure 3.33: Results for BH13, including water isotopes, grain size, ice volume content, cryostratigraphic interpretations, and radiocarbon results.
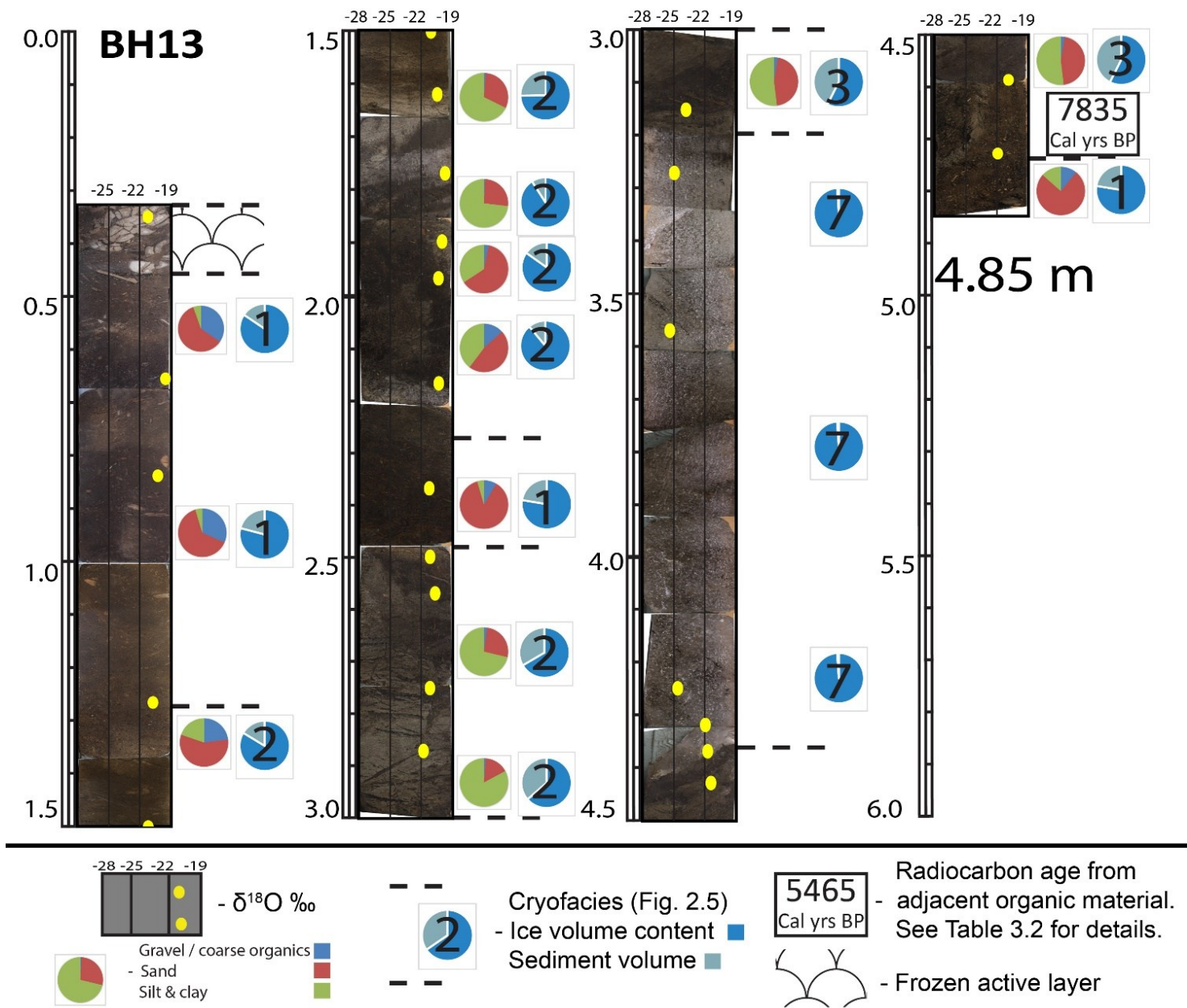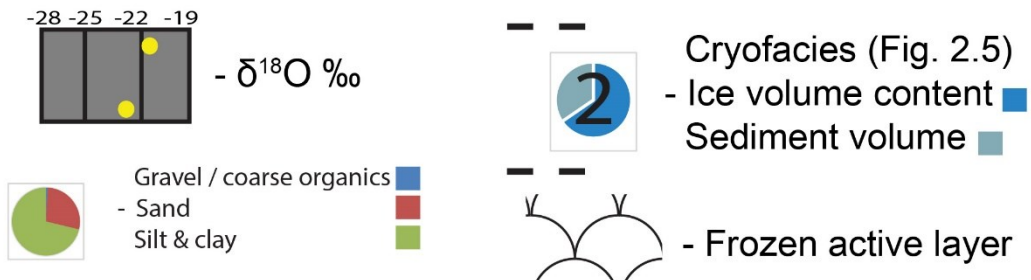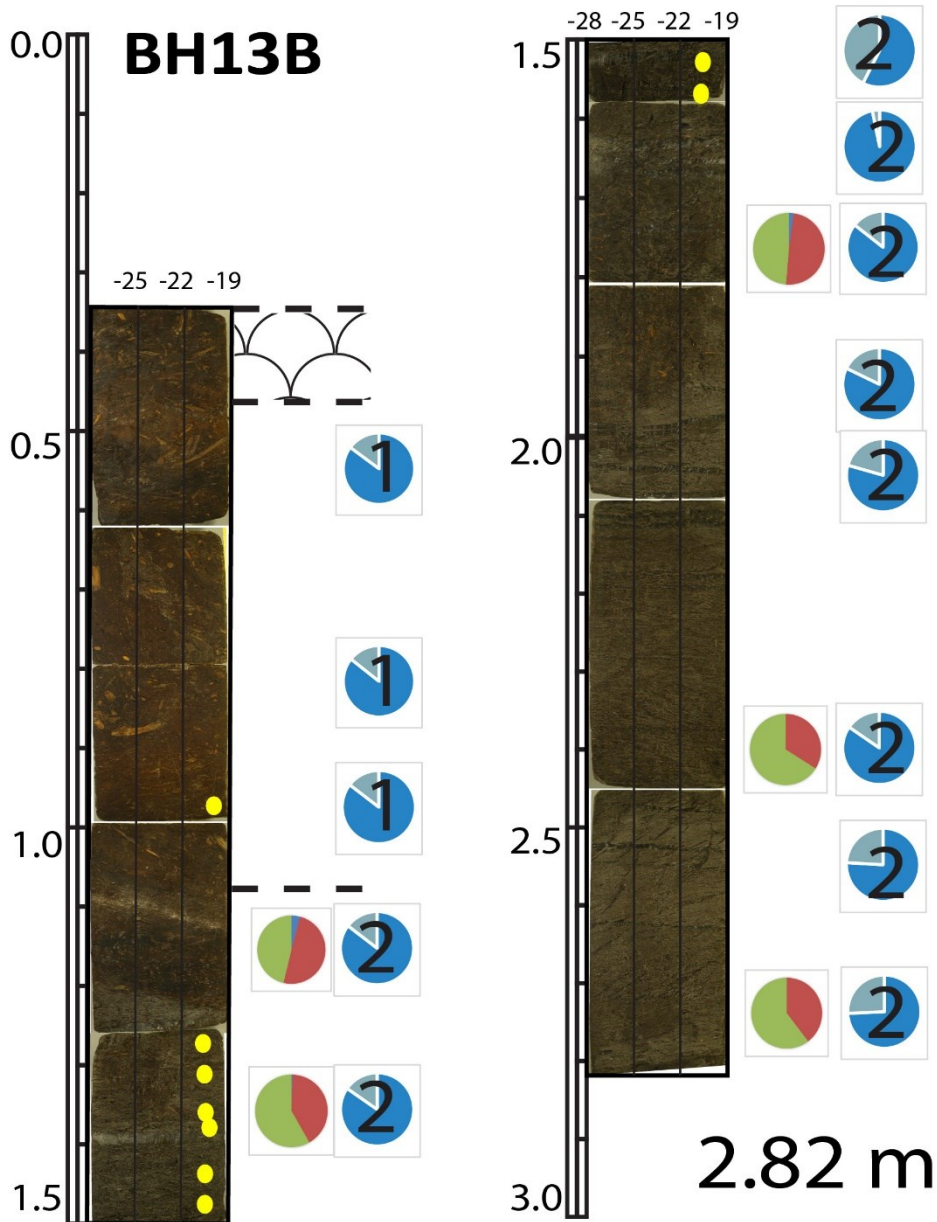
Figure 3.34: Results for BH13B, including water isotopes, grain size, ice volume content and cryostratigraphic interpretations.

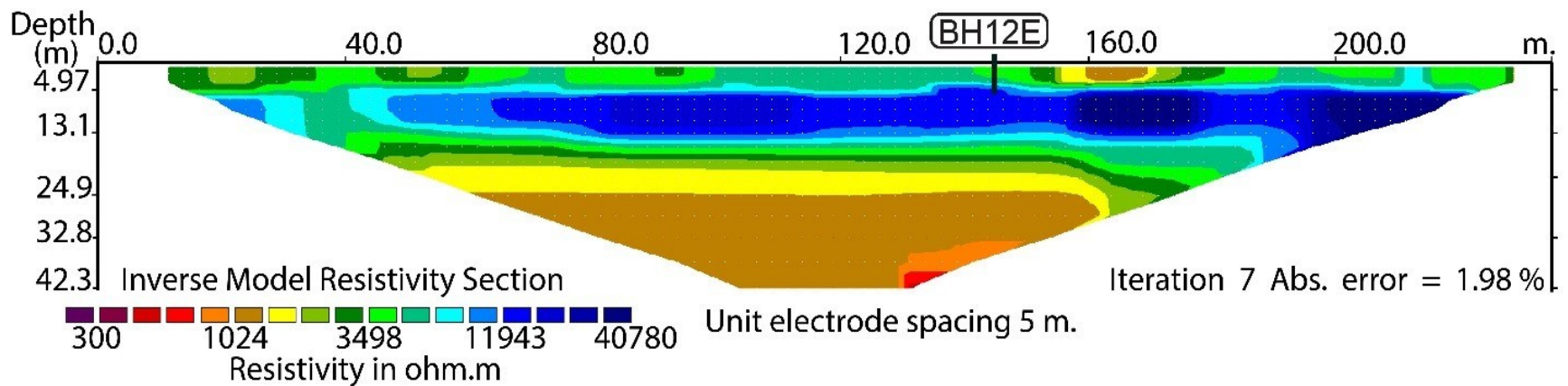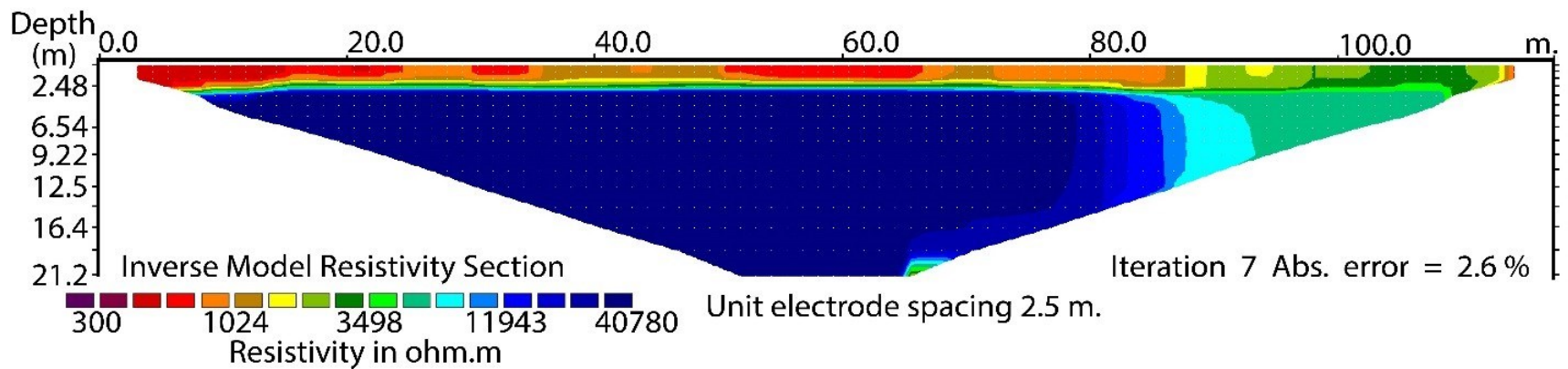Figure 3.35: ERT results for BH13 without borehole locations due to surveys locations not overlapping with borehole. Survey used 48 electrodes with a 5 m spacing and a Wenner array. Inversions were carried out using RES2DINV (Loke and Barker 1996).

BH13 and BH13B interpretations

The radiocarbon date from the base of BH13 suggests the observed material in the cores was deposited from middle Holocene to present day. The pore ice isotopes confirm a warm interglacial climate during deposition with the exception of the ice wedge in BH13 which has an average $\delta^{18}O$ value of -25.0‰. This depletion relative to the surrounding sediments can be explained by the ice wedge capturing more of the winter isotopic signal (snow pack or melt) versus the summer (rain and runoff).

The cryostratigraphic results suggest a period, not including the present day, when peat was able to establish on the surface. This peat layer is 20 cm thick and occurs between 2.48 m and 2.28 m depth, whereas the present day layer extends from the surface down to 1.28 m depth. The sediment seen between these layers was most likely deposited by either alluvial input from the nearby slopes or flooding of the valley bottom.

BH13B was drilled to collect a second core from the site for comparison. BH13B shows the same continuation of peat from the modern surface down to 1.05 m depth. Below this point, organic-rich sandy silts were encountered in the form of cryofacies 2 to the base of the borehole at 2.82 m depth.

This site is similar to BH11 in that the borehole results do not agree with the ERT survey. However, at BH13 the borehole location and ERT survey line are offset by several metres and therefore cannot be directly compared. The ERT survey shows similar results to the BH12 valley with the underlying high resistivity unit showing similar homogeneity and resistivity values. This unit is interpreted as ice-rich Pleistocene material underlying Holocene material, similar to what was observed at BH12E.

Discussion and conclusions

This study has 12 sites resulting in a total of 14 boreholes, 7 ERT surveys and two ground temperature monitoring boreholes across the study area. The combination of the ERT surveys and core results provides insight towards the complex terrain within the study area.

Within the non-glacial terrain the overlying low resistivity unit seen in the ERT surveys contains water isotopes values typical of Holocene pore ice (> -24 ‰ $\delta^{18}O$; Kotler and Burn 2000). ERT results also show the localized near surface high resistivity ice wedge bodies in the valley bottom section. Ice wedges were encountered during borehole exploration (BH19, BH12C, BH12D and BH13) and road maintenance within this upper unit throughout the study area. These findings highlight the amount of ground ice accumulation during the Holocene which is present in the near surface permafrost.

Specific to non-glacial sites is a pattern of repeating layers of organic-rich sandy silts (cryofacies 3 and 2) and peat (cryofacies 1). This pattern is common in non-glacial permafrost terrain sediments where the peat layers mark periods of a stable surface with moist conditions allowing for establishment of vegetation and the sediment layers form during sedimentation events by fluvial, eolian or colluvial deposition (Fraser and Burn 1997). Rampton (1978) recorded similar results (sections, 4-A07 and 4-A08) in the study area while mapping surficial geology of the region.

Where present, cryofacies 4 (ice-poor structureless sediment) marks a regional transition to Pleistocene permafrost sediments displaying a structureless cryostructure indicative of a thaw-unconformity coupled with a smooth trend (mixing line) towards depleted isotopic values.

Underlying cryofacies 4 (ice-poor structureless sediment), BH12E contained cryofacies 5 (ice-poor inorganic sediment), 6 (sediment-rich ice) and 7 (sediment-poor ice) which all exhibit

water isotope values, cryostructures, and radiocarbon dates consistent with an origin typical of Pleistocene silts found across unglaciated Yukon and Alaska (Froese et *al*. 2009; Schirrmeister et *al*. 2013).

BH20 and BH12E are sites that contain Pleistocene aged material confirmed through radiocarbon results. BH20 is in close proximity to two inferred paleo outwash channels and does not record the expected Pleistocene isotopic signal, whereas BH12E is located north of the glacial outwash area and displays the expected Pleistocene values. The ERT survey completed at BH20 displays a thermally degraded version of the BH12E survey with similar units observed but displaying overall lower resistivity values and lower average thicknesses. The detailed borehole and ERT data provide an indication of the distribution of both ice-rich Holocene and Late Pleistocene permafrost within the study area. The addition of stable isotopes and radiocarbon dating provides further evidence for the presence of Late Pleistocene permafrost being unconformably overlain by the ice-rich Holocene material. ERT results outline the distribution of the relict permafrost as highly resistive ice-rich material. Collectively, these results show that complex histories and the potential for long term preservation of permafrost are possible even at remarkably warm sites such as the Alaska Highway corridor.

References

Calmels, F., Allard, M., and Delisle, G. 2008. Development and decay of a lithalsa in Northern Québec: A geomorphological history. Geomorphology, **97**: 287-299.

Duk-Rodkin, A. 1999. Glacial limits map of Yukon Territory. Geological Survey of Canada, Open File 3694, Indigenous and Northern Affairs Canada Geoscience Map 1999-2, scale 1:1 000 000.

Fraser, T.A. and Burn, C.R. 1997. On the nature and origin of "muck" deposits in the Klondike area, Yukon Territory. Canadian Journal of Earth Sciences, 34: 1333-1344.

French, H., and Shur, Y. 2010. The principles of cryostratigraphy. Earth-Science Reviews, **101**: 190-206.

Froese, D.G., Zazula, G.D., Westgate, J.A., Preece, S.J., Sanborn, P.T., Reyes, A.V., and Pearce, N.J.G. 2009. The Klondike goldfields and Pleistocene environments of Beringia. GSA Today, **19**: 4-10.

Heginbottom JA, Dubreuil M-A, Harker PA. 1995. Canada – permafrost. In National Atlas of Canada, 5th edition. Natural Resources Canada: Ottawa, Canada; Plate 2.1 (MCR 4177; scale 1:7 500 000)

Hilbich, C., Hauck, C., Hoelzle, M., Scherler, M., Schudel, L., Volksch, I., Vonder Muhll, D., and Mausbacher, R. 2008. Monitoring mountain permafrost resistivity tomography: 7-year study of seasonal, annual, and long-term variations at Schilthorn, Swiss Alps. Journal of Geophysical Research, 113: 1-12.

IAEA/WMO. 2006. Global Network of Isotopes in Precipitation. The GNIP Database. http://www.iaea.org/water.

Jackson, L.E., Jr., Ward, B.C., Duk-Rodkin, A., and Hughes, O.L. 1991. The last Cordilleran ice sheet in southern Yukon Territory. Geographie Physique et Quaternaire, **45**: 341-354.

Jensen, B.J.L., Pyne-O'Donnell, S., Plunkett, G., Froese, D.G., Hughes, P.D.M., Sigl, M., McConnell, J.R., Amesbury, M.J., Blackwell, P.G., van den Bogaard, C., Buck, C.E., Charman, D.J., Clague, J.J., Hall, V.A., Koch, J., Mackay, H., Mallon, G., McColl, L., and Pilcher, J.R. 2014. Transatlantic distribution of the Alaskan White River Ash. Geology, **42**: 875-878.

Jorgenson, M.T., Romanovsky, V., Harden, J., Shur, Y., O'Donnell, J., Schuur, E.A.G., Kanevskiy, M. and Marchenko, S. 2010. Resilience and vulnerability of permafrost to climate change. Canadian Journal of Earth Sciences, 40: 1219-1236.

Jouzel, J., Merlivat, L., and Lorius, C. 1982. Deuterium excess in an East Antarctic ice core suggests higher relative humidity at the oceanic surface during the last glacial maximum. Nature, **299**: 688-691.

Kotler, E., Burn, C.R., 2000. Cryostratigraphy of the Klondike "muck" deposits, west-central Yukon Territory. Canadian Journal of Earth Sciences, 37, 849–861.

Lacelle, D. 2011. On the $\delta^{18}O$, δD and d-excess relations in meteoric precipitation and during equilibrium freezing; theoretical approach and field examples. Permafrost and Periglacial Processes, **22**: 13-25.

Loke, M.H., and Barker, R.D. 1996. Practical techniques for 3D resistivity surveys and data inversion. Geophysical Prospecting, **44**: 499-523.

Ma J.Y., Sun W., Liu X.N., Chen F.H. 2012. Variation in the Stable Carbon and Nitrogen Isotope Composition of Plants and Soil along a Precipitation Gradient in Northern China.

PLoS ONE 7(12): e51894. doi: 10.1371/journal.pone.0051894.

Mackay, R.J. 1974. Reticulate ice veins in permafrost, northern Canada. Canadian Geotechnical Journal, **11**: 230-237.

Newsome S.D., Miller G.H., Magee J.W., Fogel M.L. 2011. Quaternary record of aridity and mean annual precipitation based on d15N in ratite and dromornithid eggshells from Lake Eyre, Australia. Oecologia Springer, **167**:1151-1162.

Rampton, V.N. 1978. Surficial geology and geomorphology; Mirror Creek, Yukon Territory. Geological Survey of Canada: Ottawa, ON, Canada, Canada.

Reyes, A.V., Froese, D.G., and Jensen, B.J.L. 2010. Permafrost response to last interglacial warming; field evidence from non-glaciated Yukon and Alaska. Quaternary Science Reviews, **29**: 3256-3274.

Schirrmeister, L., Froese, D.G., Tumskoy, V., Grosse, G., Wetterich, S. (2013). Yedoma: Late Pleistocene ice- rich syngenetic permafrost of Beringia. In: S.A. Elias, The Encyclopedia of Quaternary Science, 3, 542-552.

Throop, J., Lewkowicz, A.G., and Smith, S.L. 2012. Climate and ground temperature relations at sites across the continuous and discontinuous permafrost zones, northern Canada. Canadian Journal of Earth Sciences, **49**: 865-876.

Ward, B.C., Bond, J.D., and Gosse, J.C. 2007. Evidence for a 55-50 ka (early Wisconsin) glaciation of the Cordilleran ice sheet, Yukon Territory, Canada. Quaternary Research, **68**: 141-150.

Note: A version of this chapter has been published in the proceedings of the 2015 GEOQuebec conference.

Chapter 4: Characterizing Permafrost Valley Fills Along the Alaska Highway, Southwestern Yukon

Abstract

In the Beaver Creek area of Southwestern Yukon, the Alaska Highway traverses both glaciated and non- glaciated terrain from the Last Glacial Maximum. In this area permafrost characteristics are strongly influenced by regional glacial history including the distribution of relict Pleistocene permafrost. Here we characterize the distribution and history of permafrost in a valley fill along the Alaska Highway between Beaver Creek and the Alaska border using a multidisciplinary approach. Our surveys include Electrical Resistivity Tomography (ERT), permafrost drilling, cryostratigraphy, and geochemical analyses to define the boundaries and characteristics of the valley fill. Using ERT data we mapped the widespread distribution of ice-rich organic silts of Holocene age that unconformably overlie relict syngenetic permafrost from the Late Pleistocene within the valley fill. Radiocarbon dating and stable isotope analyses of $\delta^{18}O$ and δD, combined with detailed cryostratigraphy, confirm the presence of relict syngenetic ground ice from the Late Pleistocene (>57,000 14C years BP), indicating the considerable antiquity of ice-rich permafrost at this southerly locality.

Introduction

Low relief valley fills with extensive organic-rich soils and wetlands are common features in the lowland areas of unglaciated Yukon and Alaska (Jensen et *al*. 2009; Kanevskiy et *al.* 2014). These plains and lowlands may be composed of eolian, alluvial, lacustrine, and organic sediments (Froese 2005) and may record complex local histories of sedimentation. In this

paper we investigate a single low relief valley fill in Southern Yukon using a combination of borehole data and Electrical Resistivity Tomography (ERT) surveys.

The Alaska Highway traverses Southern Yukon in the discontinuous permafrost zone (Smith and Riseborough, 2002; Throop et *al*. 2012). Between Beaver Creek and the Alaska border, the highway is constructed on both syngenetic and epigenetic permafrost. In areas of syngenetic permafrost ice volume tends to be greater than in areas of epigenetic permafrost with a distribution related to the past climate and sedimentation history at the time of formation. In the non-glaciated areas, where eolian sedimentation took place during the Late Pleistocene, ice volumes may approach 50% of the subsurface where syngenetic ice wedges accompanied aggradation (Kanevskiy et *al*. 2011; Schirrmeister et *al*. 2013). The geochemical, geochronological, and cryostratigraphical aspects of permafrost are important in understanding its origins and paleoclimatic significance (Burn et *al*. 1986). Understanding ground ice distribution along the Alaska Highway is crucial when considering continued highway maintenance and construction under a warming climate (Opel et *al*. 2011; Throop et a*l*. 2012).

Permafrost samples collected from borehole exploration provide an opportunity to investigate each of the afore mentioned aspects. $\delta^{18}O$ and δD from ice-rich permafrost samples and radiocarbon dating of organic- rich samples provide details on the origin of the sediment pore water (Lacelle et *al.* 2009). The use of detailed cryostratigraphic interpretations offers a better understanding of permafrost genetic history (Murton and French 1994; Bray et *al*. 2006; French and Shur 2010). In this study, we use borehole data combined with ERT surveys to interpret the distribution and extent of permafrost. Using this combined approach, we utilize the borehole and ERT data to: (1) map the distribution of ice-rich permafrost in a lowland valley-fill along the

Alaska Highway; and (2) determine the age of the ice rich permafrost within the valley fill.

Study area

The study area is located in Southwestern Yukon, 10 km north of Beaver Creek along the Alaska Highway in the discontinuous permafrost zone (Figure 4.1). This region is an area of meta-stable warm permafrost (Throop et *al.* 2012), making it a suitable area to study permafrost as it approaches thaw temperatures. The dominant vegetation cover in the study area is a combination of moss-sphagnum and sedge-tussock communities, often coupled with low-density black spruce. The Last Glacial Maximum (LGM) limit, as mapped by Duk-Rodkin (1999), cross cuts the Alaska Highway ~5 km south of Beaver Creek. It is assumed that terrain south of the limit is glacially influenced and material north is influenced more by periglacial processes associated with the proglacial and extraglacial environment.
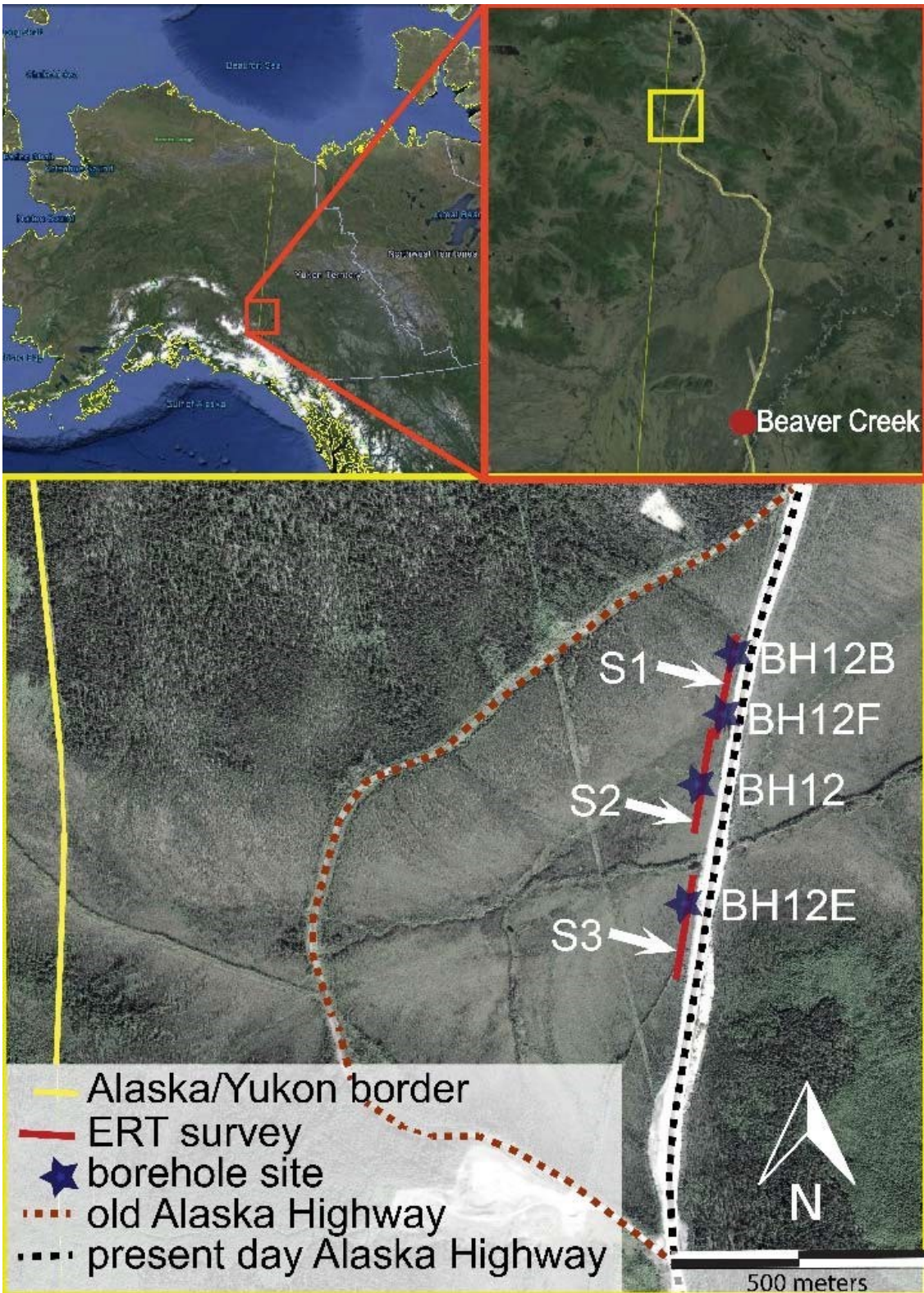
Figure 4.1: Map of the study area using images captured from Google Earth (Data SIO, NOAA, U.S. Navy, NGA, GEBCO, Image © 2015 DigitalGlobe, © 2015 Google, Image Landsat, Image IBCAO). The lower panel is indicated in the upper right panel by the yellow box.

Methodology

This project uses a multidisciplinary approach including geophysical surveys, geochemical analyses and geomorphological interpretations. In total four boreholes were drilled and three ERT surveys completed within the study area (Figure 4.1). The three electrical resistivity tomography (ERT) surveys (S1, S2 and S3; Figure 4.1) were collected with an Iris Syscal Junior switch 48, using a Wenner array. One profile was collected in the valley bottom and one on both north and south valley walls. Each survey used 48 electrodes with a 5 m spacing for a total survey length of 235 m and, using the Wenner array, reached a depth of 42 m. The surveys were inverted using RES2DINV (Loke and Barker 1996). Out of the four boreholes drilled, two were collected in the valley bottom and one on either valley wall. Each borehole intersected an ERT survey to allow for ground truthing of the ERT results. The boreholes were drilled using a portable earth drill (Calmels et *al.* 2005) and collected cores were then stored in a portable cooler on site and at the end of the day transferred to a deep freeze for storage until they could be returned to the lab. At the University of Alberta the cores were sampled for grain size analyses, ice volume content, water isotopic analyses, organic matter for radiocarbon dating, and volcanic ash, where present, for electron microprobe analyses using established methods (Jensen et *al.* 2008). Ice volume measurements were carried out using a half section of the core in order to keep a clean sample for isotope analyses. The half section of core was submerged in 1.5 litres of cold water housed in a 4 inch diameter PVC pipe and the displaced water was drained and measured with a 250 ml graduated cylinder. The ice volumes reported include pore ice. Water isotope analyses were completed on a Picarro L2130-*i* water isotope analyzer in the EAS department at the University of Alberta. The $\delta D/\delta^{18}O$ values were calibrated to VSMOW based on two standards (USGS 45 and USGS 46) run at the same time as the unknowns.

Measurement precision in this study is 0.5‰ for δD and 0.1‰ for $\delta^{18}O$ based on routine measurement of an internal lab standard. Radiocarbon samples were prepared using an Acid-Base-Acid (HCl-NaOH-HCl, both 1 molar concentration) pre-treatment at the University of Alberta and analyzed at the Keck Accelerator Mass Spectrometry Lab at the University of California, Irvine. Cryostratigraphic interpretations were completed on each core using a slightly modified version of the classification scheme outlined in Murton and French, 1994 (Figure 4.2).

Results

Cryostratigraphy

Seven cryofacies were defined based on cryostructures, ice content, grain size, sediment type, and orientation of the sedimentary layers (Figure 4.2). Throughout the valley fill cryofacies 3 (Organic-rich, ice- poor sandy silt) and 1 (ice-rich peat) repeat in each borehole with the exception of the southern borehole BH12E where cryofacies 1 is absent. BH12E is the only borehole that contains cryofacies 5 (ice-poor organic-rich sandy silt), 6 (sediment-rich ice) and 7 (sediment-poor ice). Two cryofacies assemblages have been identified based on repeating patterns or significant lithological or geochemical changes. Cryofacies assemblage one, upper unit, is defined by a repetition or presence of cryofacies 1, 2 and 3. Cryofacies assemblage two, lower unit, consists of cryofacies 4 through 7.
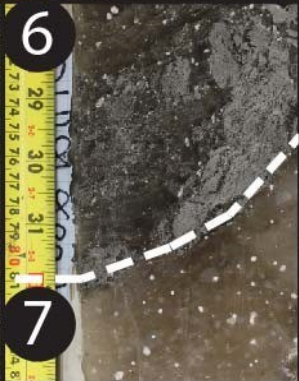
Cryofacies			
		#	Description
		1	Ice-rich structureless peat with visible wood fragments suspended in peat and crustal cryostructure.
		2	Ice-rich cryoturbated to flat lying peat or organic-rich sandy silts; may contain ash, wood fragments, and gravel. Sandy silts have parallel layered (0.2-2.5 cm thick) or non-parallel wavy lenticular ice (0.1-0.8 cm thick). Peat displays non-parallel wavy lenticular (0.3-1.2 cm thick). Ash (if present) and sand or gravel rich layers are structureless. Crustal cryostructure commonly surrounds wood fragments.
		3	Flat lying to cryoturbated sandy silt with variable organic content, gravel, peat, ash (if present) and wood fragments with moderate to low ice content. Vertical and horizontal ice layers (0.1-1.1cm thick) visible throughout. Silt contains non-parallel wavy lenticular (0.3-6.0 mm thick). Sections of peat are structureless to parallel wavy lenticular (0.1-1.0 cm thick) and wood fragments have a crustal cryostructure. Ash and coarse sandy silt are structureless.
		4	Ice-poor sandy silt with gravel; structureless cryostructure.
		5	Cryoturbated ice-poor structureless grey sandy silt, organic silt, and wood fragments throughout.
		6	Sediment-rich ice with suspended brown silt; pool ice or karst ice.
		7	Foliated sediment-poor ice with subvertical gas bubble foliations; ice wedge ice.

Figure 4.2: Images and descriptions of each cryofacies found in the study area. The classification scheme outlined by Murton and French (1994) guided these results.

Grain size and ice volume

The sediments primarily consist of silt and clay with smaller components of sand and gravel.

The ice volume content in the two valley bottom boreholes (BH12 and BH12F) is greater on average than the valley wall boreholes (BH12E and BH12B). The valley wall boreholes BH12E and BH12B have similar ice volume content throughout (Figure 4.3).

Stable isotopes

The isotopic ratios of pore ice sampled from the boreholes typically range from -19.5 to -22.4 ‰

δ^{18}O and -155 to -177 ‰ for δD. These values are typical for all cores except for the bottom two

cores from BH12B and the bottom half of BH12E, where more depleted isotopic ratios were

sampled with values between -23‰ and – 27‰ for δ^{18}O, and -180‰ to -220‰ for δD (Figure

4.3).

Chronology

Each borehole contained a layer of the eastern lobe of the White River Ash (A.D. 833–850) in

the top 2 m but no other ash layers at greater depths (Jensen et *al*. 2014). Radiocarbon dates are

plotted in Figure 4.3 and Table 4.1. Radiocarbon dates from below ~3.5 m depth at BH12E are

beyond the limit of radiocarbon dating, giving non-finite results. All radiocarbon samples were

>.3mg except one as seen in Table 1. Small mass standard FIRI-F (AKA FIRI-D ca 4510 ^{14}C yr

BP; Boaretto et *al*. 2002) is within error of its expected value (Table 4.1). The samples were also

run with a non-finite standard AVR-07-PAL-37 (Reyes et *al*. 2010). Previous work has shown

that robust woody samples from similar sediments may yield inaccurate age estimations due to

reworking of the organic material (Kennedy et *al*. 2010). The one sigma radiocarbon age ranges

from BH12B date to the early Holocene 8450-9245 Cal years BP (485 cm depth) and 8060-8180

Cal years BP (385 cm depth; Figure 4.3 and Table 4.1).

Table 4.1: Radiocarbon dates including calibrated one sigma range, non-calibrated result, error and lab (UCIAMS) number. Dates were calibrated using Calib ver. 7.1 with the intCal13 calibration curve (Reimer et *al.* 2013).

UCIAM	Sample	Mater	^{14}C age	±	Cal ^{14}C age BP
156126	BH12F-386	wood	6960	15	7760-7830
142056	BH12-433	wood	4555	20	5140-5310
156127	BH12B-191	wood	3810	15	4155-4230
156134	BH12B-264	wood	4720	20	5330-5575
156133	BH12B-385	wood	7335	15	8060-8180
156130	BH12B-485 .013mgC	grass	7960	330	8450-9245
156128	BH12E-191	wood	6385	20	7270-7406
156138	BH12E-358	wood	>50800		
156139	BH12E-466	wood	>55500		
156131	FIRI-F .015mgC	wood	4670	150	
156132	FIRI-F	wood	4540	15	
156136	AVR-07-PAL-37	wood	51500	370	
156137	AVR-07-PAL-37 .013mgC	wood	24230	300	

Geophysical surveys

The ERT surveys provide a two-dimensional view of the resistivity properties of the subsurface (Lewkowicz et *al.* 2011). The base of the active layer is not visible in the surveys due to the large electrode spacing. However, below ~1.25 m depth ground resistivity values are resolved in the model. The top of each survey shows a heterogeneous layer in terms of resistivity, with values varying between 400 and 7000 ohm-m. This variable top layer ranges in thickness from ca. 3 -20 m, and typically overlies a higher resistivity layer. The high resistivity (~12,000 ohm-m) layer varies between 10 and 25 m in thickness and is present at 6.25 m, 5.5 m, and 5.5 m depth at the north, bottom, and south valley sites respectively (Figure 4.4). The lower deposits of both valley wall surveys are dominated by a thick laterally continuous layer of lower resistivity (~1200 ohm-m). This layer dips towards the valley bottom in both surveys and is between 14 m and 35 m thick (Figure 4.4).

Discussion

The cryostratigraphic investigation highlighted that the majority of the boreholes contain repeating layers of organic-rich sandy silts (cryofacies 3) and peat (cryofacies 1) (Figure 4.3). This repeating pattern is common in permafrost sediments where the peat layers mark periods of a stable surface with moist conditions allowing for establishment of vegetation and the sediment layers form during sedimentation events by fluvial, eolian or colluvial deposition (Fraser and Burn 1997).

Rampton (1978) recorded similar results (sections 4-A07 and 4-A08) in the study area while mapping surficial geology of the region. Organic material taken from the basal section within the upper unit dates to the early Holocene in both BH12E (7270-7406 Cal yrs BP (1σ); UCIAMS-156128) and BH12B (8450-9245cal yrs BP (1σ); UCIAMS-156130). Isotopes from this unit are typical of Holocene pore-ice (> -24 ‰ δ^{18}O; Figure 4.3; Kotler and Burn 2000). Several ice wedges were encountered during test boreholes and road maintenance within this upper unit throughout the valley with the exception of the northern valley slope. ERT results also show the localized near surface high resistivity ice wedge bodies in the valley bottom section (Figure 4.4).

Beginning at 2.9 and 5 m depth in BH12E and BH12B respectively, cryofacies 4 marks the transition to Late Pleistocene permafrost sediments in the lower unit (Figure 4.3). Cryofacies 4 consists of ice-poor sandy silt and gravel exhibiting a structureless cryostructure throughout (Figure 4.2). Within BH12B cryofacies 4 contains a large vertical reticulate ice vein (40 cm long and 1cm thick) most likely as a result of thawing ice rich permafrost and subsequent refreezing in a semi-closed freezing system (Mackay 1973). Incidental with cryofacies 4 is a marked trend toward more depleted isotope values that are typical of Late Pleistocene

conditions (< -24 ‰ δ 18O; Figure 4.3; Kotler and Burn 2000). These depleted isotope values,

associated with cryofacies 4, mark the cryostratigraphic transition from polygenetic Holocene

permafrost to syngenetic Late Pleistocene permafrost. A sharp transition in pore water isotopes

is not observed within the core to support this unconformable nature of the underlying and

overlying material. This is likely due to the underlying depleted pore water isotopes mixing

with the overlying relatively enriched pore water isotopes creating the observed smooth

mixing line across the boundary. Cryofacies 5 is made up of cryoturbated ice-poor

structureless organic grey sandy silt with wood fragments throughout. Radiocarbon dates taken

from this cryofacies were non-finite indicating a minimum age for the unit of >57000 14C age

BP. This suggests deposition occurred prior to or concurrent with Reid-McConnell interglacial

period (Hopkins 1982). Cryofacies six and seven are sediment-rich pool ice and sediment-poor

ice wedge ice respectively. The isotopic values, cryostructures, and radiocarbon dates from

cryofacies 5, 6, and 7 together indicate an origin typical of Pleistocene silts found across

unglaciated Yukon and Alaska (Froese et *al*. 2009; Schirrmeister et *al*. 2013).

Figure 4.3:
Four picture
logs adjusted
using
Photoshop to
highlight
visible ice in
black. The
logs are
presented in
order from
south (left) to
north (right)
across the
valley.

BH12E

BH12

BH12F

BH12B

57
-24.14
54
-25.00
Non-Finite
-25.92
55
-26.52
59
-26.64
58
-26.72
-26.92
60
-26.98
Non-Finite
-26.94
66
-27.18
71
-27.21
-27.86
-23.62

51
-20.53
72
-21.84
67
-21.42
-22.54
69
-22.67
63
-22.80
54
-22.25
7310
-/+ 20
Cal yrs BP
69
-21.89
58
-22.08
47
-22.83
69

5.86 m

57 — 3
54
-25.00

80 — 0
-21.47

82 — 1
-19.41
84
-19.86
-21.30
76 — 2
78 — 0
-20.83
-21.15
83 — 1
-21.04
89 — 0
80 — 2
5175
-/+ 20
Cal yrs BP

83 — 1
-21.35
76

72

66
-21.69
72 — 2

74
-21.32

4.36 m

-23.54
60
61 — 2
-20.23
58 — 0
-19.91
-19.79
83
-20.34
61
-21.34
56
-20.87
61
-20.99
62

-21.52
64 — 0

64
-21.31
64
-21.14

59
-20.95
63 — 2
-21.07
63
-20.82
7795
-/+ 15
Cal yrs BP
-20.66
-20.67

4.52 m

55 — 1
-21.80
79 — 0
-20.72
-20.76
73 — 1
-21.57
68 — 0
-21.18
65 — 2
65
-21.03
4195 — 0
-/+ 15
Cal yrs BP
75
-21.33
71
-21.51
5465
-/+ 20
Cal yrs BP
75 — 2
-21.88

62
-22.10
53
-22.33
60
-22.21
8140 — 0
-/+ 15
Cal yrs BP
64
-22.33
-21.98
65
8860 — 2
-/+ 330
Cal yrs BP
no
data
72
-22.46
-23.49
-23.72
-23.91 — 3

5.83 m

121

■ - Ice   -20.79 - Delta δ¹⁸O ‰   ⌐⌐②⌐ - Cryofacies (Fig. 2)   5465   Radiocarbon age from
▦ - Ice rich organics   □ - sediments/organics with no visible ice   -/+ 20   adjacent organic material.
                  63 - Ice volume content   Cal yrs BP See Table 1 for details.

Sharply overlying these deposits and dating to the early Holocene are organic rich silts that mark the re-aggradation of permafrost following thaw degradation. Cryostratigraphic analyses reveal that cryofacies 3 most likely represents a paleo-thaw unconformity based on the structureless cryostructure, change in water isotope values, and non-conformable radiocarbon dates above and below (Kotler and Burn 2000; French and Shur 2010). This unconformity records thermal degradation and removal of the Late Pleistocene material which would have been deposited prior to and during the McConnell Glaciation (Jackson et al. 1991; Kotler and Burn 2000; Jorgenson et al. 2010; Reyes et al. 2010). This process would have continued until the active layer stabilized in Holocene sediments. The natural thickening of sediments in the valley bottom compounded with the shallow boreholes collected from the valley bottom, resulted in the valley bottom boreholes not intercepting the ice-rich Pleistocene material which the ERT results suggest persists throughout the valley bottom at depth.

Three electrical resistivity tomography surveys spanning the valley section parallel to the highway provide an improved image of the distribution of permafrost (Figure 4.1 and Figure 4.4). A high resistivity layer present at depth throughout each survey is interpreted as relict Late Pleistocene syngenetic permafrost and this is supported by the valley wall boreholes BH12E and BH12B (Figure 4.3 and Figure 4.4). In the southern survey at 5.5 m depth, this layer was sampled in BH12E and includes an ice body at ~5.6 m depth. Direct sampling of this layer provides a ground truthing for the ERT surveys. At position "A" in Figure 4.4, the high resistivity layer is absent ~45 m along the profile. As seen in Figure 4.1, the first electrode of the survey (S3) was placed within a few metres of a small pond adjacent to the highway created by a collapsed culvert. The presence of the pond has resulted in the thaw of any proximal ice

rich Late Pleistocene permafrost and truncated the high resistivity layer. Similarly, a small creek runs through the center of the valley and is prominent in the valley bottom survey where the high resistivity layer is absent (position B in Figure 4.4) and instead low resistivity values record a greater presence of liquid water within the sediments (Hilbich et *al*. 2008). Across the entire valley at a depth of 20 m to 25 m, a large low resistivity layer is present in each survey marking the depth of the ice-rich permafrost which cannot be interpreted due to lack of direct sampling.
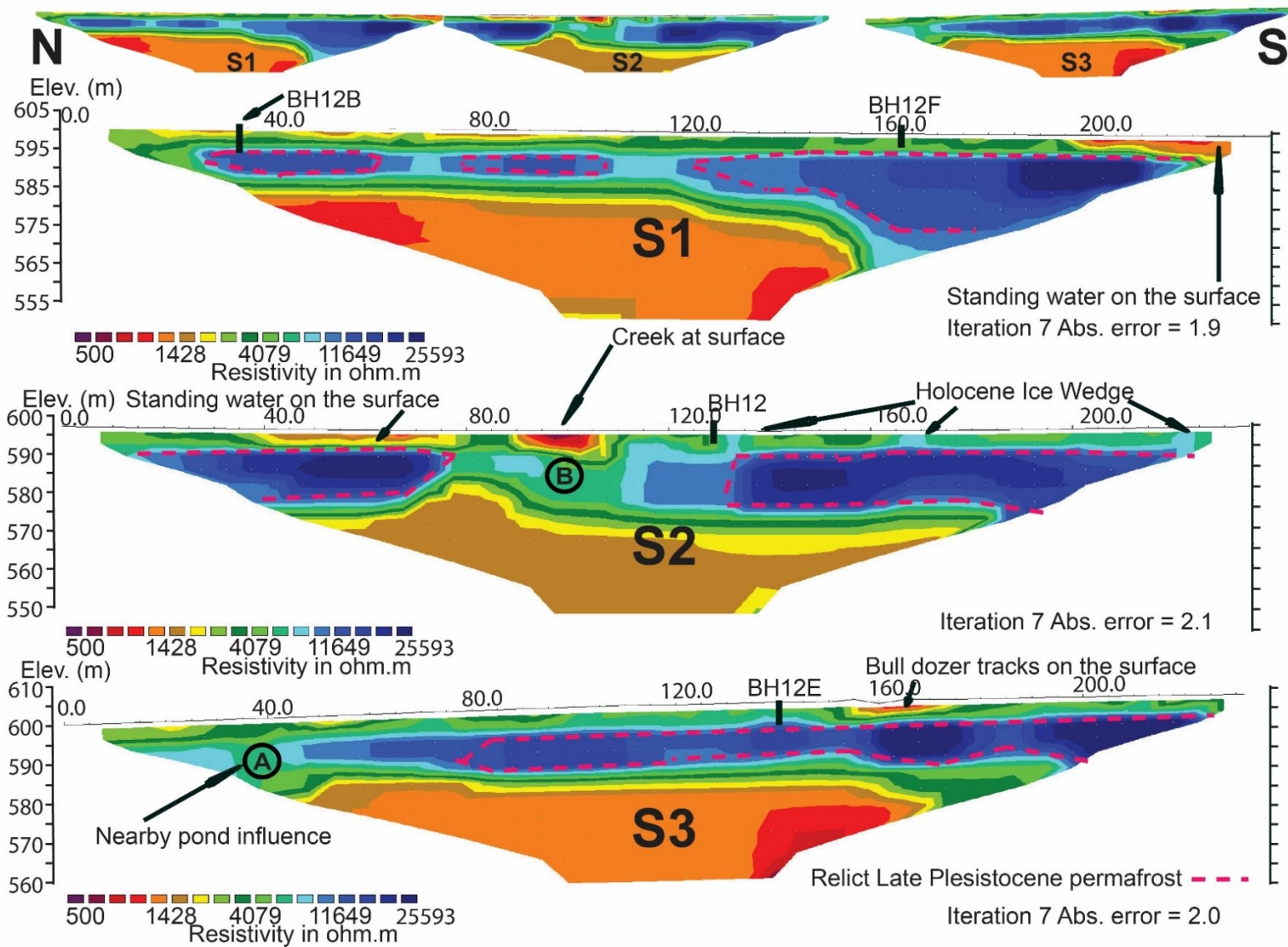
Figure 4.4: Electrical resistivity tomography results for the three surveys done across the valley from north to south. All surveys used 48 electrodes at 5 m spacing and have an Abs. error <2.2%.

Conclusions

The detailed borehole and ERT data provide an indication of the distribution of both ice-rich Holocene and Late Pleistocene permafrost within the valley fill. The addition of stable isotopes and radiocarbon dating provide further evidence for the presence of Late Pleistocene permafrost being unconformably overlain by the ice-rich Holocene material. ERT results outline the valley wide distribution of the relict permafrost as highly resistive ice-rich material. Collectively, these results show the complex valley-fill histories and the potential for long term preservation of permafrost even at remarkably warm sites such as the Alaska Highway corridor. Effective highway maintenance along the Alaska Highway relies on the understanding of permafrost distribution surrounding the highway corridor. A combination of borehole data and ERT can provide effective local scale mapping of permafrost along the highway corridor.

References

Boaretto, E., Bryant, C., Carmi, I., Cook, G., Gulliksen, S., Harkness, D., Heinemeier, J.,

McClure, J., McGee, E., Naysmith, P., Possnert, G., Scott, M., van der Plicht, H., and van Strydonck, M. 2002. Summary findings of the fourth international radiocarbon intercomparison (FIRI)(1998–2001) *Journal of Quaternary Science*, 17: 633-637.

Bray, M.T., French, H.M. and Shur, Y. 2006. Further Cryostratigraphic Observations in the CRREL Permafrost Tunnel, Fox, Alaska. *Permafrost and Periglacial Processes*, 17: 233-243.

Burn, C.R., Michel, F.A. and Smith, M.W. 1986. Stratigraphic, isotopic, and mineralogical evidence for an early Holocene thaw unconformity at Mayo, Yukon Territory. *Canadian Journal of Earth Sciences,* 23: 794-803.

Calmels, F., Gagnon, O. and Allard, M. 2005. A Portable Earth-drill System for Permafrost Studies. *Permafrost and Periglacial Processes*, 16: 311-315.

Craig, H. 1961. Standard for reporting concentrations of deuterium and oxygen-18 in natural waters. Science, **133**: 1833-1834.

Duk-Rodkin, A. 1999. Glacial limits map of Yukon Territory. Geological Survey of Canada, Open File 3694, Indigenous and Northern Affairs Canada Geoscience Map 1999-2, scale 1:1 000 000.

Fraser, T.A. and Burn, C.R. 1997. On the nature and origin of "muck" deposits in the Klondike area, Yukon Territory. *Canadian Journal of Earth Sciences,* 34: 1333-1344.

French, H.M. and Shur Y. 2010. The principles of cryostratigraphy. Earth Sciences Reviews, 101: 190-206. Froese, D.G., 2005. Surficial Geology of Flat Creek (115 O/15) Yukon Territory, Open File 4592. Geological Survey of Canada, Ottawa.

Froese, D.G., Zazula, G.D., Westgate, J.A., Sanborn, P.T., Reyes, A.V., and Pearce, N.J.G. 2009. The Klondike goldfields and Pleistocene environments of Beringia. *GSA Today*, 19: 4-10.

Hilbich, C., Hauck, C., Hoelzle, M., Scherler, M., Schudel, L., Volksch, I., Vonder Muhll, D., and Mausbacher, R. 2008. Monitoring mountain permafrost resistivity tomography: 7-year study of seasonal, annual, and long-term variations at Schilthorn, Swiss Alps. *Journal of Geophysical Research,* 113: 1-12.

Hopkins, D.M. 1982. Aspects of the paleogeography of Beringia during the Late Pleistocene. *In* Paleogeography of Beringia. *Edited by* D.M. Hopkins, J.V. Matthews, Jr., C.E. Schweger, and S.B. Young. Academic Press, New York. Pp. 3-28.

Jackson, L.E., Ward, B., Duk-Rodkin, A. and Hughes, O.E. 1991. The Last Cordilleran Ice Sheet in Southern Yukon Territory. *Géographie physique et Quaternaire,* 45: 341-354.

Jensen, B.J.L., Froese, D.G., Preece, S.J., Westgate, J.A. and Stachel, T. 2008. An Extensive middle to Late Pleistocene tephrochronologic record from east-central Alaska. *Quaternary Science Reviews*, 27: 411- 427.

Jensen, B.J.L., Pyne-O'Donnell, S., Plunkett, G., Froese, D.G., Huges, P.M.D., Sigl, M., McConnell, J.R., Amesbury, M.J., Blackwell, P.G., van den Bogaard, C., Buck, C.E., Charman, D.J., Clague, J.J., Hall, V.A., Koch, J., MacKay, H., Mallon, G., McColl, L. and Pilcher, J.R. 2014. Transatlantic distribution of the Alaskan White River Ash. *Geology*, 42: 875-878.

Jensen, M.A., Demidov, I.N., Larsen, E. and Lysa, A. 2009. Quaternary palaeoenvironments and multi- storey valley fills architecture along the Mezen and Severnaya Divina river valleys, Arkhangelsk region, NW Russia. Quaternary Science Reviews, 28: 2489-2506.

Jorgenson, M.T., Romanovsky, V., Harden, J., Shur, Y., O'Donnell, J., Schuur, E.A.G., Kanevskiy, M. and Marchenko, S. 2010. Resilience and vulnerability of permafrost to climate change. *Canadian Journal of Earth Sciences,* 40: 1219-1236.

Kanevskiy, M., Shur, Y., Fortier, D., Jorgenson, M.T. and Stephani, E. 2011.

Cryostratigraphy of late Pleistocene syngenetic permafrost (Yedoma) in northern Alaska, Itkillik River exposure. *Quaternary Research*, 75: 584-596.

Kanevskiy, M., Jorgenson, T., Shur, Y., O'Donnell, J.A., Harden, J.W., Zhuang, Q., and Fortier, D. 2014. Cryostratigraphy and Permafrost Evolution in the Lacustrine Lowlands of West-Central Alaska. *Permafrost and Periglacial Processes*, 25: 14-34.

Kennedy, K.E., Froese, D.G., Zazula, G.D. and Lauriol, B. 2010. Last Glacial Maximum age for the northwest Laurentide maximum from the Eagle River spillway and delta complex, northern Yukon. *Quaternary Science Reviews*, 29: 1288-1300.

Kotler, E. and Burn, C.R. 2000. Cryostratigraphy of the Klondike "muck" deposits, west-central Yukon Territory. *Canadian Journal of Earth Sciences,* 37: 849-861.

Lacelle, D., St-Jean, M., Lauriol, B., Clark, I.D., Lewkowicz, A., Froese, D.G., Kuehn, S.C. and Zazula, G. 2009. Burial and preservation of a 30,000 year old perennial snowbank in Red Creek valley, Ogilvie Mountains, central Yukon, Canada. *Quaternary Science Reviews*, 28: 3401-3413.

Lewkowicz, A.G., Etzelmuller, B and Smith, S. 2011. Characteristics of Discontinuous Permafrost based on Ground Temperature Measurements and Electrical Resistivity Tomography, Southern Yukon, Canada. *Permafrost and Periglacial Processes*, 22: 320-342.

Loke, M.H. and Barker, R.D. 1996. Rapid least-squares inversion of apparent resistivity pseudosections using a quasi-Newton method. *Geophysical Prospecting*, 44: 131-152.

Mackay, J.R., 1973. Reticulate Ice Veins in Permafrost, Northern Canada. *Can. Geotech. Journal,* 11: 230- 237.

Murton, J.B. and French, H.M. 1994. Cryostructures in permafrost, Tuktoyaktuk coastlands, western Arctic, *Canada. Canadian Journal of Earth Sciences*, 31: 737-747.

Opel, T., Dereviagin, A.Y., Meyer, H., Schirrmeister, L., and Wetterich, S. 2011. Palaeoclimatic information from stable water isotopes of Holocene ice wedges on the Dmitrii Laptev Strait, northeast Siberia, Russia. *Permafrost and Periglacial Processes*, 22: 84-100.

Reimer, P.J., Bard, E., Bayliss, A., Beck, J.W., Blackwell, P.G., Ramsey, C.B., Buck, C.E., Cheng, H., Edwards, R.L., Friedrich, M., Grootes, P.M., Guilderson, T.P., Haflidason, H., Hajdas, I., Hatte, C., Heaton, T.J., Hoffmann, D.L., Hogg, A.G., Hughen, K.A., Kaiser, K.F., Kromer, B., Manning, S.W., Niu, M., Reimer, R.W., Ricards, D.A., Scott, E.M., Southon, J.R., Staff, R.A., Turney, C.S.M., van der Plicht, J. 2013. IntCal13 and Marine13 Radiocarbon Age Calibration Curves 0-500,000 Years Cal BP. *Radiocarbon*, 55: 1869-1887.

Rampton, V.N. 1978. Surficial geology and geomorphology; Mirror Creek, Yukon Territory. Geological Survey of Canada: Ottawa, ON, Canada.

Reyes, A.V., Froese, D.G. and Jensen, B.J.L. 2010. Permafrost response to last interglacial warming: field evidence from non-glaciated Yukon and Alaska. *Quaternary Science Reviews*, 19: 3256-3274.

Schirrmeister, L., Froese, D.G., Tumskoy, V., Grosse, G., Wetterich, S. (2013). Yedoma: Late Pleistocene ice-rich syngenetic permafrost of Beringia. In: S.A. Elias, The Encyclopedia of Quaternary Science, 3, 542-552.

Smith, M.W. and Riseborough, D.W. 2002. Climate and the Limits of Permafrost: A Zonal Analysis. *Permafrost and Periglacial Processes*, 13: 1-15.

Throop, J., Lewkowicz, A.G. and Smith, S. 2012. Climate and ground temperature relations at sites across the continuous and discontinuous permafrost zones, northern Canada. *Canadian Journal of Earth Sciences*, 49: 865-876.

Chapter 5: Ground Based and Airborne Methods to Characterize Discontinuous Permafrost Along the Alaska Highway in the Discontinuous Permafrost Zone, Southwestern Yukon

Abstract

The Alaska Highway through Southwestern Yukon is located in the widespread discontinuous permafrost zone with many areas of the highway corridor associated with degrading permafrost. Permafrost characteristics are strongly influenced by slope, aspect, bedrock geology, surficial geology and the regional glacial history. In this study, we characterize permafrost between Beaver Creek and the Alaskan border using electrical resistivity tomography (ERT), airborne electromagnetic (AEM) geophysical surveys, permafrost drilling and core recovery, cryostratigraphy, and environmental monitoring to define the distribution and extent of permafrost in the area. Using a combination of AEM and ERT data, we are able to define boundaries between non-glaciated terrain and glaciated terrain, highlight regional bedrock geology, outline valley fill geometry, image the thermal impact of small and large scale surface water features and estimate the depth of permafrost. The outcomes from this study will assist with development of future mitigation strategies and maintenance plans for the Alaska Highway.

Introduction

In the discontinuous permafrost zone, permafrost characteristics, distribution, and thickness are strongly controlled by slope, aspect, vegetation cover, hydrology, and surficial materials. This makes extrapolating local observations challenging because of the considerable spatial heterogeneity that can exist. Several approaches have been adopted including vegetation mapping (Jorgenson et *al*. 2010), biophysical classifications (Lipovsky and McKenna 2005;

Jorgenson et *al*. 2010), and regional modelling (Shur and Jorgenson 2007; Lewkowicz et *al*. 2011; Throop et *al*. 2012). In recent years however, the use of airborne electromagnetics as a way to study regional scale permafrost has increased (Minsley et *al*. 2012; Pfaffhuber et *al*. 2013). In this paper we investigate the utility of combining airborne and ground based geophysical methods with site specific borehole results as a means to map permafrost distribution across complex terrain.

The recent geologic history strongly influences the nature and distribution of permafrost. In Southern Yukon the Alaska Highway traverses both syngenetic and epigenetic permafrost. The McConnell glacial boundary in this region (Duk-Rodkin 1999; Ward et *al*. 2007) marks the transition between thick syngenetic ice-rich permafrost preserved from the Late Pleistocene and relatively thinner epigenetic ice-rich permafrost within recently glaciated terrain. Ice volume tends to be greater in areas of syngenetic permafrost relative to areas of epigenetic permafrost with a distribution related to the past climate and sedimentation history at the time of formation. In the non-glaciated areas, where eolian sedimentation took place during the Late Pleistocene, ice volumes may approach 50% of the subsurface where syngenetic ice wedges accompanied aggradation (Kanevskiy et *al*. 2011; Schirrmeister et *al*. 2013). Previous research has shown preservation this type of ice-rich relict permafrost within non-glaciated terrain throughout Yukon (Froese et *al*. 2008; Lacelle et *al*. 2009; Pumple et *al*. 2015). The presence of this ice-rich material at depth increases the complexity and costs associated with construction and maintenance of northern infrastructure especially linear features such as roads and runways.

Permafrost samples collected from borehole exploration provide ground truthing for ground based geophysical surveys. Ground based surveys highlight local small scale features,

whereas airborne surveys provide regional scale coverage and context at a coarser resolution (Minsley et *al*. 2012; Pfaffhuber et *al*. 2013). In this study, we utilize this multidisciplinary approach to: (1) establish the spatial patterns of permafrost distribution associated with aspect, surface hydrology, valley fill geometry, and past glacial processes; and (2) determine the utility of combining these tools in a permafrost study.

Study Area

The study area is located in Southwestern Yukon, 10 km north of Beaver Creek along the Alaska Highway (Figure 5.1) and in the wide-spread discontinuous permafrost zone. The dominant vegetation cover in this region is a combination of sphagnum and tussock communities, often coupled with low-density black spruce in the lowland areas and high density white spruce or poplar in the uplands.

The local bedrock geology consists of the Dawson Range phase, Macauley Ridge Formation, Sang Creek suite and Mirror Creek Formation (Figure 5.2; Ryan et *al*. 2012). The Dawson Range phase consists of a hornblende-biotite granodiorite which commonly contains hornblende porphyritic diorite enclaves and rare orthoclase megacrysts (Ryan et *al*. 2012). The Macauley Ridge Formation is a heterolithic conglomerate and sandstone; clasts include amphibolite and hornblende-phyric intermediate volcanic rocks (Ryan et *al*. 2012). Snag Creek suite consists of gabbro and massive to strongly foliated, greenschist to amphibolite facies diabase (Ryan et *al*. 2012). Lastly, Mirror Creek Formation is phyllitic argillite with variable amounts of interbedded variably calcareous quartz siltstone, sandstone and pebbly sandstone that is folded and foliated (Ryan et *al*. 2012).

During the Late Pleistocene, glaciers sourced from the St. Elias Mountains advanced

northward as a component of the Cordilleran Ice-Sheet as far as the present day Beaver Creek town site (Figure 5.3; Rampton 1978; Duk-Rodkin 1999; Ward et *al*. 2007), producing a complex record of glacial activity and associated outwash deposits (Rampton 1978). It is assumed that material north of this limit is influenced mainly by periglacial processes associated with the proglacial and extraglacial environment. Rampton's (1978) surficial map of the region shows a large area dominated by outwash deposits north of the McConnell moraine (Figure 5.4). This area consists of the last glacial maximum (LGM) glacial fluvial material locally overlain by peat and modern fluvial deposits (Rampton 1978). North of the outwash area are undisturbed non-glacial deposits consisting of colluvium covering the topographic highs and slopes while modern fluvial activity interbeds with peat to produce thick organic soils in the valley bottoms (Rampton 1978; Pumple et *al.* 2015).
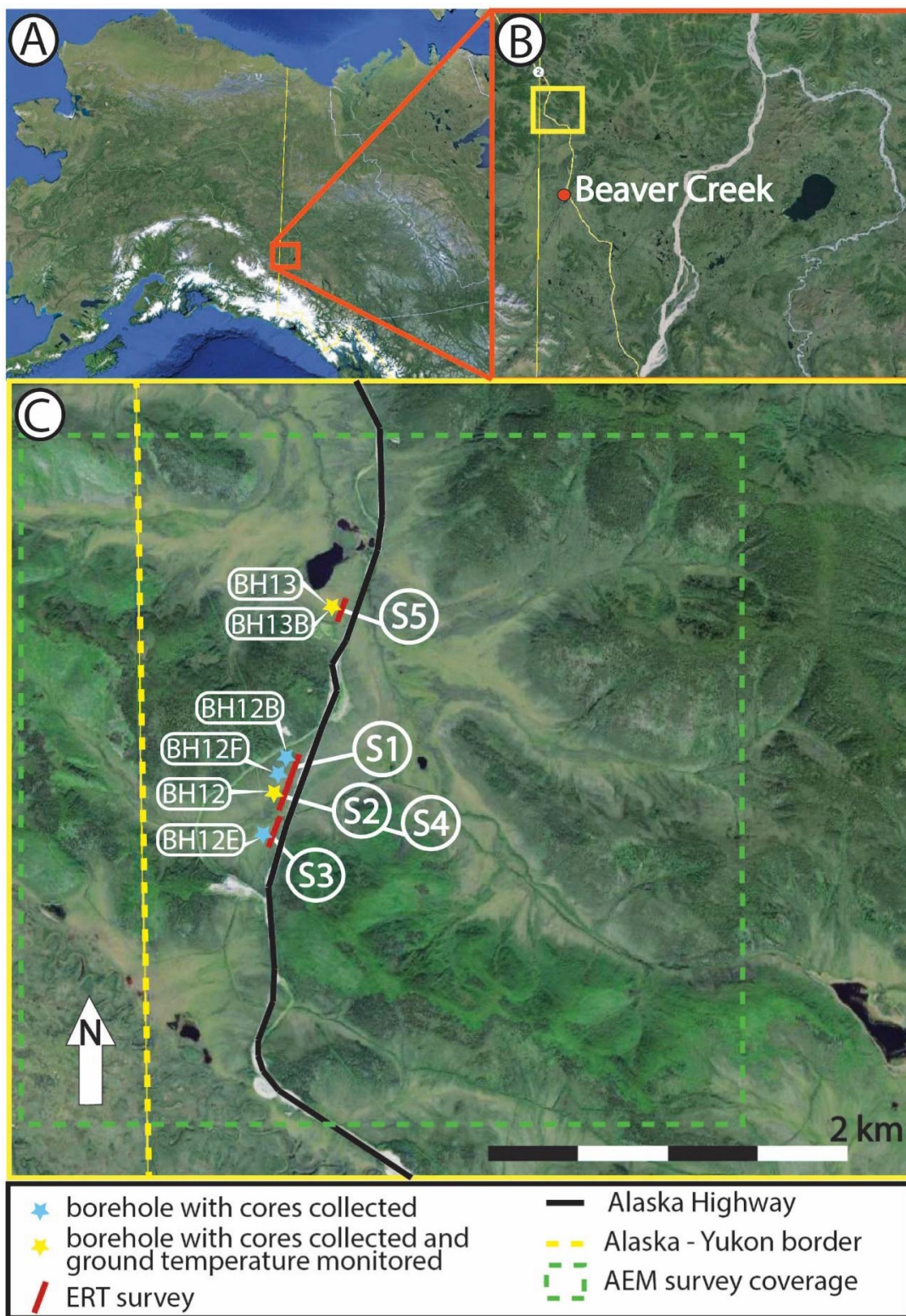
Figure 5.1. Map of the study area using images captured from Google Earth (Data SIO, NOAA, U.S. Navy, NGA, GEBCO, Image © 2015 DigitalGlobe, © 2015 Google, Image Landsat, image IBCAO). Panel C is indicated in the upper right panel by the yellow box in panel B. S1, S2, S3, S4 and S5 represent the ERT surveys discussed in this paper.
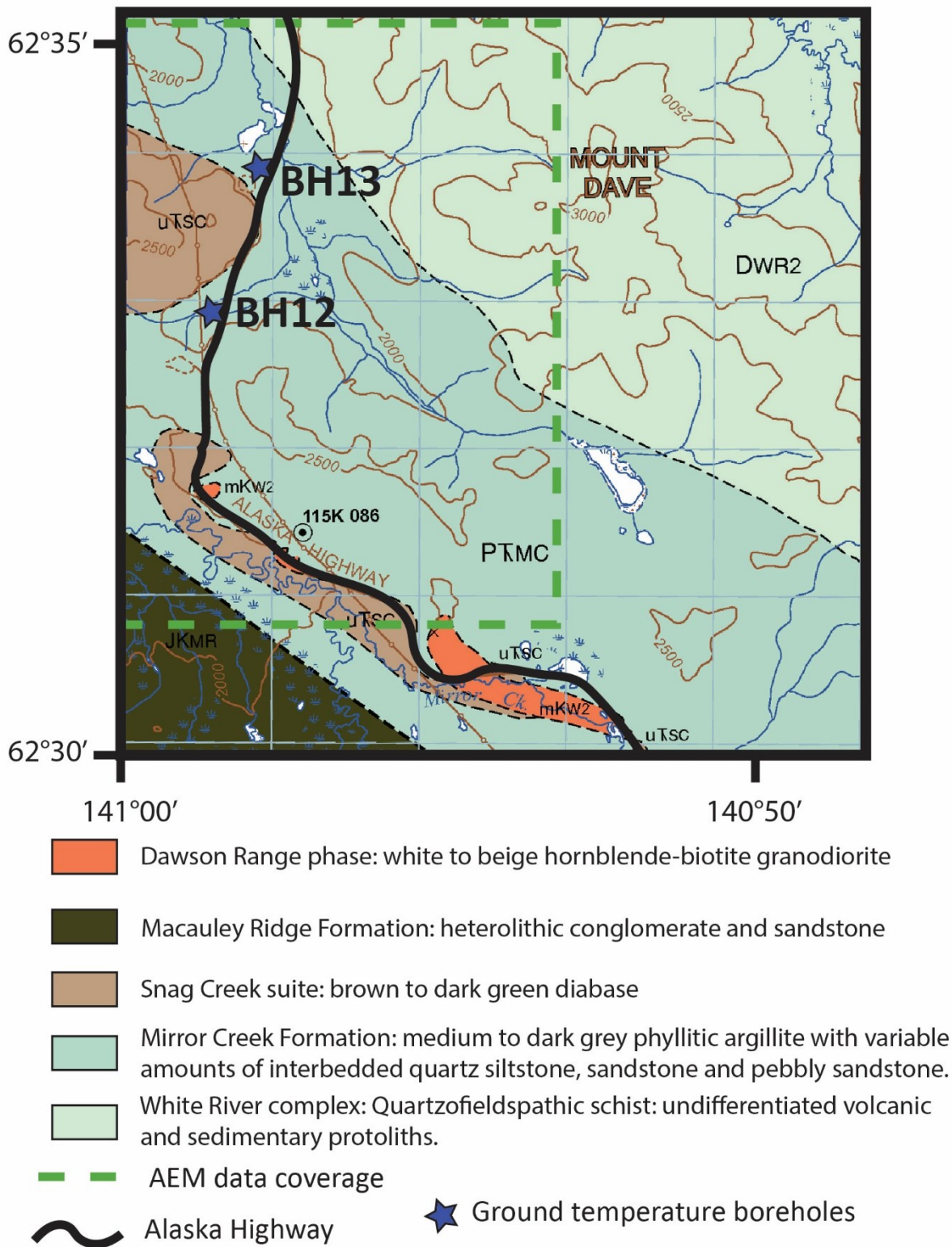
Figure 5.2: Bedrock map for area modified from Ryan et *al*. (2012).
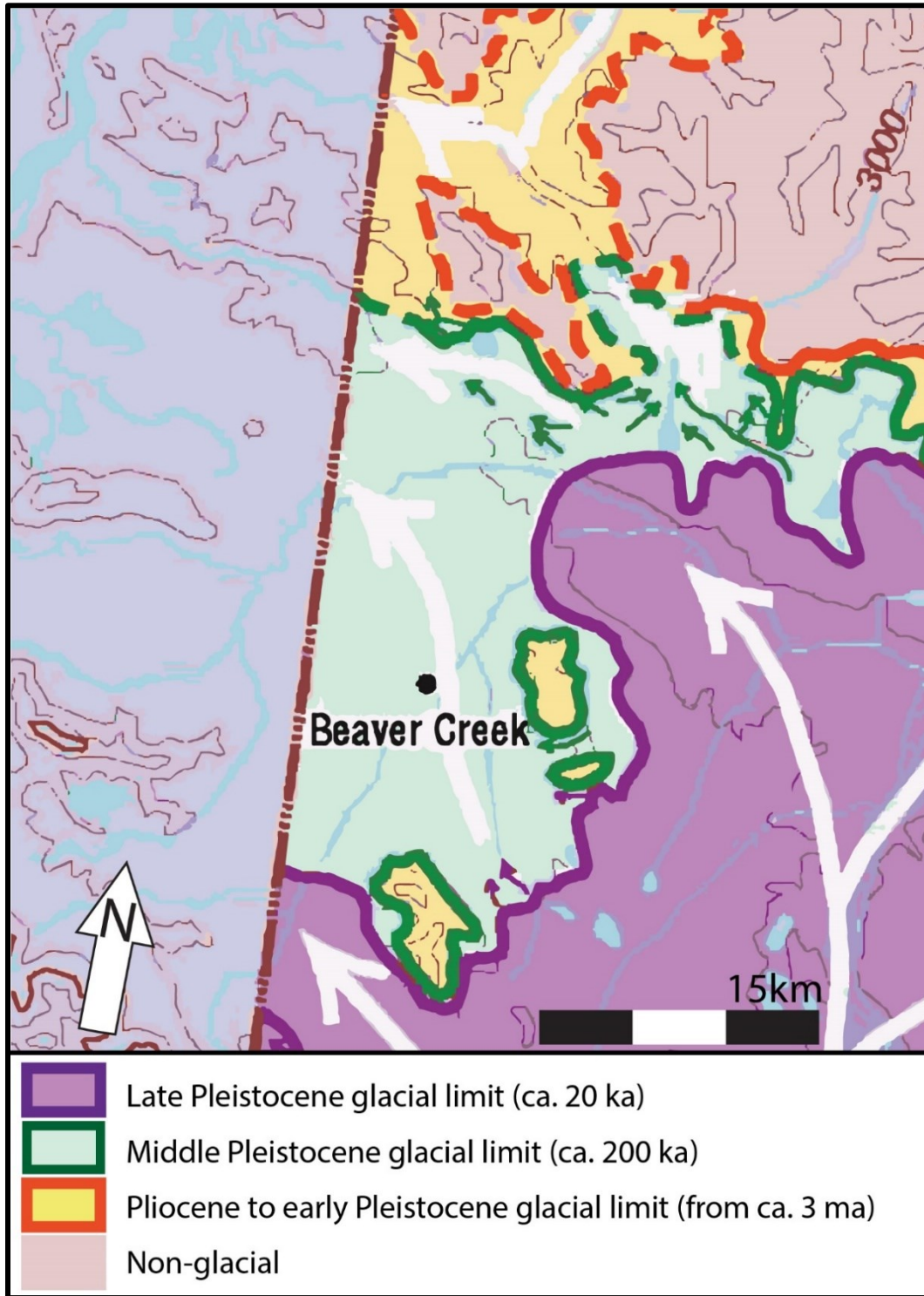
Figure 5.3: Map showing past glacial extents within Yukon created by the Geological survey of Canada in 1999 using cumulated published and unpublished material (Duk-Rodkin 1999). Dashed and solid glacial limits are interpolated and established respectively. Large white arrows indicate paleoflow direction of glacial ice and smaller coloured arrows indicate meltwater channels associated with respective glacial limits.
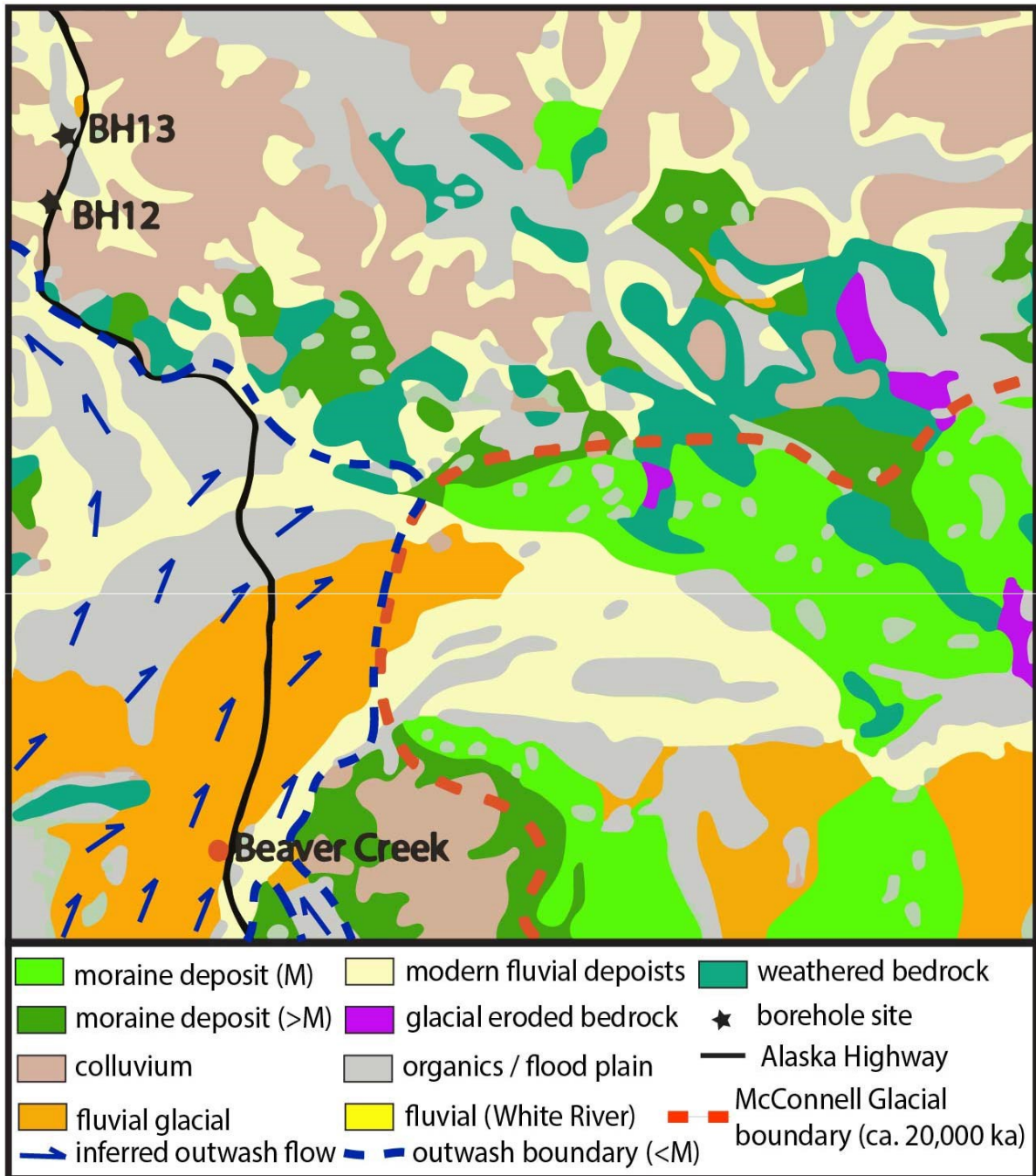
Figure 5.4: Map of region showing surficial geology as mapped by Rampton (1978).

Methods

This project uses a multidisciplinary approach including geophysical surveys, ground

temperature monitoring, cryostratigraphy, and geomorphological interpretations. In total six

boreholes were drilled, five electrical resistivity tomography (ERT) surveys completed and

one partial coverage airborne electromagnetic (AEM) data set acquired (Figure 5.1).

The AEM survey was completed as a part of a project along the Alaska Highway carried out by the United States Geological Survey (USGS) during November of 2005. As a result of this survey being carried out along the highway within Alaska, the survey covers a portion of our study area within Yukon. The methods used during this survey are the same as in Ball et *al*. (2011).

The five ERT surveys (S1, S2, S3, S4 and S5; Figure 5.1) were collected using an Iris Syscal Junior switch 48. S1, S2 and S3 used 48 electrodes with 5 m spacing for a total survey length of 235 m and, using the Wenner array, reached a depth of ~40 m. S4 and S5 used 48 electrodes with 2.5 m spacing for a total survey length of 117 m and, using the Wenner array, reached a depth of ~20 m. The surveys were inverted using RES2DINV (Loke and Barker 1996). S1, S2, S3 and S4 were collected in July of 2014 while S5 was collected in July of 2013.

Out of the six boreholes drilled, four were collected in the BH12 valley and two in the BH13 valley. Each borehole intersected an ERT survey to allow for ground truthing of the ERT results with the exception of the BH13 valley boreholes. The boreholes were drilled using a portable earth drill (Calmels et *al*. 2005) and collected cores were then stored in a portable cooler on site and at the end of the day transferred to a deep freeze for storage until returned to the University of Alberta. At the University of Alberta the cores were sampled for grain size analyses, ice volume content and cryostratigraphic interpretations following Murton and French (1994) (Pumple et *al*. 2015).

Ground temperature monitoring started at BH12 and BH13 in August and October of 2013 respectively. The ground temperature borehole at the BH12 site is a rescued government

pipeline survey borehole, whereas the temperature borehole at BH13 is a continuation of the cored borehole via water jet drilling. A full Cambell scientific weather station was installed at BH12 including a thermistor cable for ground temperatures (factory stated precision of ±0.05°C), air temperature sensor, and wind speed and direction sensor. BH13 has HOBO 4 channel external data temperature loggers (U12-008) distributed according to the depth of the borehole and available loggers. These loggers have a factory-specified precision of ±0.125°C. BH12 and BH13 record temperature to 9.5m and 13.2m depth respectively.

Results

Cryostratigraphy

Seven cryofacies are defined based on cryostructures, ice content, grain size, sediment type, and orientation of the sedimentary units (Figure 5.5). The cryofacies are as follows; cryofacies 1 (ice-rich peat), cryofacies 2 (ice-rich organic sandy silt), cryofacies 3 (ice-poor organic sandy silt), cryofacies 4 (ice-poor structureless inorganic sandy silt), cryofacies 5 (ice-poor cryoturbated inorganic silt), cryofacies 6 (sediment-rich ice) and cryofacies 7 (sediment-poor ice) (Figure 5.5). Throughout the upper surface of the valley bottom, ice-rich peat and organic silt are interbedded and cross cut by ice wedges (Pumple et *al.* 2015). The underlying sediments in the valley walls consist of inorganic ice-rich to ice-poor silts again cross cut by ice wedges at depth as observed at BH12E (Figure 5.6; Pumple et *al.* 2015). For detailed core descriptions including radiocarbon dates see Pumple et *al.* (2015).
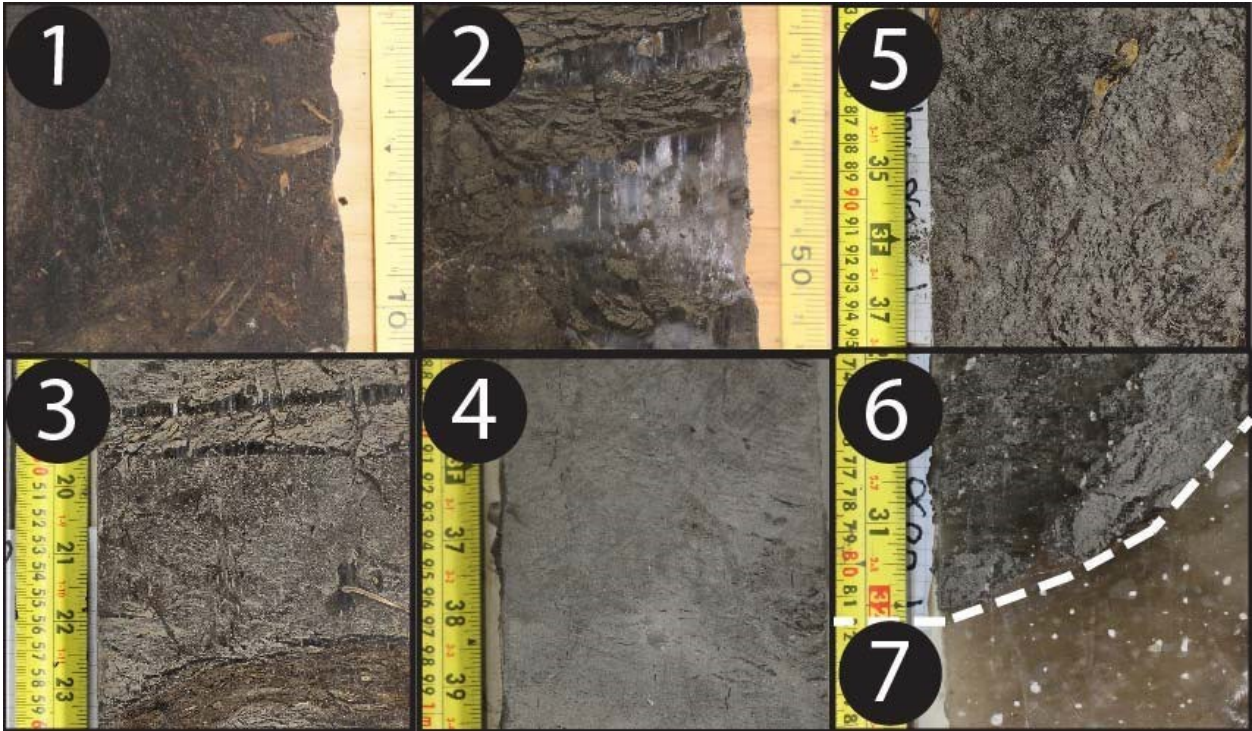
Figure 5.5: Images of each cryofacies found in the study area. Cryofacies defined following Murton and French (1994).

Grain size and ice volume

The sediments primarily consist of silt and clay with lesser components of sand, gravel and peat with a small organic rich silt component. The ice volume content in BH12, BH12F, BH13 and BH13B (valley bottom boreholes) is greater on average than BH12E and BH12B (valley wall boreholes) (Figure 5.6).
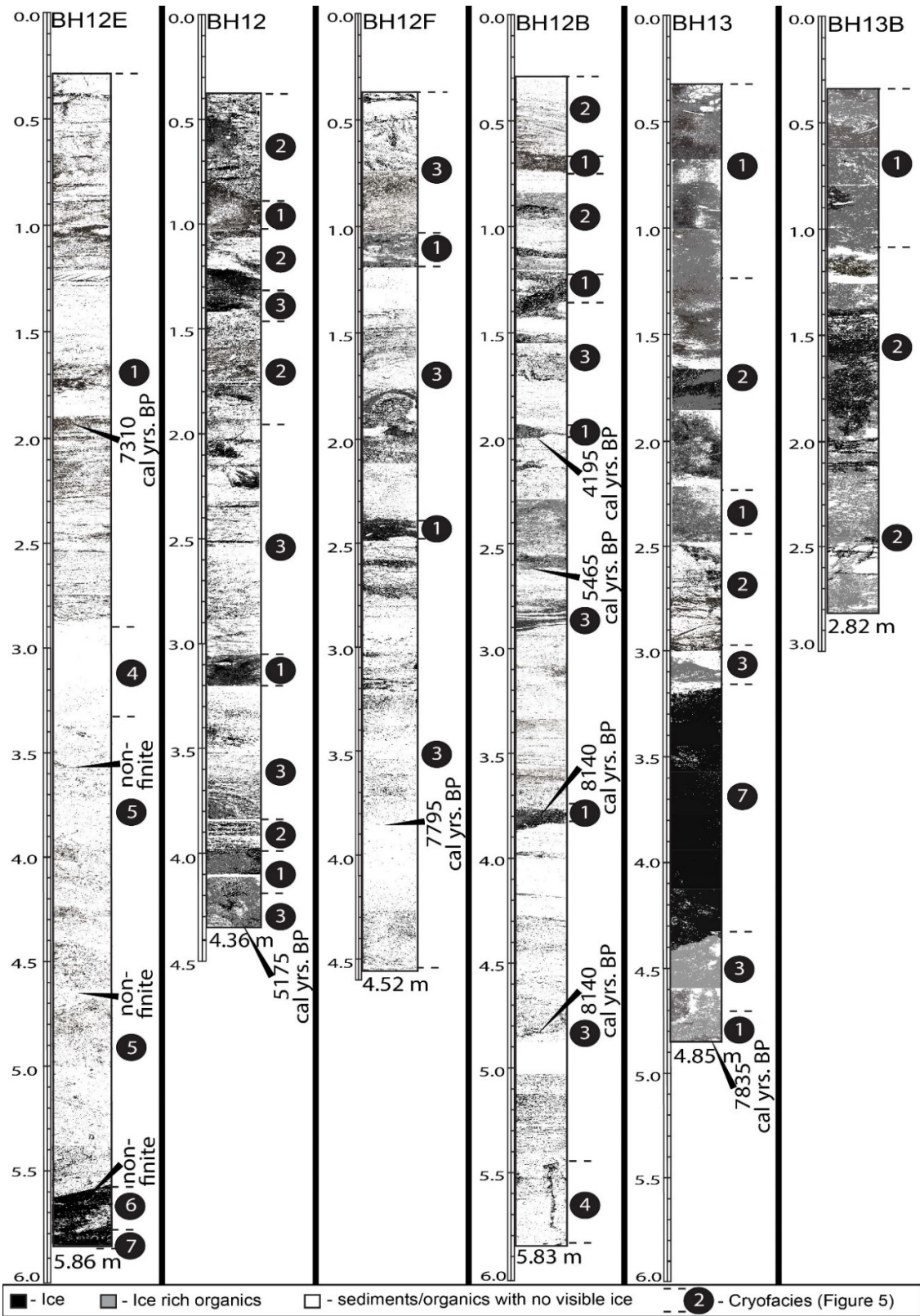
Figure 5.6: Six picture logs adjusted using Photoshop to highlight visible ice in black. The logs are presented in order from south (left) to north (right) across the study area. Median one sigma radiocarbon results are visible along the right side of each log.

Ground temperatures

Ground temperatures have been collected from BH12 and BH13 since August and October

2013 respectively. BH12 records ground temperatures to a depth of 9.5 m using a thermistor

cable with 11 measuring points. The BH12 ground temperature rate of decay was still variable

at depth thus an average of the last two measured decay rates (-0.045°C/m) was used to

calculate the depth of permafrost. BH13 records ground temperatures to a depth of 13.2 m

using a total of 5 temperature loggers which display a steady decrease in temperature of

~-0.044°C/m. Based on the observed annual temperature fluctuations at the base of both BH13

and BH12 the point of zero amplitude is beyond the base of each borehole. Therefore the

permafrost depths determined through linear extrapolation are not accurate and are not

included in this paper.

Geophysical surveys

The ERT surveys provide a two-dimensional view of the resistivity properties within the

subsurface (Lewkowicz et *al.* 2011). The base of the active layer is not visible in the surveys

due to the large electrode spacing. However, from ~1.25 m depth and below ground resistivity

values are resolved in the model. The top of each 235 m survey shows a low resistivity unit

with values ranging between 500 and 9000 Ωm. This variable top unit ranges in thickness

from ca. 3-6 m, and typically overlies a higher resistivity unit. The underlying high resistivity

(~12,000 Ωm) unit varies between 10 m and 25 m in thickness (Figure 5.7). A third unit of

low resistivity material (~1200 Ωm) marks the base of both valley wall surveys. This unit dips

towards the valley bottom in both surveys and ranges in thickness between 14 and 35 m

(Figure 5.7). The two 117.5 m surveys only reach a depth of 20 m and therefore are

142

dominated by the high resistivity unit. S2, a 235 m survey, was followed by S4, a 117.5 m

survey, using the same survey line and first electrode position on the same day. S4 shows the

increased resolution provided by the 2.5 m electrode spacing by outlining the vertical high

resistivity features in the upper lower resistivity unit. S5 is a 117.5 m survey from the BH13

site and shows a thinner more resistive upper unit overlying a similar high resistivity unit at
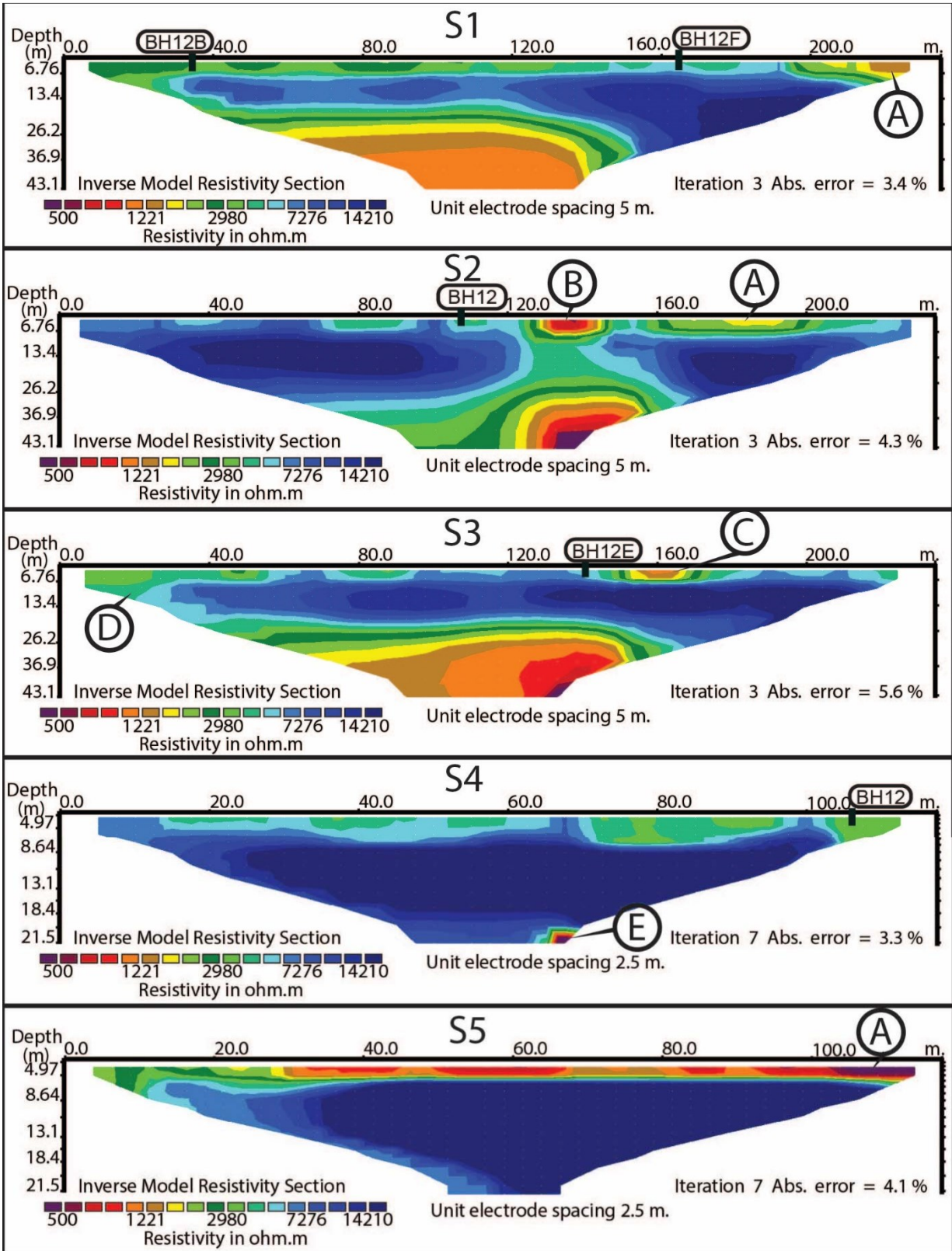
depth.

Figure 5.7: ERT results with borehole locations marked. Points A, B, C and D are areas of visible permafrost degradation. Point E is a low resistivity anomaly at depth. Surveys S1, S2,

144

and S3 used 48 electrodes with a 5 m spacing whereas surveys S4 and S5 used a 2.5 m spacing. All surveys used a Wenner array and inversions were carried out using RES2DINV (Loke and Barker 1996).

The AEM survey displays both plan view slices at variable depths and large cross sections of the study area. These resistivity images show clear variations in resistivity values between the bedrock highs and sediment dominated valley bottoms (Figure 5.8a, 5.8b and 5.9). The bedrock highs observed in Figure 5.9 at position 'D' have contradicting resistivity values suggesting they are cored by different rock formations (Figure 5.2). A second regional scale feature noted is a sharp transition from high resistivity to the north and low resistivity to the south visible in the southwest corner of the 40 m depth slice in Figure 5.8b and at position 'A' in Figure 5.9. Thaw lakes represent small scale features which are common throughout the area and are incidental with low resistivity values as seen at position 'E' and 'F' in Figure 5.9.
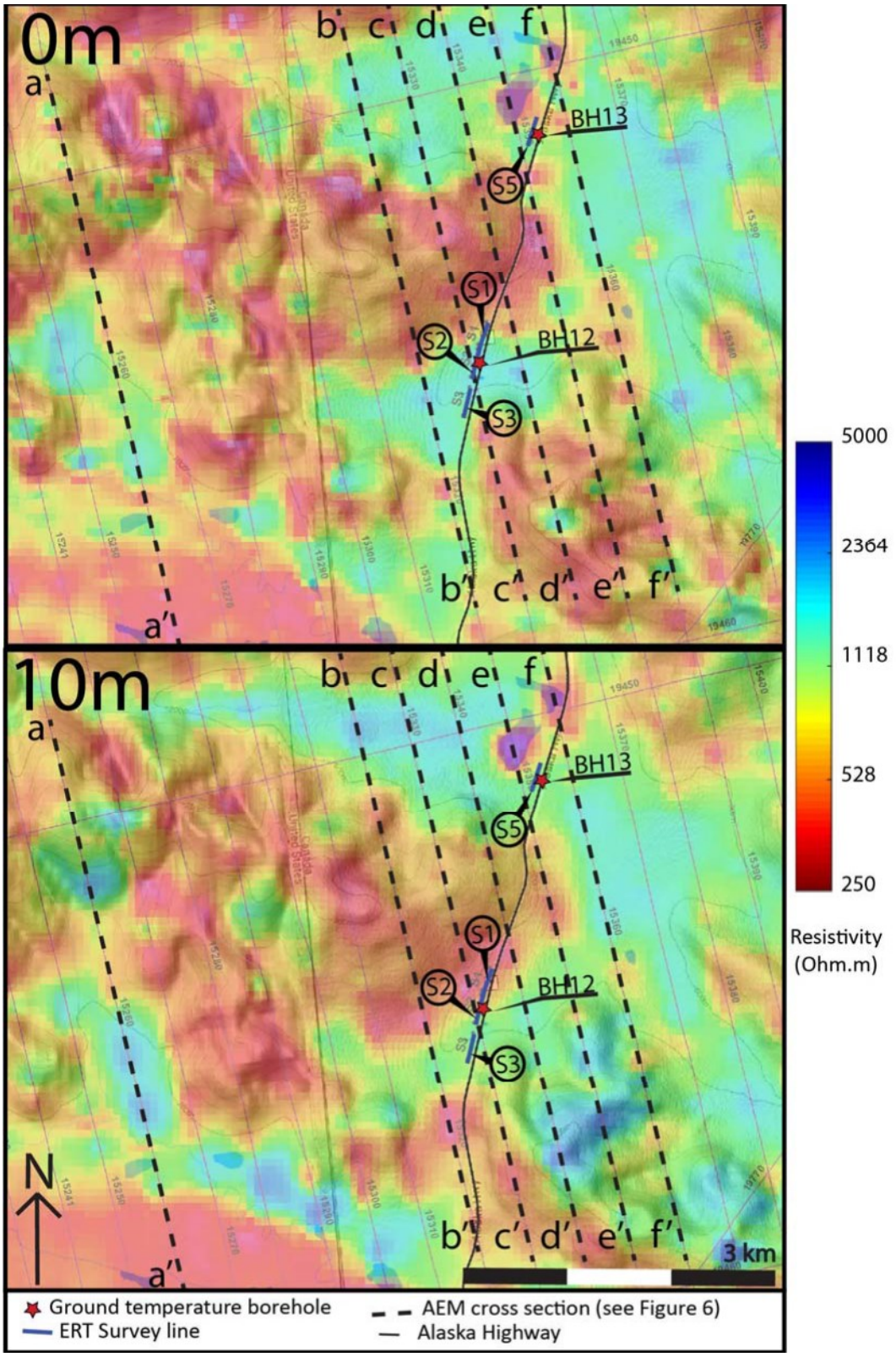
Figure 5.8a: Plan view AEM data slices from indicated depths. S1, S2, S3 and S5 are ERT survey locations (Figure 5.7). The AEM cross sections indicated in this figure are displayed in Figure 5.9. Google terrain is underlying the AEM results.
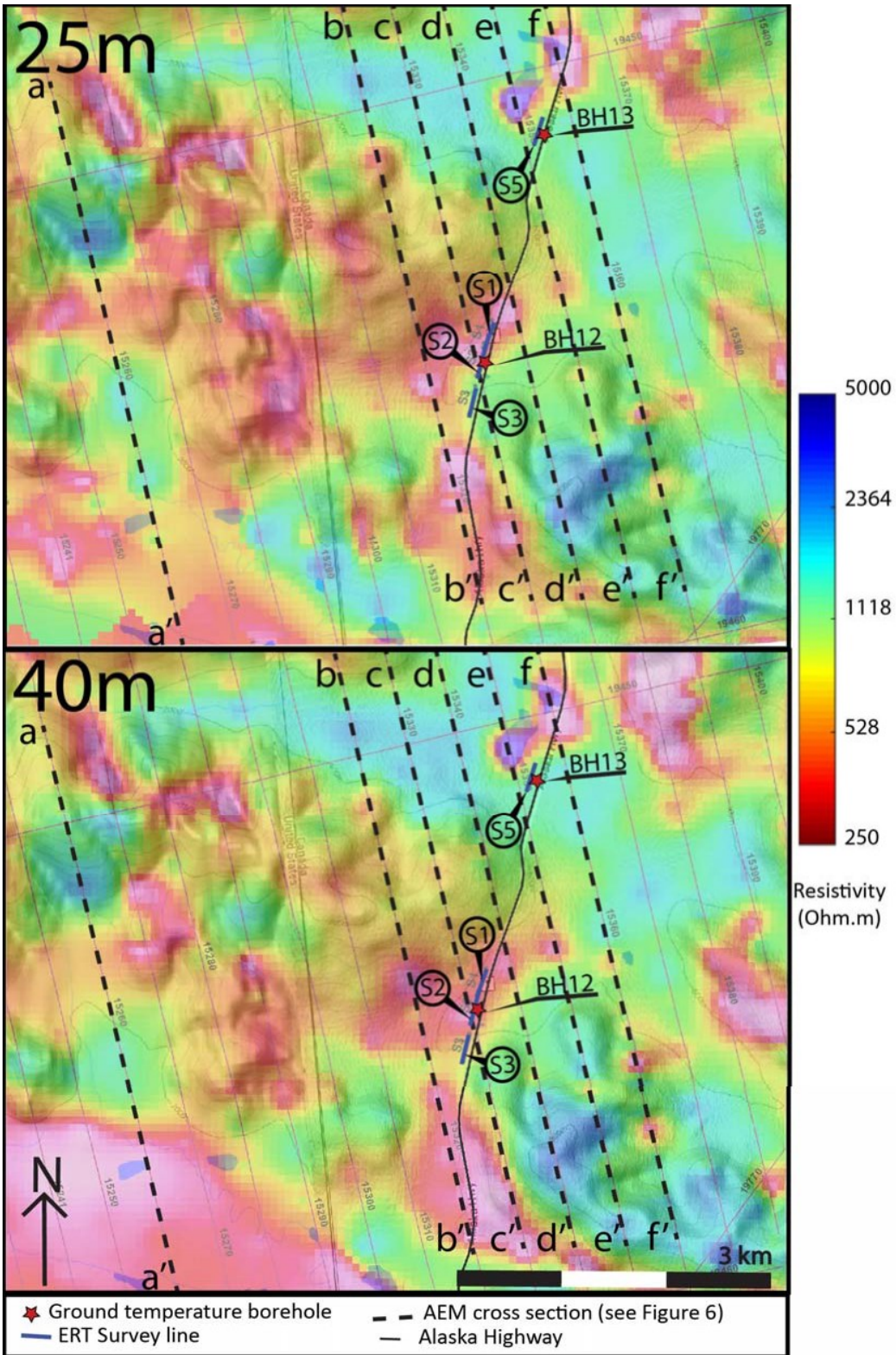
Figure 5.8b: Plan view AEM data slices from indicated depths. S1, S2, S3 and S5 are ERT survey locations (Figure 5.7). The AEM cross sections indicated in this figure are displayed in Figure 5.9. Google terrain is underlying the AEM results.
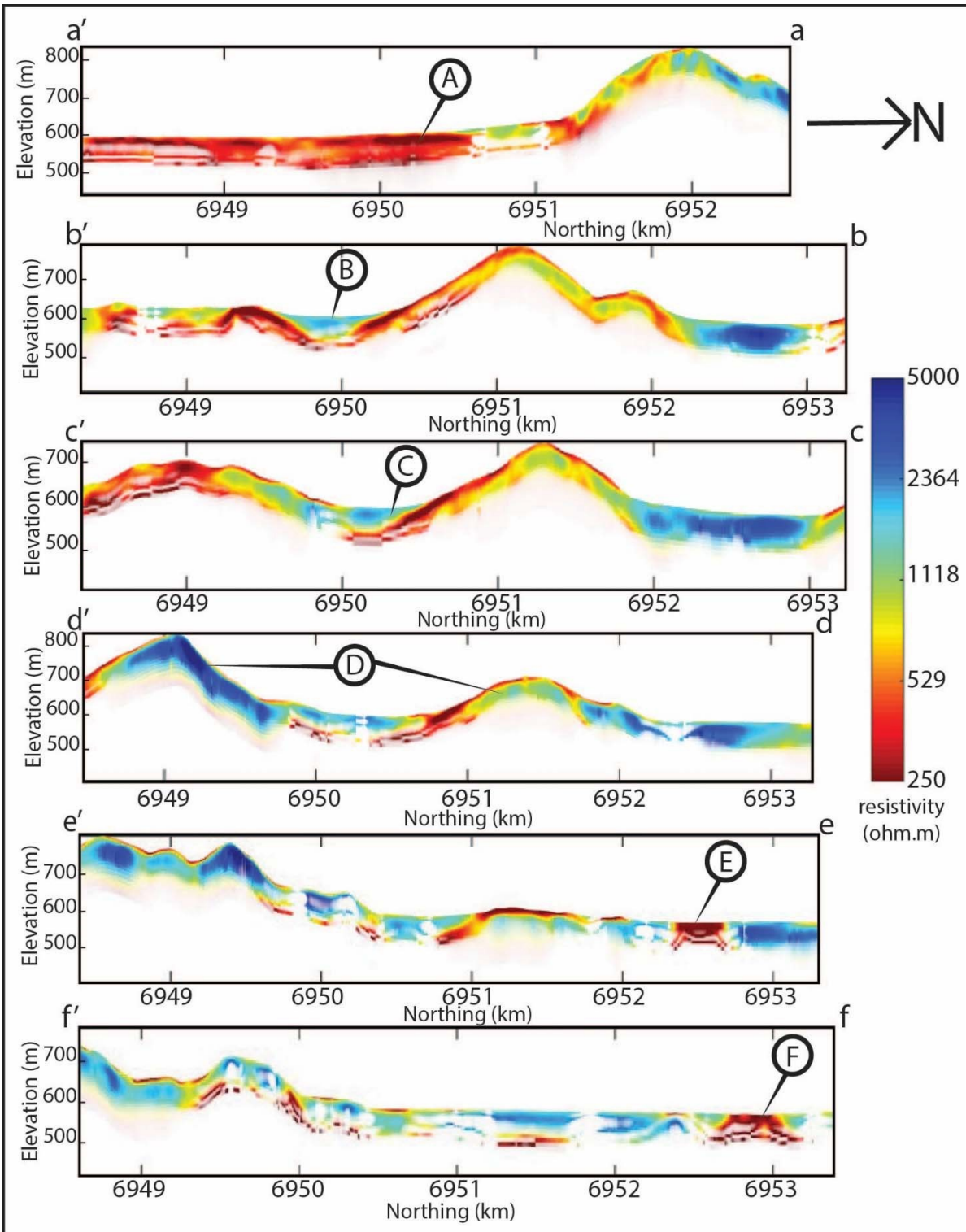
Figure 5.9: AEM cross sections collecting resistivity data to an average depth of ~90 m. Locations of each survey within the study can be seen in Figure 5.8a and 5.8b. Point "A" is located at a sharp transition between low resistivity glacial outwash lowlands and high resistivity non-glacial uplands. Points "B" and "C" show the clear outline of the high resistivity valley bottom fill. Point "D" indicates the contrasting resistivity values between the two bedrock highs and points "E" and "F" show the steep sided low resistivity values underlying two local well-established thaw lakes.

Discussion

Site specific features: cores and temperatures

The BH12 valley contains four borehole sites where cores were collected (Figure 5.1). BH12 and BH12F are two valley bottom boreholes which display ice-rich sandy silt with variable organic content throughout (Figure 5.6). As seen in Figure 5.4, BH12 and BH12F are located in the alluvial material in the valley bottom and surrounded by colluvium (Rampton 1978). The core from these boreholes display the ice-rich nature of the upper ~4.5 m of permafrost within the valley bottom (Figure 5.6). Additionally, BH12C and BH12D are boreholes which were abandoned due to ice-wedge ice being encountered within the upper 3 m at each site when the aim was to collect a continuous sedimentary record. These two boreholes are located near BH12E on the north aspect valley slope.

Core samples from the two valley wall sites BH12B and BH12E display a clear decrease in ice and organic content of the sediments incidental with cryofacies 4 (ice-poor structureless inorganic silt) at depth. The cryostratigraphy within each core varies with BH12E having a greater ice volume content on average and displaying cryofacies 5 (ice-poor cryoturbated inorganic silt), 6 (sediment-rich ice) and 7 (sediment- poor ice) at depth (Figure 5.6). BH12E is the only borehole to intersect these cryofacies at depth. Cryofacies 7 is interpreted as ice-wedge ice based on the sub vertical bubble foliations observed within it. Previous research on these cores discovered that the deposits below cryofacies 4 have an origin typical of Pleistocene silts found across unglaciated Yukon and Alaska where the subsurface can contain 50% or more ground ice (Froese et *al*. 2009; Kanevskiy et *al*. 2011; Schirrmeister et *al*. 2013; Pumple et *al*. 2015).

The cryostratigraphic results from BH13 and BH13B have highlighted some similarities and

differences between the BH12 and BH13 sites. The cores collected from BH13 show similar cryofacies including cryofacies 7 (sediment-poor ice) encountered at ~2.8m depth (Figure 5.6).

All of the core collected from the two valley sites with exception of BH12E have displayed interbedding of cryofacies 1, 2 and 3 to an average depth of 4 m. Cryofacies 4, observed in BH12E and BH12B marks a transition from Holocene ice-rich organic sandy silts to Pleistocene inorganic ice-poor to ice-rich silts (Pumple et *al.* 2015).

Valley specific features: ERT

The position of the five ERT surveys running north-south within the valley bottom at BH12 and BH13 can be seen in Figure 5.1. The top low resistivity unit in S2 and S3 displays vertical features associated with high resistivity values extending from the top of the survey to the underlying high resistivity unit (Figure 5.7). These features have been identified as ice wedges both through direct sampling (BH12C and BH12D) and observation during the excavation of a transecting ditch in June 2013 (Pumple et *al.* 2015). Core results support the ERT findings in that the top low resistivity unit's average thickness is ~5-6m. It is inferred this top unit extends across the valley as a relatively continuous layer.

In each survey the top low resistivity (500-9000 Ωm) unit is underlain by a high resistivity (~12,000 Ωm) unit at depth (Figure 5.7). BH12E is the only borehole to intersect the high resistivity unit in the form of an ice body at ~5.6 m depth. Direct sampling of this unit provides a ground truthing for the ERT surveys. However, the presence of ice-wedge ice alone does not explain the high resistivity values observed, as the top low resistivity unit too contains ice wedges. The difference is the high resistivity unit developed over a longer time period and

during the Late Pleistocene, a time where the consistent cold dry climate was conducive to ice-wedge development resulting in much larger and more extensive ice-wedge polygon networks (Kanevskiy et *al*. 2014; Pumple et *al*. 2015).

The overall thickness of the high resistivity unit is thinnest in S1 as well the overlying low resistivity unit in this survey displays a much lower average resistivity relative to that seen in S2 and S3. These two observations highlight the impact of S1's southern aspect. However, it is likely this is compounded by the northward shrub and tree densification causing an increase in captured windblown snow which amplifies the insulating factor during the winter (Burn 1998; Jorgenson et *al*. 2010). Moreover, the underlying ice-rich inorganic silts are inferred to extend across the valley based on the ERT results displaying a mostly continuous high resistivity unit at depth.

Below the high resistivity unit is again a low resistivity unit (>2000 Ωm; Figure 5.7). This bottom unit within S1 and S3 most likely represents the initial colluvium input from the valley walls based on the low resistivity values and position within the valley fill.

Similar to the ERT results from the BH12 sites, BH13 valley bottom ERT survey S5 displays a high resistivity unit at depth. BH13 and BH13B are not incidental with the S5 Survey line and therefore cannot provide ground truthing. Nevertheless, a few differences are noted between the ERT surveys S5 and S4 (Figure 5.7). Overlying the high resistivity unit within S5 is again a top low resistivity unit but with slightly lower resistivity values (500-3700 Ωm) compared to the top units observed in S1, S2 and S3. The lower values observed at this site are due to the increased amount of surface water within the tussocks and saturated peat (Hilbich et *al*. 2008). Similar to S4, S5 shows the high resistivity material extending to the bottom of the survey at 21 m depth.

At position E in S4 a low resistivity anomaly is observed and based on S2 the resistivity values associated with this anomaly are inaccurate and are likely caused by the proximity of the underlying low resistivity unit and poor instrument accuracy along the fringes of the survey. The absence of such anomalies in S5 suggests the high resistivity material is thicker at the BH13 site relative to the BH12 site. Based on this observation it is inferred that the BH13 site has a greater permafrost thickness relative to BH12 site. However, due to the restricted depth of observation in the ERT surveys it is not possible to estimate depth of permafrost. The area of low resistivity observed at positions A, B and C in Figure 5.7 are incidental with ponding water, an active stream, and an overgrown excavator track respectively. As seen in the ERT results the presence of ponding water and an active stream have caused local permafrost degradation, seen here as low resistivity values due to the increase in water present (Hilbich et al. 2008). The low resistivity values observed at position D represent permafrost degradation caused by ponding water due to a collapsed culvert running under the highway. The degradation observed at positions C and D are anthropogenic and common along the highway. Past research has shown that similar shallow anthropogenic permafrost disturbances will see reestablishment of local permafrost over time (Calmels et al. 2012).

These findings demonstrate that the combination of borehole exploration and ERT surveys can provide great insight into local permafrost extent and active permafrost degradation within the shallow sub surface (Lewkowicz et al. 2011).

Regional features: AEM

Bedrock geology

A large difference in resistivity can be observed in Figures 5.8a, 5.8b and 5.9 (d-d' position

'D') when comparing the topographic high seen in the southeast corner versus the east-west trending high in the center of the image. This contradiction is due to the topographic high's difference in bedrock geology as seen in Figure 5.2. Telford et *al*. (1990) reports measured resistivity ranges for gabbro and argillites as $10^3 - 10^6$ and 8-10 x 10^2 Ωm respectively. However, the opposite relation is seen in the AEM results with the argillites displaying a much higher average resistivity value. One reason for this discrepancy could be that Telford et *al*. (1990) tested pure dry (unless otherwise stated) gabbro and argillite samples whereas the rock formation descriptions seen in Figure 5.2 mention various interbedded rock types. The compound effect of these attributes on recorded resistivity is difficult to quantify without directly testing the rock formation itself. A second reason for the variable bedrock resistivity values could be the degree of weathering. Weathered rocks exhibit lower resistivity values due to increased porosity and permeability.

Surficial geology

As seen in Figure 5.4, the surficial geology of the region is complex and controlled by both topography and past glacial regimes (Rampton 1978). In this map colluvium dominates the slopes coming off of the topographic highs (Rampton 1978). The AEM results have the majority of these sloped surfaces displaying low resistivity values overall (Figure 5.8a and 5.8b). The valley bottoms and lowlands show a mixture of alluvial and peat which display high resistivity values overall (Figure 5.8a and 5.8b; Rampton 1978). Moraine deposits from the McConnell glaciation are visible south of the inferred glacial boundary (red dashed line; Figure 5.4) and we propose that the fluvial deposits observed in the south western corner of the map are at depth remnants of McConnell outwash deposits. The AEM data provides support to

this through the homogenous low resistivity values within this area at 40 m depth and the quick

thickening of the same values at position 'A' in the AEM cross section (a- a') through the area

(Figures 5.8a, 5.8b and 5.9).

Sediments at depth

Past research has shown this site is located within non-glacial terrain and as a result would

have undergone extended periods of colluvium deposition during the most recent glacial

period (Pumple et *al*. 2015). The colluvium deposits are likely the cause of the low resistivity

values at depth within the south facing slopes of the non-glacial terrain (Figure 5.8b).

Overlying the valley bottom colluvium as seen in the ERT results (Figure 8) is fine grained

ice-rich Pleistocene silts deposited through a combination of eolian and alluvial sources

(Pumple et *al*. 2015). This high resistivity fine-grained ice-rich sediment dominates the

valley fill as observed in the AEM cross sections c-c' and b-b' at positions 'C' and 'B' in

Figure 5.9 along with the underlying low resistivity colluvium. At BH13, the valley fill

appears to be again dominated by high resistivity material but with a greater observed

thickness as seen in Figure 5.9 cross section e-e'. This observation supports a similar

observation made on the ERT results when comparing permafrost depth at the BH12 and

BH13 valley bottom sites.

Thaw lakes and taliks

The BH13 valley bottom is also home to several established thaw lakes northwest of the

BH13 site (Figure 5.10). Several studies have modeled the development of similar thaw lakes

suggesting a timeline of over a 1000 years for complete development of a through talik
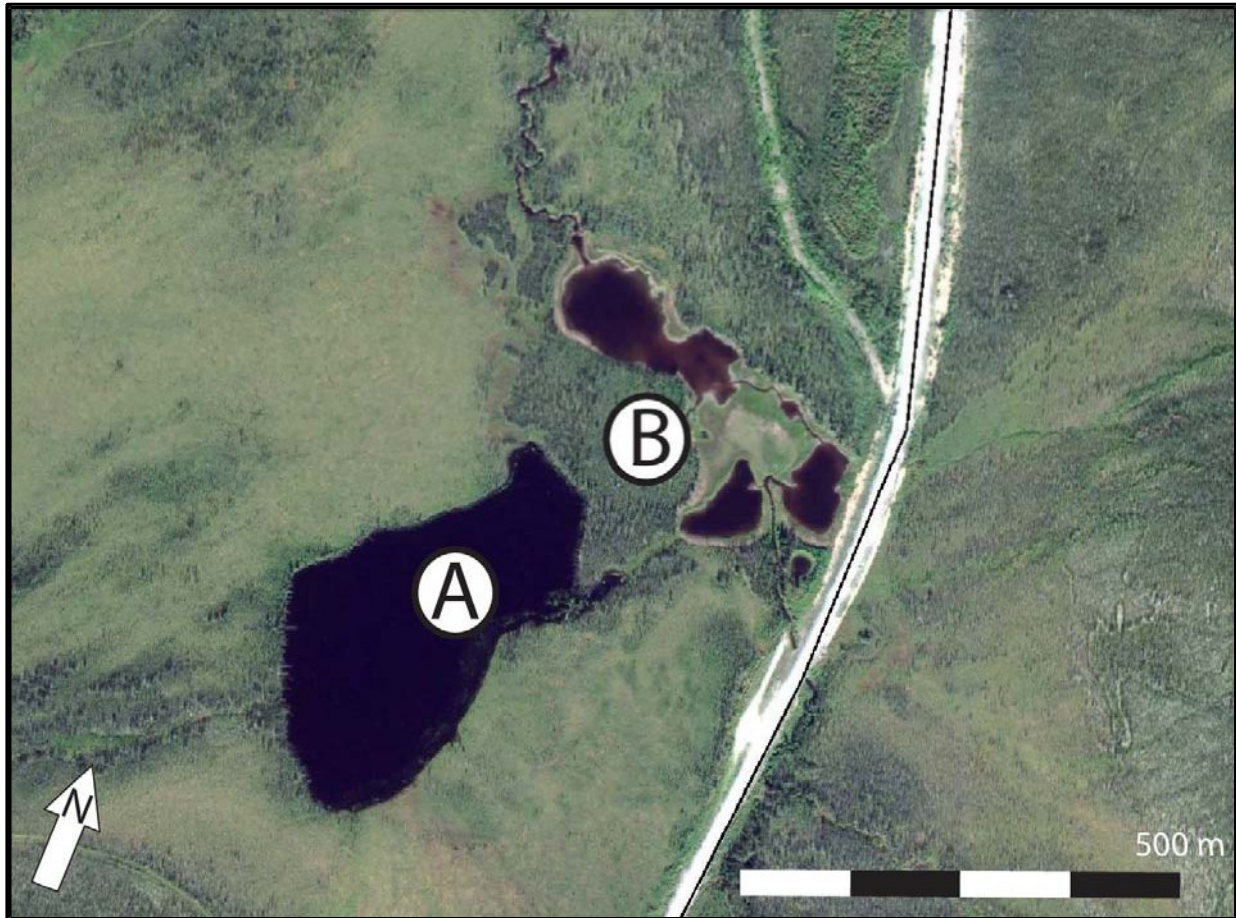
Figure 5.10: Satellite image of thaw lakes northwest of BH13 sites (image taken August 2010). Image captured from Google Earth (Data SIO, NOAA, U.S. Navy, NGA, GEBCO, Image © 2015 DigitalGlobe, © 2015 Google, Image Landsat, image IBCAO).

depending on the climate projections used (Feng et *al*. 2012; Wellman et *al*. 2013). The thaw lake at position 'A' in Figure 5.10 is ~300 m wide and ~500 m long trending northeast and with an unknown depth is associated with a through talik observed at position 'E' in Figure 5.9. The low resistivity values extend to the base of the AEM survey suggesting the lake has completely thawed the underlying permafrost (Figure 5.9).

The small lakes at position 'B' within Figure 5.10 are clearly located within a larger partially drained lake basin. The permafrost beneath this basin is also completely thawed (position 'F' in Figure 5.9). Although the lakes at position 'B' are smaller than the single large lake at position 'A' the talik associated with the smaller lakes appears larger. This suggests that the large

155

partially drained lake basin at position 'B' must have partially drained recently. This speculation can be confirmed through the use of satellite imagery taken the same year the AEM survey was completed (2005). Figure 5.11 displays a satellite image from June 2005 showing the small lakes flooding into one another.
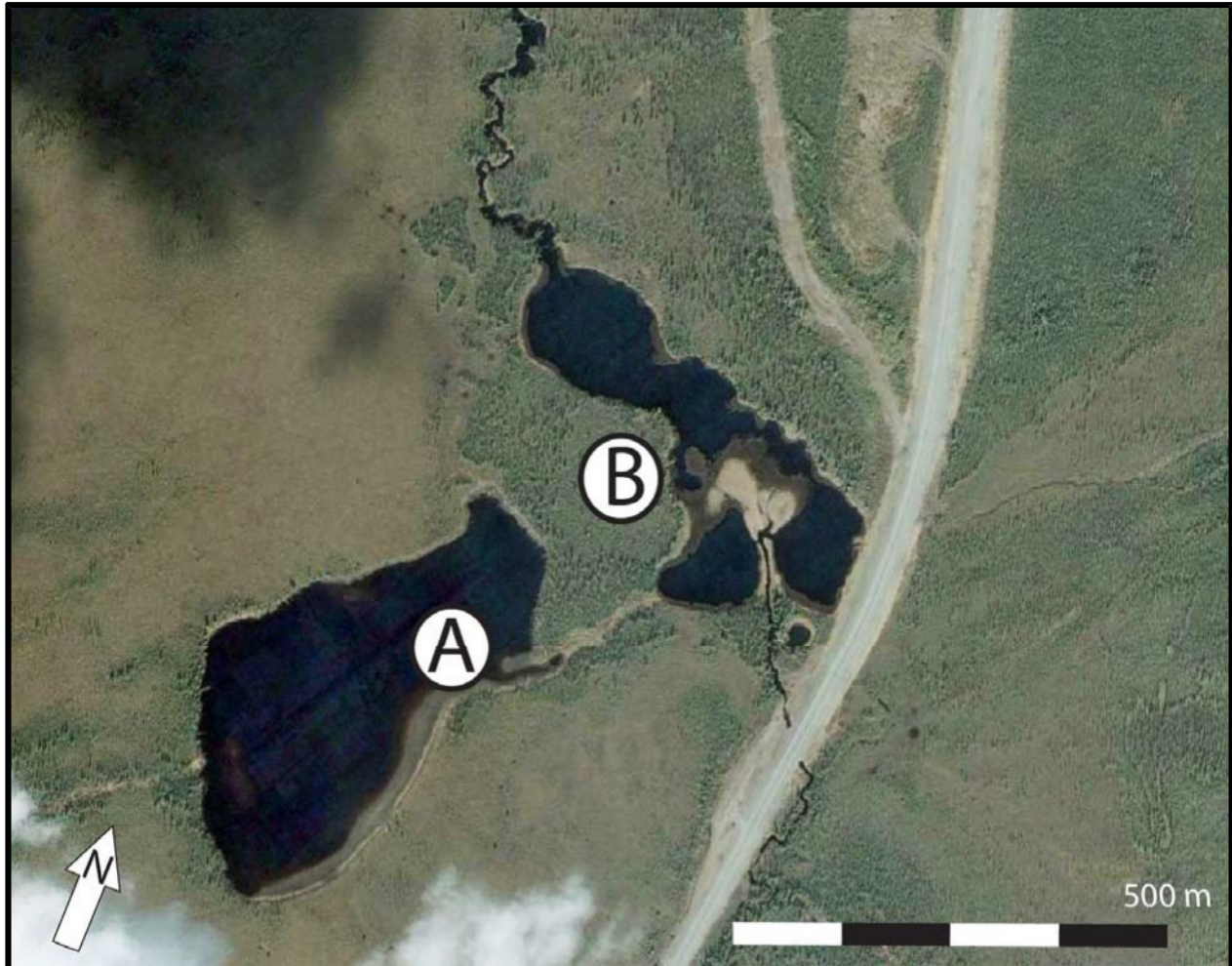
Figure 5.11: Satellite image of thaw lakes northwest of BH13 sites (image taken June 2005). Image captured from Google Earth (Data SIO, NOAA, U.S. Navy, NGA, GEBCO, Image © 2015 DigitalGlobe, © 2015 Google, Image Landsat, image IBCAO).

Depth of permafrost

Based on the AEM cross sections in Figure 5.9 and the assumption that AEM resistivity values below ~ 500 Ωm represent thawed material, maximum permafrost depths within BH12

and BH13 valley bottoms are 70±5 m and >90 m respectively.

Utility of a multidisciplinary approach

The results from the AEM survey highlight regional scale features within the landscape including bedrock geology, surficial geology, valley fill geometry, and the thermal impact of thaw lakes. Adding the site specific details from borehole exploration and ERT surveys to the AEM results provides a robust method to map permafrost dynamics across complex terrain. This combination also provided insights into the landscape evolution that most likely took place within this region. Figure 5.12 shows a conceptual model of landscape evolution at the BH12 valley site based on the data collected throughout this study.
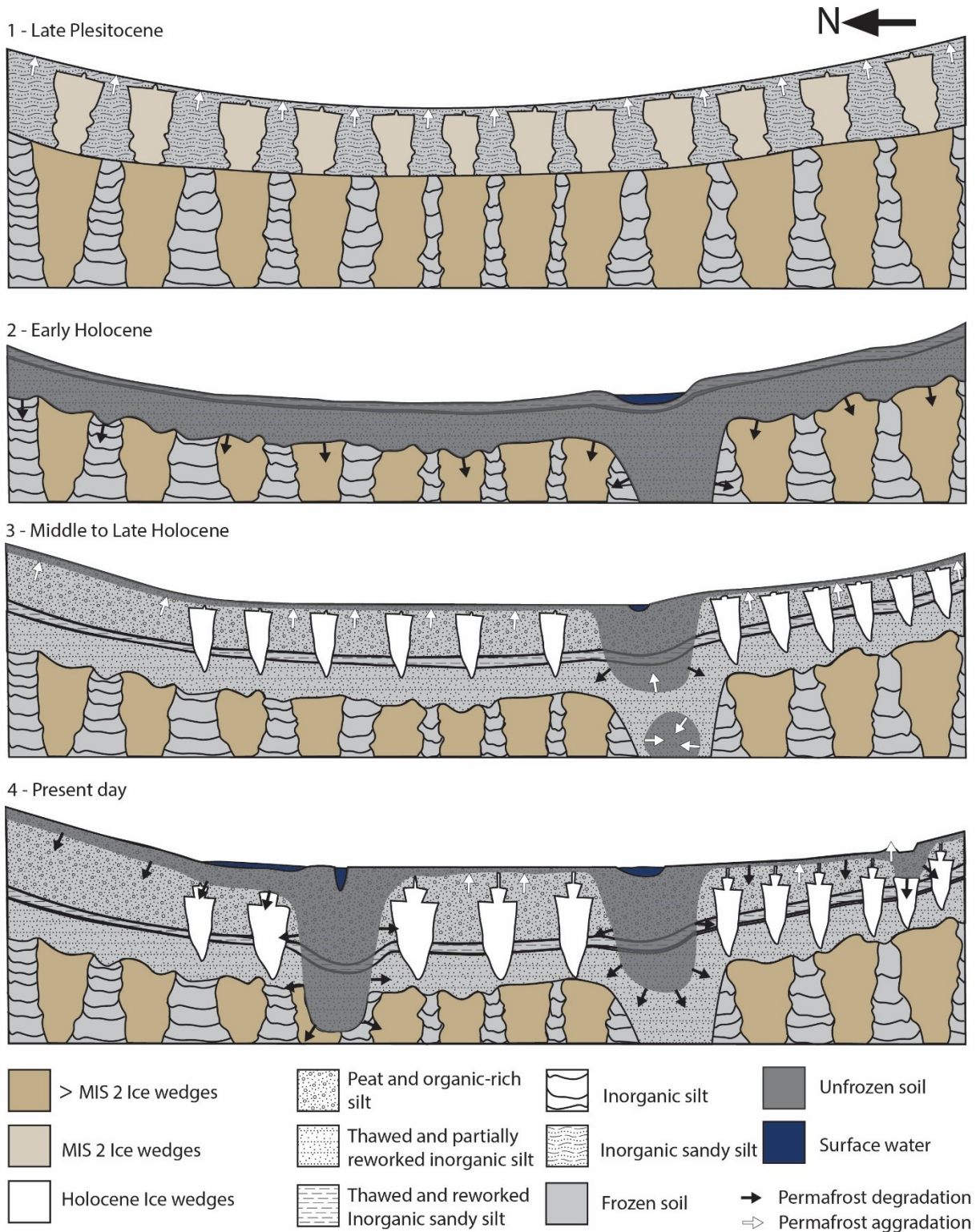
Figure 5.12: Conceptual model of the BH12 valley site showing the landscape evolution from the Late Pleistocene to the present. This image is not to scale.

Conclusions

Combining AEM, ERT and borehole data provides insight into both regional and local scale features on the surface and within the subsurface of the study area. AEM results outline large scale features including regional bedrock geology, glacial versus non glacial terrain, valley fill geometries, permafrost depth, and thaw lake basins. ERT results outline small scale features within the valley bottoms including the distribution of the relict permafrost as a high resistivity ice-rich material; local permafrost degradation both natural and anthropogenic; and shallow ice-wedge networks. Borehole results provided ground truthing for the ERT surveys through direct sampling of material from the survey line. Collectively, these results show the relation between permafrost and the local bedrock and surficial geology within this northern section of the Alaska Highway corridor. Effective highway maintenance along the Alaska Highway relies on the understanding of permafrost distribution surrounding the highway corridor. A combination of AEM, ERT and borehole data can provide effective regional scale mapping of permafrost.

Future Considerations

If directly compared, the AEM and ERT surveys do not agree with each other. This is due to the difference in sensitivities of each system with ERT being more sensitive to high resistivity values compared to AEM. The trend of the flight lines within the AEM survey differ from that of the ERT surveys and therefore the two cannot be directly compared. Future work combining these methods should have the ERT survey lines incidental with the AEM flight lines where possible and always have borehole locations incidental with the ERT survey lines.

References

Ball, L.B., Smith, B.D., Minsley, B.J., Abraham, D.J., Voss, C.I., Deszez-Pan, M. and Cannia, J.C., 2011. Airborne electromagnetic and magnetic survey data of the Yukon Flats and Ft. Wainwright areas, central Alaska, June 2010, U.S. Geol. Surv. Open File Rep., 2011-1304, 28 pp.

Burn, C.R. 1998. The response (1958-1997) of permafrost and near-surface ground temperatures to forest fire, Takhini River valley, southern Yukon Territory. Canadian Journal of Earth Sciences, **35**: 184-199.

Calmels, F., Froese, D.G., and Clavano, W.R. 2012. Cryostratigraphic record of permafrost degradation and recovery following historic (1898-1992) surface disturbances in the klondike region, central yukon territory 1,2. Canadian Journal of Earth Sciences, **49**: 938-952.

Calmels, F., Gagnon, O., and Allard, M. 2005. A portable earth-drill system for permafrost studies. Permafrost and Periglacial Processes, **16**: 311-315.

Duk-Rodkin, A. 1999. Glacial limits map of Yukon Territory. Geological Survey of Canada, Open File 3694, Indigenous and Northern Affairs Canada Geoscience Map 1999-2, scale 1:1 000 000.

Feng, L., Qingbai, W., Zhang, T., and Fujun, N. 2012. Modelling open-talik formation and permafrost lateral thaw under a thermokarst lake, Beiluhe Basin, Qinghai-Tibet Plateau. Permafrost and Periglacial Processes, **23**: 312-321.

Froese, D.G., Westgate, J.A., Reyes, A.V., Enkin, R.J., and Preece, S.J. 2008. Ancient permafrost and a future, warmer Arctic. Science, **321**: 1648-1648.

Hilbich, C., Hauck, C., Hoelzle, M., Scherler, M., Schudel, L., Volksch, I., Vonder Muhll, D., and Mausbacher, R. 2008. Monitoring mountain permafrost resistivity tomography: 7-year study

of seasonal, annual, and long-term variations at Schilthorn, Swiss Alps. Journal of Geophysical Research, 113: 1-12.

Israel, S., Murphy, D.C., Bennett, V., Mortensen, J.K. and Crowley, J.L., 2011. New insights into the geology and mineral potential of the Coast Belt in southwestern Yukon. In: Yukon Exploration and Geology 2010, K.E. MacFarlane, L.H. Weston and C. Relf (eds.), Yukon Geological Survey, p. 101-123.

Jorgenson, M.T., Romanovsky, V., Harden, J., Shur, Y., O'Donnell, J., Schuur, E.A.G., Kanevskiy, M. and Marchenko, S. 2010. Resilience and vulnerability of permafrost to climate change. Canadian Journal of Earth Sciences, 40: 1219-1236.

Kanevskiy, M., Jorgenson, T., Shur, Y., O'Donnell, J.A., Harden, J.W., Zhuang, Q., and Fortier, D. 2014. Cryostratigraphy and permafrost evolution in the lacustrine lowlands of west-central Alaska. Permafrost and Periglacial Processes, **25**: 14-34.

Lewkowicz, A.G., Etzelmuller, B., and Smith, S.L. 2011. Characteristics of discontinuous permafrost based on ground temperature measurements and electrical resistivity tomography, southern Yukon, Canada. Permafrost and Periglacial Processes, **22**: 320-342.

Lipovsky, P.S. and McKenna, K., 2005. Local-scale biophysical mapping for integrated resource management, Watson Lake area (NTS 105A/2), Yukon. Yukon Geological Survey, Open File 2005-6, report and CD-ROM, 74 p.

Loke, M.H., and Barker, R.D. 1996. Practical techniques for 3D resistivity surveys and data inversion. Geophysical Prospecting, **44**: 499-523.

Murphy, D.C., Mortensen, J.K. and van Staal, C., 2009. 'Windy-McKinley' terrane, western Yukon: new data bearing on its composition, age, correlation and paleotectonic settings. In: Yukon Exploration and Geology 2008, L.H. Weston, L.R. Blackburn and L.L. Lewis (eds.), Yukon Geological Survey, p. 195-209.

Murton, J.B., and French, H.M. 1994. Cryostructures in permafrost, Tuktoyaktuk coastlands, western Arctic Canada. Canadian Journal of Earth Sciences = Revue Canadienne des Sciences de la Terre, **31**: 737-747.

Pumple, J., Froese, D., and Calmels, F. 2015. Characterizing permafrost valley fills along the Alaska Highway, southwest Yukon. In Proceedings GeoQuébec 2015-68th Canadian Geotechnical Conference and 7th Canadian Permafrost conference, 20-23 September 2015, Québec, Canada.

Rampton, V.N. 1978. Surficial geology and geomorphology; Mirror Creek, Yukon Territory. Geological Survey of Canada: Ottawa, ON, Canada, Canada.

Schirrmeister, L., Froese, D.G., Tumskoy, V., Grosse, G., Wetterich, S. (2013). Yedoma: Late Pleistocene ice- rich syngenetic permafrost of Beringia. In: S.A. Elias, The Encyclopedia of Quaternary Science, 3, 542-552.

Shur, Y.L., and Jorgenson, M.T. 2007. Patterns of permafrost formation and degradation in relation to climate and ecosystems. Permafrost & Periglacial Processes, 18: 7.

Telford, W.M., Geldart, L.P., and Sheriff, R.E. 1990. Applied geophysics. 2nd edition. Applied geophysics.2nd edition.

Throop, J., Lewkowicz, A.G., and Smith, S.L. 2012. Climate and ground temperature relations at sites across the continuous and discontinuous permafrost zones, northern Canada. Canadian Journal of Earth Sciences = Revue Canadienne des Sciences de la Terre, **49**: 865-876.

Ward, B.C., Bond, J.D., and Gosse, J.C. 2007. Evidence for a 55-50 ka (early Wisconsin) glaciation of the Cordilleran ice sheet, Yukon Territory, Canada. Quaternary Research, **68**: 141-150.

Wellman, T.P., Voss, C.I., and Walvoord, M.A. 2013. Impacts of climate, lake size, and supra- and sub- permafrost groundwater flow on lake-talik evolution, Yukon Flats, Alaska (USA). Hydrogeology Journal, **21**: 281-298.

Chapter 6: Conclusions and Future Work

The surficial geology along the Alaska Highway within Southern Yukon is made complex through the combination of widespread polygenetic permafrost and past glacial processes. The cryostratigraphic, geophysical, and geochemical results from this study provide the foundation for permafrost characterization and identification of preserved relict permafrost within the study area. These results benefit the Yukon Highway Public Works with their continued maintenance and construction along the highway and adds to the growing library of permafrost research in the region.

In total 14 boreholes were drilled, 7 ERT surveys completed and 2 boreholes instrumented for ground temperature monitoring along a 50 km section of the highway centralized around Beaver Creek, Yukon. The cores collected resulted in ~240 pore water isotope samples, ~200 ice volume and grain size analyses and 17 AMS radiocarbon dates. The regularities and irregularities observed between sites underpin the utility of the methodology used to capture both regional and site specific dynamics.

Site locations in this study are defined based on the temporal and/or spatial relation with the recent glacial advance in the area, the McConnell Glaciation (Duk-Rodkin 1999; Ward et *al*. 2007). BH16 and BH15 are glacial sites based on Rampton's (1978) surficial map of the area and non-conclusive core results. The glacial history of BH17 could not be determined due to its proximity to the inferred glacial boundary based on Rampton (1978) and non-conclusive core results. BH11, BH18 and BH19 are located north of the McConnell glacial boundary but within the glacial outwash area based on Rampton's (1978) surficial map and non-conclusive core results. BH12 sites, BH13 sites and BH20 sites are located outside of both the glacial and glacial outwash areas of the McConnell Glaciation based on Rampton's (1978) surficial map

and supporting geophysical surveys and conclusive core results.

The cryostratigraphic interpretations define two cryofacies assemblages based on the repetition or presence of certain cryofacies, associated pore water isotopes and radiocarbon results. Cryofacies assemblage 1 consists of a repetition or presence of cryofacies 1 (ice-rich peat), 2 (ice-rich organic sandy silt) and 3 (ice-poor organic sandy silt). This cryofacies assemblage is associated with organic-rich sediments and enriched pore water isotopes typical of the Holocene (> -24 ‰ $\delta^{18}O$; Kotler and Burn 2000). 12 radiocarbon dates were sampled from this cryofacies assemblage with the oldest one sigma median age being 13340 Cal. yrs. BP (Table 3.2). The ERT results displayed this cryofacies assemblage as a low resistivity (400-8500 Ωm) layer with an average thickness of 6 m. The ERT also outlined the distribution of ice wedges (~8000 Ωm) and local thermal impact of surface waters (~600 Ωm). The ice-rich nature of this cryofacies assemblage is amplified in valley bottoms and north facing slopes by a notable presence of ice wedges at depth (~2 m below the surface). This cryofacies assemblage was observed at each borehole throughout the study area suggesting it represents the typical regional Holocene sedimentary record.

Where present, cryofacies 4 (ice-poor structureless inorganic sandy silt) marks a distinct decrease in the organic content and ice content of the cores at depth. Also associated with cryofacies 4 is a steady trend towards depletion in the pore water isotopes and non-conformable radiocarbon dates above and below. The combination of these findings suggest cryofacies 4 most likely represents a paleo-thaw unconformity between overlying Holocene aged material (cryofacies assemblage 1) and underlying Pleistocene aged sediments (cryofacies assemblage 2) (Kotler and Burn 2000; French and Shur 2010).

Cryofacies assemblage 2 consists of cryofacies 4 (ice-poor structureless inorganic sandy silt),

cryofacies 5 (ice-poor inorganic sediment), cryofacies 6 (sediment-rich ice) and cryofacies 7 (sediment-poor ice) which all contain water isotopes, cryostructures, and radiocarbon dates consistent with an origin typical of Pleistocene silts found across unglaciated Yukon and Alaska (< -24 ‰ δ ^{18}O; Kotler and Burn 2000; Froese et *al*. 2009; Schirrmeister et *al*. 2013). A total of 5 radiocarbon dates were sampled from cryofacies assemblage 2, all of which were non-finite indicating a minimum age of >57000 14C age BP (Table 3.2). Cryofacies assemblage 2 appeared as a high resistivity unit (> 8500 Ωm) with a thickness ranging from 8 m in south facing sloped sites (BH12B) and 20 m in valley bottom sites (BH12 and BH13). The direct sampling of this high resistivity layer at BH12E shows a sharp transition from cryofacies 5 (ice-poor inorganic sediment) to cryofacies 6 (sediment-rich ice) underlain by cryofacies 7 (sediment-poor ice). Cryofacies 7 is interpreted as ice wedge ice based on the observation of foliated ice structures. Therefore the likely cause for the resistivity values observed is the presence of a partially degraded polygonal ice wedge network dating to the Pleistocene similar to the landscape evolution suggested in Kanevskiy et *al.* (2014). Cryofacies assemblage 2 was only observed at BH12E, BH12B and BH20, however it is inferred to extend to BH13, BH13B, BH12, BH12F, and BH20B based on their close proximity and similar ERT results. Moreover, cryofacies assemblage 2, where present, provides evidence of the local area's non-glacial origin.

Notwithstanding the close proximity of the most recent glacial boundary relict Pleistocene permafrost was encountered throughout the study area underlying ice-rich polygenetic Holocene permafrost. This discovery displays the resiliency of ice-rich permafrost similar to past research (Froese et *al*. 2008; Lacelle et *al*. 2009; Jorgenson et *al*. 2010, Calmels et *al*. 2012) but at lower latitudes and close proximity to recent glacial activity.

In addition to the findings of this study, the utility of combining site specific borehole and ERT results with regional scale AEM results has been displayed in chapter 5. Future studies like this could benefit from running or obtaining the AEM data first and following up with ground based methods. This approach would allow for high accuracy and efficiency when choosing ground based sites and comparing their results with the AEM data. Studies using this approach could provide detailed regional permafrost maps along the Alaska Highway corridor. Extensive AEM surveys have been completed by the USGS along the Alaska Highway within Alaska and could act as a foundation and guide for future similar studies within Alaska. Additional work includes drilling deep (>20 m) boreholes with core collection at each site and installing ground temperature loggers to allow for complete characterization of the permafrost at depth; extending AEM data to cover the entire study area; collecting new ERT data that is incidental with AEM flight lines; and investigating drained thaw lake basins to better understand the associated isotopic values.

References

Calmels, F., Froese, D.G., and Clavano, W.R. 2012. Cryostratigraphic record of permafrost degradation and recovery following historic (1898-1992) surface disturbances in the klondike region, central yukon territory 1,2. Canadian Journal of Earth Sciences, **49**: 938-952.

Duk-Rodkin, A. 1999. Glacial limits map of Yukon Territory. Geological Survey of Canada, Open File 3694, Indigenous and Northern Affairs Canada Geoscience Map 1999-2, scale 1:1 000 000.

French, H., and Shur, Y. 2010. The principles of cryostratigraphy. Earth-Science Reviews, **101**: 190-206.

Froese, D.G., Zazula, G.D., Westgate, J.A., Preece, S.J., Sanborn, P.T., Reyes, A.V., and Pearce, N.J.G. 2009. The Klondike goldfields and Pleistocene environments of Beringia. GSA Today, **19**: 4-10.

Froese, D.G., Westgate, J.A., Reyes, A.V., Enkin, R.J., and Preece, S.J. 2008. Ancient permafrost and a future, warmer Arctic. Science, **321**: 1648-1648.

Jorgenson, M.T., Romanovsky, V., Harden, J., Shur, Y., O'Donnell, J., Schuur, E.A.G., Kanevskiy, M. and Marchenko, S. 2010. Resilience and vulnerability of permafrost to climate change. Canadian Journal of Earth Sciences, 40: 1219-1236.

Kanevskiy, M., Jorgenson, T., Shur, Y., O'Donnell, J.A., Harden, J.W., Zhuang, Q., and Fortier, D. 2014. Cryostratigraphy and permafrost evolution in the lacustrine lowlands of west-central Alaska. Permafrost and Periglacial Processes, **25**: 14-34.

Kotler, E., Burn, C.R., 2000. Cryostratigraphy of the Klondike "muck" deposits, west-centralYukon Territory. Canadian Journal of Earth Sciences, 37, 849–861.

Lacelle, D., St-Jean, M., Lauriol, B., Clark, I.D., Lewkowicz, A., Froese, D.G., Kuehn, S.C., and Zazula, G. 2009. Burial and preservation of a 30,000 year old perennial snowbank in Red Creek valley, Ogilvie Mountains, central Yukon, Canada. Quaternary Science Reviews, **28**: 3401-3413.

Murton, J.B., and French, H.M. 1994. Cryostructures in permafrost, Tuktoyaktuk coastlands, western Arctic Canada. Canadian Journal of Earth Sciences = Revue Canadienne des Sciences de la Terre, **31**: 737-747.

Rampton, V.N. 1978. Surficial geology and geomorphology; Mirror Creek, Yukon Territory. Geological Survey of Canada: Ottawa, ON, Canada, Canada.

Schirrmeister, L., Froese, D.G., Tumskoy, V., Grosse, G., Wetterich, S. (2013). Yedoma: Late Pleistocene ice- rich syngenetic permafrost of Beringia. In: S.A. Elias, The Encyclopedia of Quaternary Science, 3, 542-552.

Ward, B.C., Bond, J.D., and Gosse, J.C. 2007. Evidence for a 55-50 ka (early Wisconsin) glaciation of the Cordilleran ice sheet, Yukon Territory, Canada. Quaternary Research, **68**: 141-150.

Bibliography

Amundson, R., Austin, A.T., Schuur, E.A.G., Yoo, K., Matzek, V., Kendall, C., Uebersax, A., Brenner, D., and Baisden, W.T. 2003. Global patterns of the isotopic composition of soil and plant nitrogen. Global Biogeochemical Cycles, **17**: 31.01-31.01.

Anisimov, O.A., and Nelson, F.E. 1996. Permafrost and global warming; strategies of adaptation. In Edited by Springer: New York, NY, United States, United States, pp. 440-449.

Astley, B.N., and Delaney, A.J. 2008. Permafrost delineation near Fairbanks, Alaska, using geophysical techniques. Extended Abstracts - International Conference on Permafrost, **9**: 9-10.

Ball, L.B., Smith, B.D., Minsley, B.J., Abraham, D.J., Voss, C.I., Deszez-Pan, M. and Cannia, J.C., 2011. Airborne electromagnetic and magnetic survey data of the Yukon Flats and Ft. Wainwright areas, central Alaska, June 2010, U.S. Geol. Surv. Open File Rep., 2011-1304, 28 pp.

Boaretto, E., Bryant, C., Carmi, I., Cook, G., Gulliksen, S., Harkness, D., Heinemeier, J., McClure, J., McGee, E., Naysmith, P., Possnert, G., Scott, M., van der Plicht, H., and van Strydonck, M. 2002. Summary findings of the fourth international radiocarbon intercomparison (FIRI) (1998–2001) *Journal of Quaternary Science*, 17: 633-637.

Boggs, S., Jr. 1987. Principles of sedimentology and stratigraphy. Merrill Publ. Co.: Columbus, OH, United States, United States.

Bray, M.T., French, H.M. and Shur, Y. 2006. Further Cryostratigraphic Observations in the CRREL Permafrost Tunnel, Fox, Alaska. *Permafrost and Periglacial Processes*, 17: 233-243.

Brown, J., Ferrians, O.J.J., Heginbottom, J.A. and Melnikov, E.S. (1997). International Permafrost Association Circum-Arctic Map of Permafrost and Ground Ice Conditions, Scale

1:10,000,000. U.S. Geological Survey.

Burn, C.R. 1998. The response (1958-1997) of permafrost and near-surface ground temperatures to forest fire, Takhini River valley, southern Yukon Territory. Canadian Journal of Earth Sciences, 35: 184-199.

Burn, C.R., Michel, F.A. and Smith, M.W. 1986. Stratigraphic, isotopic, and mineralogical evidence for an early Holocene thaw unconformity at Mayo, Yukon Territory. *Canadian Journal of Earth Sciences,* 23: 794-803.

Calmels, F., Allard, M., and Delisle, G. 2008. Development and decay of a lithalsa in Northern Québec: A geomorphological history. Geomorphology, **97**: 287-299.

Calmels, F., Froese, D.G., and Clavano, W.R. 2012. Cryostratigraphic record of permafrost degradation and recovery following historic (1898-1992) surface disturbances in the klondike region, central yukon territory 1,2. Canadian Journal of Earth Sciences, 49: 938-952.

Calmels, F., Gagnon, O. and Allard, M. 2005. A Portable Earth-drill System for Permafrost Studies. *Permafrost and Periglacial Processes*, 16: 311-315.

Chesson, L.A., Bowen, G.J., Ehleringer, J.R., 2010. Analysis of the hydrogen and oxygen stable isotope ratios of beverage waters without prior water extraction using isotope ratio infrared spectroscopy. Rapid Communications in Mass Spectrometry, 24, 3205-3213.

Cormie, A.B., and Schwarcz, H.P. 1996. Effects of climate on deer bone delta ^{15}N and delta ^{13}C; lack of precipitation effects on delta ^{15}N for animals consuming low amounts of C (sub 4) plants. Geochimica et Cosmochimica Acta, **60**: 4161-4166.

Craig, H. 1961. Standard for reporting concentrations of deuterium and oxygen-18 in natural waters. Science, **133**: 1833-1834.

Dansgaard, W. 1964. Stable isotopes in precipitation. Tellus XVI, **4**: 436-468.

Duk-Rodkin, A. 1999. Glacial limits map of Yukon Territory. Geological Survey of Canada, Open File 3694, Indigenous and Northern Affairs Canada Geoscience Map 1999-2, scale 1:1 000 000.

Epstein, S. and Mayeda, T. 1953. Variation of ^{18}O content of waters from natural sources. Geochimica et Cosmochimica Acta, **4**: 213-224.

Feng, L., Qingbai, W., Zhang, T., and Fujun, N. 2012. Modelling open-talik formation and permafrost lateral thaw under a thermokarst lake, Beiluhe Basin, Qinghai-Tibet Plateau. Permafrost and Periglacial Processes, **23**: 312-321.

Fraser, T.A. and Burn, C.R. 1997. On the nature and origin of "muck" deposits in the Klondike area, Yukon Territory. Canadian Journal of Earth Sciences, 34: 1333-1344.

French, H., 2011. Frozen sediments and previously-frozen sediments. Geological Society, London, Special Publications, 354 (1), 153-166.

French, H., and Shur, Y. 2010. The principles of cryostratigraphy. Earth-Science Reviews, **101**: 190-206.

Froese, D.G., 2005. Surficial Geology of Flat Creek (115 O/15) Yukon Territory, Open File 4592. Geological Survey of Canada, Ottawa.

Froese, D.G., Westgate, J.A., Reyes, A.V., Enkin, R.J., and Preece, S.J. 2008. Ancient permafrost and a future, warmer Arctic. Science, **321**: 1648-1648.

Froese, D.G., Zazula, G.D., Westgate, J.A., Preece, S.J., Sanborn, P.T., Reyes, A.V., and

Pearce, N.J.G. 2009. The Klondike goldfields and Pleistocene environments of Beringia. GSA Today, **19**: 4-10.

Gupta, P., Noone, D., Galewsky, J., Sweeney, C., and Vaughn, B.H. 2009. A new laser-based, field-deployable analyzer for laboratory-class stable isotope measurements in water. Geochimica et Cosmochimica Acta, **73**: A480-A480.

Heginbottom JA, Dubreuil M-A, Harker PA. 1995. Canada – permafrost. In National Atlas of Canada, 5th edition. Natural Resources Canada: Ottawa, Canada; Plate 2.1 (MCR 4177; scale 1:7 500 000).

Hilbich, C., Hauck, C., Hoelzle, M., Scherler, M., Schudel, L., Volksch, I., Vonder Muhll, D., and Mausbacher, R. 2008. Monitoring mountain permafrost resistivity tomography: 7-year study of seasonal, annual, and long-term variations at Schilthorn, Swiss Alps. Journal of Geophysical Research, 113: 1-12.

Hopkins, D.M. 1982. Aspects of the paleogeography of Beringia during the Late Pleistocene. *In* Paleogeography of Beringia. *Edited by* D.M. Hopkins, J.V. Matthews, Jr., C.E. Schweger, and S.B. Young. Academic Press, New York. Pp. 3-28.

Huscroft, C.A., and Lipovsky, P.S. 2003. Climate change and periglacial landslide activity in south-western Yukon Territory. EOS, Transactions, American Geophysical Union, **84**: @AbstractC21B-0811.

IAEA/WMO (2015). Global Network of Isotopes in Precipitation. The GNIP Database. Accessible at: http://www.iaea.org/water.

Israel, S., Murphy, D.C., Bennett, V., Mortensen, J.K. and Crowley, J.L., 2011. New insights into the geology and mineral potential of the Coast Belt in southwestern Yukon. In: Yukon Exploration and Geology 2010, K.E. MacFarlane, L.H. Weston and C. Relf (eds.), Yukon Geological Survey, p. 101-123.

Jackson, L.E., and Harington, C.R. 1991. Middle Wisconsinan mammals, stratigraphy, and sedimentology at the Ketza River site, Yukon Territories. Géographie Physique et Quaternaire, **45**: 69-77.

Jackson, L.E., Jr., Ward, B.C., Duk-Rodkin, A., and Hughes, O.L. 1991. The last Cordilleran ice sheet in southern Yukon Territory. Géographie Physique et Quaternaire, **45**: 341-354.

Jensen, B.J.L., Froese, D.G., Preece, S.J., Westgate, J.A. and Stachel, T. 2008. An Extensive middle to Late Pleistocene tephrochronologic record from east-central Alaska. *Quaternary Science Reviews*, 27: 411- 427.

Jensen, B.J.L., Pyne-O'Donnell, S., Plunkett, G., Froese, D.G., Hughes, P.D.M., Sigl, M., McConnell, J.R., Amesbury, M.J., Blackwell, P.G., van den Bogaard, C., Buck, C.E., Charman, D.J., Clague, J.J., Hall, V.A., Koch, J., Mackay, H., Mallon, G., McColl, L., and Pilcher, J.R. 2014. Transatlantic distribution of the Alaskan White River Ash. Geology, **42**: 875-878.

Jensen, M.A., Demidov, I.N., Larsen, E. and Lysa, A. 2009. Quaternary palaeoenvironments and multi- storey valley fills architecture along the Mezen and Severnaya Divina river valleys, Arkhangelsk region, NW Russia. Quaternary Science Reviews, 28: 2489-2506.

Jorgenson, M.T., Romanovsky, V., Harden, J., Shur, Y., O'Donnell, J., Schuur, E.A.G., Kanevskiy, M. and Marchenko, S. 2010. Resilience and vulnerability of permafrost to climate change. Canadian Journal of Earth Sciences, 40: 1219-1236.

Jouzel, J., Merlivat, L., and Lorius, C. 1982. Deuterium excess in an East Antarctic ice core suggests higher relative humidity at the oceanic surface during the last glacial maximum. Nature, **299**: 688-691.

Kanevskiy, M., Jorgenson, T., Shur, Y., O'Donnell, J.A., Harden, J.W., Zhuang, Q., and

Fortier, D. 2014. Cryostratigraphy and permafrost evolution in the lacustrine lowlands of west-central Alaska. Permafrost and Periglacial Processes, **25**: 14-34.

Kanevskiy, M., Shur, Y., Fortier, D., Jorgenson, M.T. and Stephani, E. 2011. Cryostratigraphy of late Pleistocene syngenetic permafrost (Yedoma) in northern Alaska, Itkillik River exposure. *Quaternary Research*, 75: 584-596.

Kennedy, K.E., Froese, D.G., Zazula, G.D. and Lauriol, B. 2010. Last Glacial Maximum age for the northwest Laurentide maximum from the Eagle River spillway and delta complex, northern Yukon. *Quaternary Science Reviews*, 29: 1288-1300.

Kotler, E. and Burn, C.R. 2000. Cryostratigraphy of the Klondike "muck" deposits, west-central Yukon Territory. *Canadian Journal of Earth Sciences,* 37: 849-861.

 Kurita, N., Newman, B.D., Araguas-Araguas, L., and Aggarwal, P. 2012. Evaluation of continuous water vapor dD and d18O measurements by off-axis integrated cavity output spectroscopy. Atmospheric Measurement Techniques, 5: 2069-2080.

Lacelle, D. 2011. On the delta ^{18}O, delta D and D-excess relations in meteoric precipitation and during equilibrium freezing; theoretical approach and field examples. Permafrost and Periglacial Processes, **22**: 13- 25.

Lacelle, D., St-Jean, M., Lauriol, B., Clark, I.D., Lewkowicz, A., Froese, D.G., Kuehn, S.C., and Zazula, G. 2009. Burial and preservation of a 30,000 year old perennial snowbank in Red Creek valley, Ogilvie Mountains, central Yukon, Canada. Quaternary Science Reviews, **28**: 3401-3413.

Lewkowicz, A.G., Etzelmuller, B and Smith, S. 2011. Characteristics of Discontinuous Permafrost based on Ground Temperature Measurements and Electrical Resistivity Tomography, Southern Yukon, Canada. *Permafrost and Periglacial Processes*, 22: 320-342.

Lipovsky, P.S. and McKenna, K., 2005. Local-scale biophysical mapping for integrated resource management, Watson Lake area (NTS 105A/2), Yukon. Yukon Geological Survey, Open File 2005-6, report and CD-ROM, 74 p.

Loke, M.H. and Barker, R.D. 1996. Rapid least-squares inversion of apparent resistivity pseudosections using a quasi-Newton method. *Geophysical Prospecting*, 44: 131-152.

Loke, M.H., and Barker, R.D. 1996. Practical techniques for 3D resistivity surveys and data inversion. Geophysical Prospecting, **44**: 499-523.

Lundberg, M. 2013. The Alaska Highway: The road to North America's last frontier. PR Distributing, 4.

Ma J.Y., Sun W., Liu X.N., Chen F.H. 2012. Variation in the Stable Carbon and Nitrogen Isotope Composition of Plants and Soil along a Precipitation Gradient in Northern China. PLoS ONE 7(12): e51894. doi: 10.1371/journal.pone.0051894.

Mackay, J. R., 1972. The world of underground ice. Annals of the Association of American Geographers, 62 (1), 1-22.

Mackay, J.R., 1973. Reticulate Ice Veins in Permafrost, Northern Canada. *Can. Geotech. Journal,* 11: 230- 237.

Matthews, J.V., Jr., Schweger, C.E., and Hughes, O.L. 1990. Plant and insect fossils from the Mayo Indian Village section (central Yukon); new data on middle Wisconsinan environments and glaciation. Géographie Physique et Quaternaire, **44**: 15-26.

Meyer, H., Schönicke, L., Wand, U., Hubberten, H.W., Friedrichsen, H., 2000. Isotope studies of hydrogen and oxygen in ground ice – experiences with the equilibration technique. Isotopes in Environmental and Health Studies, 36 (2), 133-149.

Minsley B.J., Abraham J.D., Smith B.D., Cannia J.C., Voss C.I., Jorgenson M.T., Walvoord M.A., Wylie B.K., Anderson L., Ball L.B., Deszcz-Pan M., Wellman T.P., Ager T.A., 2012. Airborne electromagnetic imaging of discontinuous permafrost. Geophysical Research Letters 39: L02503. DOI: 10. 1029/2011GL050079.

Murphy, D.C., Mortensen, J.K. and van Staal, C., 2009. 'Windy-McKinley' terrane, western Yukon: new data bearing on its composition, age, correlation and paleotectonic settings. In: Yukon Exploration and Geology 2008, L.H. Weston, L.R. Blackburn and L.L. Lewis (eds.), Yukon Geological Survey, p. 195-209.

Murton, J.B. and French, H.M. 1994. Cryostructures in permafrost, Tuktoyaktuk coastlands, western Arctic, *Canada. Canadian Journal of Earth Sciences*, 31: 737-747.

Newsome S.D., Miller G.H., Magee J.W., Fogel M.L. 2011. Quaternary record of aridity and mean annual precipitation based on d15N in ratite and dromornithid eggshells from Lake Eyre, Australia. Oecologia Springer, **167**:1151-1162.

Opel, T., Dereviagin, A.Y., Meyer, H., Schirrmeister, L., and Wetterich, S. 2011. Palaeoclimatic information from stable water isotopes of Holocene ice wedges on the Dmitrii Laptev Strait, northeast Siberia, Russia. *Permafrost and Periglacial Processes*, 22: 84-100.

Pastick, N.J., Jorgenson, M.T., Wylie, B.K., Minsley, B.J., Ji, L., Walvoord, M.A., Smith, B.D., Abraham, J.D., and Rose, J.R. 2013. Extending airborne electromagnetic surveys for regional active layer and permafrost mapping with remote sensing and ancillary data, Yukon Flats ecoregion, central Alaska. Permafrost and Periglacial Processes, **24**: 184-199.

Popov, A.I., Rozenbaum, G.E., and Tumel', N.V. 1985. Kriolitologiya. Izd. Mosk. Univ. : Moscow, USSR, USSR. PRISM Climate Group, Oregon State University, http://prism.oregonstate.edu, created February 2000.

Pumple, J., Froese, D., and Calmels, F. 2015. Characterizing permafrost valley fills along the Alaska Highway, southwest Yukon. In Proceedings GeoQuébec 2015-68th Canadian Geotechnical Conference and 7th Canadian Permafrost conference, 20-23 September 2015, Québec, Canada.

Rampton, V.N. 1978. Surficial geology and geomorphology; Mirror Creek, Yukon Territory. Geological Survey of Canada: Ottawa, ON, Canada, Canada.

Reimer, P.J., Bard, E., Bayliss, A., Beck, J.W., Blackwell, P.G., Ramsey, C.B., Buck, C.E., Cheng, H., Edwards, R.L., Friedrich, M., Grootes, P.M., Guilderson, T.P., Haflidason, H., Hajdas, I., Hatte, C., Heaton, T.J., Hoffmann, D.L., Hogg, A.G., Hughen, K.A., Kaiser, K.F., Kromer, B., Manning, S.W., Niu, M., Reimer, R.W., Richards, D.A., Scott, E.M., Southon, J.R., Staff, R.A., Turney, C.S.M., and van, D.P. 2013. IntCal13 and Marine13 radiocarbon age calibration curves 0-50,000 years cal BP. Radiocarbon, **55**: 1869-1887.

Reyes, A.V., Froese, D.G. and Jensen, B.J.L. 2010. Permafrost response to last interglacial warming: field evidence from non-glaciated Yukon and Alaska. *Quaternary Science Reviews*, 19: 3256-3274.

Schirrmeister, L., Froese, D.G., Tumskoy, V., Grosse, G., Wetterich, S. (2013). Yedoma: Late Pleistocene ice-rich syngenetic permafrost of Beringia. In: S.A. Elias, The Encyclopedia of Quaternary Science, 3, 542-552.

Shur, Y.L., and Jorgenson, M.T. 2007. Patterns of permafrost formation and degradation in relation to climate and ecosystems. Permafrost & Periglacial Processes, 18: 7.
Smith, M.W. and Riseborough, D.W. 2002. Climate and the Limits of Permafrost: A Zonal Analysis. *Permafrost and Periglacial Processes*, 13: 1-15.

Stevenson, B.A., Kelly, E.F., McDonald, E.V., and Busacca, A.J. 2005. The stable carbon isotope composition of soil organic carbon and pedogenic carbonates along a bioclimatic

gradient in the Palouse region, Washington State, USA. Geoderma, **124**: 37-47.

Stuiver, M., and Polach, H.A. 1977. Discussion; reporting of C-14 data. Radiocarbon, **19**: 355-363.

Szpak, P., Groecke, D.R., Debruyne, R., MacPhee, R.D.E., Guthrie, R.D., Froese, D.G., Zazula, G.D., Patterson, W.P., and Poinar, H.N. 2010. Regional differences in bone collagen delta ^{13}C and delta ^{15}N of Pleistocene mammoths; implications for paleoecology of the Mammoth Steppe. Palaeogeography, Palaeoclimatology, Palaeoecology, **286**: 88-96.

Telford, W.M., Geldart, L.P., and Sheriff, R.E. 1990. Applied geophysics. 2nd edition. Applied geophysics.2nd edition.

Throop, J., Lewkowicz, A.G. and Smith, S. 2012. Climate and ground temperature relations at sites across the continuous and discontinuous permafrost zones, northern Canada. *Canadian Journal of Earth Sciences*, 49: 865-876.

U.S. Geological Survey, 2012a. Report of Stable Isotopic Composition, Reference Material USGS45, Reston, VA.   http://isotopes.usgs.gov/lab/referencematerials/USGS45.pdf.

Ward, B.C., Bond, J.D., and Gosse, J.C. 2007. Evidence for a 55-50 ka (early Wisconsin) glaciation of the Cordilleran ice sheet, Yukon Territory, Canada. Quaternary Research, **68**: 141-150.

Wellman, T.P., Voss, C.I., and Walvoord, M.A. 2013. Impacts of climate, lake size, and supra- and sub- permafrost groundwater flow on lake-talik evolution, Yukon Flats, Alaska (USA). Hydrogeology Journal, **21**: 281-298.

Yershov, E.D. 1998. Studies in Polar Research: General Geocryology. Cambridge University Press, United Kingdom.

Zech, M., Zech, R., and Glaser, B. 2007. A 240,000 year stable carbon and nitrogen isotope record from a loess-like palaeosol sequence in the Tumara Valley, northeast Siberia. Chemical Geology, **242**: 307-318.

APPENDIX A: Ice Volume Content Results

Sample	Total weight (wet) (g)	Total volume	Dry weight (g)	Dry volume (cm^3)	Ice Volume (cm^3)	Ice volume content (%)
BH11-100	498.3	405	243.5	230	278	69
BH11-125	437.5	381	170.4	171	291	77
BH11-143	448.0	691	64.8	79	418	60
BH11-167	420.6	350	173.8	145	269	77
BH11-192	466.3	410	191.7	184	300	73
BH11-216	452.7	385	171.5	160	307	80
BH11-250	609.9	399	374.1	287	257	65
BH11-275	606.5	377	404.6	295	220	58
BH11-305	463.7	316	272.2	220	209	66
BH11-326	622.5	397	409.5	313	232	59
BH11-347	485.8	308	314.1	275	187	61
BH11-374	595.3	407	350.9	326	267	65
BH11-404	448.1	348	233.2	288	234	67
BH11-414	306.8	307	67.5	108	261	85
BH11-443	472.0	365	232.0	225	262	72
BH11-464	540.8	441	213.3	213	357	81
BH11-487	492.1	362	274.2	277	238	66
BH11-504	429.9	408	153.2	320	302	74
BH11-535	498.1	474	153.0	410	376	79
BH11-571	627.7	474	346.3	332	307	65
BH11-590	769.8	427	590.4	397	196	46

Sample	Total weight (wet) (g)	Total volume (cm^3)	Dry weight (g)	Dry volume (cm^3)	Ice Volume (cm^3)	Ice volume content (%)
BH12-74	443.8	382	157.9	179	312	82
BH12-104a	337.1	310	98.3	132	260	84
BH12-104b	436.9	400	150.0	205	313	78
BH12-141	490.4	461	222.8	268	292	63
BH12-178	440.8	398	138.6	165	330	83
BH12-193	355.3	291	153.3	129	220	76
BH12-210	416.7	330	198.1	201	238	72
BH12-254	513.6	404	245.9	205	292	72
BH12-283	529.2	445	229.5	223	327	74
BH12-320a	398.8	289	215.0	222	200	69
BH12-320b	388.0	352	128.7	193	283	80
BH12-352	501.0	407	216.8	190	310	76
BH12-384	385.4	434	186.2	226	217	50
BH12-393	249.8	268	47.1	64	221	83
BH12-405a	241.7	260	39.7	150	220	85
BH12-405b	334.2	325	69.2	122	289	89
BH12-436	426.6	400	131.6	185	322	80

Sample	Total weight (wet) (g)	Total volume (cm^3)	Dry weight (g)	Dry volume (cm^3)	Ice Volume (cm3)	Ice volume content (%)
BH12B-62-1	404.3	338	155.4	139	272	68
BH12B-83-2	535.9	372	308.9	247	248	56
BH12B-83-2 (top)	434.5	390	156.9	244	303	65
BH12B-121-3	454.8	343	212.9	162	264	65
BH12B-155-4	542.7	372	302.4	255	262	59
BH12B-155-4 (top)	335.4	331	113.5	173	242	61
BH12B-191-5	404.4	298	214.7	149	207	58
BH12B-191-5 (top)	334.0	266	155.5	120.5	195	62
BH12B-227-6	461.2	364	222.8	172	260	60
BH12B-227-6 (top)	464.6	347	263.0	224	220	53
BH12B-264-7	454.9	351	216.1	153	261	62
BH12B-294-8	427.1	321	225.5	177	220	58
BH12B-333-9	502.4	357	297.4	209	224	53
BH12B-333-9 (top)	410.6	326	196.6	166.5	233	60
BH12B-363-10	451.5	319	263.6	223	205	54
BH12B-363-10	404.5	323	201.5	155	221	58
BH12B-385-11	390.4	325	163.0	130	248	64
BH12B-421-12	567.9	338	407.3	252	175	44
BH12B-421-12	469.7	313	276.0	178	211	57
BH12B-455-13	509.3	342	291.1	222	238	58
BH12B-455-13	372.4	239	212.0	137	175	62
BH12B-485-14	433.1	333	207.4	148	246	62
BH12B-485-14	446.6	311	239.6	158	226	61
BH12B-524-15	723.7	500	401.6	279	351	59
BH12B-524-15	283.1	206	150.1	86	145	59
BH12B-545-16	363.8	220	247.7	144	127	48
BH12B-545-16	404.4	239	280.9	172	135	47
BH12B-583-17	511.0	282	382.2	256.5	141	42

Sample	Total weight (wet) (g)	Total volume (cm^3)	Dry weight (g)	Dry volume (cm^3)	Ice Volume (cm^3)	Ice volume content (%)
BH12E-55-1	512.6	412	188.6	174	353	72
BH12E-55-1 (top)	447.0	296	283.7	239	178	51
BH12E-86-2	376.1	301	157.3	141	239	67
BH12E-86-2 (top)	342.4	303	135.0	112.5	226	63
BH12E-121-3	417.1	346	153.5	110	288	70
BH12E-152-4	450.7	339	219.1	178	253	63
BH12E-152-4 (top)	382.7	321	140.8	106	264	69
BH12E-191-5	476.0	347	269.9	243	225	54
BH12E-191-5 (top)	410.3	305	210.7	157	218	60
BH12E-228-6	381.3	333	131.3	133	273	69
BH12E-259-7	499.7	353	248.8	159	274	65
BH12E-259-7 (top)	464.8	313	266.3	180.5	216	58

Sample	Total weight (wet) (g)	Total volume (cm^3)	Dry weight (g)	Dry volume (cm^3)	Ice Volume (cm^3)	Ice volume content (%)
BH12E-286-8	474.3	325	230.4	145	266	69
BH12E-286-8 (top)	429.6	311	271.2	258	173	47
BH12E-322-9	519.1	322	350.0	247	184	48
BH12E-322-9 (top)	504.8	302	318.6	213	203	57
BH12E-358-10	465.5	349	237.1	199	249	60
BH12E-358-10 (top)	522.0	307	342.1	248	196	54
BH12E-394-11	445.1	324	242.0	212	222	57
BH12E-394-11 (top)	472.9	332	272.9	257	218	55
BH12E-430-12	443.5	311	246.0	211	215	58
BH12E-430-12 (top)	457.6	334	244.4	256	233	59
BH12E-466-13	473.6	359	230.4	251	265	62
BH12E-502-14	427.7	324	217.3	268	230	60
BH12E-539-15	518.7	397	233.8	206	311	66
BH12E-566-16	330.6	300	82.3	43	271	76

Sample	Total weight (wet) (g)	Total volume (cm^3)	Dry weight (g)	Dry volume (cm^3)	Ice Volume (cm^3)	Ice volume content (%)
BH12F-74-1	539.9	348	308.8	237	252	61
BH12F-74-1 (top)	298.0	232	146.6	146	165	60
BH12F-101-2	412.6	317	210.6	203	220	58
BH12F-101-2 (top)	352.1	314	122.2	106	251	67
BH12F-138-3	511.9	360	296.8	241	235	55
BH12F-138-3 (top)	300.0	309	77.0	221	243	66
BH12F-175-4	505.6	347	253.4	164	275	67
BH12F-175-4 (top)	483.0	395	219.4	156	287	61
BH12F-211-5	440.2	351	201.8	182	260	62
BH12F-211-5(top)	393.2	329	174.2	154	239	61
BH12F-248-6	390.6	390	103.0	127	314	68
BH12F-286-7	675.5	468	350.9	231	354	64
BH12F-286-7 (top)	316.8	297	108.7	94	227	64
BH12F-314-8	543.6	326	332.3	235	230	59
BH12F-348-9	448.0	325	223.3	165	245	63
BH12F-386-10	432.7	341	196.6	147	258	63
BH12F-386-10 (top)	382.3	316	155.3	107	248	66
BH12F-417-11	552.4	340	345.8	225	225	56
BH12F-452-12	458.4	337	236.0	157	243	61

Sample	Total weight (wet) (g)	Total volume (cm^3)	Dry weight (g)	Dry volume (cm^3)	Ice Volume (cm^3)	Ice volume content (%)
BH13-68a	376.1	407	78.2	224	325	80
BH13-68b	393.9	408	78.2	273	344	84
BH13-100	374.9	406	80.3	254	321	79
BH13-137	402.8	436	68.6	80	365	84
BH13-164	436.4	424	146.2	187	317	75
BH13-185	287.8	325	17.1	39	295	91
BH13-221a	397.4	423	68.8	141	358	85
BH13-221b	315.4	353	28.1	79	313	89
BH13-250	333.3	376	65.9	no data	292	78
BH13-277	395.0	372	168.3	no data	247	67
BH13-303	504.5	410	265.7	no data	261	64
BH13-335	-	-	-	-	ICE	99
BH13-344	-	-	-	-	ICE	99
BH13-361	-	-	-	-	ICE	99
BH13-374	-	-	-	-	ICE	99
BH13-393	-	-	-	-	ICE	99
BH13-410	-	-	-	-	ICE	99
BH13-430	-	-	-	-	ICE	99
BH13-458	386.2	375	188.9	no data	215	57
BH13-485	413.0	414	118.4	no data	321	78

Sample	Total weight (wet) (g)	Total volume (cm^3)	Dry weight (g)	Dry volume (cm^3)	Ice Volume (cm^3)	Ice volume content (%)
BH13B-61 (46-61)	447.3	450	96.0	233	383	85
BH13B-99 (79-90)	363.9	386	60.7	238	331	86
BH13B- 181 (169-181)	438.9	467	72.3	103	400	86
BH13B-126 (112-126)	477.3	479	114.5	202	396	83
BH13B-126 (99-112)	455.9	466	91.0	222	398	85
BH13B-157 (135-147)	321.4	329	65.9	80	279	85
BH13B-157 (147-157)	212.2	328	39.2	41	189	58
BH13B-181 (157-169)	366.9	367	41.2	45	355	97
BH13B-209 (181-197)	440.0	447	103.3	126	367	82
BH13B-209 (197-209)	485.1	446	160.4	162	354	79
BH13B-245 (233-245)	436.6	431	102.5	124	365	85
BH13B-282 (246-257)	441.5	400	163.1	170	304	76
BH13B-282 (269-282)	428.6	429	136.5	155	319	74

Sample	Total weight (wet) (g)	Total volume (cm^3)	Dry weight (g)	Dry volume (cm^3)	Ice Volume (cm^3)	Ice volume content (%)
BH15-70 (58-70)	420.9	390	138.6	141	308	79
BH15-104 (71-82)	462.6	428	170.0	177	319	75
BH15-104 (93-104)	490.7	378	246.9	240	266	70
BH15-146 (108-123)	624.8	470	332.7	287	319	68
BH15-146 (135-146)	398.6	382	90.5	84	336	88
BH15-171 (138-149)	405.3	404	109.0	148	323	80
BH15-171 (149-160)	379.9	402	98.4	242	307	76
BH15-207 (195-207)	406.3	423	62.2	142	375	89
BH15-236 (208-222)	527.0	461	190.7	156	367	80
BH15-236 (222-236)	531.4	482	186.5	208	376	78
BH15-272 (261-272)	475.7	363	237.6	211	260	72
BH15-300 (285-300)	712.4	466	449.8	379	286	61

Sample	Total weight (wet) (g)	Total volume (cm^3)	Dry weight (g)	Dry volume (cm^3)	Ice Volume (cm^3)	Ice volume content (%)
BH16-69 (47-59)	431.4	395	136.1	224	322	82
BH16-69 (59-69)	394.4	326	173.8	130	241	74
BH16-101 (91-101)	382.5	337	156.6	116	246	73
BH16-122 (113-122)	392.0	305	168.3	145	244	80
BH16-159 (147-159)	476.2	419	178.5	160	325	77
BH16-175 (156-175)	770.4	643	332.0	284	478	74
BH16-202 (172-188)	748.1	512	451.2	311	324	63
BH16-202 (188-202)	701.5	419	466.9	275	256	61

Sample	Total weight (wet) (g)	Total volume (cm^3)	Dry weight (g)	Dry volume (cm^3)	Ice Volume (cm^3)	Ice volume content (%)
BH17-70 (48-61)	446.2	465	80.5	212	399	86
BH17-105 (81-94)	486.6	442	156.8	153	360	81
BH17-136 (105-115)	384.6	376	142.6	144	264	70
BH17-136 (126-136)	431.3	373	152.5	138	304	82
BH17-166 (135-145)	461.6	316	255.0	143	225	71
BH17-166 (155-166)	477.3	382	177.8	81	327	86
BH17-206 (194-206)	467.1	353	245.9	209	241	68
BH17-232 (221-232)	318.8	296	227.0	290	100	34
BH17-256 (245-256)	599.6	339	383.1	269	236	70
BH17-274 (262-274)	539.0	399	381.5	270	172	43

Sample	Total weight (wet) (g)	Total volume (cm^3)	Dry weight (g)	Dry volume (cm^3)	Ice Volume (cm^3)	Ice volume content (%)
BH18-78 (46-57)	531.5	360	311.9	246	240	67
BH18-78 (57-66)	358.2	294	114.3	87	266	91
BH18-78 (66-78)	469.0	402	153.1	136	345	86
BH18 143 (122-130)	358.8	312	136.8	104	242	78
BH18- 143 (130-143)	537.9	431	224.8	164	342	79
BH18-112 (100-112)	464.8	423	153.1	156	340	80
BH18-112 (78-89)	459.0	343	148.9	113	338	99
BH18-112 (89-100)	425.4	402	105.8	81	349	87
BH18-143 (111-122)	381.3	334	160.0	195	241	72
BH18-174 (142-153)	420.7	366	155.0	115	290	79
BH18-174 (163-174)	507.0	403	236.8	161	295	73
BH18-211 (175-187)	489.1	397	207.0	183	308	78
BH18-211 (199-211)	691.0	459	402.2	275	315	69
BH18-245 (231-243)	687.4	410	454.6	309	254	62
BH18-257 (246-257)	498.3	272	336.4	191	177	65
BH18-286 (273-286)	600.5	337	432.9	297	183	54
BH18-308 (298-308)	570.0	326	398.1	267	187	58

Sample	Total weight (wet) (g)	Total volume (cm^3)	Dry weight (g)	Dry volume (cm^3)	Ice Volume (cm^3)	Ice volume content (%)
BH19-72 (48-60)	427.5	373	145.1	107	308	83
BH19-72 (60-72)	506.5	392	240.4	225	290	74
BH19-92 (80-92)	410.5	389	123.8	151	313	80
BH19-262 (245-262)	692.2	445	479.6	420	232	52

Sample	Total weight (wet) (g)	Total volume (cm^3)	Dry weight (g)	Dry volume (cm^3)	Ice Volume (cm^3)	Ice volume content (%)
BH20-88 (78-88)	313.4	319	57.9	76	279	87
BH20-113 (100-113)	549.4	429	262.1	207	313	73
BH20-138 (113-125)	416.0	384	103.3	112	341	89
BH20-138 (125-138)	435.1	396	131.4	146	331	84
BH20-173 (161-173)	506.5	376	267.6	219	261	69
BH20-211 (199-211)	545.2	409	268.8	211	302	74
BH20-233 (222-233)	530.3	380	288.8	238	263	69
BH20-261 (247-261)	801.8	480	514.7	360	313	65
BH20-293 (283-293)	476.9	255	306.5	143	186	73
BH20-329 (316-329)	628.4	364	439.7	307	206	57
BH20-359 (345.5-359)	667.0	425	415.4	270	275	65
BH20-381 (369-381)	544.5	357	309.8	177	256	72
BH20-403 (391-403)	529.2	356	300.4	265	250	70
BH20-421 (411-421)	385.7	286	182.6	147	222	77
BH20-456 (445-456)	454.6	341	220.4	190	256	75
BH20-477 (468-477)	368.9	219	258.0	227	121	55

APPENDIX B: Grain Size Results

Sample #	>2mm (%)	>425um (%)	>150um (%)	>75um (%)	>45um (%)	<45um (%)	Dry Bulk Weight (g)
BH11-100	0	6	14	11	13	56	242.2
BH11-104	3	11	10	11	11	54	97.8
BH11-125	1	11	32	21	11	24	170.0
BH11-143	0	23	14	14	11	37	64.5
BH11-167	0	30	15	14	10	32	173.5
BH11-192	0	28	16	13	9	34	191.4
BH11-216	0	31	16	11	6	36	170.8
BH11-250	0	0	1	2	11	87	373.5
BH11-275	0	1	1	6	7	59	404.3
BH11-305	0	2	1	6	21	71	271.6
BH11-326	0	4	3	4	4	66	408.6
BH11-347	0	12	6	5	4	74	313.5
BH11-374	0	29	13	8	4	46	350.5
BH11-404	1	18	17	20	35	8	232.9
BH11-141	0	27	21	20	12	20	67.1
BH11-443	0	38	19	16	21	6	231.7
BH11-464	0	34	20	18	23	5	213.3
BH11-487	0	42	19	15	17	6	274.1
BH11-504	9	22	18	19	19	13	152.9
BH11-535	17	23	15	16	16	12	152.9
BH11-571	2	21	14	13	15	36	346.3
BH11-590	29	22	22	8	6	13	590.2

Sample #	>2mm (%)	>425um (%)	>150um (%)	>75um (%)	>45um (%)	<45um (%)	Dry Bulk Weight (g)
BH12-74	1	12	8	9	9	61	157.1
BH12-104b	2	10	12	17	17	42	149.7
BH12-141	5	28	55	9	1	0	219.1
BH12-178	3	6	6	9	11	65	130.8
BH12-193	0	2	3	5	7	83	151.7
BH12-210	1	4	5	8	11	71	197.6
BH12-254	0	2	2	4	9	83	244.9
BH12-283	0	2	3	4	7	84	228.3
BH12-320	1	2	4	8	14	71	214.4
BH12-320b	6	12	11	12	11	48	128.2
BH12-352	0	1	1	2	7	89	215.3
BH12-384	1	4	3	5	9	78	185.2
BH12-393	0	3	3	5	7	82	46.0
BH12-405a	5	29	19	18	14	14	39.1
BH12-405b	1	12	9	10	11	55	68.8
BH12-436	1	8	8	9	11	63	131.2

Sample #	>2mm (%)	>425um (%)	>150um (%)	>75um (%)	>45um (%)	<45um (%)	Dry Bulk Weight (g)
BH12B-62 (bot)	0	3	8	10	27	52	146.0
BH12B-83 (bot)	0	4	8	11	39	38	300.0
BH12B-121	1	5	8	7	35	45	204.0
BH12B-155	0	3	24	11	21	40	293.1
BH12B-191	0	1	4	6	34	54	206.4
BH12B-227	0	1	6	6	22	64	213.3
BH12B-264	3	5	8	9	29	46	206.9
BH12B-294	1	2	8	7	18	64	216.7
BH12B-333	0	2	5	6	26	59	288.0
BH12B-363	1	3	7	7	24	57	254.1
BH12B-385	1	5	10	11	24	49	154.0
BH12B-421	1	3	6	8	34	48	397.5
BH12B-455	0	1	2	5	23	69	281.9
BH12B-485	0	1	4	7	18	69	197.2
BH12B-524	1	6	9	10	38	36	392.0
BH12B-545	0	1	3	8	25	63	239.1
BH12B-583	3	7	4	8	37	41	373.6

Sample #	>2mm (%)	>425um (%)	>150um (%)	>75um (%)	>45um (%)	<45um (%)	Dry Bulk Weight (g)
BH12E-55 (bot)	1	2	14	15	21	47	180.0
BH12E-86 (bot)	0	2	11	13	22	52	148.7
BH12E-121 (bot)	0	1	5	7	22	65	144.8
BH12E-152 (bot)	0	1	4	8	26	60	210.2
BH12E-191 (bot)	0	2	6	7	25	60	260.7
BH12E-228 (bot)	2	6	9	11	32	41	122.5
BH12E-259 (bot)	3	2	2	5	35	54	240.2
BH12E-286 (bot)	0	1	3	7	49	40	121.1
BH12E-322 (bot)	1	1	2	6	31	60	340.9
BH12E-358 (bot)	1	2	5	8	23	61	228.9
BH12E-394 (bot)	1	3	10	10	19	57	232.8
BH12E-430 (bot)	1	5	8	8	20	59	237.1
BH12E-466 (bot)	0	4	8	9	18	61	221.3
BH12E-502 (bot)	1	4	8	11	18	59	208.4
BH12E-539 (bot)	0	2	4	10	25	58	225.3
BH12E-566 (bot)	0	1	3	6	18	72	88.3

Sample #	>2mm (%)	>425um (%)	>150um (%)	>75um (%)	>45um (%)	<45um (%)	Dry Bulk Weight (g)
BH12F-74 (bot)	1	3	5	6	41	45	299.3
BH12F-101 (bot)	0	4	8	8	13	66	202.0
BH12F-138 (bot)	0	1	5	6	19	69	287.7
BH12F-175 (bot)	1	3	6	8	51	32	276.5
BH12F-211 (bot)	0	1	6	6	32	55	192.8
BH12F-248 (bot)	2	7	17	18	25	30	94.4
BH12F-286 (bot)	0	1	2	4	55	37	341.8
BH12F-314 (bot)	1	2	3	6	52	37	323.3
BH12F-386 (bot)	0	3	5	10	45	37	187.6
BH12F-417 (bot)	0	0	1	5	56	38	337.3
BH12F-453 (bot)	0	1	2	6	44	46	227.5

Sample #	>2mm (%)	>425um (%)	>150um (%)	>75um (%)	>45um (%)	<45um (%)	Dry Bulk Weight (g)
BH13B-126	4	11	15	11	12	46	113.4
BH13B-157	1	6	10	10	15	58	66.5
BH13B-181	2	10	12	10	17	49	72.7
BH13B-209	0	2	4	6	14	73	161.0
BH13B-245	0	2	8	8	16	66	101.6
BH13B-282	0	2	8	9	21	60	135.8

Sample #	>2mm (%)	>425um (%)	>150um (%)	>75um (%)	>45um (%)	<45um (%)	Dry Bulk Weight (g)
BH13-68a	34	30	12	10	7	5	76.3
BH13-68b	60	18	6	5	5	6	77.5
BH13-100	32	26	16	16	5	5	71.7
BH13-137	23	19	13	13	11	20	67.9
BH13-164	2	4	7	18	14	95	144.7
BH13-185	1	2	4	8	12	73	16.5
BH13221a	13	15	11	10	11	40	68.5
BH13-221b	3	20	16	13	13	34	27.5
BH13-250	8	31	34	15	6	5	32.8
BH13-277	2	4	5	7	11	71	122.7
BH13-303	1	2	2	4	8	83	225.7
BH13-458	3	9	11	12	14	52	102.0
BH13-485	11	25	17	18	16	13	71.4

Sample #	>2mm (%)	>425um (%)	>150um (%)	>75um (%)	>45um (%)	<45um (%)	Dry Bulk Weight (g)
BH15-70 (58-70)	0	4	15	16	15	50	137.1
BH15-104 (93-104)	0	4	10	9	14	63	246.6
BH15-146 (135-146)	0	3	7	8	12	69	90.5
BH15-236 (222-236)	1	7	11	10	14	57	186.5
BH15-272 (261-272)	1	3	7	7	12	70	236.0
BH15-300 (285-300)	0	2	7	7	24	61	448.8

Sample #	>2mm (%)	>425um (%)	>150um (%)	>75um (%)	>45um (%)	<45um (%)	Dry Bulk Weight (g)
BH16-69 (59-69)	2	5	14	12	11	56	174.3
BH16-101 (91-101)	19	6	11	11	11	42	155.9
BH16-122 (113-122)	13	7	12	12	12	45	167.6
BH16-159 (147-159)	8	3	10	11	13	54	179.1
BH16-175 (156-175)	1	2	17	10	15	55	332.3
BH16-202 (188-202)	38	22	15	9	6	11	466.6

Sample #	>2mm (%)	>425um (%)	>150um (%)	>75um (%)	>45um (%)	<45um (%)	Dry Bulk Weight (g)
BH17-105 (81-94)	1	4	11	12	12	60	157.4
BH17-136 (126-136)	1	3	9	9	12	66	153.1
BH17-166 (135-145)	0	2	5	7	17	68	254.6
BH17-232 (221-232)	0	1	2	6	19	72	329.9
BH17-256 (245-256)	0	1	2	6	27	64	384.4
BH17-274 (262-274)	1	2	4	8	31	53	382.3

Sample #	>2mm (%)	>425um (%)	>150um (%)	>75um (%)	>45um (%)	<45um (%)	Dry Bulk Weight (g)
BH18-78 (46-56)	0	3	12	8	17	60	311.7
BH18-78 (66-78)	0	2	10	11	17	59	153.9
BH18-112 (78-89)	0	2	12	12	14	60	139.2
BH18-143 (130-143)	0	2	9	8	21	60	225.5
BH18-174 (142-153)	0	2	7	6	15	69	154.9
BH18-174 (163-174)	0	2	11	9	19	59	199.5
BH18-211 (175-187)	0	2	10	8	15	64	206.4
BH18-211 (199-211)	0	0	2	4	30	64	401.4
BH18-245 (231-243)	0	1	2	5	29	63	454.3
BH18-257 (246-257)	1	1	4	6	35	53	336.1
BH18-286 (273-286)	0	2	3	7	42	46	433.0
BH18-308 (298-308)	0	1	2	4	48	45	396.8

Sample #	>2mm (%)	>425um (%)	>150um (%)	>75um (%)	>45um (%)	<45um (%)	Dry Bulk Weight (g)
BH19-72 (60-72)	0	4	14	12	13	56	237.8
BH19-92 (809-92)	0	6	14	15	16	49	120.6
BH19-262 (245-262)	0	3	9	11	23	54	471.5

Sample #	>2mm (%)	>425um (%)	>150um (%)	>75um (%)	>45um (%)	<45um (%)	Dry Bulk Weight (g)
BH20-88 (78-88)	0	8	17	16	14	44	58.0
BH20-113 (100-113)	0	1	6	9	20	65	262.4
BH20-138 (125-138)	0	3	10	12	18	58	132.8
BH20-173 (161-173)	0	1	3	6	16	74	267.4
BH20-206 (194-206)	0	2	7	9	19	63	246.9
BH20-211 (199-211)	0	2	3	6	14	75	280.1
BH20-233 (222-233)	0	3	4	7	21	65	288.0
BH20-261 (247-261)	0	1	1	5	45	48	515.3
BH20-293 (283-293)	0	1	2	5	30	62	307.2
BH20-329 (316-329)	0	1	3	6	40	50	440.6
BH20-359 (345-359)	0	2	3	5	20	71	416.0
BH20-381 (369-381)	0	1	6	6	16	71	310.1
BH20-403 (391-403)	0	1	5	6	17	70	300.3
BH20-421 (411-421)	0	2	4	6	16	72	183.5
BH20-456 (445-456)	0	2	3	5	13	76	222.3
BH20-477 (468-477)	0	1	5	6	18	70	258.7

APPENDIX C: Radiocarbon Results

Sample	Cal yrs. BP	14C yrs. BP	±	UCIAMS #	Material
BH12F-386	7795	6960	15	156126	wood
BH12-433	5175	4555	20	142056	wood
BH12B-191	4195	3810	15	156127	wood
BH12B-264	5465	4720	20	156134	wood
BH12B-385	8140	7335	15	156133	wood
BH12B-485 .013mgC	8860	7960	330	156130	grass
BH12E-191	7310	6385	20	156128	wood
BH12E-358	non-finite	>50800		156138	wood
BH12E-466	non-finite	>55500		156139	wood
BH12E-566	non-finite	>50800		156129	wood
BH12E-566	non-finite	>53400		156135	wood
BH13-480-485	7835	6995	25	142057	wood
BH18-286-Mid	11260	9875	25	167481	Wood
BH20-233-210-227	13340	11490	25	167480	Wood
BH20-293-260-266	10245	9105	35	167478	Wood
BH20-456-Mid	non-finite	>48800		167477	Wood
BH11-510-520 .16mgC	10935	9570	40	142058	wood

APPENDIX D: Water Isotope Results

Site	Epoch	Sample	Depth (cm)	δ H (‰)	δ ^{18}O (‰)	d-excess (‰)
BH11	Holoce	BH11-100 (65-70)	(65-70)	-167.64	-21.32	2.92
BH11	Holoce	BH11-100 (84-91)	(84-91)	-171.06	-21.81	3.45
BH11	Holoce	BH11-125 (105-110)	(105-110)	-173.26	-22.18	4.18
BH11	Holoce	BH11-143 (125-130)	(125-130)	-171.52	-21.86	3.36
BH11	Holoce	BH11-167 (150-155)	(150-155)	-183.87	-23.43	3.57
BH11	Holoce	BH11-192 (175-180)	(175-180)	-183.51	-23.46	4.17
BH11	Holoce	BH11-216 (195-200)	(195-200)	-179.66	-22.54	0.66
BH11	Holoce	BH11-250 (230-235)	(230-235)	-174.60	-21.14	-5.48
BH11	Holoce	BH11-275 (250-255)	(250-255)	-171.50	-20.76	-5.42
BH11	Holoce	BH11-275 (270-275)	(270-275)	-168.99	-20.31	-6.55
BH11	Holoce	BH11-305 (285-290)	(285-290)	-168.72	-20.50	-4.72
BH11	Holoce	BH11-305 (295-305)	(295-305)	-165.11	-20.09	-4.39
BH11	Holoce	BH11-326 (320-326)	(320-326)	-164.33	-19.74	-6.41
BH11	Holoce	BH11-347 (340-347)	(340-347)	-162.97	-19.29	-8.65
BH11	Holoce	BH11-379 (367-374)	(367-374)	-163.60	-19.50	-7.60
BH11	Holoce	BH11-404 (396-404)	(396-404)	-162.05	-19.29	-7.71
BH11	Holoce	BH11-414 (409-414)	(409-414)	-160.18	-18.99	-8.24
BH11	Holoce	BH11-443 (415-422)	(415-422)	-157.97	-19.14	-4.88
BH11	Holoce	BH11-443 (433-443)	(433-443)	-160.39	-19.15	-7.16
BH11	Holoce	BH11-443 (433-443)	(433-443)	-160.69	-18.92	-9.34
BH11	Holoce	BH11-464 (443-448)	(443-448)	-163.39	-19.28	-9.13
BH11	Holoce	BH11-464 (460-464)	(460-464)	-159.51	-18.83	-8.87
BH11	Holoce	BH11-487 (464-470)	(464-470)	-161.15	-19.02	-8.99
BH11	Holoce	BH11-487 (480-487)	(480-487)	-160.49	-19.11	-7.62
BH11	Holoce	BH11-571 (535-545)	(535-545)	-160.03	-19.08	-7.38
BH11	Holoce	BH11-571 (555-563)	(555-563)	-161.40	-18.93	-9.96
BH11	Holoce	BH11-571 (563-571)	(563-571)	-160.75	-19.05	-8.35
BH11	Holoce	BH11-590 (571-577)	(571-577)	-159.31	-18.89	-8.19

Site	Epoch	Sample	Depth (cm)	δ H (‰)	δ ^{18}O (‰)	d-excess (‰)
BH12	Holoce	BH12-74 (40-50)	(40-50)	-161.55	-20.66	3.73
BH12	Holoce	BH12-74 (65-70)	(65-70)	-155.01	-19.41	0.27
BH12	Holoce	BH12-107 (85-90)	(85-90)	-157.97	-19.86	0.91
BH12	Holoce	BH12-141 (115-122)	(115-122)	-164.57	-20.64	0.55
BH12	Holoce	BH12-141 (123-128)	(123-128)	-165.83	-21.03	2.41
BH12	Holoce	BH12-141 (128-133)	(128-133)	-166.6	-20.79	-0.28
BH12	Holoce	BH12-178 (150-155)	(150-155)	-167.17	-21.05	1.21
BH12	Holoce	BH12-178 (156-162)	(156-162)	-166.32	-21.02	1.84
BH12	Holoce	BH12-178 (173-178)	(173-178)	-169.71	-21.35	1.09
BH12	Holoce	BH12-193 (185-193)	(185-193)	-169.57	-21.49	2.37
BH12	Holoce	BH12-216 (210-216)	(210-216)	-169.21	-21.54	3.07
BH12	Holoce	BH12-254 (220-225)	(220-225)	-170.70	-21.67	2.65
BH12	Holoce	BH12-254 (240-245)	(240-245)	-171.16	-21.69	2.36
BH12	Holoce	BH12-288 (260-265)	(260-265)	-174.06	-21.81	0.38
BH12	Holoce	BH12-288 (280-288)	(280-288)	-173.11	-21.79	1.21
BH12	Holoce	BH12-320 (295-300)	(295-300)	-169.36	-21.32	1.20
BH12	Holoce	BH12-320 (315-320)	(315-320)	-171.43	-21.47	0.33
BH12	Holoce	BH12-352 (335-340)	(335-340)	-167.97	-21.3	2.43
BH12	Holoce	BH12-384 (350-355)	(350-375)	-164.68	-20.87	2.28
BH12	Holoce	BH12-384 (370-375)	(370-375)	-165.41	-20.83	1.23
BH12	Holoce	BH12-393 (387-393)	(387-393)	-163.73	-21.15	5.47
BH12	Holoce	BH12-436 (430-436)	(430-436)	-165.25	-21.04	3.07

Site	Epoch	Sample	Depth (cm)	δ H (‰)	δ ^{18}O (‰)	d-excess (‰)
BH12	Holoce	BH12B-62-1-1top	32	-169.91	-21.80	4.47
BH12	Holoce	BH12B-62-1-2mid	47	-159.83	-20.22	1.93
BH12	Holoce	BH12B-62-1-3bot	62	-163.47	-20.72	2.26
BH12	Holoce	BH12B-83-2-1top	69	-164.96	-20.84	1.80
BH12	Holoce	BH12B-83-2-2mid	75	-164.24	-20.66	1.03
BH12	Holoce	BH12B-83-2-3bot	83	-163.95	-20.76	2.13
BH12	Holoce	BH12B-121-3-1top	95	-168.44	-21.28	1.79
BH12	Holoce	BH12B-121-3-2mid	107	-169.67	-21.47	2.12
BH12	Holoce	BH12B-121-3-3bot	121	-171.77	-21.57	0.81
BH12	Holoce	BH12B-155-4-1top	132	-172.19	-21.57	0.39
BH12	Holoce	BH12B-155-4-2mid	143	-169.41	-21.18	0.03
BH12	Holoce	BH12B-155-4-3bot	155	-167.77	-20.96	-0.09
BH12	Holoce	BH12B-191-5-1top	167	-169.57	-21.16	-0.29
BH12	Holoce	BH12B-191-5-2mid	179	-169.88	-21.11	-1.00
BH12	Holoce	BH12B-191-5-3bot	191	-168.96	-21.03	-0.69
BH12	Holoce	BH12B-227-6-1top	203	-170.26	-21.26	-0.15
BH12	Holoce	BH12B-227-6-3mid	215	-169.89	-21.13	-0.88
BH12	Holoce	BH12B-227-6-3bot	227	-169.59	-21.12	-0.64
BH12	Holoce	BH12B-264-7-1top	239	-170.41	-21.26	-0.34
BH12	Holoce	BH12B-264-7-2mid	251	-171.17	-21.35	-0.40
BH12	Holoce	BH12B-264-7-3bot	264	-171.24	-21.51	0.81
BH12	Holoce	BH12B-294-8-1top	274	-172.13	-21.50	-0.13
BH12	Holoce	BH12B-294-8-2mid	284	-174.77	-21.91	0.52
BH12	Holoce	BH12B-294-8-3bot	294	-174.43	-21.88	0.60
BH12	Holoce	BH12B-333-9-1top	307	-174.79	-21.97	0.97
BH12	Holoce	BH12B-333-9-2mid	320	-174.84	-21.78	-0.64
BH12	Holoce	BH12B-333-9-3bot	333	-175.80	-22.10	1.03
BH12	Holoce	BH12B-363-10-1top	343	-177.60	-22.45	2.00
BH12	Holoce	BH12B-363-10-2mid	353	-177.32	-22.33	1.32
BH12	Holoce	BH12B-363-10-3bot	363	-175.45	-22.11	1.41
BH12	Holoce	BH12B-385-11-1top	374	-177.00	-22.31	1.49
BH12	Holoce	BH12B-385-11-3bot	385	-176.69	-22.21	1.02
BH12	Holoce	BH12B-421-12-1top	397	-176.10	-22.35	2.73
BH12	Holoce	BH12B-421-12-2mid	410	-174.67	-22.22	3.09
BH12	Holoce	BH12B-421-12-3bot	421	-175.65	-22.33	3.01
BH12	Holoce	BH12B-455-13-1top	432	-174.17	-22.19	3.36
BH12	Holoce	BH12B-455-13-2mid	441	-171.67	-21.98	4.17
BH12	Holoce	BH12B-455-13-3bot	455	-172.60	-21.98	3.20
BH12	Holoce	BH12B-485-14-1top	465	-172.04	-22.01	4.06
BH12	Holoce	BH12B-485-14-2mid	475	-172.17	-21.93	3.27
BH12	Holoce	BH12B-485-14-3bot	485	-172.52	-21.99	3.42
BH12	Holoce	BH12B-524-15-1top	498	-173.98	-22.31	4.50

Site	Epoch	Sample	Depth (cm)	δ H (‰)	δ ^{18}O (‰)	d-excess (‰)
BH12	Holoce	BH12B-524-15-2mid	511	-175.98	-22.46	3.72
BH12	Holoce	BH12B-524-15-3bot	524	-177.60	-22.78	4.61
BH12	Holoce	BH12B-545-16-1top	534	-181.15	-23.21	4.55

Site	Epoch	Sample	Depth (cm)	δ H (‰)	δ ^{18}O (‰)	d-excess (‰)
BH12	Holocene	BH12B-545-16-3bot	54	-182.19	-23.49	5.69
BH12	Pleistoce	BH12B-583-17-1top	55	-184.27	-23.64	4.88
BH12	Pleistoce	BH12B-583-17-2mid	57	-184.66	-23.72	5.11
BH12	Pleistoce	BH12B-583-17-3bot	58	-185.28	-23.91	6.01

Site	Epoch	Sample	Depth (cm)	δ H (‰)	δ ^{18}O (‰)	d-excess (‰)
BH12E	Holocene	BH12E-55-1-1top	35	-164.35	-20.75	1.64
BH12E	Holocene	BH12E-55-1-3bot	45	-163.17	-20.53	1.09
BH12E	Holocene	BH12E-86-2-1top	60	-167.09	-21.25	2.91
BH12E	Holocene	BH12E-86-2-2mid	70	-171.47	-21.84	3.23
BH12E	Holocene	BH12E-86-2-3bot	86	-169.07	-21.64	4.05
BH12E	Holocene	BH12E-121-3-1top	95	-168.05	-21.42	3.27
BH12E	Holocene	BH12E-121-3-2mid	105	-179.99	-22.85	2.80
BH12E	Holocene	BH12E-121-3-3bot	120	-177.50	-22.54	2.82
BH12E	Holocene	BH12E-152-4-1top	130	-176.90	-22.45	2.70
BH12E	Holocene	BH12E-152-4-2mid	140	-179.51	-22.67	1.89
BH12E	Holocene	BH12E-152-4-3bot	150	-179.78	-22.76	2.30
BH12E	Holocene	BH12E-191-5-1top	160	-179.58	-22.80	2.85
BH12E	Holocene	BH12E-191-5-2mid	170	-177.14	-22.47	2.59
BH12E	Holocene	BH12E-191-5-3bot	180	-176.19	-22.25	1.82
BH12E	Holocene	BH12E-228-6-1top	195	-173.76	-22.17	3.60
BH12E	Holocene	BH12E-228-6-2mid	210	-170.83	-21.69	2.71
BH12E	Holocene	BH12E-228-6-3bot	225	-170.02	-21.70	3.61
BH12E	Holocene	BH12E-259-7-1top	235	-170.48	-21.89	4.63
BH12E	Holocene	BH12E-259-7-2mid	245	-170.70	-22.07	5.84
BH12E	Holocene	BH12E-259-7-3bot	255	-171.08	-22.08	5.59
BH12E	Holocene	BH12E-286-8-1top	265	-174.14	-22.45	5.48
BH12E	Holocene	BH12E-286-8-2mid	275	-176.81	-22.83	5.83
BH12E	Holocene	BH12E-286-8-3bot	285	-180.16	-23.20	5.41
BH12E	Pleistoce	BH12E-322-8-1top	295	-183.05	-23.62	5.91
BH12E	Pleistoce	BH12E-322-8-2mid	305	-187.09	-24.05	5.31
BH12E	Pleistoce	BH12E-322-8-3bot	315	-190.17	-24.40	5.03
BH12E	Pleistoce	BH12E-358-10-1top	330	-191.26	-24.51	4.79
BH12E	Pleistoce	BH12E-358-10-2mid	340	-195.24	-25.00	4.76
BH12E	Pleistoce	BH12E-358-10-3bot	350	-199.38	-25.53	4.85
BH12E	Pleistoce	BH12E-394-11-1top	365	-203.43	-25.92	3.96
BH12E	Pleistoce	BH12E-394-11-2mid	375	-205.03	-26.28	5.21

Site	Epoch	Sample	Depth (cm)	δ H (‰)	δ ^{18}O (‰)	d-excess (‰)
BH12E	Pleistoce	BH12E-394-11-3bot	385	-205.95	-26.52	6.21
BH12E	Pleistoce	BH12E-430-12-1top	400	-205.98	-26.48	5.86
BH12E	Pleistoce	BH12E-430-12-2mid	410	-208.06	-26.64	5.09
BH12E	Pleistoce	BH12E-430-12-3bot	425	-209.48	-26.81	5.01
BH12E	Pleistoce	BH12E-466-13-1top	435	-208.93	-26.72	4.80
BH12E	Pleistoce	BH12E-466-13-2mid	450	-210.77	-26.91	4.54
BH12E	Pleistoce	BH12E-466-13-3bot	465	-210.60	-26.92	4.79
BH12E	Pleistoce	BH12E-502-14-1top	475	-210.68	-26.97	5.08
BH12E	Pleistoce	BH12E-502-14-2mid	485	-211.43	-26.98	4.41
BH12E	Pleistoce	BH12E-502-14-3bot	495	-212.92	-27.31	5.52
BH12E	Pleistoce	BH12E-539-15-1top	510	-211.13	-26.94	4.37
BH12E	Pleistoce	BH12E-539-15-2mid	520	-211.18	-26.96	4.48
BH12E	Pleistoce	BH12E-539-15-3bot	535	-212.01	-27.18	5.43
BH12E	Pleistoce	BH12E-566-16-1top	545	-210.37	-26.85	4.42
BH12E	Pleistoce	BH12E-566-16-2mid	555	-211.92	-27.03	4.29
BH12E	Pleistoce	BH12E-566-16-3bot	565	-212.61	-27.21	5.07
BH12E	Pleistoce	BH12E-587-17-1top	575	-218.24	-27.65	2.98
BH12E	Pleistoce	BH12E-586-17-2mid	580	-220.12	-27.86	2.76
BH12E	Pleistoce	BH12E-586-17-3bot	585	-220.49	-27.70	1.13

Site	Epoch	Sample	Depth (cm)	δ H (‰)	δ ^{18}O (‰)	d-excess (‰)
BH12F	Holocene	BH12F-74-1-1top	42	-184.34	-23.54	3.96
BH12F	Holocene	BH12F-74-1-2mid	52	-162.83	-20.54	1.49
BH12F	Holocene	BH12F-74-1-3bot	72	-160.25	-20.23	1.59
BH12F	Holocene	BH12F-101-2-1top	78	-159.64	-19.91	-0.36
BH12F	Holocene	BH12F-101-2-2mid	88	-171.49	-21.70	2.11
BH12F	Holocene	BH12F-101-2-3bot	98	-166.65	-20.94	-0.68
BH12F	Holocene	BH12F-138-3-1top	109	-158.99	-19.79	-0.70
BH12F	Holocene	BH12F-138-3-2mid	119	-162.73	-20.34	-0.01
BH12F	Holocene	BH12F-138-3-3bot	129	-171.55	-21.54	0.77
BH12F	Holocene	BH12F-175-4-1top	140	-172.66	-21.58	-0.01
BH12F	Holocene	BH12F-175-4-2mid	152	-170.60	-21.34	0.10
BH12F	Holocene	BH12F-175-4-3bot	168	-170.52	-21.26	-0.46
BH12F	Holocene	BH12F-211-5-1top	180	-168.04	-20.87	-1.08
BH12F	Holocene	BH12F-211-5-2mid	195	-167.77	-20.71	-2.06
BH12F	Holocene	BH12F-211-5-3bot	207	-169.40	-20.99	-1.47
BH12F	Holocene	BH12F-248-6-1top	216	-171.54	-21.34	-0.81
BH12F	Holocene	BH12F-248-6-2mid	228	-172.93	-21.57	-0.40
BH12F	Holocene	BH12F-248-6-3bot	240	-172.19	-21.52	-0.06
BH12F	Holocene	BH12F-286-7-1top	255	-169.71	-21.21	0.01
BH12F	Holocene	BH12F-286-7-2mid	268	-171.42	-21.42	-0.05
BH12F	Holocene	BH12F-286-7-3bot	279	-170.05	-21.31	0.40
BH12F	Holocene	BH12F-314-8-1top	295	-169.52	-21.13	-0.51
BH12F	Holocene	BH12F-314-8-2mid	307	-168.99	-21.14	0.13
BH12F	Holocene	BH12F-314-8-3bot	312	-169.99	-21.18	-0.54
BH12F	Holocene	BH12F-348-9-1top	323	-168.38	-20.95	-0.80
BH12F	Holocene	BH12F-348-9-2mid	334	-167.79	-20.87	-0.83
BH12F	Holocene	BH12F-348-9-3bot	346	-168.86	-21.07	-0.30
BH12F	Holocene	BH12F-386-10-1top	355	-167.88	-20.75	-1.92
BH12F	Holocene	BH12F-386-10-2mid	367	-167.94	-20.82	-1.34
BH12F	Holocene	BH12F-386-10-3bot	378	-166.60	-20.57	-2.04
BH12F	Holocene	BH12F-417-11-1top	385	-167.02	-20.65	-1.84
BH12F	Holocene	BH12F-417-11-2mid	399	-167.62	-20.75	-1.62
BH12F	Holocene	BH12F-417-11-3bot	408	-166.50	-20.66	-1.24
BH12F	Holocene	BH12F-452-12-1top	420	-167.90	-20.85	-1.10
BH12F	Holocene	BH12F-452-12-2mid	435	-166.11	-20.67	-0.72
BH12F	Holocene	BH12F-452-12-3bot	448	-166.65	-20.67	-1.33

Site	Epoch	Sample	Depth (cm)	δ H (‰)	δ ^{18}O (‰)	d-excess (‰)
BH13	Holocene	BH13-33-45	37	-166.18	-21.20	3.39
BH13	Holocene	BH13-68 (63-68)	67	-158.61	-19.50	-2.60
BH13	Holocene	BH13-81-87	85	-167.92	-20.25	-5.95
BH13	Holocene	BH13-137 (125-	127	-167.41	-20.70	-1.79
BH13	Holocene	BH13-164 (147-152)	150	-169.15	-21.16	0.13
BH13	Holocene	BH13-164 (160-164)	162	-165.02	-20.54	-0.67
BH13	Holocene	BH13-185 (175-180)	177	-159.54	-19.78	-1.33
BH13	Holocene	BH13-221 (185-192)	190	-161.96	-20.06	-1.46
BH13	Holocene	BH13-221 (195-200)	197	-164.29	-20.42	-0.92
BH13	Holocene	BH13-221 (215-221)	217	-164.61	-20.39	-1.52
BH13	Holocene	BH13-235-240	237	-172.02	-21.34	-1.31
BH13	Holocene	BH13-250-235	250	-171.27	-21.26	-1.20
BH13	Holocene	BH13-277 (255-260)	257	-165.62	-20.76	0.42
BH13	Holocene	BH13-277 (271-277)	275	-170.54	-21.27	-0.42
BH13	Holocene	BH13-303 (285-290)	287	-175.85	-21.90	-0.62
BH13	Holocene	BH13-310-320	315	-189.83	-23.89	1.25
BH13	Holocene	BH13-335 (320-335)	327	-195.92	-24.97	3.86
BH13	Holocene	BH13-361 (355-361)	357	-197.55	-25.41	5.73
BH13	Holocene	BH13-430 (420-430)	425	-193.12	-24.66	4.15
BH13	Holocene	BH13-430-446-BULK	432	-175.68	-22.05	0.75
BH13	Holocene	BH13-430-446-ICE	437	-175.42	-21.84	-0.67
BH13	Holocene	BH13-430-446-SED	443	-171.10	-21.54	1.22
BH13	Holocene	BH13-405 (460-465)	463	-163.16	-20.91	4.13
BH13	Holocene	BH13-480-485	483	-171.22	-21.94	4.32

Site	Epoch	Sample	Depth (cm)	δ H (‰)	δ ^{18}O (‰)	d-excess (‰)
BH13B	Holocene	BH13B-99 (90-99)	95	-162.64	-20.13	-1.56
BH13B	Holocene	BH13B-157 (126-127)	126	-164.64	-20.82	1.94
BH13B	Holocene	BH13B-157 (127-133)	13	-166.40	-20.73	-0.57
BH13B	Holocene	BH13B-157 (133-136)	13	-165.55	-20.67	-0.22
BH13B	Holocene	BH13B-157 (136-137)	13	-163.48	-20.42	-0.15
BH13B	Holocene	BH13B-157 (141-146)	14	-164.65	-20.69	0.88
BH13B	Holocene	BH13B-157 (146-150)	14	-164.29	-20.71	1.38
BH13B	Holocene	BH13B-157 (150-152)	15	-164.14	-20.50	-0.11
BH13B	Holocene	BH13B-157 (152-157)	157	-163.73	-20.62	1.24

Site	Epoch	Sample	Depth (cm)	δ H (‰)	δ ^{18}O (‰)	d-excess (‰)
BH15	Holocene	BH15-146 (135-146)	130	-163.76	-21.11	5.15
BH15	Holocene	BH15-171 (138-149)	148	-165.34	-21.15	3.83
BH15	Holocene	BH15-171 (161-171)	168	-167.67	-21.39	3.49
BH15	Holocene	BH15-272 (247-257)	250	-167.15	-21.21	2.54
BH15	Holocene	BH15-300 (290-300)	295	-167.78	-21.29	2.57

Site	Epoch	Sample	Depth (cm)	δ H (‰)	δ ^{18}O (‰)	d-excess (‰)
BH16	Holocene	BH16-69-66-69	66-69	-168.30	-21.29	2.03
BH16	Holocene	BH16-159-152-155	152-155	-182.69	-22.12	-5.71

Site	Epoch	Sample	Depth (cm)	δ H (‰)	δ ^{18}O (‰)	d-excess (‰)
BH17	Holocene	BH17-70 (30-40)	30-40	-169.74	-21.46	1.98
BH17	Holocene	BH17-166-155-166	155-166	-180.21	-22.41	-0.93
BH17	Holocene	BH17-232-202-212	202-212	-182.22	-22.88	0.79
BH17	Holocene	BH17-256-232-246	232-246	-179.59	-22.60	1.19
BH17	Holocene	BH17-256-246-256	246-256	-176.90	-22.38	2.11

Site	Epoch	Sample	Depth (cm)	δ H (‰)	δ ^{18}O (‰)	d-excess (‰)
BH18	Holocene	BH18-78-69-73	70	-174.04	-22.58	6.58
BH18	Holocene	BH18-112-108-110	110	-170.94	-21.40	0.29
BH18	Holocene	BH18-143-132-133	133	-177.02	-22.34	1.74
BH18	Holocene	BH18-176-172-175	174	-183.65	-23.37	3.32
BH18	Holocene	BH18-245-223-234	230	-189.73	-24.17	3.60
BH18	Holocene	BH18-286-267-286	270	-185.60	-23.57	2.97

Site	Epoch	Sample	Depth (cm)	δ H (‰)	δ ^{18}O (‰)	d-excess (‰)
BH19	Holocene	BH19-92-90-92	90-92	-168.98	-21.28	1.29
BH19	Holocene	BH19-185-180-185	180-185	-186.26	-23.56	2.20

Site	Epoch	Sample	Depth (cm)	δ H (‰)	δ ^{18}O (‰)	d-excess (‰)
BH20	Holocene	BH20-88-86-88	86-88	-176.20	-22.06	0.30
BH20	Holocene	BH20-138-133-138	133-138	-180.77	-22.15	-3.59
BH20	Holocene	BH20-173-161-173	161-173	-185.85	-23.00	-1.88
BH20	Holocene	BH20-211-200-210	200-210	-189.09	-23.65	0.14
BH20	Holocene	BH20-233-227-233	227-233	-190.60	-24.09	2.11
BH20	Holocene	BH20-261-256-261	256-261	-193.93	-24.46	1.72
BH20	Pleistoce	BH20-293-282-293	282-293	-195.69	-24.93	3.71
BH20	Pleistoce	BH20-329-315-329	315-329	-198.90	-25.37	4.07
BH20	Pleistoce	BH20-381-355-369	355-369	-200.85	-25.76	5.26
BH20	Pleistoce	BH20-403-391-403	391-403	-203.33	-26.16	5.98
BH20	Pleistoce	BH20-421-403-411	403-411	-203.27	-26.05	5.14
BH20	Pleistoce	BH20-456-445-456	445-456	-192.67	-23.95	-1.11
BH20	Pleistoce	BH20-477-456-465	456-465	-189.40	-23.72	0.34

APPENDIX E: Carbon and Nitrogen Isotope Results

Sample	Epoch	Sample weight (mg)	% N	δ ^{15}N (‰)	% C	δ ^{13}C (‰)	C:N
BH12-55-1-Top	Holocene	41.407	0.47	2.71	9.40	-25.52	20.0
BH12-74-65-70	Holocene	19.519	0.81	2.03	14.76	-25.98	18.2
BH12-178-173-178	Holocene	29.176	0.62	1.94	11.66	-25.61	18.9
BH12-288-260-265	Holocene	48.643	0.25	1.43	3.83	-25.67	15.6
BH12-352-335-340	Holocene	34.548	0.37	1.39	6.63	-25.92	17.9
BH12-393-387-393	Holocene	39.768	0.53	2.08	8.65	-25.77	16.3

Sample	Epoch	Sample weight (mg)	% N	δ ^{15}N (‰)	% C	δ ^{13}C (‰)	C:N
BH12B-62-1-BOT	Holocene	39.202	0.26	2.41	4.40	-25.51	17.0
BH12B-121-3-Bot	Holocene	46.801	0.21	1.71	3.40	-25.84	16.2
BH12B-191-5-Bot	Holocene	29.070	0.13	2.35	2.33	-25.45	18.5
BH12B-264-7-Top	Holocene	25.187	0.50	2.36	8.34	-25.48	16.6
BH12B-333-9-Bot	Holocene	52.906	0.27	3.25	4.39	-24.75	16.1
BH12B-421-12-Top	Holocene	39.943	0.10	3.41	1.15	-25.02	12.1
BH12B-485-14-Top	Holocene	49.155	0.17	3.51	2.00	-23.51	12.0
BH12B-524-15-Bot	Holocene	60.573	0.08	4.32	1.54	-16.13	19.3
BH12B-545-16-Bot	Holocene	36.340	0.07	4.03	1.09	-21.18	14.6
BH12B-583-17-Bot	Pleistocen	51.527	0.07	3.43	1.09	-18.26	16.0
BH12B-583-17-MID	Pleistocen	58.490	0.06	3.53	0.94	-17.54	16.2

Sample	Epoch	Sample weight (mg)	% N	δ ^{15}N (‰)	% C	δ ^{13}C (‰)	C:N
BH12E-86-2-Bot	Holocene	31.511	0.68	2.59	14.39	-25.45	21.2
BH12E-121-3-Bot	Holocene	35.969	0.23	2.33	3.7	-25.29	16.0
BH12E-152-4-Bot	Holocene	50.676	0.38	2.16	6.0	-25.46	16.0
BH12E-191-Bot	Holocene	37.954	0.46	2.22	8.4	-25.56	18.1
BH12E-191-Bot-D	Holocene	20.477	0.46	2.19	8.3	-25.56	18.0
BH12E-259-7-Mid	Holocene	34.611	0.22	1.80	3.9	-24.21	17.8
BH12E-259-7-Top	Holocene	56.599	0.17	2.08	2.8	-24.33	17.1
BH12E-286-8-Top	Holocene	64.897	0.08	2.56	1.4	-18.35	17.8
BH12E-286-8-Top-D	Holocene	30.088	0.08	2.57	1.3	-18.38	18.2
BH12E-322-8-Top	Pleistocene	34.893	0.06	2.79	1.0	-15.68	18.1
BH12E-322-9-Bot	Pleistocene	37.842	0.05	2.48	1.0	-13.77	22.1
BH12E-358-10-Bot	Pleistocene	46.265	0.25	0.11	4.3	-24.32	17.5
BH12E-394-11-Mid	Pleistocene	39.775	0.26	0.73	4.0	-24.26	15.9
BH12E-430-12-Top	Pleistocene	53.379	0.16	0.15	3.0	-23.12	18.9
BH12E-466-13-Top	Pleistocene	46.048	0.23	-0.93	4.2	-24.41	18.4
BH12E-502-14-Top	Pleistocene	56.371	0.14	0.32	2.2	-21.83	16.5
BH12E-539-15-Mid	Pleistocene	24.182	0.27	-0.65	4.2	-24.64	15.9
BH12E-539-15-Mid-D	Pleistocene	34.753	0.27	-0.75	4.2	-24.70	15.5
BH12E-566-16-Mid	Pleistocene	51.076	0.23	-0.85	3.7	-24.26	16.4
BH12E-566-16-Mid-D	Pleistocene	37.305	0.23	-0.82	3.6	-24.27	16.3

Sample	Epoch	Sample weight (mg)	% N	δ ^{15}N (‰)	% C	δ ^{13}C (‰)	C:N
BH12F-74-1-Mid	Holocene	29.232	0.21	2.05	4.03	-26.04	19.2
BH12F-138-3-Bot	Holocene	35.954	0.28	3.12	4.17	-25.83	14.9
BH12F-286-7-Bot	Holocene	21.529	0.08	2.24	1.33	-25.53	16.0
BH12F-386-10-Mid	Holocene	48.017	0.25	2.21	4.17	-25.86	16.5
BH12F-452-12-Mid	Holocene	42.540	0.11	2.65	2.38	-23.47	21.3